COLLECTED PAPERS on Dressed Photon Science nd Technogy

Vol. 29

August 2013 – July 2014

Prof. Motoichi OHTSU

MEMBERS

(From April 1, 2014)

*[I] The University of Tokyo**

Professor

Motoichi OHTSU[(a-d)] (Dr. Eng.)

Associate Professor

Takashi YATSUI (Dr. Eng.)

Graduate Students (Doctor Candidate)

Hajime TANAKA
Jun Hyoung KIM

Graduate Students (Master Course)

Maiku YAMAGUCHI
Masaki IKEGAWA

Undergraduate Students

Ryosuke NAGUMO
Katsuhiro NISHIOKA

Secretary

Noriko KUROKI
Kumiko NOZAWA
Chikako UEOKA
Mamiko ITABASHI

a) Also a director "Nanophotonics Research Center, The Institute of Engineering Innovation, School of Engineering The University of Tokyo"
b) Also a director, "Preparatory research phase, Research and Development Program of Innovative Energy Efficiency Technology, and NEDO (New Energy and Industrial Technology Development Organization)
c) Also a director, NPO-Research Institute of Nanophotonics

(*)
Department of Electronics Engineering and Information Systems,
Graduate School of Engineering,
The University of Tokyo
(Room 215, Bldg. Eng. 9)
2-11-16 Yayoi, Bunkyo-ku, Tokyo 113-8656, Japan
Phone: +81-3-5841-1189
FAX: +81-3-5841-1140
E-mail: ohtsu@ee.t.u-tokyo.ac.jp
URL:http://uuu.t.u-tokyo.ac.jp/

東京大学大学院 工学系研究科 電気系工学専攻
〒113-8656　東京都文京区弥生 2-11-16　工学部 9 号館 215 号室
電話: 03-5841-1189, ファックス: 03-5841-1140
E-mail: ohtsu@ee.t.u-tokyo.ac.jp
URL: http://uuu.t.u-tokyo.ac.jp/

*[II] Preparatory research phase, Research and Development Program of Innovative Energy Efficiency Technology, NEDO project**

Professor

Motoichi OHTSU (Dr. Eng.)

Associate Professor

Takashi YATSUI (Dr. Eng.)

Researcher

Tadashi KAWAZOE (Dr. Sci.)
Wataru NOMURA (Dr. Eng.)
Naoya TATE (Dr. Info. Sci.)

Research Assistant

Ayako MIZUSHIMA
Etsuko OTA

Secretary

Noriko KUROKI
Kumiko NOZAWA

(*)
Department of Electronics Engineering and Information Systems,
Graduate School of Engineering,
The University of Tokyo
(Room 219, Bldg. Eng. 9)
2-11-16 Yayoi, Bunkyo-ku, Tokyo 113-8656, Japan
Phone: +81-3-5841-1670
FAX: +81-3-5841-1140
E-mail: info@ nanophotonics.t.u-tokyo.ac.jp
URL: http://uuu.t.u-tokyo.ac.jp/

東京大学大学院 工学系研究科 電気系工学専攻
〒113-8656 東京都文京区弥生 2-11-16 工学部 9 号館 219 号室
電話：+81-3-5841-1670, ファックス: +81-3-5841-1140
E-mail: info@ nanophotonics.t.u-tokyo.ac.jp
URL: http://uuu.t.u-tokyo.ac.jp/

*[Ⅲ]Nanophotonics Research Center**

Director

Motoichi OHTSU, Professor (core member)

Members

Kazuo HOTATE, Professor (core member)
Hitoshi TABATA, Professor (core member)
Masaki TANAKA, Professor (core member)
Takao SOMEYA, Professor
Yuichiro KATO, Associate Professor
Shinobu OHYA, Associate Professor
Masakazu SUGIYAMA, Associate Professor
Takashi YATSUI, Associate Professor
Munetoshi SEKI, Assistant Professor
Masanori KUBOTA, Assistant Professor
Tadashi KAWAZOE, Researcher
Wataru NOMURA, Researcher
Naoya TATE, Researcher

(*)
Institute of Engineering Innovation,
School of Engineering, The University of Tokyo
(Room 219, Bldg. Eng. 9)
2-11-16 Yayoi, Bunkyo-ku, Tokyo 113-8656, Japan
Phone: +81-3-5841-1670
FAX: +81-3-5841-1140
E-mail: info@ nanophotonics.t.u-tokyo.ac.jp
URL: http://www.npc.t.u-tokyo.ac.jp/

東京大学大学院 工学系研究科　総合研究機構
〒113-8656 東京都文京区弥生 2-11-16 工学部 9 号館 219 号室
電話：+81-3-5841-1670, ファックス: +81-3-5841-1140
E-mail: info@ nanophotonics.t.u-tokyo.ac.jp
URL: http://www.npc.t.u-tokyo.ac.jp/

*[Ⅳ] Nanophotonics Engineering Organization**

Director

Motoichi OHTSU

(*)
Nanophotonics Engineering Organization,
Specified Nomprofit Corporation
1-20-10 Sekiguchi, Bunkyo-ku, Tokyo 112-0014, Japan
Phone: +81-3-3267-6790. Fax: +81-3-5261-9788
E-mail: ohtsu-rinps@nanophotonics.t.u-tokyo.ac.jp
URL: http://www.nanophotonics.info/

特定非営利法人 ナノフォトニクス工学推進機構
〒112-0014 東京都文京区関口 1-20-10
電話: 03-3267-6790, ファックス: 03-5261-9788
E-mail: ohtsu-rinps@nanophotonics.t.u-tokyo.ac.jp
URL: http://www.nanophotonics.info/

LIST OF PAPERS

[(pp. XX-XX); pages in this issue of the COLLECTED PAPERS**]**

[I] ORIGINAL PAPERS

[7] M. Yamaguchi, T. Kawazoe, and M. Ohtsu, "Evaluating the coupling strength of electron–hole pairs and phonons in a 0.9 μm-wavelength silicon light emitting diode using dressed-photon–phonons," Appl. Phys. A, Volume 115, Issue 1, April 2014, pp. 119-125.
[Invited Paper]

(pp. 47-53)

[8] N. Wada, M. A. Tran, T. Kawazoe, and M. Ohtsu, "Measurement of multimode coherent phonons in nanometric spaces in a homojunction-structured silicon light emitting diode," Appl. Phys. A, Volume 115, Issue 1, April 2014, pp. 113-118.
[Invited Paper]

(pp. 55-60)

[9] M. A. Tran, T. Kawazoe, and M. Ohtsu, "Fabrication of a bulk silicon p–n homojunction-structured light-emitting diode showing visible electroluminescence at room temperature," Appl. Phys. A, Volume 115, Issue 1, April 2014, pp. 105-111.
[Invited Paper]

(pp. 61-67)

[10] T. Yatsui, W. Nomura, T. Mano, H. T. Miyazaki, K. Sakoda, T. Kawazoe, and M. Ohtsu, "Emission from a dipole-forbidden energy state in a GaAs quantum-ring induced by dressed photon," Appl. Phys. A, Volume 115, Issue 1, April 2014, pp. 1–4.
[Invited Paper]

(pp. 69-72)

[11] M. Naruse, N. Tate, Y. Ohyagi, M. Hoga, T. Matsumoto, H. Hori, A. Drezet, S. Huant, and M. Ohtsu, "Optical near-field–mediated polarization asymmetry induced by two-layer nanostructures," Opt. Express, Vol. 21, Issue 19, September 2013, pp. 21857-21870.

(pp. 73-86)

[12] S.-J. Kim, M. Naruse, M. Aono, M. Ohtsu, and M. Hara, "Decision Maker based on Nanoscale Photo-excitation Transfer," Scientific Report, Vol. 3, Article number 2370, August 2013, pp. 1-6.

(pp. 87-92)

[13] Y. Miyauchi, M. Iwamura, S. Mouri, T. Kawazoe, M. Ohtsu, and K. Matsuda, "Brightening of excitons in carbon nanotubes on dimensionality modification," Nature Photonics, Vol. 7, September 2013, pp. 715-719.

(pp. 93-97)

[14] N. Tate, M. Naruse, Y. Liu, T. Kawazoe, T. Yatsui, and M. Ohtsu, "Experimental demonstration and stochastic modeling of autonomous formation of nanophotonic droplets," Appl. Phys. B, Vol. 112, Issue 4, September 2013, pp. 587-592.

(pp. 99-104)

[II] PRESENTATIONS IN INTERNATIONAL CONFERENCES

[1] M. Ohtsu, "Dressed Photon Technology," IUMRS-ICEM2014 Programs, International Conference on Electronic Materials 2014 (IUMRS - ICEM2014), June10-14, 2014, Taipei, Taiwan, p. 11.
[Plenary speech]

(pp. 105)

[2] N. Tate and M. Ohtsu, "Nanophotonic droplet: a novel optical device consists of autonomously-coupled quantum dots," Program & Abstracts of 2013 Energy Materials Nanotechnology Meeting (2013 EMN Fall), December 7-10, 2013, Orlando, USA, p. 172.
[Invited Presentation]

(pp. 107)

[3] M. Naruse, N. Tate, M. Aono, S.-J. Kim, and M. Ohtsu, "Nanophotonics for computing and security applications," Program & Abstracts of 2013 Energy Materials Nanotechnology Meeting (2013 EMN Fall), December 7-10, 2013, Orlando, USA, p. 160.
[Invited Presentation]

(pp. 109)

[4] M. Naruse, N. Tate, M. Aono, and M. Ohtsu, "Near-field nanophotonics for computing and security," International conference on Hot Topics in Physical Informatics (HotPI), November 10-13, 2013, Changsha, China. (Abstracts unpublished)
[Invited Presentation]

(pp. 111)

[5] T. Yatsui and M. Ohtsu, "Dressed Photon-phonon Technology for Ultra Flat Surface," Proceedings of the International Conference Nanomaterials Application & Properties 2013, Nanomaterials Application & Properties 2013, September 16-21, 2013, Crimea, Ukraine, paper number: 5.2, 01PCSI09.
[Plenary talk]

(pp. 113-115)

[6] N. Tate, M. Naruse, and M. Ohtsu, "Basics of optical processing system based on nanophotonic droplets," Abstracts of The JSAP-OSA Joint Symposia 2013, The JSAP-OSA Joint Symposia 2013, September 16-20, 2013, Kyoto, Japan, paper number: 17p-D5-1.
[Invited Presentation]

(pp. 117)

[7] M. Naruse, T. Yatsui, W. Nomura, T. Kawazoe, M. Aida, and M. Ohtsu, "Multiscale Surface Roughness Measure for Dressed-Photon-Phonon Etching," Proceedings of the 2013 International Symposium on Nonlinear Theory and its Applications (NOLTA2013), The 2013 International Symposium on Nonlinear Theory and its Applications (NOLTA2013), September 8-11, 2013, Santa Fe, USA, pp. 499-502 .

(pp. 119-122)

[III] REVIEW PAPERS

[1] T. Yatsui, W. Nomura, F. Stehlin, O. Soppera, M. Naruse, and M. Ohtsu, "Challenge in realizing ultra-flat material surfaces," Beilstein Journal of Nanotechnology, Volume 4, December 2013, pp.875–885.

(pp. 123-133)

[2] T. Yatsui and M. Ohtsu, "Development of super polishing technology using dressed-photon phonon nano-polishing," Journal of Japan Laser Processing Society, Vol. 20, No.2, July, 2013, pp. 130-132.
【八井崇、大津元一、「ドレストフォトンナノポリッシングを用いた超平滑加工技術の開発」、『レーザー加工学会誌』、第 20 巻、第 2 号、2013 年 7 月、pp. 130-132】

(pp. 135-137)

[IV] PUBLISHED BOOKS

[1] M. Ohtsu, *Introduction to Dressed Photons*, Maruzen Planet Co., Tokyo, March 2014, (135pages)
【大津元一, 「ドレス光子はやわかり」, (丸善プラネット, 東京, 2014 年 3 月) (135 ページ)】

(pp. 139-143)

[2] M. Aono, S.-J. Kim, M. Naruse, M. Wakabayashi, H. Hori, M. Ohtsu, and M. Hara, "A Nanophotonic Computing Paradigm: Problem-Solving and Decision-Making Systems Using Spatiotemporal Photoexcitation Transfer Dynamics," in *Nanophotonic Information Physics* (ed. by M. Naruse), Springer-Verlag, Berlin, January 2014, pp.223-244.

(pp. 145)

[3] N. Tate, M. Naruse and M. Ohtsu, "Engineering of a Nanometric Optical System Based on Optical Near-Field Interactions for Macro-Scale Applications," in *Nanophotonic Information Physics* (ed. by M. Naruse), Springer-Verlag, Berlin, January 2014, pp.161-182.

(pp. 147)

[4] M. Naruse, N. Tate, M. Aono, and M. Ohtsu, "Nanointelligence: Information Physics Fundamentals for Nanophotonics," *Nanophotonic Information Physics* (ed. by M. Naruse), Springer, Berlin, 2014, pp. 1-39.

(pp. 149)

[5] M. Ohtsu, *Dressed Photons*, Springer-Verlag, Berlin, November 2013. (324 pages)

(pp. 151-156)

[6] M. Ohtsu (ed.), *Handbook of Nano-Optucs and Nanophotonics*, Springer-Verlag, Berlin, June 2013. (1071 pages)

(pp. 157-163)

[Ⅴ] AWARDS

[1] K. Suzuki, Dean's Award from the Faculty of Engineering and The Best Bachelor Thesis Award, “Green SiC-LEDs by dressed-photon—phonon annealing,” March 2014.
鈴木健太郎、「工学部長賞」および「優秀卒業論文賞」
受賞対象題目「ドレスト光子フォノン援用アニールによる緑色 SiC-LED」（2014 年 3 月）

[2] V. Q. Huy, The Best Bachelor Thesis Award, “Ultraviolet SiC-LEDs by dressed-photon—phonon annealing,” March 2014.
ヴォ クオック フイ、「優秀卒業論文賞」
受賞対象題目「ドレスト光子フォノン援用アニールによる紫外 SiC-LED」（2014 年 3 月）

[3] N. Wada, Dean's Award from the Graduate School of Engineering and The Best Master Thesis Award, “Controlling the emission spectral profiles of bulk Si-LEDs by coherent phonon and analysis of the emission mechanisms”, March 2014.
和田直樹、工学系研究科長賞」および「優秀修士論文賞」
受賞対象題目「コヒーレントフォノン制御によるバルク Si-LED の発光スペクトルの形状制御と発光機構の解明」（2014 年 3 月）

[4] M. Yamaguchi, The Best Poster Presentation Award, “Study on emission spectra of Si-LEDs based on the dressed-photon—phonon scattering model,” The 14th Meeting of The Laser Society (Tokyo Section), March 2014.
山口真生、 2014 年 第 14 回 レーザー学会 東京支部研究会「ポスター講演優秀賞」
受賞対象題目「ドレスト光子-フォノン散乱モデルによる Si-LED の発光スペクトルの考察」（2014 年 3 月）

[5] K. Suzuki, The Best Presentation Award, “Fabrication of 532nm-wavelength SiC-LEDs by phonon-assisted annealing,” The 5th Nanophotonics Student Workshop, November 2013.
鈴木健太郎、第 5 回 ナノフォトニクス学生研究講演会「優秀発表賞」

受賞対象題目「フォノン援用アニールを用いた 532nm 帯発光の SiC-LED 作製」（2013 年/11 月）

[6] N. Wada, The Excellent Presentation Award for Young Scientists, “Emission spectral control by manipulating phonons in a homo-junctioned Si-LEDs,” The 35th Annual Meeting of Japan Society of Applied Physics, November 2013.
和田直樹、第 35 回（2013 年秋季）応用物理学会「講演奨励賞」
受賞対象題目「ホモ接合 Si-LED 内のフォノン操作による発光スペクトル制御」（2013 年 11 月）

[I] ORIGINAL PAPERS

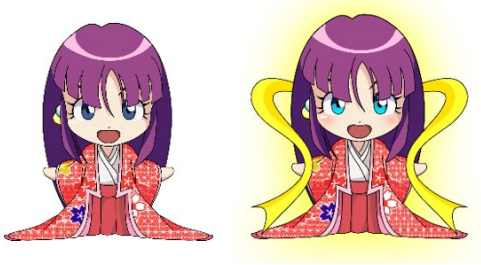

Coupling of Er light emissions to plasmon modes on In_2O_3: Sn nanoparticle sheets in the near-infrared range

Hiroaki Matsui,[1,2,a)] Wasanthamala Badalawa,[2] Takayuki Hasebe,[3] Shinya Furuta,[4] Wataru Nomura,[2] Takashi Yatsui,[2] Motoichi Ohtsu,[2] and Hitoshi Tabata[1,2]
[1]*Department of Bioengineering, The University of Tokyo, 1-3-7 Hongo, Bunkyo-ku, Tokyo 113-8656, Japan*
[2]*Department of Electrical Engineering and Information Systems, The University of Tokyo, 1-3-7 Hongo, Bunkyo-ku, Tokyo 113-8656, Japan*
[3]*Central Customs Laboratory, Ministry of Finance, 5-3-6 Kashiwanoha, Kashiwa, Chiba 270-0882, Japan*
[4]*Tomoe Works Co. Ltd., 1-3-6 Namiyoke, Minato-ku, Osaka 552-0001, Japan*

(Received 20 April 2014; accepted 20 July 2014; published online 30 July 2014)

Near-infrared Er photoluminescence (PL) is markedly modified using a plasmonic In_2O_3: Sn nanoparticle (NP) sheet. Modeling and optical measurements reveal the presence of different electric fields (*E*-field) in the NP sheet. The local *E*-field excited at the interface between the NP sheet and Er-emitting layer of ZnO contributes significantly towards the spectral modifications of Er PL due to matching with the photon energy of Er PL. We also determine the critical temperature for Er PL modifications, which is related to the energy transfer efficiency between Er transition dipoles in ZnO and the plasmon modes on the NP sheet. © *2014 AIP Publishing LLC*.
[http://dx.doi.org/10.1063/1.4892004]

Local surface plasmon resonances (LSPRs) in doped oxide semiconductor nanoparticles (NPs) such as In_2O_3: Sn (ITO) and ZnO: Al have received interest for plasmonic materials in the near-infrared (NIR) range.[1–3] Recent research has focused on the fundamental properties of LSPRs, such as the tuning of LSPR energy based on the static and dynamic control of free carriers.[4,5] Our group has reported sensing platforms using ITO-based surface plasmons.[6] It is important to study LSPRs in doped oxide semiconductor NPs from a practical point of view. Furube *et al.* found that ITO NP sheets enhanced two-photon absorptions of dye molecules.[7] Moreover, theoretical contributions that explain the properties of ITO NP sheets have progressed.[8,9]

For the investigation of metal NPs, the use of NP sheets provides powerful methods in surface-enhanced Raman and fluorescence spectroscopies.[10,11] When metal NPs are placed in close proximity to one another, coupling LSPR occurs in the gap between NPs. The magnitude of LSPR increases with the strength due to interparticle coupling, which is related to collective plasmonic excitations.[12] This mode is expected for a luminescent enhancement, as confirmed using hybrid structures consisting of Ag NPs and InGaN/GaN quantum wells (QWs).[13] However, LSPR energies on metal NP sheets are mainly limited to the visible region. The use of doped oxide semiconductor NPs extends to longer wavelengths in the NIR range. In particular, plasmon coupling to light emissions at 1.54 μm from Er ions is important for the development of optical telecommunications.[14] Studies concerning the coupling of Er emissions to plasmon modes on doped oxide semiconductors have yet to be reported.

In this Letter, we report on the coupling of optically active Er ions with the plasmon modes of ITO NP sheets in the NIR range. The structural and optical properties of NPs and respective NP sheets are investigated in addition to theoretical aspects. Er-doped ZnO (ZnO: Er) was chosen for the emitting layers given its expected behavior as an optical amplifier in the waveguides.[15,16] A remarkable change of luminescence from Er ions positioned close to the NP sheets is observed. The plasmonic coupling of Er emission to the NP sheet is discussed in terms of temperature-dependent Er photoluminescence (PL).

X-ray diffraction (XRD) patterns of NPs show broad peaks characteristic of colloidal ITO NPs with a crystalline nature [Fig. 1(a)].[17] Fabrications of the NPs are described in Sec. 1 of the supplementary material.[18] The *a*-axis length increased from 10.087 Å to 10.152 Å following doping with Sn atoms. Local structures of NPs were obtained by transmittance electron microscopy (TEM) [inset of Fig. 1(a)]. The electron diffraction patterns revealed that the lattice interval (d_{222}) of the (222) plane at the center region (0.301 nm) was similar to that at the edge region in the NP (0.302 nm) [inset of Fig. 1(b)]. The results of energy-dispersive X-ray microscopy showed that the Sn content [Sn] at the center region (5.4%) was similar to that at the edge region (5.2%), indicating that Sn impurities in the NP were spatially homogeneous [Fig. 1(b)]. The diameter of NPs obtained from TEM was about 20 nm, as also confirmed by dynamic light scattering [Fig. 1(c)]. However, crystallite sizes based on Scherrer's equation from the (222) peak of XRD patterns were estimated as 1.58 and 2.20 nm for un-doped and doped NPs, respectively [Sec. 2 of the supplementary material].[18–20] Broadening of the line-width of the XRD pattern is related to structural imperfections such as defects and strains. The difference between crystalline and particle sizes is due to the presence of structural defects in the NPs. Additionally, the optical properties of NPs were measured using a near-infrared spectrometer. The extinction spectrum of NPs showed an asymmetric shape with a LSPR peak at 0.680 eV, which was fitted by Mie absorption with a frequency-dependent damping factor with ionized impurity scattering.

[a)]Author to whom correspondence should be addressed: Electronic mail: hiroaki@ee.t.u-tokyo.ac.jp

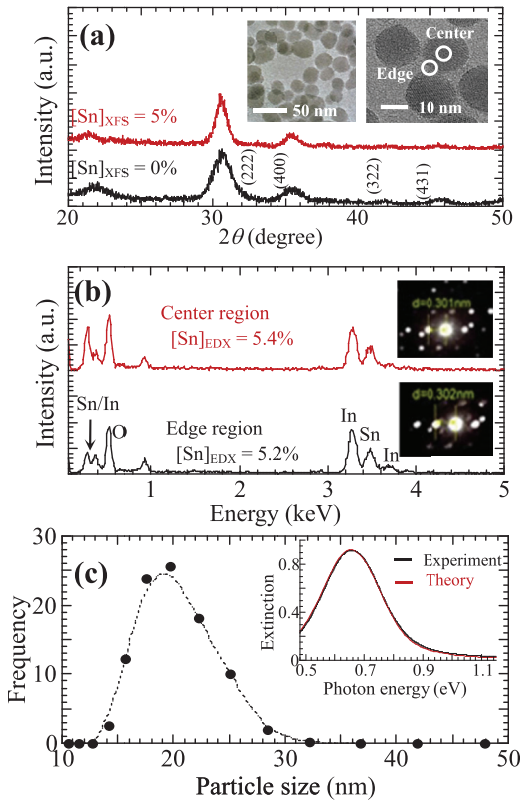

FIG. 1. (a) XRD patterns of ITO NPs with Sn contents of 0% and 5%. Inset shows low-resolution (left) and high-resolution (right) TEM images of an ITO NP with a Sn content of 5%. (b) EDX spectra at the center and edge regions in the NP. Inset represents ED patterns of the (222) plane at the center and edge. (c) Distribution of particle size estimated by dynamic light scattering. Inset represents the extinction spectrum of NPs dispersed in toluene. A red line shows the parameter fitting using Mie absorption with ionized impurity scattering.

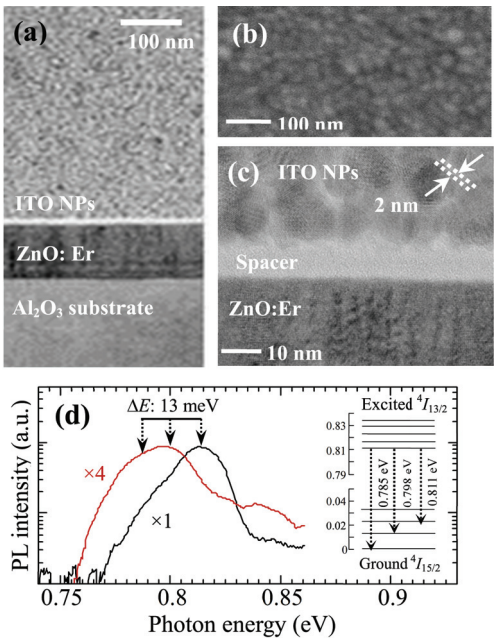

FIG. 2. (a) Cross-section TEM image of a hybrid structure consisting of an NP sheet and ZnO: Er layer. (b) Surface SEM morphology of the NP sheet. (c) Cross-section TEM image of the hybrid structure focused on the interface between the NP sheet and ZnO: Er layer. (d) Er PL spectra at 10 K of coated (red line) and uncoated (black line) ZnO: Er layers. Inset indicates an energy-level diagram of the Stark levels of Er emission.

This is used as index of the optical characteristic of an isolated ITO NP [inset of Fig. 1(c) and Sec. 3 of the supplementary material].[18,21]

Plasmon coupling to Er light emission was achieved using a hybrid structure comprising an ITO NP sheet and ZnO: Er layer (Er content: 1%). A ZnO: Er layer (80-nm thickness) was grown on a *c*-face sapphire by pulsed laser ablation. ArF excimer laser pulses were focused on ZnO: Er targets located 3.5 cm from the substrate in an O_2 flow of 10^{-3} Pa. The NP sheet (300-nm thickness) was deposited on the ZnO: Er layer with a SiO_2 spacer by spin-coating, and then heat-treated at 250 °C in an Ar atmosphere. The spacer provided spatial separation of the NP sheet from the ZnO: Er layer. Scanning electron microscopy (SEM) revealed that the surface morphology of the NP sheet comprised a closed-packed structure with a slight size distribution [Fig. 2(b)]. Examination of a cross-section TEM image revealed that the gap length between NPs was about 2 nm, and the separation distance between the NP sheet and ZnO: Er layer was 10 nm [Fig. 2(c)]. The plasmon-enhanced PL is related to the separation distance between the emitting layers and metal nanostructures. PL is damped by energy transfer at the smaller distances when the emitting layers and metal nanostructures are in close contact, which is suppressed with increasing separation distance. It is reported that plasmon-enhanced PL on metal-emitter systems, such as Ag-InGaN/GaN QWs, Au-CdSe QDs, and Ag-Eu^{3+} emitters, has been obtained with separation distances of around 10 nm.[22–24] A spacer thickness of 10 nm between the NP sheet and ZnO: Er layer was chosen for experiments.

NIR PL was dispersed using a 30-cm single monochromator with a liquid-nitrogen-cooled InGaAs detector. A He-Cd laser was used as the excitation source. PL excitation and luminescence collection were performed from the substrate side. A ZnO: Er layer without the NP sheet (uncoated ZnO: Er) showed a maximum peak of 0.811 eV at 10 K [black line in Fig. 2(d)], corresponding to energy transitions from the excited $^4I_{13/2}$ to ground $^4I_{15/2}$ states of Er ions [inset of Fig. 2(d)]. Furthermore, a shoulder structure at 0.798 eV is ascribed to Stark splittings with the several sub-bands because Er ions in ZnO are located in six-fold configurations with bonding to neighboring oxygen atoms.[25] In contrast, the PL peak of the ZnO: Er layer with the NP sheet (coated ZnO: Er) showed a redshift of 13 meV compared to that of the uncoated ZnO: Er layer [red line in Fig. 2(d)], and is close to an energy interval of a Stark sub-band. The PL intensity of the coated ZnO layer was four-fold higher than that of the uncoated ZnO layer. Above all, a strongly increased spectral composition compared to that of the uncoated ZnO: Er layer was found in the low photon energy region of the spectrum. This indicated that the proximal NP sheet modulated the luminescent transitions in the Stark sub-bands of Er ions. A similar behavior has also been observed for Er PL from SiO_2: Er layers with Ag nanogratings related to surface plasmons at Ag-SiO_2: Er interfaces.[26]

In an effort to clarify plasmon-related Er PL, the optical response of the NP sheets deposited on glass substrates was examined in preliminary experiments [inset of Fig. 3(a)]. No peak structure in extinction spectra was observed in the NIR

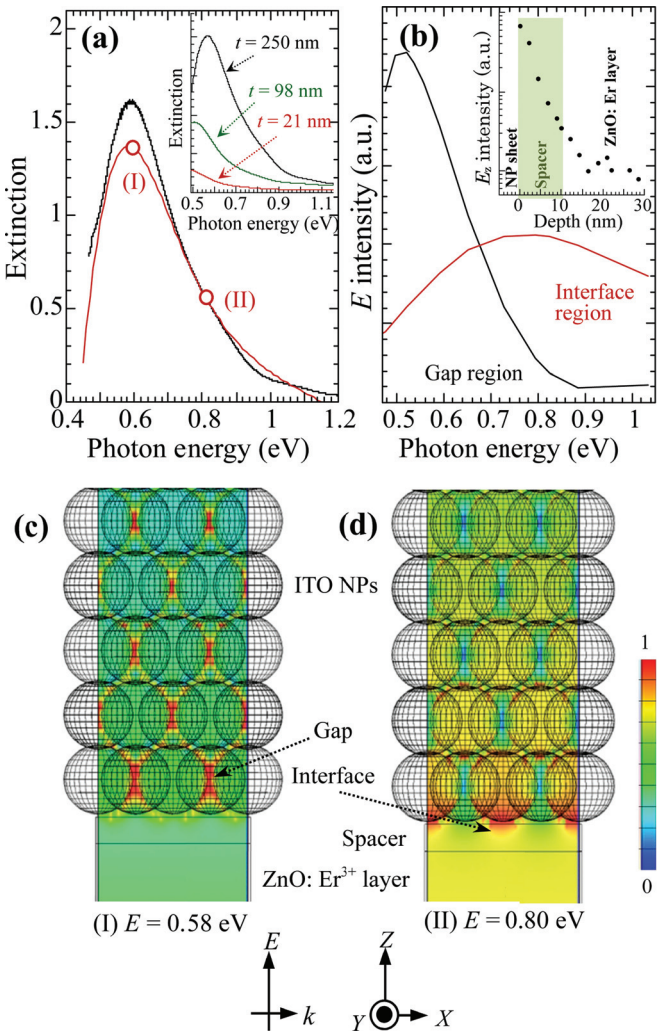

FIG. 3. (a) Extinction spectra of the NP sheet with a thickness (t) of 300 nm. Experimental data (black) are compared with theoretical data (red) calculated using the FDTD simulation. Inset indicates extinction spectra of the NP sheet with different thicknesses on glass substrates. (b) E intensities at the gap (black) and interface (red) as a function of photon energy. Inset indicates a decay length of E_z intensity along the z direction at 0.80 eV. Electric field distributions at photon energies of 0.58 eV and 0.80 eV are shown in (c) and (d), respectively.

range at thicknesses of 21 and 98 nm, while NP sheets with a thickness of 260 nm provided a clear peak at around 0.58 eV. A shoulder structure appeared simultaneously at around 0.80 eV. The extinction spectra of the NP sheets comprised two optical components, which were also found in the NP sheet on the ZnO: Er layer [black line in Fig. 3(a)]. The extinction spectra of NP sheets revealed an asymmetric feature of high photon energy, which differed from those of NPs [inset of Fig. 1(c)]. The difference in extinction spectrum between NPs and NP sheets is related to the excitation mechanism of plasmon resonance, which was clarified using a finite-difference time-domain (FDTD) simulation.

The modeled NP sheet has a hexagonally packed structure with an interparticle distance of 2 nm, which was positioned on the ZnO: Er layer with a spacer of 10 nm. The dielectric constants of NPs were taken from ellipsometric data of an ITO layer.[6] The refractive index ($n = 1.437$) of capric acid was applied to the medium between the NPs since capric acid was used for the organic ligands on the NP surfaces.[27] The modeled structure was illuminated with light directed in the Z-direction from the ZnO: Er layer side. The direction of the electric field was perpendicular to the light and parallel to the X direction. Furthermore, the hybrid structure was simulated using periodic boundary conditions along the X and Y axes. The electric field distribution was simulated at the XZ plane. The calculated extinction spectrum of the NP sheet was dependent on the number of NP layers. The extinction spectra enhanced with increasing number of NP layers [Figure S2(a) of supplementary material].[18] No peak structure in extinction spectra was observed for NP sheets with 1 or 5 NP layers, while NP sheets with 7, 10, or 22 NP layers showed a peak structure in the NIR range. The dependence of the change in extinction spectrum on the number of NP layers may be related to inter-coupling between NPs along the Z-direction. In particular, for a model of a NP sheet with 22 NP layers, the calculated extinction spectrum was similar to the experimental extinction spectrum [red line in Fig. 3(a)].[18]

The spatial distribution of the electric field (E-field) was dependent on the excitation photon energy. The E-field (I) at 0.58 eV was strongly localized in the gap between the NPs [Fig. 3(c)]. This was due to plasmon coupling between the NPs, as characterized by the redshift observed for the LSPR energy of the isolated NPs. In contrast, the E-field (II) at 0.80 eV appeared at an interface between the NP sheet and ZnO: Er layer [Fig. 3(d)]. Figure 3(b) shows E-field intensities at the gap and interface as a function of photon energy. The maximum E-field at the gap was obtained at 0.58 eV, while the E-field at the interface showed a maximum peak at 0.80 eV. The NP sheet exhibited different E-fields at both the gap and interface in the NIR range, which could account for the two optical components in the extinction spectrum. Besides, the penetration depth of the E-field into the ZnO: Er layer acts as an important factor to change Er PL. The E_z intensity along the z-direction of E-field (II) at the interface exponentially decayed into the ZnO: Er layers by passing through the spacer layer [inset of Fig. 3(b)], which allows coupling of plasmons with Er emission. The magnitude of E-field (II) at the interface was dependent on the number of NP layers in the NP sheet. The highest E-field (II) was obtained in a NP sheet with 22 NP layers, which simultaneously provided a large penetration depth for E_z intensity [Figures 2(b) and 2(c) of supplementary material]. Accordingly, the FDTD calculations revealed that a thick NP sheet with a thickness of 300 nm was effective in enhancing Er PL.

The coupling of Er emission to the NP sheet will be discussed in relation to the temperature-dependent Er PL spectra [Figs. 4(a) and 4(b)]. The PL peak positions of the coated ZnO: Er layer moved to low photon energies with increasing temperature, which was close to that observed for the uncoated ZnO: Er layer at 50 K [Fig. 4(c)]. Moreover, the enhanced PL intensity at 10 K of the coated ZnO: Er layer gradually weakened with increasing temperature, and then returned to the PL intensity of the uncoated ZnO: Er layer at 50 K [Fig. 4(d)]. The spectral modifications of Er PL were simultaneously induced with PL enhancement.

An Arrhenius plot of the PL intensity (I_{Er}) for the uncoated ZnO: Er layer could be fitted with two nonradiative recombination channels [Fig. 5][28]

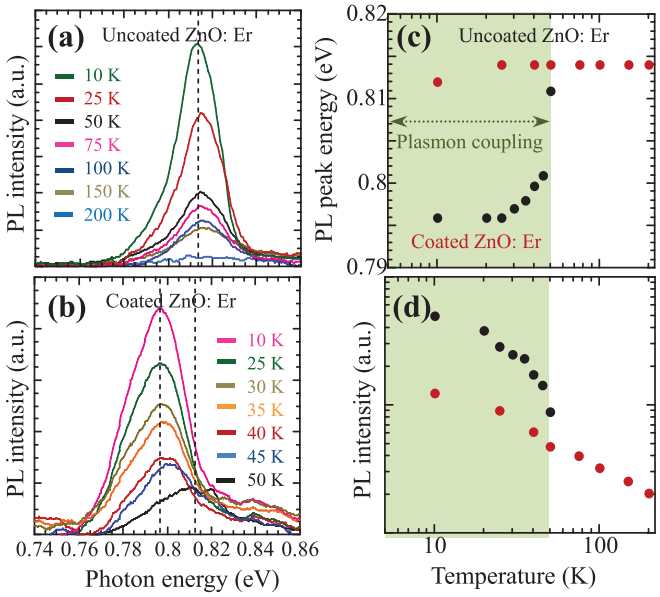

FIG. 4. (a) Temperature dependence of Er PL spectra in the NIR range for uncoated (a) and coated (b) ZnO: Er layers. (c) Er PL peak energy as a function of temperature for uncoated (black) and coated (red) ZnO: Er layers. (d) Dependence of Er PL intensity on temperature for uncoated (black) and coated (red) ZnO: Er layers.

$$\frac{I_{Er}(T)}{I_0} = \frac{1}{1 + A\exp\left(-\frac{E_A}{k_B T}\right) + B\exp\left(-\frac{E_B}{k_B T}\right)}, \quad (1)$$

where I_0 is the PL intensity at 10 K, and A and B represent rate constants. E_A and E_B values were 7.6 and 48 meV, respectively. Er PL is due to energy transfer processes as follows. Electron-hole pairs formed in ZnO after the UV excitation result in nonradiative energy transfer to Er ions, producing Er PL in place of excitonic luminescence. The small E_A should be related to the thermal dissociation energy of electron-hole pairs. This dominates energy transfer efficiency from the ZnO host to Er ions that determines a quantum yield of Er PL at the low temperatures.[29,30] The first nonradiative channel with the small E_A is related to the enhanced Er PL at low temperatures below 50 K [green line in Fig. 5]. In contrast, the large E_B at the high temperatures corresponds to thermally activated PL quenching [blue line in Fig. 5], contributing to no plasmon coupling to Er PL.

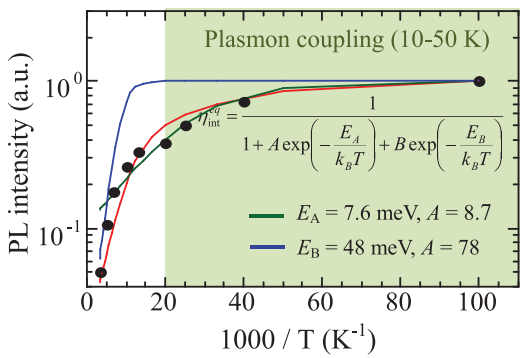

FIG. 5. Dependence of PL intensity on temperature for the ZnO: Er layer. Values obtained for parameters were $A = 8.7$, $E_A = 7.6$ meV, $B = 78$, and $E_B = 48$ meV.

Energy coupling between transition dipoles of emitters and plasmons of metal NPs is dependent on the quantum yield of the emitter, which has been reported for metal NPs combined with light emissions from dyes, QDs and QWs.[31–33] In the Persson model, the energy coupling efficiency (ϕ_{ET}) can be written by the separation distance (d) between the ZnO: Er layer and the NP sheet as follows:[34]

$$\phi_{ET} = \frac{1}{1 + \left(\frac{d}{d_o}\right)^4}, \quad (2)$$

$$d_0 = \left(\frac{0.225 c^3 \Phi}{\omega^2 \omega_F k_F}\right), \quad (3)$$

where c is the speed of light. Φ and ω ($4.1 \times 10^6\,s^{-1}$) are the quantum yield and emission frequency of the Er PL, respectively. ω_F ($8.3 \times 10^{15}\,s^{-1}$) and k_F ($3 \times 10^9\,m^{-1}$) are the Fermi frequency and Fermi wave vector of the ITO NP, respectively. ϕ_{ET} is only dependent on the Φ value of the Er PL because the d value was set to 10 nm in the hybrid structure. It was thought that the coupling of Er PL to the NP sheet was only observed at low temperatures below 50 K where Er PL with high Φ values could be realized, while a low Φ weakened plasmon coupling to Er PL at high temperatures.

In summary, we found a remarkable change of Er PL by coupling with the ITO NP sheets. Experimental and theoretical aspects revealed that the extinction spectra of NP sheets comprised two optical components with different E-fields in the NIR range. The spectral modifications of Er PL were related to the E-field at the interface that matched the luminescent energy of the Er ions, and was further explained by considering the temperature dependence of Er PL. This study demonstrated the possibility of alternative plasmonic materials on doped oxide semiconductor NPs.

This work was supported in part by a grant-i-Aid for JSPS Core-to-Core Program, A. Advanced Research Network, and Materials Design through Computics from MEXT Japan (No. 25104708).

[1]M. D. Losego, A. Y. Efremenko, C. L. Rhodes, M. G. Cerruti, S. Franzen, and J. P. Maria, J. Appl. Phys. **106**, 024903 (2009).
[2]W. Badalawa, H. Matsui, A. Ikehata, and H. Tabata, Appl. Phys. Lett. **99**, 011913 (2011).
[3]G. V. Naik, J. Kim, and A. Boltasseva, Opt. Mater. Express. **1**, 1090 (2011).
[4]R. Buonsanti, A. Llordes, S. Aloni, B. A. Helms, and D. J. Milliron, Nano Lett. **11**, 4706 (2011).
[5]G. Garcia, R. Buonsanti, E. L. Runnerstrom, R. J. Mendelsberg, A. Llordes, A. Anders, T. Richardson, and D. J. Milliron, Nano Lett. **11**, 4415 (2011).
[6]H. Matsui, W. Badalawa, A. Ikehata, and H. Tabata, Adv. Opt. Mater. **1**, 397 (2013).
[7]A. Furube, T. Yoshinaga, M. Kanehara, M. Eguchi, and T. Teranishi, Angew. Chem., Int. Ed. **51**, 2640 (2012).
[8]T. G. Pedersen and J. Jung, J. Appl. Phys. **113**, 114904 (2013).
[9]Z. Jakšić, M. Milinović, and D. Randjelović, J. Mech. Eng. **58**, 397 (2013).
[10]Y. K. Park, S. H. Yoo, and S. Park, Lagmuir **24**, 4370 (2008).
[11]Y. Matsumoto, R. Kanemoto, T. Itoh, S. Nakanishi, M. Ishikawa, and V. Biju, J. Phys. Chem. C **112**, 1345 (2008).
[12]M. Toma, K. Toma, K. Michioka, Y. Ikezoe, D. Obara, K. Okamoto, and K. Tamada, Phys. Chem. Chem. Phys. **13**, 7459 (2011).

[13]L. W. Jang, D. W. Jeon, T. Sahoo, D. S. Jo, J. W. Ju, S. J. Lee, J. H. Baek, J. K. Yang, J. H. Song, A. Y. Polyakov, and I. H. Lee, Opt. Express **20**, 2116 (2012).
[14]G. N. van den Hoven, E. Snoeks, A. Polman, C. van Dam, J. W. M. van Uffelen, and M. K. Smit, J. Appl. Phys. **79**, 1258 (1996).
[15]M. Kohls, M. Bonanni, L. Spanhel, D. Su, and M. Giersig, Appl. Phys. Lett. **81**, 3858 (2002).
[16]S. Kumuro, T. Katsumata, T. Morikawa, X. Zhao, H. Isshiki, and Y. Aoyagi, Appl. Phys. Lett. **76**, 3935 (2000).
[17]Z. Sun, J. He, A. Kumbhar, and J. Fang, Langmuir **26**, 4246 (2010).
[18]See supplementary material at http://dx.doi.org/10.1063/1.4892004 for fabrications, crystalline evaluations, and optical properties of ITO NPs, and FDTD calculations of ITO NP sheets.
[19]A. L. Patterson, Phys. Rev. B **56**, 972 (1939).
[20]J. S. An, S. C. Kim, S. H. Hahn, S. K. Ko, and E. J. Kim, J. Korean Phys. Soc. **45**, 162912 (2004).
[21]H. Matsui, S. Furuta, and H. Tabata, Appl. Phys. Lett. **104**, 211903 (2014).
[22]K. Okamoto, I. Niki, A. Sherer, Y. Narukawa, T. Mukai, and Y. Kawakami, Appl. Phys. Lett. **87**, 071012 (2005).
[23]Y. H. Chan, J. Chen, S. E. Wark, S. L. Skiles, D. H. Son, and J. D. Batteas, ACS Nano **3**, 1735 (2009).
[24]A. Pillonnet, A. Bertheolt, A. Pereira, O. Benamara, S. Derom, G. C. Frances, and A. M. Jurdyc, Appl. Phys. Lett. **100**, 153115 (2012).
[25]M. Ishii, S. Komuro, T. Morikawa, and Y. Aoyangi, J. Appl. Phys. **89**, 3679 (2001).
[26]J. Kalkman, C. Strohhöfer, B. Gralak, and A. Polman, Appl. Phys. Lett. **83**, 30 (2003).
[27]N. Adriaanse, H. Dekker, and J. Coopes, Recl. Trav. Chim. Pays-Bas **83**, 557 (1964).
[28]R. Boyn, Phys. Status Solidi B **148**, 11 (1988).
[29]F. Xiao, R. Chen, Y. Q. Shen, Z. L. Dong, H. H. Wang, Q. Y. Zhang, and H. D. Sun, J. Phys. Chem. C **116**, 13458 (2012).
[30]W. Badalawa, H. Matsui, T. Osone, N. Hasuike, H. Harima, and H. Tabata, J. Appl. Phys. **109**, 053502 (2011).
[31]H. Matsui, W. Nomura, T. Yatsui, M. Ohtsu, and H. Tabata, Opt. Lett. **36**, 3735 (2011).
[32]A. Yoshida and N. Kometani, J. Phys. Chem. C **114**, 2867 (2010).
[33]X. R. Su, W. Zhang, L. Zhou, X. N. Peng, D. W. Pang, S. D. Liu, Z. K. Zhou, and Q. Q. Qang, Appl. Phys. Lett. **96**, 043106 (2010).
[34]T. Pons, I. L. Medintz, K. E. Sapsford, S. Higasiya, A. F. Grimes, D. S. English, and H. Mattoussi, Nano Lett. **7**, 3157 (2007).

Hindawi Publishing Corporation
Advances in Optical Technologies
Volume 2014, Article ID 958327, 8 pages
http://dx.doi.org/10.1155/2014/958327

Research Article

Emission Spectral Control of a Silicon Light Emitting Diode Fabricated by Dressed-Photon-Phonon Assisted Annealing Using a Short Pulse Pair

Tadashi Kawazoe,[1,2] Naoki Wada,[1] and Motoichi Ohtsu[1,2]

[1] *Department of Electrical Engineering and Information Systems, Graduate School of Engineering, The University of Tokyo, 2-11-16 Yayoi, Bunkyo-ku, Tokyo 113-8656, Japan*
[2] *Nanophotonic Research Center, Graduate School of Engineering, The University of Tokyo, 2-11-16 Yayoi, Bunkyo-ku, Tokyo 113-8656, Japan*

Correspondence should be addressed to Tadashi Kawazoe; kawazoe@ee.t.u-tokyo.ac.jp

Received 24 April 2014; Accepted 5 June 2014; Published 6 July 2014

Academic Editor: Takashi Yatsui

We fabricated a high-efficiency infrared light emitting diode (LED) via dressed-photon-phonon (DPP) assisted annealing of a p-n homojunctioned bulk Si crystal. The center wavelength in the electroluminescence (EL) spectrum of this LED was determined by the wavelength of a CW laser used in the DPP-assisted annealing. We have proposed a novel method of controlling the EL spectral shape by additionally using a pulsed light source in order to control the number of phonons for the DPP-assisted annealing. In this method, the Si crystal is irradiated with a pair of pulses having an arrival time difference between them. The number of coherent phonons created is increased (reduced) by tuning (detuning) this time difference. A Si-LED was subjected to DPP-assisted annealing using a 1.3 μm ($h\nu$ = 0.94 eV) CW laser and a mode-locked pulsed laser with a pulse width of 17 fs. When the number of phonons was increased, the EL emission spectrum broadened toward the high-energy side by 200 meV or more. The broadening towards the low-energy side was reduced to 120 meV.

1. Introduction

Direct transition type semiconductors are mainly used in semiconductor light emitting diodes (LEDs) [1, 2]. The reason for this is that the probability of electric dipole transitions, in other words, the radiative recombination probability, is high. Also, the emission wavelength is determined by the bandgap energy, E_g, of the material used. Therefore, for example, InGaAsP epitaxially grown on an InP substrate is mainly used as the active layer for near-infrared LEDs with emission wavelengths of 1.00–1.70 μm (0.73–1.24 eV), which includes the optical fiber communication wavelength band. Shortcomings with this approach are that InP is highly toxic [3], and In is a rare resource. Silicon (Si), on the other hand, is a semiconductor having low toxicity and no concerns about depletion of resources; however, its emission efficiency is low since it is an indirect transition type semiconductor. Therefore, Si is usually not suitable as a material for use in LEDs. Nevertheless, there is a great demand for the use of Si in light emitting devices, and there has been extensive research into improving its emission efficiency. For example, there has been research into making Si emit light in the visible region by utilizing the quantum size effect of Si and by using porous Si [4], a Si/SiO_2 superlattice structure [5, 6], and Si nanoprecipitates in SiO_2 [7], as well as research into making Si emit light in the near-infrared region by doping it with light-emitting materials, such as erbium (Er)-doped Si [8] and silicon-germanium (Si-Ge) [9]. However, the reported external quantum efficiencies and power conversion efficiencies of LEDs using these materials have been low, at 0.5% and 0.8%, respectively [10].

On the other hand, using a homojunction-structured Si bulk crystal, we realized a high-efficiency, wideband LED in which the spatial distribution of the dopant density in

the Si was modified via a novel process of dressed-photon-phonon assisted annealing (DPP-assisted annealing) [11], and we achieved an external quantum efficiency of 40% and a power conversion efficiency of 50% [12]. A dressed photon (DP) is a quasi-particle created when a photon couples with an electron-hole pair in a nanometric region. Similarly, a dressed-photon-phonon (DPP) is a quasi-particle created when a DP couples with a phonon in a nanometric region. We have also succeeded in developing a Si laser [13], an infrared Si photodetector [14], and a Si relaxation oscillator [15], by using DPP-assisted annealing. These devices operate based on transitions mediated by DPPs, and the center wavelength of the electroluminescence (EL) spectrum is determined by the wavelength of the light source used for creating the DPPs. Since a DPP is a state in which a DP is coupled with a phonon in the material, the EL spectrum of the Si-LED described above has a large number of sidebands that are regularly arranged with a spacing corresponding to the optical phonon energy, centered on the photon energy of the light used in the DPP-assisted annealing. These sidebands are caused by coherent phonons (CPs) contributing to light emission. In typical light emitting devices, such sidebands originating from phonons (phonon sidebands) are observed in the photoluminescence spectrum, but are not observed in the EL spectrum. The observation of such sidebands in the EL spectrum, as described above, is a phenomenon unique to LEDs fabricated using DPPs. By using this phenomenon, it is possible to control the shape of the EL spectrum of a Si-LED by controlling the number of CPs created during the DPP-assisted annealing. In this paper, we report the results of our experiments in which we succeeded in controlling the generation of CPs by using a pair of pulses during the DPP-assisted annealing, allowing us to control the shape of the emission spectrum of a Si-LED.

2. Si-LED Fabrication and Principle of Sideband Creation

First, for fabricating a Si-LED, ion implantation is used to form an inhomogeneous spatial distribution of the dopant (boron: B) in a Si p-n homojunction substrate. Although the inhomogeneously concentrated B serves as the origin of the created DPPs, the created DPPs are not converted to propagating light that is detected outside the LED. However, if DPP-assisted annealing is used, it is possible to modify the spatial distribution of the B concentration so that the DPPs are converted to propagating light with high efficiency [12]. In the DPP-assisted annealing, a Si p-n homojunction substrate is irradiated with CW laser light while applying a forward-bias current, to control the thermal diffusion rate of the B. With this method, it has been demonstrated that the emission wavelength of a Si-LED does not depend on the bandgap energy, E_g, of the material used, but is determined by the photon energy, $h\nu_{\text{anneal}}$, of the radiated light [16]. In the present work, we performed DPP-assisted annealing by radiating CW laser light having a photon energy ($h\nu_{\text{anneal}} = 0.94$ eV) lower than E_g of silicon ($= 1.14$ eV). The principle will be described below. For more details, refer to [12].

During DPP-assisted annealing, the radiated light is not absorbed by the Si crystal at positions in the B distribution where DPPs are not created under irradiation. Thus, the energy of the electrons injected from the forward bias current is converted to thermal energy and is subsequently dissipated via intraband relaxation or nonradiative relaxation. Therefore, the B distribution randomly varies due to thermal diffusion. On the other hand, at positions where DPPs are readily created, the radiated light interacts with electron-hole pairs and phonons, whereby DPPs are created. In this case, the injected electrons emit propagating light via stimulated emission driven by localized DPPs. In other words, since part of the energy of the injected electrons is dissipated not in the form of thermal energy but in the form of optical energy, thermal diffusion becomes more difficult. In the two processes described above, the B concentration distribution in the Si crystal is modified, in a self-organized manner, to a structure suitable for the creation of DPPs and their subsequent conversion to propagating light, and then reaches an equilibrium state. The B distribution in this state is suitable for stimulated emission with the photon energy of the light irradiation, $h\nu_{\text{anneal}}$, and since the spontaneous emission probability is proportional to the stimulated emission probability, this p-n homojunction functions as a Si-LED that emits propagating light.

Next, the mechanism of sideband creation will be explained. Figure 1(a) is an energy level diagram showing electronic states in a Si-LED fabricated by DPP-assisted annealing, and Figure 1(b) is a diagram in which an intermediate DPP level has been added to the band structure. The state $|E_g; \text{el}\rangle \otimes |E_{\text{ex}}; \text{phonon}\rangle$ in the figure is a state represented by the direct product of the ground state $|E_g; \text{el}\rangle$ of the electron and the excited phonon state $|E_{\text{ex}}; \text{phonon}\rangle$. Transitions to this state $|E_g; \text{el}\rangle \otimes |E_{\text{ex}}; \text{phonon}\rangle$ have been shown to occur only due to absorption or emission of photons via DPPs [11]. When this is illustrated in the electronic band structure, it is a localized state in which DPP-mediated excitation can take place and, therefore, it is indicated by a constant-energy straight line (horizontal solid or broken line), as shown in Figure 1(b), due to wavenumber uncertainty. Although an adequate explanation of the conventional light emission process in Si-LEDs has been possible until now with only Figure 1(a), Figure 1(b) is also presented in the present paper to emphasize the significance of phonons. In the light emission process of Si-LEDs, since electrons are excited to the state $|E_{\text{ex}}; \text{el}\rangle$ by current injection, the initial state $|E_{\text{ex}}; \text{el}\rangle \otimes |E_{\text{ex}_{\text{thermal}}}; \text{phonon}\rangle$ in the light emission process exists close to the X point in the conduction band in Figure 1(b). Here, $|E_{\text{ex}_{\text{thermal}}}; \text{phonon}\rangle$ is the thermally excited state of the phonon. Similarly, since the final state $|E_g; \text{el}\rangle \otimes |E_{\text{ex}_{\text{thermal}}}; \text{phonon}\rangle$, reached after the light emission, corresponds to the energy state of holes created by the injected current, the state $|E_g; \text{el}\rangle$ concentrates in the vicinity of the Γ point at the top of the valence band. The state $|E_{\text{ex}_{\text{thermal}}}; \text{phonon}\rangle$ is limited to phonons that can exist at room temperature, according to Bose statistics. In other words, the states $|E_{\text{ex}}; \text{el}\rangle \otimes |E_{\text{ex}_{\text{thermal}}}; \text{phonon}\rangle$ and $|E_g; \text{el}\rangle \otimes |E_{\text{ex}_{\text{thermal}}}; \text{phonon}\rangle$ are the initial state and the final state in the usual indirect transition.

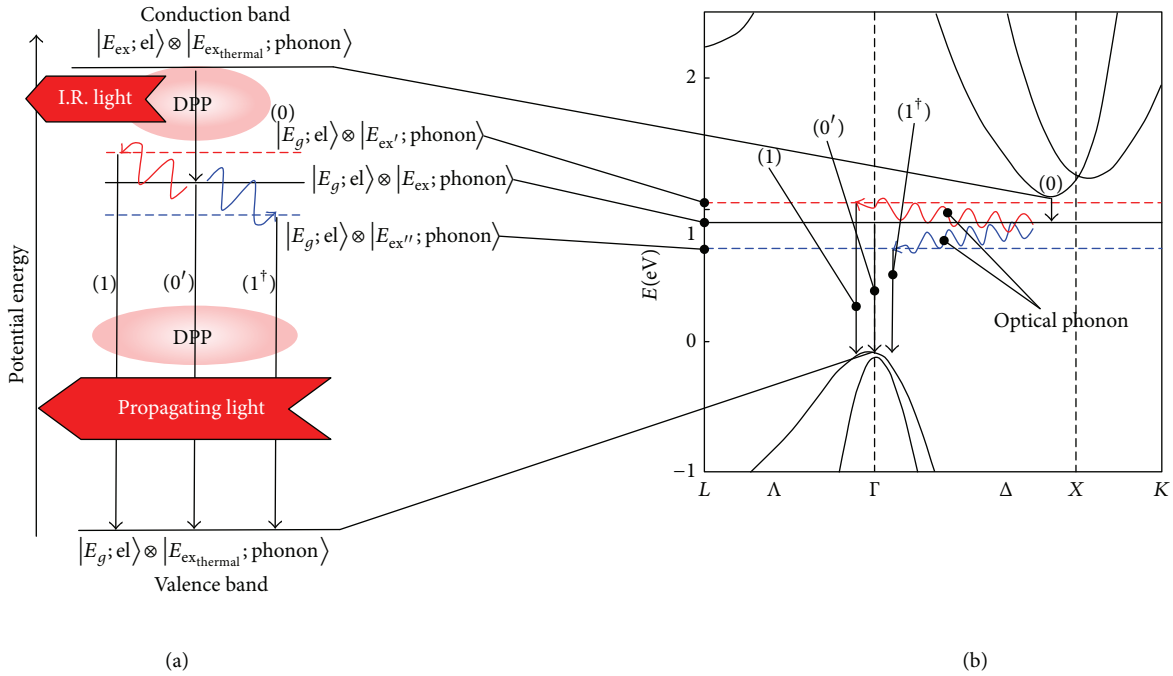

FIGURE 1: Diagram for explaining DPP-mediated transitions, showing (a) energy levels and (b) levels that can be reached via DPP-mediated transitions in electronic band structure of Si crystal.

Next, the processes (0), (0′), (1), and (1†) in Figure 1 will be explained. As the first-step, process (0) occurs. Processes (0′), (1), and (1†) occur as the second step. These processes involve externally observable transitions, in other words, photon emission. Processes (0) and (0′) are transitions that do not require a phonon, whereas processes (1) and (1†) require an optical phonon. Similarly, (n) and ($n^{\dagger}$) are transitions involving n optical phonons ($n = 2, 3, 4, \ldots$).

Process (0) is the first-step transition from the initial state $|E_{ex};el\rangle \otimes |E_{ex_{thermal}};phonon\rangle$ of electrons injected near the X point by the current to the intermediate state $|E_g;el\rangle \otimes |E_{ex};phonon\rangle$, which can be reached via a DPP-mediated transition. It corresponds to the energy relaxation from the bottom of the conduction band ($E_g = 1.14$ eV) to the state $|E_g;el\rangle \otimes |E_{ex};phonon\rangle$ (in this paper, the energy of this state was experimentally determined to be 0.94 eV). This transition is allowable via emission of a large number of phonons or via the emission of infrared light. However, the probability of the transition via phonon emission is small because the simultaneous emission of about 10 phonons is required at room temperature (thermal energy 25 meV). On the other hand, in the transition via infrared light emission, since the electronic state changes from $|E_{ex};el\rangle$ to $|E_g;el\rangle$, the selection rule required for photon emission is fulfilled. In addition, this transition is a direct transition in wavenumber space, as shown in Figure 1(b). Therefore, the probability of this transition is higher than the probability of a transition via phonon emission. In real space, this process is a transition from the state $|E_{ex};el\rangle \otimes |E_{ex_{thermal}};phonon\rangle$, which is broadened to the extent of the electron coherence length, to the localized state $|E_g;el\rangle \otimes |E_{ex};phonon\rangle$. The reason why infrared light can be emitted in this transition is that part of the electron energy can be dissipated as infrared light via a DPP having an energy that is resonant with this infrared light.

Process (0′) is the second-step transition from the intermediate state $|E_g;el\rangle \otimes |E_{ex};phonon\rangle$ to $|E_g;el\rangle \otimes |E_{ex_{thermal}};phonon\rangle$. The photon energy emitted during this process is equal to $h\nu_{anneal}$. Since this is a transition between the same electronic states $|E_g;el\rangle$, the selection rule required for photon emission is governed by a phonon, and the state $|E_g;el\rangle \otimes |E_{ex};phonon\rangle$ is also a state that can be reached via a DPP-meditated transition. The Si-LED fabricated by DPP-assisted annealing has a high probability of conversion from a DPP to propagating light, and almost all of the electrons in the state $|E_g;el\rangle \otimes |E_{ex};phonon\rangle$ relax by emitting photons with energy $h\nu_{anneal}$.

Process (1) is the second-step transition from the intermediate state $|E_g;el\rangle \otimes |E_{ex};phonon\rangle$ to the final state $|E_g;el\rangle \otimes |E_{ex_{thermal}};phonon\rangle$ by absorption of an optical phonon. Since the first-step transition due to process (0) is an infrared light emission process, optical phonons are created via the Raman process. If the electrons in the state $|E_g;el\rangle \otimes |E_{ex};phonon\rangle$ are scattered to the Γ point by absorbing optical phonons, the second step transition from the state $|E_g;el\rangle \otimes |E_{ex'};phonon\rangle$ to the state $|E_g;el\rangle \otimes |E_{ex_{thermal}};phonon\rangle$ becomes possible, resulting in photon emission, as in the case of a direct transition-type semiconductor. This is process (1) shown in Figure 1(b). Here, $|E_{ex};phonon\rangle$ and $|E_{ex'};phonon\rangle$ are the excited states that the phonon reached before and after absorbing optical phonons. The energy of the emitted photons is $h\nu_{anneal} + h\nu_p$, where $h\nu_p$ is the energy of the optical phonon.

Process (1†) represents the second-step transition from the intermediate state $|E_g;el\rangle \otimes |E_{ex};phonon\rangle$ to the final state

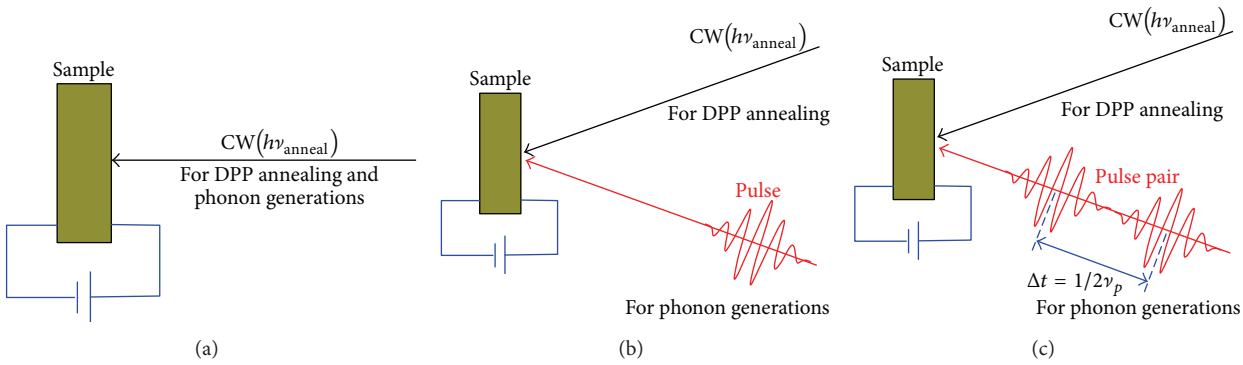

FIGURE 2: Illustration of DPP-assisted annealing using (a) CW light (conventional process); (b) CW light and a light pulse; and (c) CW light and two light pulses.

$|E_g; \text{el}\rangle \otimes |E_{\text{ex}_{\text{thermal}}}; \text{phonon}\rangle$, which occurs via emission of an optical phonon. Thus, it is conjugate to process (1). In this process, $|E_{\text{ex}''}; \text{phonon}\rangle$ in Figure 1 shows the phonon excited state after the emission of the optical phonon. The emitted photon energy is $h\nu_{\text{anneal}} - h\nu_p$.

Similarly, processes (n) and $(n^{\dagger})$ are transitions in which n optical phonons are absorbed or emitted. Since, in practice, the processes (n) and $(n^{\dagger})$ occur simultaneously, sidebands with photon energies $h\nu_{\text{anneal}} - nh\nu_p$ and $h\nu_{\text{anneal}} + nh\nu_p$ appear in the emission spectrum. The relationship between the nth order sideband energy and the photon energy $h\nu_{\text{anneal}}$ is the same as that of an nth order Raman scattering process with respect to the zero-phonon line. As is well-known, in Raman scattering, when a large number of phonons are excited, the electrons absorb them, emitting light. On the other hand, when a small number of phonons are excited, the electrons emit phonons, emitting light [17]. Thus, the intensity of these sidebands changes according to the number of phonons. This suggests that the intensity of the sidebands can be controlled by controlling the number of phonons.

3. Principle of Controlling the Number of Phonons

The number of created phonons can be controlled by a method involving multiphoton absorption or coherent phonon (CP) excitation using pulsed light. Since the Si crystal is heated by DPP-assisted annealing in the present work, resonant absorption to a specific exciton state for creation of coherent phonons is not possible by using a high-power CW-laser optical source. This is because the high-power CW laser excitation dose not change only the phonon structures but also DP state. Therefore, we decided to selectively create phonons via CP excitation using ultrashort pulsed light. The principle of the CP excitation in this case can be understood as an impulsive stimulated Raman scattering (ISRS) process, which is a kind of stimulated Raman scattering [18]. The duration and the repletion rate of the used pulsed light were 17 fs and 80 MHz, respectively. Therefore, its duty ratio was 1.3×10^{-6}. The Raman process is based on the third order optical nonlinearity. Therefore, the enough laser power for the control of CP generation using the ultrashort pulsed light is 2.3×10^{-18} times lower than that using the CW laser. Thus, in the experiment, the adverse effect was reduced to the negligible small coming from the DP generation by the additional laser excitation for the CP control.

In ISRS, the frequency component of the pulsed light irradiating the crystal includes coherent frequency components ν and $\nu - \nu_p$ with sufficiently high intensity, where ν_p is the phonon vibration frequency. Therefore, when the crystal is irradiated with pulsed light, the electrons absorb light with energy $h\nu$ and exhibit stimulated emission of light with energy $h\nu - h\nu_p$. At this time, it is possible to create CPs having an energy $h\nu_p$. Since these CPs are coherent, it is possible to control the creation of CPs by a single pulse or multiple pulses of light and causing them to interfere. In other words, unlike conventional DPP-assisted annealing in which the Si crystal is irradiated with CW light, CP creation is controlled by irradiating the Si crystal with pulsed light in addition to CW light. Therefore, it is possible to control the intensities of the sidebands in the EL spectrum. In the following, we describe the case where the Si-LED is irradiated with a single pulse of light during the DPP-assisted annealing and the case where the Si-LED is irradiated with a pair of light pulses.

(1) Irradiation with a Single Light Pulse. In the conventional DPP-assisted annealing, as shown in Figure 2(a), the CW light plays the role of decreasing the thermal diffusion rate by means of stimulated emission. In our approach, as shown in Figure 2(b), a light pulse is also radiated, together with the CW light. Since the light pulse excites multimode CPs via ISRS, the coupling probability of electron-hole pairs, photons, and CPs increases. As a result, the probability of electrons absorbing phonons and emitting light increases because the number of excited phonons increases as the light emission intensity increases. Therefore, the intensity of the sidebands having energy $h\nu_{\text{anneal}} + nh\nu_p$ increases, and the intensity of sidebands having energy $h\nu_{\text{anneal}} - nh\nu_p$ decreases. Thus, compared with an Si-LED fabricated by irradiation with only CW light, it is expected that the EL spectral shape of the Si-LED will show a higher light emission intensity at energies higher than $h\nu_{\text{anneal}}$ and conversely a lower light emission intensity at energies lower than $h\nu_{\text{anneal}}$.

(2) Irradiation with Two Light Pulses (Light Pulse Pair). Since the CPs created by ISRS are coherent and thus have the ability

to interfere, as described above, let us consider the case where a Si crystal is sequentially irradiated with two coherent light pulses having an arrival time difference Δt. If the value of Δt is a half-integer multiple of the vibration period, $1/\nu_p$, of the phonons ($n/2\nu_p$; $n = 1, 3, 5, \ldots$), as shown in Figure 2(c), it is known that the excited CPs destructively interfere [19]. On the other hand, they constructively interfere when Δt is an integer multiple of the vibration period (n/ν_p; $n = 1, 2, 3, \ldots$). That is to say, by radiating a pair of light pulses, it is possible to control the creation of CPs so as to be suppressed or enhanced. Thus, by adjusting the value of Δt, it is possible to perform various types of sideband control as compared with (1) above.

As an example, in the case of $\Delta t = 1/2\nu_p$, we will explain how the CP creation is controlled and how, as a result of this, the EL spectrum is controlled. The value $\Delta t = 1/2\nu_p$ corresponds to one period of vibration of a phonon with frequency $2\nu_p$. Therefore, by radiating a pair of pulses having this value Δt, the number of phonons of frequency ν_p decreases, whereas the number of phonons of frequency $2\nu_p$ increases. Thus, the probability of process ($1^\dagger$) increases, by which electrons emit phonons of frequency ν_p and emit light, resulting in a higher probability of electrons absorbing phonons of frequency $2\nu_p$ and emitting light. In other words, as a result of the reduction in the number of phonons with frequency ν_p, the intensity of the sideband at energy $h\nu_{\text{anneal}} - h\nu_p$ becomes higher than that of the sideband at energy $h\nu_{\text{anneal}} + h\nu_p$. At the same time, as a result of the increase in the number of phonons with frequency $2\nu_p$, the intensity of the sideband at energy $h\nu_{\text{anneal}} - 2h\nu_p$ becomes lower than that of the sideband at energy $h\nu_{\text{anneal}} + 2h\nu_p$. The above discussion can also be extended to an explanation of the case where the sideband intensity at energy $h\nu_{\text{anneal}} - (2n-1)\nu_p$ increases, and that at energy $h\nu_{\text{anneal}} + (2n-1)\nu_p$ decreases. It can be also extended to the case where the sideband intensity at energy $h\nu_{\text{anneal}} - 2n\nu_p$ decreases, and that at energy $h\nu_{\text{anneal}} + 2n\nu_p$ increases. For controlling the number of phonons during the DPP-assisted annealing, we irradiate two light pulses with delay times of $\Delta t = 1/\nu_{p,\text{exp}}$ (= 64.1 fs), $1/2\nu_{p,\text{exp}}$ (= 32.1 fs), and $1/4\nu_{p,\text{exp}}$ (= 16.0 fs).

4. Fabrication of Si-LED and Evaluation of EL Spectrum

To fabricate a Si-LED, we doped a 625 μm-thick n-type Si (100) substrate with arsenic (As) at a concentration of about 10^{15} cm^{-3}. The resulting resistivity was 10 Ωcm. Next, we formed a p-n homojunction by ion implantation of boron (B) with a dose of 5×10^{13} cm^{-2} and an acceleration energy of 700 keV. Then, we deposited a transparent ITO film with a thickness of 150 nm on the surface of the p layer and a Cr/Al film with a thickness of 80 nm on the surface of the n layer, both by RF sputtering, to form an anode and a cathode, respectively. The device fabrication conditions up to this point were the same as those reported in [12]. In DPP-assisted annealing, we used CW laser light with energy $h\nu_{\text{anneal}} = 0.94$ eV (wavelength 1.3 μm) as the light source for creating DPs. As the pulsed light source for creating CPs, we used a mode-locked laser with a photon energy of 1.55 eV (wavelength 0.8 μm), a pulse width of 17 fs, and a repetition frequency of 80 MHz. To verify the DPP-assisted annealing method, we employed the following four samples.

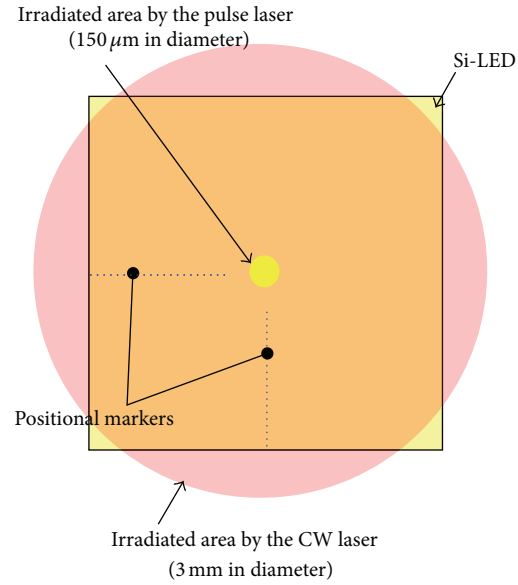

Figure 3: Irradiation spots of CW light and pulsed light on sample surface during DPP-assisted annealing.

(a) Sample 1. Sample 1 was irradiated with pulsed light (average power 100 mW, spot diameter 150 μm) and CW light ($h\nu_{\text{anneal}} = 0.94$ eV, power 1 W, spot diameter 3 mm). It was annealed with a voltage of 20 V and a current of 145 mA for 1 hour (Figure 2(b)).

(b) Samples 2–4. Of the CPs created by pulsed light irradiation, we selected optical phonons with the highest creation probability [20] ($h\nu_p = 65$ meV ($\nu_p = 15.6$ THz); indicated as $h\nu_{p,\text{exp}}$ below) as the phonons to be controlled. The samples were irradiated with CW light and a pair of light pulses with $\Delta t = 1/\nu_{p,\text{exp}}$ (= 64.1 fs), $1/2\nu_{p,\text{exp}}$ (= 32.1 fs), and $1/4\nu_{p,\text{exp}}$ (= 16.0 fs). They were annealed with a voltage of 25 V and a current of 120 mA for 1 hour (Figure 2(c)). The other experimental conditions were the same as those used for Sample 1 above. In the following, samples for $\Delta t = 1/\nu_{p,\text{exp}}$, $1/2\nu_{p,\text{exp}}$, and $1/4\nu_{p,\text{exp}}$ are referred to as Samples 2, 3, and 4, respectively.

To eliminate the contributions of variations in the sizes and shapes of the electrode and the substrate to the experimental results, the CW light was radiated onto the entire surface of the sample, and the pulsed light was radiated only at the center of the region irradiated with the CW light, as shown by the red and yellow circles, respectively, in Figure 3. With the samples prepared with this method, the EL spectral shapes in these two circles were different. By taking this difference between the intensities of these EL spectra, it was possible to eliminate the contributions above and to examine the details of the changes in the EL spectra depending on the presence/absence of the pulsed light irradiation. Experimental results are shown below.

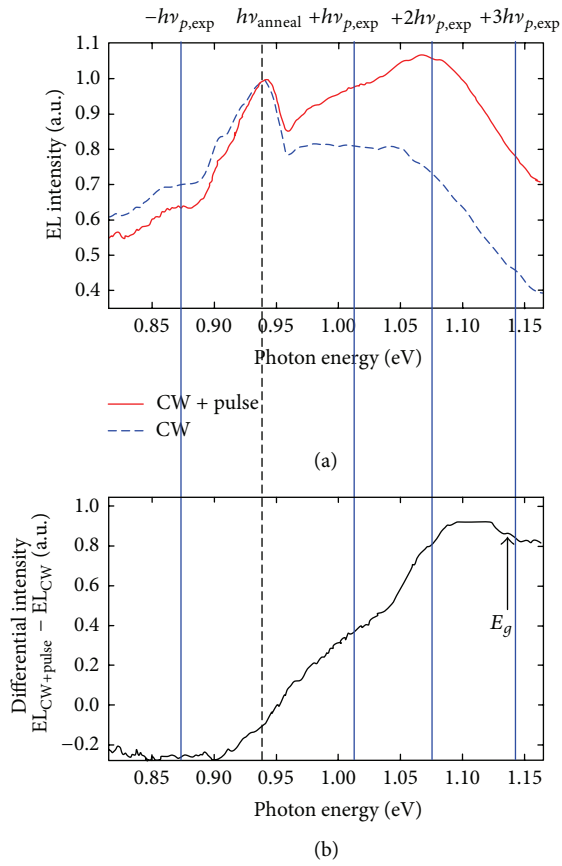

FIGURE 4: (a) EL spectra of Sample 1 after DPP-assisted annealing with the method in Figure 2(b). Red solid curve: area irradiated with CW light and pulsed light. Blue broken curve: area irradiated only with CW light. (b) Differential EL spectrum.

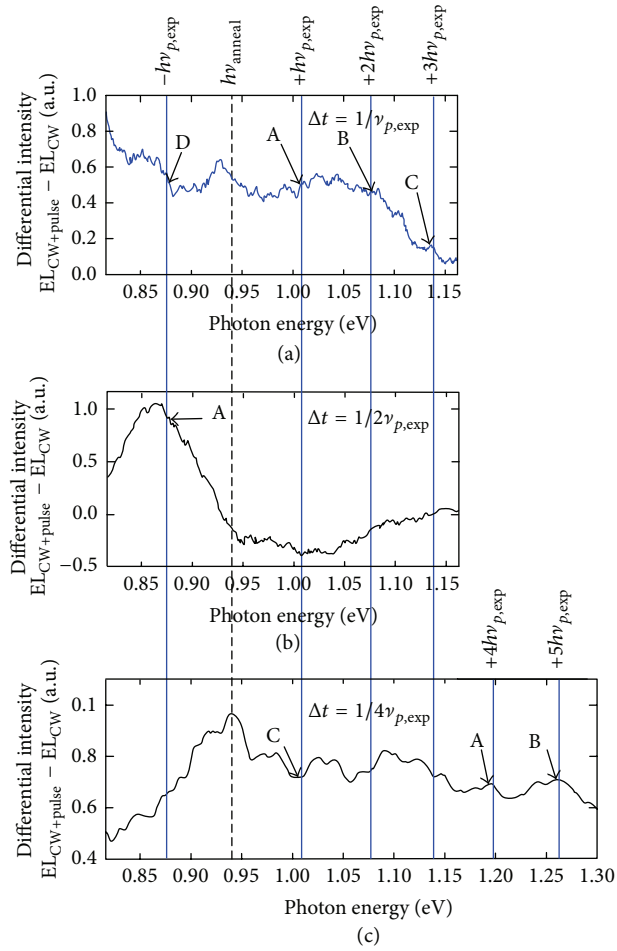

FIGURE 5: Differential EL spectra. (a) Sample 2 with $\Delta t = 1/\nu_{p,\exp}$. (b) Sample 3 with $\Delta t = 1/2\nu_{p,\exp}$. (a) Sample 4 with $\Delta t = 1/4\nu_{p,\exp}$.

(a) Sample 1. Figure 4(a) shows, for Sample 1, the EL spectrum of the part irradiated with only the CW light (blue broken curve: EL_{CW}) and the EL spectrum of the part irradiated with the CW light and the pulsed light (red solid curve: $\text{EL}_{\text{CW+pulse}}$). Figure 4(b) shows the difference between their intensities ($\text{EL}_{\text{CW+pulse}} - \text{EL}_{\text{CW}}$; differential EL spectrum). By irradiating the sample with the pulsed light, the EL intensity at higher energies increased, and the intensity of the +1 and +2 order sidebands of the optical phonons (energy $h\nu_{p,\exp}$ = 65 meV) increased. In the differential EL spectrum, we also confirmed band-edge light emission and an increase in the intensity of the +3 order sideband. However, since we did not perform mode selection by using a pair of pulses, the spectra of the sidebands were extremely broad. The increase in intensity of these sidebands is explained by the creation of a large number of CPs by ISRS, using the pulsed light, as explained in Section 3. In other words, since a large number of CPs are created, the process in which CPs are absorbed becomes dominant, resulting in light emission. In addition, the increase in light emission at the band edge is considered to be a consequence of the increased number of phonons due to CP creation causing an increased probability of a direct transition between electronic bands.

On the other hand, in the sideband corresponding to the −1 order optical phonons, the EL intensity is decreased by the incident pulsed light during DPP-assisted annealing. This is because process ($1^{\dagger}$), in which optical phonons and light are emitted, is suppressed due to CPs created by the pulsed light.

(b) Sample 2. Figure 5(a) shows the differential EL spectrum for Sample 2. In this sample, small bumps (arrows A, B, and C) are observed at the positions of the +1 to +3 order optical phonon sidebands ($h\nu_{p,\exp}$ = 65 meV). They are due to the selective creation of optical phonons $nh\nu_{p,\exp}$ ($n = 1, 2, 3, \ldots$), which were mode-selected by irradiating this sample with a pair of pulses with $\Delta t = 1/\nu_{p,\exp}$. On the other hand, a region with reduced light emission, like that seen in Figure 4(b), was not observed in the region whose energy is lower than $h\nu_{\text{anneal}}$ (arrow D). The reason for this is that the number of created optical phonons is half or less of that in the case of Sample 1 because ISRS is a second-order nonlinear process, and the energy of the pulses irradiating this sample is one-half of the energy of the pulses irradiating Sample 1. This is due to the

suppression of process ($1^{\dagger}$), in which light emission occurs while phonons are emitted.

(c) Sample 3. Figure 5(b) shows the differential EL spectrum for Sample 3. In this sample, the intensity of the −1 order sideband increased (arrow A). The reason for this is that, with $\Delta t = 1/2\nu_{p,\mathrm{exp}}$, the number of odd-numbered harmonic components was decreased, and the number of even-numbered harmonic components was increased. In other words, since the electrons had an increased probability of emitting the +1 order phonons, process ($1^{\dagger}$) was dominant, and the intensity of the −1 order sideband increased. On the other hand, process (1), in which light emission occurs while phonons are absorbed, is suppressed. Therefore, since the high-order modes are also suppressed, a region exhibiting reduced optical phonon sidebands is observed at energies higher than $h\nu_{\mathrm{anneal}}$, which is the opposite to what is shown in Figure 4(b).

(d) Sample 4. Figure 5(c) shows the differential EL spectrum for Sample 4. The intensities of the +1 order and +2 order sidebands were decreased, and those of the +4 order and +5 order sidebands were increased. A reason for this is that, with $\Delta t = 1/4\nu_{p,\mathrm{exp}}$, the number of +2 order harmonic phonons was decreased, and that the number of +4 order harmonic phonons was increased. The reason for the increase in the number of optical phonons in the +5 order is considered to be because the values of $1/4\nu_{p,\mathrm{exp}}$ and $1/5\nu_{p,\mathrm{exp}}$ are close. As a result, the intensity of the +1 order sideband is decreased. In other words, this is because the +1 order optical phonons are absorbed for creating the +4 order and +5 order harmonic phonons. The reason why the generation of the +5 order sideband dominates over generation of the +1 order sideband is that the energy of the +5 order sideband is higher than the bandgap energy, E_g, of Si, and this is a phonon scattering process that is resonant with the electronic level. As a result, process (1) is suppressed, and the intensity of the +1 order sideband is decreased. On the other hand, since the overall number of optical phonons is increased, process ($1^{\dagger}$) is suppressed, as in the case of Figure 4(b). As a result, a region with reduced light emission, similar to that seen in Figure 4(b), is observed in the region at energy $h\nu_{\mathrm{anneal}} - nh\nu_{p,\mathrm{exp}}$.

Figure 6 shows EL spectra of the regions irradiated with the light pulses for Samples 2 and 3. In Sample 2, the numbers of phonons of the fundamental ($h\nu_{p,\mathrm{exp}}$) and the harmonics ($nh\nu_{p,\mathrm{exp}}$; $n = 2, 3, \ldots$) were all increased, and therefore, the phonon absorption probability of the electrons increased, resulting in higher light emission at higher energies. In Sample 3, on the other hand, due to the interference of CPs, the number of odd-order harmonic components of the phonons was decreased, and the number of even-order harmonic components was increased; therefore, the absorption probability of phonons of odd-order harmonic components was decreased, resulting in relatively higher light emission at lower energies. The above results indicate that the EL spectral shape of the Si-LED was successfully controlled by changing the conditions of the pair of light pulses radiated during DPP-assisted annealing. That is, the intensity at energies

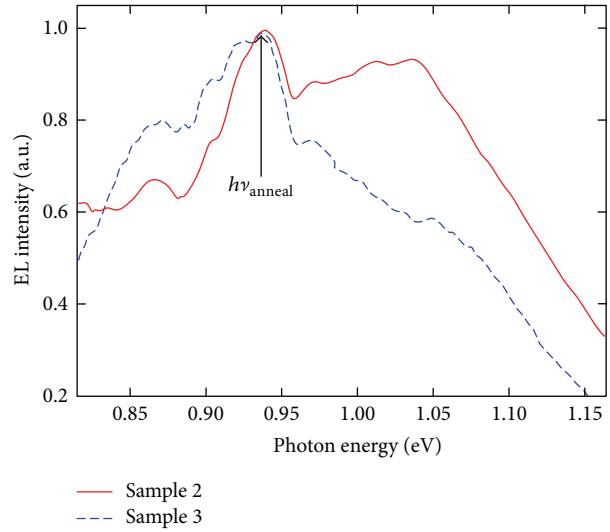

FIGURE 6: EL spectra after annealing for Samples 2 and 3.

higher than $h\nu_{\mathrm{anneal}}$ is increased, and that at lower energies is decreased. Furthermore, conversely, the intensity at energies lower than $h\nu_{\mathrm{anneal}}$ is increased, and that at higher energies is decreased.

In DPP-assisted annealing without using a pulsed light source, the broadening (half width at half maximum, HWHM) towards lower energies was 250 meV or greater, and the broadening (HWHM) towards higher energies was 50 meV. In contrast, in the EL spectrum of the Si-LED fabricated using a pulsed light source for creating phonons, the EL spectrum was broadened towards higher energies by 200 meV or greater (HWHM), and the broadening towards lower energies was reduced to 120 meV (HWHM).

5. Conclusion

In DPP-assisted annealing, we successfully controlled the spectral shape of a Si LED by radiating a pair of light pulses for creating CPs. In the EL spectrum, the intensity of sidebands due to phonons could be controlled by the number of phonons during DPP annealing. The peak wavelength in the EL spectrum was determined by the wavelength of the light source used in DPP-assisted annealing. In order to broaden the EL spectrum toward higher energy, a pair of light pulses having $\Delta t = 1/4\nu_{p,\mathrm{exp}}$ was radiated. Conversely, to broaden the EL spectrum towards lower energies, a pair of light pulses having $\Delta t = 1/2\nu_{p,\mathrm{exp}}$ was radiated. As a result, the EL spectrum was broadened towards higher energies by 200 meV or greater (HWHM), and the broadening towards lower energies was reduced to 120 meV (HWHM).

Conflict of Interests

The authors declare that there is no conflict of interests regarding the publication of this paper.

References

[1] Z. I. Alferov, "The history and future of semiconductor heterostructures," *Semiconductors*, vol. 32, no. 1, pp. 1–14, 1998.

[2] R. A. Milano, P. D. Dapkus, and G. E. Stillman, "An analysis of the performance of heterojunction for fiber optic communications," *IEEE Transactions on Electron Devices*, vol. 29, no. 2, pp. 266–274, 1982.

[3] National Toxicology Program, "NTP technical report on the toxicology and carcinogenesis studies of indium phosphide (CAS No. 22398-80-7) in F344/N rats and B6C3F1 mice (inhalation studies)," Tech. Rep. NTP TR 499, U.S. Department of health and human services, Public Health Service, National Institute of Health, 2001.

[4] K. D. Hirschman, L. Tsybeskov, S. P. Duttagupta, and P. M. Fauchet, "Silicon-based visible light-emitting devices integrated into microelectronic circuits," *Nature*, vol. 384, no. 6607, pp. 338–341, 1996.

[5] Z. H. Lu, D. J. Lockwood, and J.-M. Baribeau, "Quantum confinement and light emission in SiO_2/Si superlattices," *Nature*, vol. 378, no. 6554, pp. 258–260, 1995.

[6] L. Dal Negro, R. Li, J. Warga, and S. N. Basu, "Sensitized erbium emission from silicon-rich nitride/silicon superlattice structures," *Applied Physics Letters*, vol. 92, no. 18, Article ID 181105, 2008.

[7] T. Komoda, J. Kelly, F. Cristiano et al., "Visible photoluminescence at room temperature from microcrystalline silicon precipitates in SiO2 formed by ion implantation," *Nuclear Instruments and Methods in Physics Research B*, vol. 96, no. 1-2, pp. 387–391, 1995.

[8] S. Yerci, R. Li, and L. Dal Negro, "Electroluminescence from Er-doped Si-rich silicon nitride light emitting diodes," *Applied Physics Letters*, vol. 97, no. 8, Article ID 081109, 2010.

[9] S. K. Ray, S. Das, R. K. Singha, S. Manna, and A. Dhar, "Structural and optical properties of germanium nanostructures on Si(100) and embedded in high-k oxides," *Nanoscale Research Letters*, vol. 6, no. 1, article 224, 10 pages, 2011.

[10] M. A. Green, J. Zhao, A. Wang, P. J. Reece, and M. Gal, "Efficient silicon light-emitting diodes," *Nature*, vol. 412, no. 6849, pp. 805–808, 2001.

[11] T. Kawazoe, K. Kobayashi, S. Takubo, and M. Ohtsu, "Nonadiabatic photodissociation process using an optical near field," *Journal of Chemical Physics*, vol. 122, no. 2, Article ID 024715, 2005.

[12] T. Kawazoe, M. A. Mueed, and M. Ohtsu, "Highly efficient and broadband Si homojunction structured near-infrared light emitting diodes based on the phonon-assisted optical near-field process," *Applied Physics B*, vol. 104, no. 4, pp. 747–754, 2011.

[13] T. Kawazoe, M. Ohtsu, K. Akahane, and N. Yamamoto, "Si homojunction structured near-infrared laser based on a phonon-assisted process," *Applied Physics B: Lasers and Optics*, vol. 107, pp. 659–663, 2012.

[14] H. Tanaka, T. Kawazoe, and M. Ohtsu, "Increasing Si photodetector photosensitivity in near-infrared region and manifestation of optical amplification by dressed photons," *Applied Physics B*, vol. 108, no. 1, pp. 51–56, 2012.

[15] N. Wada, T. Kawazoe, and M. Ohtsu, "An optical and electrical relaxation oscillator using a Si homojunction structured light emitting diode," *Applied Physics B: Lasers and Optics*, vol. 108, no. 1, pp. 25–29, 2012.

[16] M. A. Tran, T. Kawazoe, and M. Ohtsu, "Fabrication of a bulk silicon p-n homojunction-structured light-emitting diode showing visible electroluminescence at room temperature," *Applied Physics A: Materials Science and Processing*, vol. 115, no. 1, pp. 105–111, 2014.

[17] S. K. Arora, A. J. Kothari, R. G. Patel, K. M. Chauha, and B. N. Chudasama, "Optical absorption in gel grown cadmium tartrate single crystals," *Journal of Physics*, vol. 28, no. 1, pp. 48–52, 2006.

[18] Y.-X. Yan, E. B. Gamble Jr., and K. A. Nelson, "Impulsive stimulated scattering: general importance in femtosecond laser pulse interactions with matter, and spectroscopic applications," *The Journal of Chemical Physics*, vol. 83, no. 11, pp. 5391–5399, 1985.

[19] M. Hase, K. Mizoguchi, H. Harima et al., "Optical control of coherent optical phonons in bismuth films," *Applied Physics Letters*, vol. 69, no. 17, pp. 2474–2476, 1996.

[20] P. Giannozzi, S. de Gironcoli, P. Pavone, and S. Baroni, "Ab initio calculation of phonon dispersions in semiconductors," *Physical Review B*, vol. 43, no. 9, pp. 7231–7242, 1991.

Hindawi Publishing Corporation
Advances in Optical Technologies
Volume 2014, Article ID 569684, 8 pages
http://dx.doi.org/10.1155/2014/569684

Research Article

Demonstration of Controlling the Spatiotemporal Dynamics of Optical Near-Field Excitation Transfer in Y-Junction Structure Consisting of Randomly Distributed Quantum Dots

Wataru Nomura,[1] Makoto Naruse,[2] Masashi Aono,[3,4] Song-Ju Kim,[5] Tadashi Kawazoe,[1] Takashi Yatsui,[1] and Motoichi Ohtsu[1]

[1] *School of Engineering, The Nanophotonics Research Center, The University of Tokyo, 2-11-16 Yayoi, Bunkyo-ku, Tokyo 113-8656, Japan*
[2] *Photonic Network Research Institute, National Institute of Information and Communications Technology, 4-2-1 Nukui-kita, Koganei, Tokyo 184-8795, Japan*
[3] *Earth-Life Science Institute, Tokyo Institute of Technology, 2-12-1 Ookayama, Meguro-ku, Tokyo 152-8550, Japan*
[4] *PRESTO, Japan Science and Technology Agency, 4-1-8 Honcho, Kawaguchi-shi, Saitama 332-0012, Japan*
[5] *WPI Center for Materials Nanoarchitectonics (MANA), National Institute for Materials Science, 1-1 Namiki, Tsukuba, Ibaraki 305-0044, Japan*

Correspondence should be addressed to Wataru Nomura; nomura@nanophotonics.t.u-tokyo.ac.jp

Received 10 March 2014; Accepted 24 March 2014; Published 27 April 2014

Academic Editor: Chennupati Jagadish

Solution searching devices that operate on the basis of controlling the spatiotemporal dynamics of excitation transfer via dressed photon interactions between quantum dots have been proposed. Long-range excitation transfer based on dressed photon interactions between randomly distributed quantum dots is considered to be effective in realizing such devices. Here, we successfully controlled the spatiotemporal dynamics of excitation transfer using a Y-junction structure consisting of randomly dispersed CdSe/ZnS core-shell quantum dots. This Y-junction structure has two "output ends" and one "tap end." By exciting one output end with control light, we observed increased excitation transfer to the other output end via a state-filling effect. Conversely, we observed reduced excitation transfer to the output ends by irradiating the tap end with control light, due to excitation of defect levels in the tap end. These results show the possibility of controlling the optical excitation transfer dynamics between multiple quantum dots.

1. Introduction

Light excitation in quantum dots (QDs) generates dressed photons, which are light fields localized in the vicinity of the QDs, giving rise to dressed photon interactions with other nearby matter, as well as excitation energy transfer via these interactions [1]. In particular, various optical functional devices, such as logic gates called nanophotonic devices [2–4], light-harvesting devices [5], and optical signal transmitting systems [6, 7], have been realized using QDs formed of CuCl, ZnO, InAs, CdSe, and so forth, based on optical near-field excitation transfer between QDs. Nanophotonic devices have been shown to function as logic gates, such as AND, NOT, and XOR logic gates [2–4]. These devices consist of two or three closely spaced QDs having different energy levels, and by inputting a light beam serving as a power supply and another light beam serving as a control signal, excitation energy transfer between the QDs is controlled so that the light emitted from one of the QDs serves as the output.

On the other hand, novel solution searching and decision making devices using a QD array provided with multiple output QDs have recently been proposed [8–10]. In these devices, by inputting control signals to the output QDs based on certain rules, the probability of the optical excitation being transferred uniformly to each QD is controlled to obtain a solution. In these operations, it is necessary to control the spatiotemporal dynamics of the optical excitation transfer between spatially distributed QDs. The features of these

devices are that they operate at high speed with low energy consumption since they are driven by excitation transfer based on dressed photon interactions [11]. The proposed solution searching device finds a solution to a nondeterministic polynomial (NP) time complete problem, the satisfiability problem (SAT), much faster than the WalkSAT algorithm, which is one of the fastest stochastic local search algorithms [9, 12]. The proposed decision making device exhibits high efficiency and adaptability in solving decision making problems [10].

However, although it would be ideal to utilize the models discussed in [8–10], it would be technically challenging to directly implement their architecture. One reason for this is that, in order to implement and operate this device, it is essential to fabricate a QD array in which QDs of strictly selected dimensions and number must be precisely located with nanometer-order positioning precision, as reported in [8], which is technologically demanding from the viewpoint of fabrication as the first step. In addition, another reason is the technical challenge of having to guide the control light to multiple output QDs and separately observe the output signals coming from them.

In contrast to this approach, we distributed an extremely large number of identical-size QDs randomly, and by using a structure in which an output QD is provided at the terminal end, we experimentally demonstrated the possibility of optical excitation energy transfer over distances of micrometer order via repeated dressed photon interactions between the QDs [6]. Using such a randomly distributed QD structure overcomes the fabrication difficulties mentioned above, and because of the possibility of scaling up the technique to micrometer order, it is expected that it will also be possible to overcome the technical challenges related to control and observation.

In the work reported in this paper, using a structure in which multiple QDs are randomly distributed, we experimentally investigated control of the spatiotemporal dynamics of optical excitation transfer based on dressed photon interactions between the QDs, which is a requirement for the realization of solution searching and decision making devices. Section 2 describes fundamental principles. Section 3 describes the fabricated device, experimental setup, energy transfer measurement, and characterizations. Section 4 concludes the paper.

2. Principle

First, we will explain optical excitation transfer due to dressed photon interactions and suppression of this process. As shown in Figure 1, a small QD (QD1) and a large QD (QD2) are placed in close proximity. A first excited state E11 in QD1 is resonant with a second excited state E22 in QD2 due to their size ratio of 1 : 1.43 [13]. When QD1 is excited by excitation light P_{in1}, a dressed photon is generated in the vicinity of QD1. The excitation energy in QD1 is transferred to E22 by dressed photon interactions and then relaxes to E21, which is the first excited state in QD2, via intersubband relaxation. Thus, the excitation energy is transferred unidirectionally (Figure 1(a)). This is observed as emitted light P_{out2} from QD2. However, if E21, which is the level to which the excitation relaxes, has already been excited by control light P_{in2}, the excitation energy transferred to E22 cannot relax to E21, but it is transferred back to E11, and nutation occurs between E11 and E22 (Figure 1(b)). This is observed as emitted light P_{out1} from QD1, or when there is a QD in the vicinity, this leads to an increase in the probability of excitation transfer to that QD. Based on this principle, assuming that QD1, having multiple QD2's in the vicinity, is excited, by irradiating one QD2 with P_{in2}, the probability of excitation transfer to the other QD2's is changed; in other words, it is possible to control the spatiotemporal dynamics.

Next, we will explain optical excitation transfer based on dressed photon interactions in a randomly distributed QD structure. In this structure, as shown in Figure 1(c), identical-size QDs (QD1) are randomly distributed in close proximity to each other, and QD2's are placed at one location to serve as an output. The input light P_{in1} incident on the QD1's at one end undergoes repeated dressed photon interactions between the QD1's and eventually arrives at the QD2's, where it is output as emitted light P_{out2} from E21. Because the optical excitation is transferred with high probability by QDs having strong dressed photon interactions, optical excitation transfer with high energy efficiency is possible regardless of the QD1 distribution, and it has been experimentally verified that it is possible to transfer the excitation over a distance of more than 10 μm [6].

The experimental model used in this paper is shown in Figure 1(d). The green color in the figure represents a Y-junction QD1 structure consisting of a group of QD1's randomly distributed in close proximity to each other, in the form of strips with a width of 1 μm and a length of 7.5 μm extending in a radiating pattern in three directions from the center O. The ends of the Y-junction are labeled A, B, and C. QD2 structures serving as output ports, where QD2's are grouped together in squares with a side length of 3 μm, are connected at A and B so as to overlap with the QD1 structure. From A and B, called "output ends", we obtain output signals that are observed as radiation. In addition, A and B also serve as terminals for inputting control light. On the other hand, end C, which we call a "tap end," is not connected to any QD2's. The detailed experimental conditions used in this model are omitted. Figure 1(e) shows an energy band diagram in which the section including points A-O-B is illustrated one-dimensionally. When excitation light P_{in1}, serving as an input signal, is incident on the center point O in the QD1 structure, optical excitation is generated in QD1 and is transferred through the QD1 structure by undergoing repeated energy transfer due to dressed photon interactions between the QD1's. Since the optical excitation transferred to QD2 reaches E21 via intersubband relaxation, no reverse flow of the transfer occurs, and therefore the optical excitation is transferred to the ends, A and B, where the QD2 structures are provided. At this time, if end B is irradiated with control light P_{in2} that excites QD2, QD2 is excited, and the excitation light transferred from QD1 does not relax to E21, and thus excitation transfer is not observed. Therefore, a reverse flow of the optical excitation occurs at

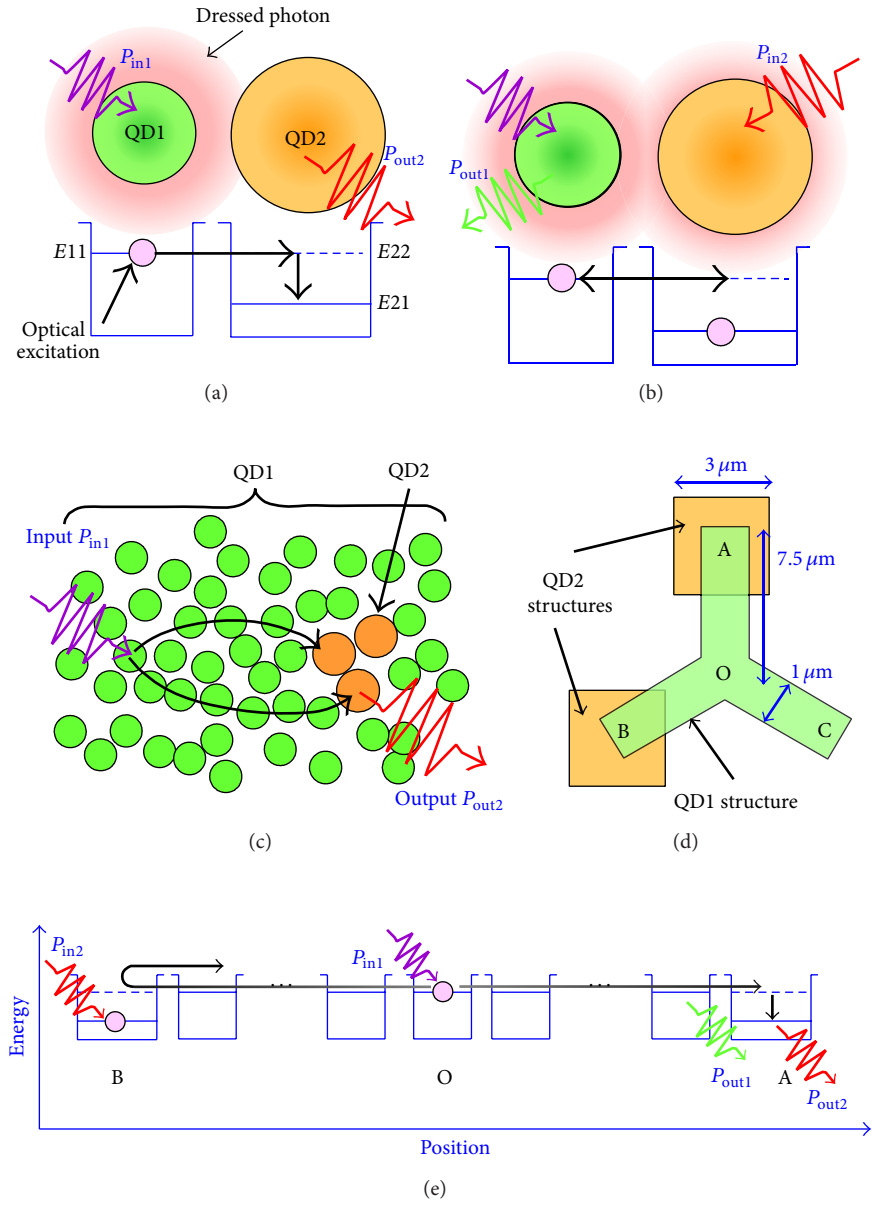

FIGURE 1: (a), (b) Schematic illustration of optical excitation transfer from QD1 to QD2 via dressed photon interactions, where (a) shows the case where energy transfer occurs from QD1 to QD2 and (b) shows the case where control light is incident on QD2, thus suppressing energy transfer. (c) Schematic diagram of long-range optical excitation transfer system. Green and yellow circles represent QD1's and QD2's, respectively. (d) Schematic diagram of experimental model. Green and yellow regions represent groups of QD1 and QD2 structures consisting of randomly distributed QD1's and QD2's, respectively. (e) Energy diagram schematically showing the experimental model from point B to point A.

end B, and the level of excitation transfer to A, which is the other output end, increases. At locations where the excitation transfer is increased, the emitted light P_{out1} and P_{out2} from QD1 and QD2 both increase, and, therefore, we can confirm that the excitation transfer is controlled by evaluating the increase in P_{out1} at end A when end B is irradiated with control light P_{in2}. Note that even if end C is irradiated with control light P_{in2}, a change like that occurring at points A and B is not expected to occur since the excitation state of the QDs does not change.

3. Experiments

3.1. Device. In our experiments, we used commercially available CdSe/ZnS core-shell QDs (manufactured by Quantum Design, Inc.). As QD1 and QD2 described in the previous section, we selected QDs with core-diameters of $d_1 = 2.5$ nm and $d_2 = 3.2$ nm, respectively. Their first excited states, estimated from absorption spectra, were E11 = 2.36±0.08 eV and E21 = 2.11±0.06 eV, respectively. As described above, E11 is resonant with E22, which is the second excited state of QD2 [14].

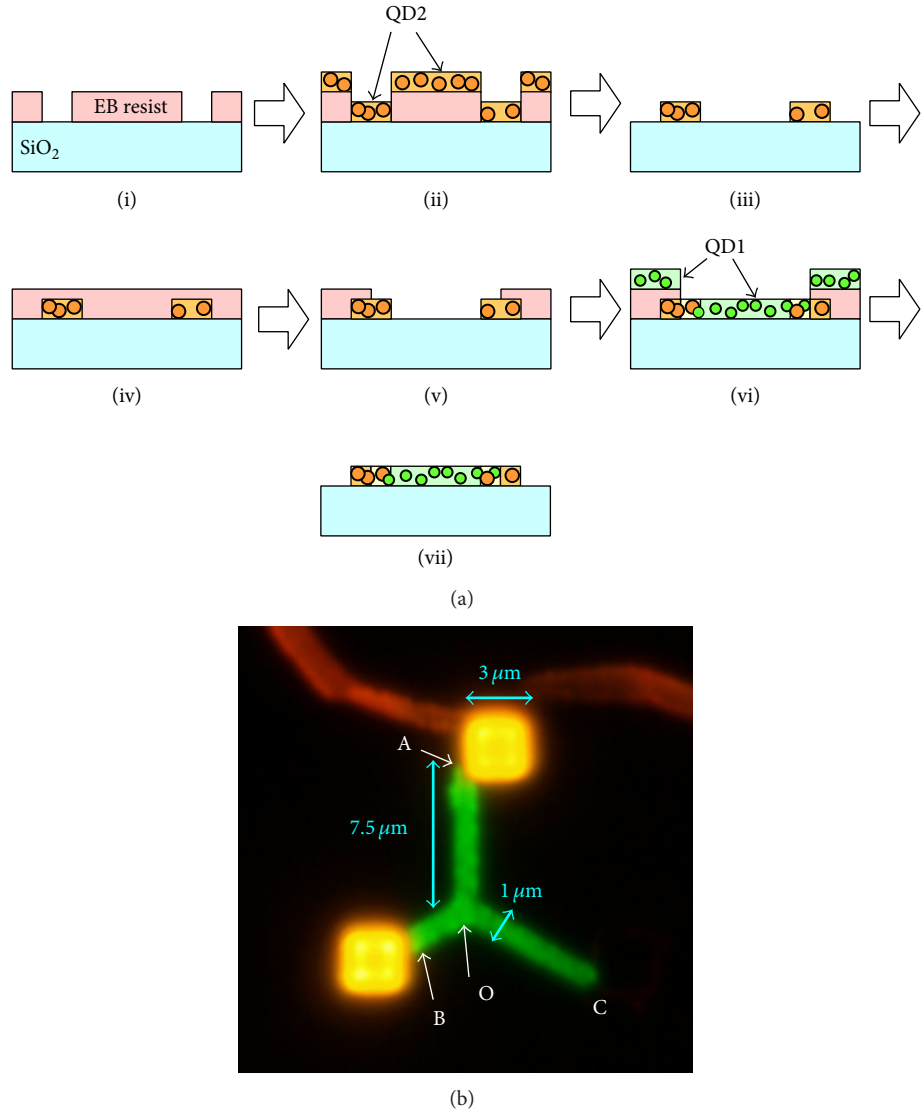

FIGURE 2: (a) Cross-sectional illustrations of sample fabrication process. (i) E-beam resist is applied to SiO_2 substrate, and regions where QD2 structures are to be formed are drawn by e-beam lithography. (ii) QD2 solution is dropped onto substrate and allowed to dry. (iii) E-beam resist is removed to obtain QD2 structures. (iv) E-beam resist is applied again. (v) Region where QD1 structure is to be formed is drawn by e-beam lithography. (vi) QD1 solution is dropped onto resist and allowed to dry. (vii) E-beam resist is removed to obtain the sample. (b) Fluorescence microscope image of sample excited by mercury vapor lamp.

The outside of the shell was modified with a carboxyl group. The solution was dropped onto a substrate and allowed to dry, affording a group of randomly distributed QDs located in close proximity with a center-to-center distance of about 10 to 20 nm.

We fabricated samples using the procedure shown in Figure 2(a). First, by using e-beam lithography on a silica substrate, in e-beam resist (ZEP-520A, Zeon Corp.), we drew locations at which QD2's were to be deposited (Figure 2(a)(i)). Next, the QD2 solution was dropped onto the substrate and allowed to dry (Figure 2(a)(ii)). Then, after removing the resist, we obtained the QD2 structure on the substrate (Figure 2(a)(iii)). Next, e-beam resist was applied on this structure (Figure 2(a)(iv)), and using e-beam lithography, we drew Y-junction locations where QD1's were to be deposited by aligning the positions so as to contact the QD2 structure (Figure 2(a)(v)). After developing the resist, we dropped the QD1 solution onto the substrate (Figure 2(a)(vi)). Finally, the resist was removed to obtain the Y-junction QD1 structure (Figure 2(a)(vii)). Figure 2(b) shows a fluorescence microscope image obtained when the fabricated sample was excited with a mercury-vapor lamp. The QD1 structure and the QD2 structure were observed as green and yellow colors, respectively. Because points A and B were set at positions where the QD1 and QD2 structures were initially in contact, in practice the distances OA and OB of the fabricated samples were about 6.8 μm and 3.3 μm, respectively. Point C, which did not possess the QD2 structure, was set at a position 7 μm away from O.

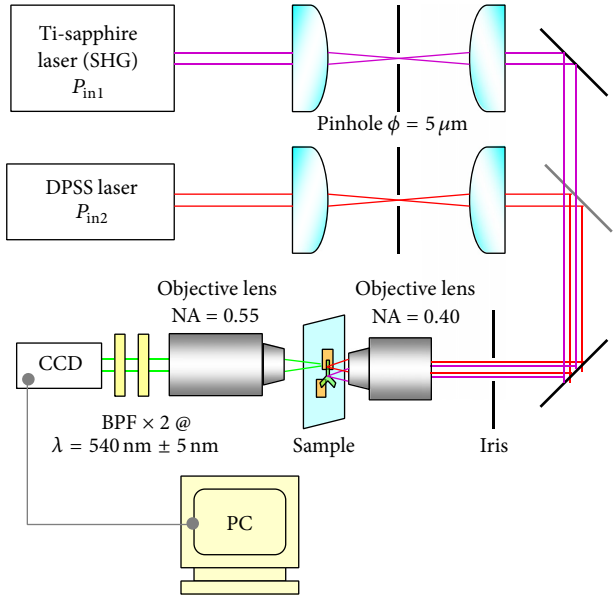

FIGURE 3: Schematic diagram of experimental setup for measurement.

3.2. Experimental Setup. The experimental setup used for performing measurements is shown in Figure 3. For the excitation light P_{in1}, we used the 2nd harmonic wave of a mode-locked Ti : sapphire laser (Mira 900, Coherent, Inc.) with a photon energy $h\nu_1 = 3.44$ eV, a pulse width of 2 ps, and a repetition frequency of 80 MHz, and for the control light P_{in2}, we used a CW diode-pumped solid state (DPSS) laser with a photon energy $h\nu_2 = 2.11$ eV. The incident powers of P_{in1} and P_{in2} were 5 μW and 10 μW, respectively, and the beam spot diameters were both 5 μm. The beams from the two lasers were shaped by passing them through pinholes with 5 μm diameter apertures; then, using a half-mirror, the beams irradiated the sample from the back surface of the substrate via an objective lens with a numerical aperture NA = 0.4. As described in the previous section, because it is possible to observe the change in excitation transfer at the output end as a variation in the emitted light P_{out1} from QD1, we evaluated this in order to make it easier to separate it from the control light. The light emitted from QD1 was observed using an electron multiplying CCD camera (Hamamatsu ImagEM C9100-13H, Hamamatsu Photonics K.K.) after passing through an objective lens with NA = 0.55 and two bandpass filters with transmission wavelengths of 540 ± 5 nm, which is close to the wavelength of P_{out1}. The acquired images were 512 × 512 pixel, 16-bit grayscale images, and the resolution was 0.37 μm/pixel.

As an example of the measurement results, Figure 4(a) shows a CCD image acquired when O and A were irradiated with excitation light P_{in1} and control light P_{in2}, respectively. The green and yellow broken lines show the QD1 and QD2 structures, respectively. Point O was irradiated with P_{in1}, and we observed that the light emitted from the QD1 structure spread out in three directions due to transfer of the excitation. A cross-sectional brightness profile taken along the light-blue dotted line in this figure is shown by the red solid line in Figure 4(b). The black solid line shows the case where point O was irradiated with only P_{in1}. The red solid line is higher in a portion of the QD1 structure serving as the transfer path OB and the point B having the QD2 structure, confirming the tendency for the optical excitation directed towards point B to be increased due to the influence of P_{in2} incident on point A.

3.3. Energy Transfer in Y-Junction Structure. To evaluate the intensity of the emitted light, we used the brightness values acquired with the CCD camera, where the total brightness of 3 × 3 pixels was defined as emission intensity, I. While irradiating point O with P_{in1}, we measured I_{ij}, where i indicates the output end A or B, and j indicates where the control-light P_{in2} is irradiated, that is, to the input terminal A, B, or C. Also, when no control light is irradiated, we represent this by $j = 0$. Concerning the characteristics of the device under study, described in Section 3.1, there are four representative categories:

(a) Reference: without any P_{in2} ($j = 0$);

(b) Case 1: emission end and control-light input terminal are the same point ($i = j$);

(c) Case 2: emission end and control-light input terminal are opposite points ($(i, j) = (A, B)$ or (B, A));

(d) Case 3: control-light input terminal is point C ($j = C$).

The evaluation was performed using the relative intensity change, ΔI_{ij}, defined as $\Delta I_{ij} = (I_{ij} - I_{i0})/I_{i0}$. At this time, if ΔI_{ij} is positive in Case 2, excitation transfer from one end at which the control light is input to the other end will be increased, and control of the excitation transfer will be observed.

Figure 4(c) shows a plot of ΔI_{ij} obtained in Cases 1, 2, and 3. First, we evaluated Case 1 (i.e., $i = j$), as shown by the blue bars in Figure 4(c); they took positive values $\Delta I_{AA} = 3.9 \times 10^{-2}$ and $\Delta I_{BB} = 3.7 \times 10^{-2}$, confirming that the emitted light was stronger. This is the effect of controlling the excitation transfer, and regarding energy transfer in the regions where QD1 and QD2 coexist, we obtained results showing that it is possible to control the excitation transfer also among multiple QDs. This indicates that an AND-gate operation was manifested with multiple randomly distributed QDs, as reported in [3].

Next, we evaluated Case 2 (i.e., $i \neq j = A, B$), as shown by the red bars in Figure 4(c); they also took positive values $\Delta I_{AB} = 7.3 \times 10^{-2}$ and $\Delta I_{BA} = 3.1 \times 10^{-2}$, confirming that the emitted light was stronger. ΔI_{AB} was higher than ΔI_{BA} because the wider overlapped area of QD1 and QD2 structures at point B provided more variation of excitation transfer than that at point A. This difference can be reduced by preparing finer structures and will not disturb the proper operation of solution exploring algorithms. From these results, we confirmed that the excitation transfer was suppressed by the incident control light. These results show that it is possible to control the optical excitation transfer dynamics in a randomly distributed QD structure. Since the relative change ΔI was reduced by losses involved in the optical excitation transfer, we expect that larger values will

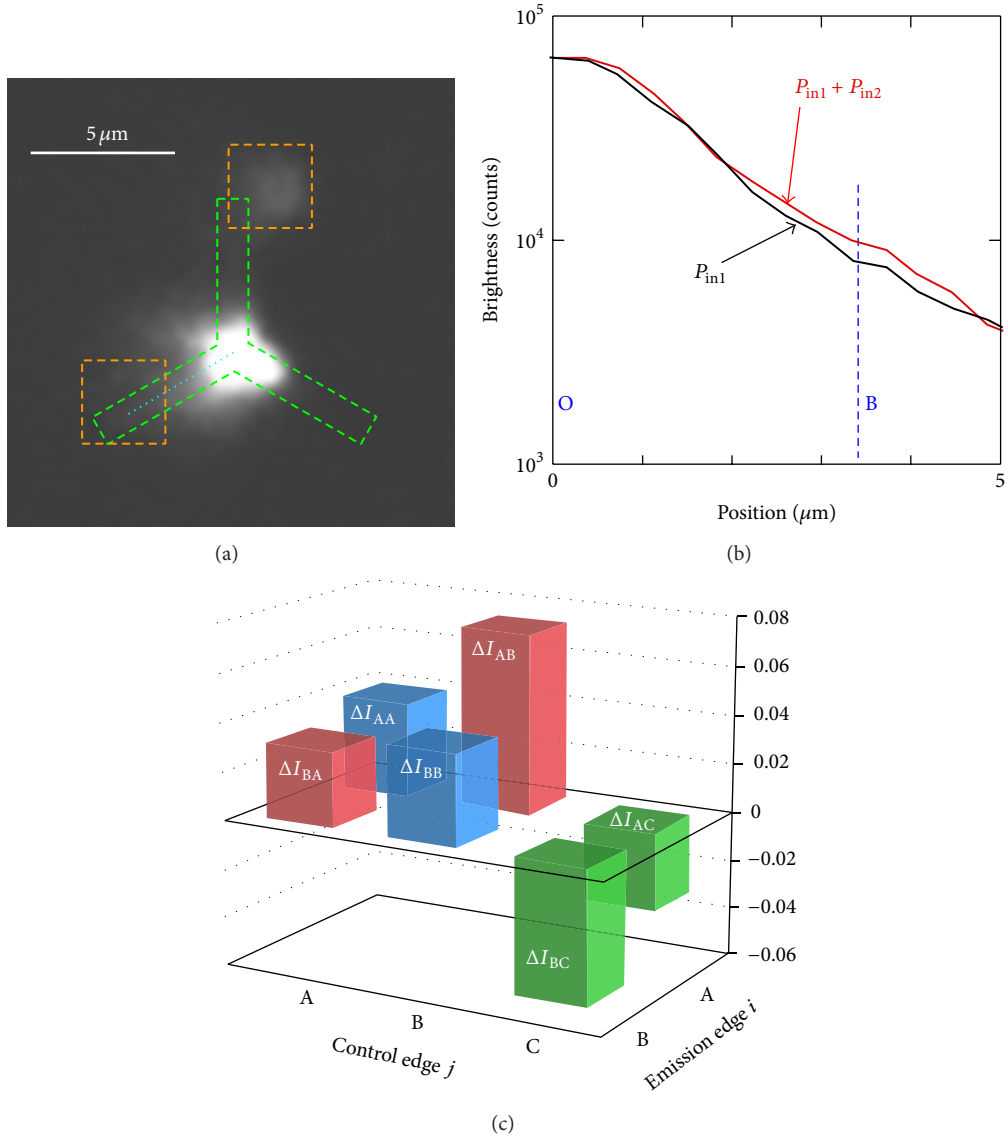

FIGURE 4: (a) Image of light emission from E11 in sample, acquired with CCD camera. Points O and A are irradiated with light P_{in1} and P_{in2}, respectively. Green and yellow broken lines represent the QD1 and QD2 structures, respectively. (b) Cross-sectional profile of emission intensity from E11, acquired with CCD. The red solid line is the cross-sectional profile taken along the light-blue dotted line in (a). The black solid line is the cross-sectional profile taken along the same location, when point O was irradiated with P_{in1} only. The 0 μm base point and the blue broken line indicate point O and point B, respectively. (c) Graph of relative change ΔI_{ij} in emission intensity from E11. Blue, red, and green bars represent Cases 1, 2, and 3, respectively.

be possible by designing a structure having shorter distances OA and OB.

3.4. Discussion on Negative Intensity Change. Moreover, we evaluated Case 3 (i.e. j = C), as shown by the green bars in Figure 4(c); they took negative values $\Delta I_{AC} = -3.2\times10^{-2}$ and $\Delta I_{BC} = -5.5\times10^{-2}$. Ideally, QD1 should be transparent to P_{in2}; however, in our experiments, defect levels with energies lower than E11 in QD1 were excited by P_{in2} [15, 16]. We consider that this excitation prevented the excitation in E11 from slow and nonradiative relaxation via the defect levels.

To verify this, we performed photoluminescence measurements on the QD1 structure. In this experiment, we used samples having only the QD1 structure, fabricated with the same process as that used to fabricate the measurement samples, and we performed measurements with an experimental setup in which the bandpass filters and the CCD camera in the setup shown in Figure 3 were replaced with a spectrometer. The incident powers of P_{in1} and P_{in2} were 5 μW and 770 μW, respectively, and the beams irradiated the sample in spot diameters of 10 μm. The emission intensities were integrated in the range $2.25 < h\nu < 2.29$ eV, corresponding to the peak wavelength of P_{out1}, and were normalized to the

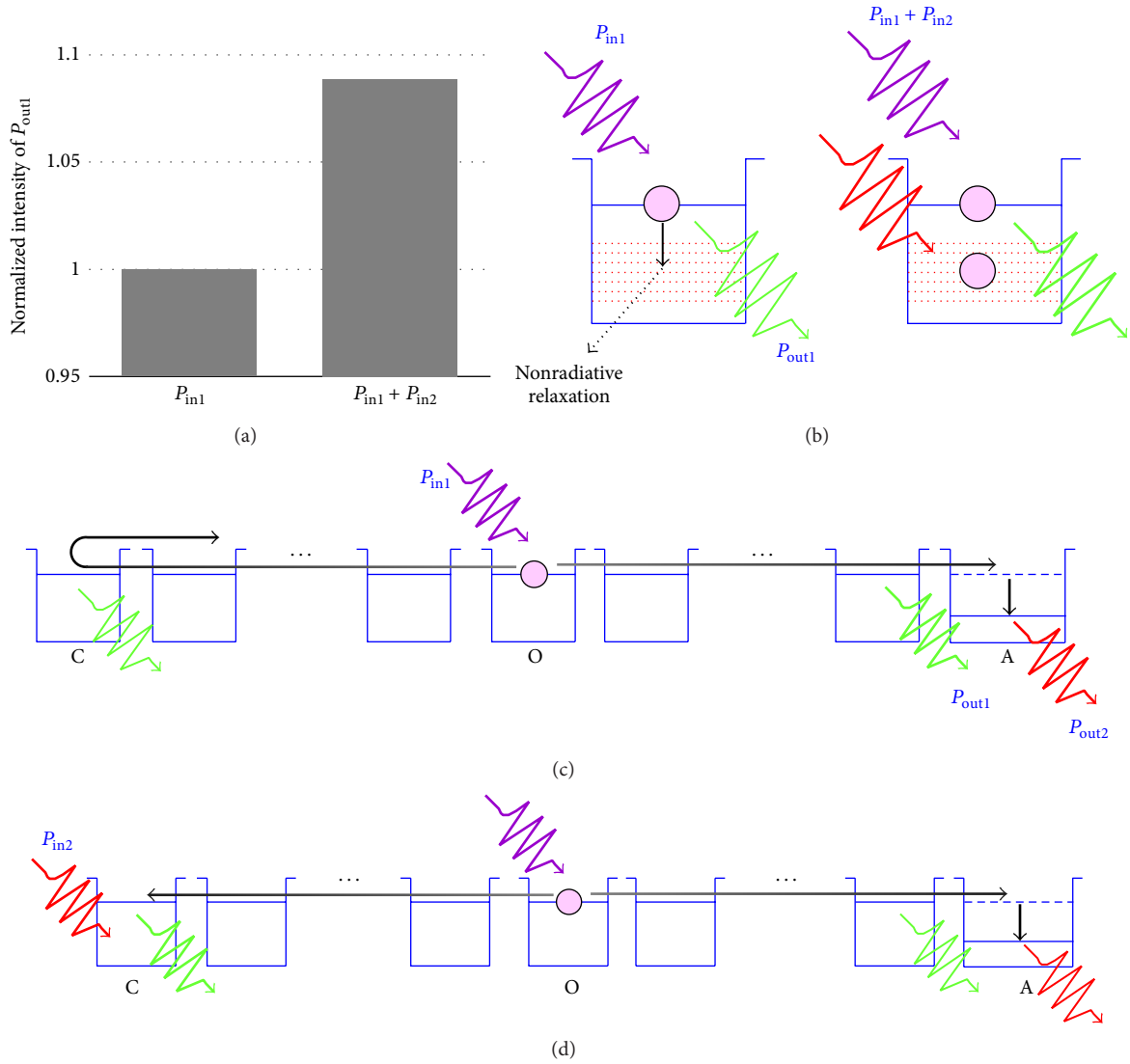

FIGURE 5: (a) Normalized intensity of emitted light P_{out1} from E11, showing cases where the QD1 structure was irradiated with only P_{in1} and with both P_{in1} and P_{in2}. (b) Schematic image of emission from QD1 with only P_{in1} or with both P_{in1} and P_{in2}. (c), (d) Energy diagram schematically showing the experimental sample from point C to point A: (c) without P_{in2}, (d) point C irradiated with P_{in2}.

emission intensity when only P_{in1} was radiated and were compared. As a result, the emission intensity for the case where P_{in1} and P_{in2} were simultaneously radiated was 1.09, showing that the emitted light was increased by radiating P_{in2} (Figure 5(a)). This was the result of defect levels in QD1 being excited by P_{in2}, suppressing the nonradiative relaxation process from E11 via defect levels, which increased the emitted light (Figure 5(b)).

From this result, the negative ΔI values in Case 3 can be explained as follows. Without P_{in2}, the excitation transferred to end C reflects and enhances P_{out1} at ends A and B (Figure 5(c)). By irradiating end C with P_{in2}, P_{out1} at C increases due to excitation of defect levels in QD1, and the reflection decreases (Figure 5(d)). As a result, P_{out1} at ends A and B decreases by irradiation of C with P_{in2}. This differs from the principle of excitation transfer suppression described in Section 2 and Figure 1(e) but indicates the possibility of another method of controlling the spatiotemporal dynamics of excitation transfer. Also, this increased light emission due to the fact that excitation of defect levels can also occur in QD1 at points A and B; however, the energy transfer suppression effect due to excitation of E21 should be larger than this because absorption of P_{in2} ($h\nu_2 = 2.11$ eV) in QD2 is 24 times higher than that in QD1. Thus, the effect of excitation of defect levels at ends A and B is negligible.

4. Summary

In summary, to show the possibility of controlling the spatiotemporal dynamics of optical excitation transfer based on dressed photon interactions between multiple randomly distributed quantum dots (QDs), we conducted experiments

to control excitation transfer using randomly distributed QD structures. Using CdSe/ZnS core-shell QDs, we fabricated a Y-junction structure composed of randomly distributed QDs (QD1 structure). Optical excitation incident at the center of this structure was transferred to a QD2 structure serving as an output end located 3–7 μm away, and by irradiating a QD2 structure at another end with control light P_{in2}, we observed a maximum increase of 7.3×10^{-2}. Thus, we have shown, for the first time, that it is possible to control the spatiotemporal dynamics of optical excitation transfer in a randomly distributed QD structure. Our findings will lead to simplified implementation and driving of solution searching and decision making devices based on the optical excitation transfer dynamics between QDs and will contribute to their practical realization. On the other hand, when control light P_{in2} was incident on the output end that did not have a QD2 structure, we found that the amount of excitation energy transferred to the output end was reduced by a maximum of 5.5×10^{-2}. This was thought to be because the light emission from QD1 was increased due to excitation of defect levels in QD1, and the amount of excitation energy transferred to the end provided with the QD2 structure serving as an output was reduced. This effect acted in a direction causing a reduction in excitation transfer, opposite to the increased transfer level due to excitation of the QD2 structure, indicating the possibility of a different kind of control of the spatiotemporal dynamics. This result is expected to lead to the development of novel computing device architectures in the future.

Conflict of Interests

The authors declare that there is no conflict of interests regarding the publication of this paper.

Acknowledgment

A part of this work was supported by the "Development of Next-generation High-performance Technology for Photovoltaic Power Generation System" Program, NEDO, Japan.

References

[1] M. Ohtsu, T. Kawazoe, T. Yatsui, and M. Naruse, "Nanophotonics: application of dressed photons to novel photonic devices and systems," *IEEE Journal on Selected Topics in Quantum Electronics*, vol. 14, no. 6, pp. 1404–1417, 2008.

[2] T. Kawazoe, K. Kobayashi, S. Sangu, and M. Ohtsu, "Demonstration of a nanophotonic switching operation by optical near-field energy transfer," *Applied Physics Letters*, vol. 82, no. 18, pp. 2957–2959, 2003.

[3] T. Kawazoe, M. Ohtsu, S. Aso et al., "Two-dimensional array of room-temperature nanophotonic logic gates using InAs quantum dots in mesa structures," *Applied Physics B: Lasers and Optics*, vol. 103, no. 3, pp. 537–546, 2011.

[4] A. Karimkhani and M. K. Moravvej-Farshi, "Design of three-input nanophotonic and gates," *Journal of the Optical Society of America B: Optical Physics*, vol. 26, no. 5, pp. 1084–1090, 2009.

[5] T. Kawazoe, K. Kobayashi, and M. Ohtsu, "Optical nanofountain: a biomimetic device that concentrates optical energy in a nanometric region," *Applied Physics Letters*, vol. 86, no. 10, Article ID 103102, pp. 1–3, 2005.

[6] W. Nomura, T. Yatsui, T. Kawazoe, M. Naruse, and M. Ohtsu, "Structural dependency of optical excitation transfer via optical near-field interactions between semiconductor quantum dots," *Applied Physics B: Lasers and Optics*, vol. 100, pp. 181–187, 2010.

[7] P. Holmström, L. Thylén, and A. Bratkovsky, "Composite metal/quantum-dot nanoparticle-array waveguides with compensated loss," *Applied Physics Letters*, vol. 97, Article ID 073110, 2010.

[8] M. Naruse, M. Aono, S.-J. Kim et al., "Spatiotemporal dynamics in optical energy transfer on the nanoscale and its application to constraint satisfaction problems," *Physical Review B*, vol. 86, Article ID 125407, 2012.

[9] M. Aono, M. Naruse, S.-J. Kim et al., "Amoeba-inspired nanoarchitectonic computing: solving intractable computational problems using nanoscale photoexcitation transfer dynamics," *Langmuir*, vol. 29, no. 254, pp. 7557–7564, 2013.

[10] S.-J. Kim, M. Naruse, M. Aono, M. Ohtsu, and M. Hara, "Decision maker based on nanoscale photo-excitation transfer," *Scientific Reports*, vol. 3, Article ID 2370, 2013.

[11] M. Naruse, H. Hori, K. Kobayashi, P. Holmström, L. Thylén, and M. Ohtsu, "Lower bound of energy dissipation in optical excitation transfer via optical near-field interactions," *Optics Express*, vol. 18, no. 23, pp. A544–A553, 2010.

[12] U. Schöning, "A probabilistic algorithm for k-SAT and constraint satisfaction problems," in *Proceedings of the 40th IEEE Symposium on Foundations of Computer Science*, pp. 410–414, 1999.

[13] N. Sakakura and Y. Masumoto, "Persistent spectral-hole-burning spectroscopy of CuCl quantum cubes," *Physical Review B—Condensed Matter and Materials Physics*, vol. 56, no. 7, pp. 4051–4055, 1997.

[14] C. Trallero-Giner, A. Debernardi, M. Cardona, E. Menéndez-Proupín, and A. I. Ekimov, "Optical vibrons in CdSe dots and dispersion relation of the bulk material," *Physical Review B—Condensed Matter and Materials Physics*, vol. 57, no. 8, pp. 4664–4669, 1998.

[15] M. Y. Valakh, Y. G. Sadfyev, N. O. Korsunska et al., "Deep-level defects in CdSe/ZnSe QDs and giant anti-stokes photoluminescence," *Semiconductor Physics, Quantum Electronics and Optoelectronics*, vol. 5, no. 3, pp. 254–257, 2002.

[16] M. Danek, K. F. Jensen, C. B. Murray, and M. G. Bawendi, "Synthesis of luminescent thin-film CdSe/ZnSe quantum dot composites using CdSe quantum dots passivated with an overlayer of ZnSe," *Chemistry of Materials*, vol. 8, no. 1, pp. 173–180, 1996.

Novel wavelength conversion with nanophotonic droplet consisting of coupled quantum dots

Naoya Tate,[1,2,*] Wataru Nomura,[1,2] Tadashi Kawazoe,[1,2] and Motoichi Ohtsu[1,2]

[1]*Department of Electrical Engineering and Information Systems, School of Engineering, The University of Tokyo, 2-11-16 Yayoi, Bunkyo-ku, Tokyo, 113-8656, Japan*

[2]*Nanophotonics Research Center, School of Engineering, The University of Tokyo, 2-11-16 Yayoi, Bunkyo-ku, Tokyo, 113-8656, Japan*

[*]*tate@nanophotonics.t.u-tokyo.ac.jp*

Abstract: The concept of nanophotonic droplets, which are individual spherical polymer structures containing accurately coupled heterogeneous quantum dots, has been previously demonstrated. Such combinations are theoretically promising for their ability to induce novel optical functions. In this paper, we focus on the implementation of wavelength conversion as one of the fundamental optical functions of nanophotonic droplets. A novel mechanism involved in the formation of nanophotonic droplets and results of experimental verification of wavelength conversion using formed nanophotonic droplets are described. By a quantitative comparison with a corresponding sample consisting of randomly dispersed quantum dots, the effectiveness of proposal was successfully demonstrated.

OCIS codes: (220.4241) Nanostructure fabrication; (230.5590) Quantum-well, -wire and -dot devices; (230.7405) Wavelength conversion devices; (350.4238) Nanophotonics and photonic crystals.

References and links

1. S. A. Swanson, G. M. Wallraff, J. P. Chen, W. Zhang, L. D. Bozano, K. R. Carter, J. R. Salem, R. Villa, and J. C. Scott, "Stable and efficient fluorescent red and green dyes for external and internal conversion of blue OLED emission," Chem. Mater. **15**(12), 2305–2312 (2003).
2. H. Song and S. Lee, "Red light emitting solid state hybrid quantum dot–near-UV GaN LED devices," Nanotechnology **18**(25), 255202 (2007).
3. Y.-L. Lee, B.-M. Huang, and H.-T. Chien, "Highly efficient CdSe-sensitized TiO_2 photoelectrode for quantum-dot-sensitized solar cell applications," Chem. Mater. **20**(22), 6903–6905 (2008).
4. C. X. Guo, H. B. Yang, Z. M. Sheng, Z. S. Lu, Q. L. Song, and C. M. Li, "Layered graphene/quantum dots for photovoltaic devices," Angew. Chem. Int. Ed. Engl. **49**(17), 3014–3017 (2010).
5. S. Sygletos, R. Bonk, T. Vallaitis, A. Marculescu, P. Vorreau, J. Li, R. Brenot, F. Lelarge, G.-H. Duan, W. Freude, and J. Leuthold, "Filter assisted wavelength conversion with quantum-Dot SOAs," J. Lightwave Technol. **28**(6), 882–897 (2010).
6. Y. Yonezawa, H. Kurokawa, and T. Sato, "Excitation energy transfer between J-aggregates of cyanine dyes in mixed monolayer assemblies," J. Lumin. **54**(5), 285–295 (1993).
7. M. Watanabe, M. Herren, and M. Morita, "Picosecond luminescence and excitation energy transfer in J- and H-aggregates of cyamine dyes on colloidal silica," J. Lumin. **58**(1–6), 198–201 (1994).
8. G. Springholz, V. Holy, M. Pinczolits, and G. Bauer, "Self-organized growth of three- dimensional quantum-dot crystals with fcc-like stacking and a tunable lattice constant," Science **282**(5389), 734–737 (1998).
9. A. Luque, A. Martí, C. Stanley, N. López, L. Cuadra, D. Zhou, J. L. Pearson, and A. McKee, "General equivalent circuit for intermediate band devices: Potentials, currents and electroluminescence," J. Appl. Phys. **96**(1), 903–909 (2004).
10. K. Akahane, N. Yamamoto, and M. Tsuchiya, "Highly stacked quantum-dot laser fabricated using a strain compensation technique," Appl. Phys. Lett. **93**(4), 041121 (2008).
11. S. Tomić, T. S. Jones, and N. M. Harrison, "Absorption characteristics of a quantum dot array induced intermediate band: Implications for solar cell design," Appl. Phys. Lett. **93**(26), 263105 (2008).
12. A. Takata, R. Oshima, Y. Shoji, K. Akahane, and Y. Okada, "Growth of multi-stacked InAs/GaNAs quantum dots grown with As_2 source in atomic hydrogen-assisted molecular beam epitaxy," Physica E **42**(10), 2745–2748 (2010).
13. M. Ohtsu, K. Kobayashi, T. Kawazoe, T. Yatsui, and M. Naruse, eds., *Principles of Nanophotonics* (Taylor and Francis, 2008).
14. M. Ohtsu, *Dressed Photons* (Springer-Verlag, 2013).

Received 7 Mar 2014; revised 11 Apr 2014; accepted 14 Apr 2014; published 21 Apr 2014

15. S. Yukutake, T. Kawazoe, T. Yatsui, W. Nomura, K. Kitamura, and M. Ohtsu, "Selective photocurrent generation in the transparent wavelength range of a semiconductor photovoltaic device using a phonon-assisted optical near-field process," Appl. Phys. B **99**(3), 415–422 (2010).
16. H. Fujiwara, T. Kawazoe, and M. Ohtsu, "Nonadiabatic multi-step excitation for the blue–green light emission from dye grains induced by the near-infrared optical near-field," Appl. Phys. B **98**(2–3), 283–289 (2010).
17. T. Kawazoe, M. A. Mueed, and M. Ohtsu, "Highly efficient and broadband Si homojunction structured near-infrared light emitting diodes based on the phonon-assisted optical near-field process," Appl. Phys. B **104**(4), 747–754 (2011).
18. K. Kitamura, T. Kawazoe, and M. Ohtsu, "Homojunction-structured ZnO light-emitting diodes fabricated by dressed-photon assisted annealing," Appl. Phys. B **107**(2), 293–299 (2012).
19. T. Kawazoe, H. Fujiwara, K. Kobayashi, and M. Ohtsu, "Visible light emission from dye molecular grains via infrared excitation based on the nonadiabatic transition induced by the optical near field," J. Sel. Top. Quantum Electron. **15**(5), 1380–1386 (2009).
20. N. Wada, T. Kawazoe, and M. Ohtsu, "An optical and electrical relaxation oscillator using a Si homojunction structured light emitting diode," Appl. Phys. B **108**(1), 25–29 (2012).
21. N. Tate, Y. Liu, T. Kawazoe, M. Naruse, T. Yatsui, and M. Ohtsu, "Fixed-distance coupling and encapsulation of heterogeneous quantum dots using phonon-assisted photo-curing," Appl. Phys. B **110**(1), 39–45 (2013).
22. N. Tate, Y. Liu, T. Kawazoe, M. Naruse, T. Yatsui, and M. Ohtsu, "Nanophotonic droplet: a nanometric optical device consisting of size- and number-selective coupled quantum dots," Appl. Phys. B **110**(3), 293–297 (2013).
23. N. Tate, M. Naruse, Y. Liu, T. Kawazoe, T. Yatsui, and M. Ohtsu, "Experimental demonstration and stochastic modeling of autonomous formation of nanophotonic droplets," Appl. Phys. B **112**(4), 587–592 (2013).
24. A. Yariv, "Second-harmonics generation and parametric oscillation," in *Introduction to Optical Electronics*, 1st ed. (Holt, Rinehert and Winston, 1985), Chap. 8, pp. 177–221.
25. P. W. Atkins, "Spectroscopy2: Electronic transitions," in *Physical Chemistry*, 6th ed. (Oxford University, 1998), Chap. 17, pp. 497–526.
26. M. Ohtsu, ed., *Progress in Nano-Electro-Optics II* (Springer-Verlag, 2004).
27. T. Kawazoe, K. Kobayashi, J. Lim, Y. Narita, and M. Ohtsu, "Direct observation of optically forbidden energy transfer between CuCl quantum cubes via near-field optical spectroscopy," Phys. Rev. Lett. **88**(6), 067404 (2002).
28. T. Kawazoe, K. Kobayashi, and M. Ohtsu, "Optical nanofountain: A biomimetic device that concentrates optical energy in a nanometric region," Appl. Phys. Lett. **86**(10), 103102 (2005).

1. Introduction

Various application fields, such as energy technology and information communication, require high-performance wavelength conversion to resolve fundamental issues related to the mismatch between the wavelengths emitted by light sources and the wavelengths at which detectors are most sensitive. One of the promising ideas for realizing high-yield wavelength conversion is to use fluorescent materials, such as quantum dots (QDs) and fluorescent dyes [1–5]. Because such materials exhibit high quantum yield in their absorption and emission processes, effective wavelength conversion is expected. Among various ideas for using fluorescent materials, there have been some proposals to mix and couple heterogeneous materials to realize novel emission mechanisms based on their combinations [1,6,7]. The most attractive advantage of such proposals is that absorption and emission wavebands can be readily tuned by controlling the mixing and coupling conditions of components to meet the requirements of various applications. However, the behavior of this mechanism fundamentally depends on the relative spatial positions of the components in the mixed structure. Therefore, it is technically difficult to ensure homogeneity and stability of their optical functions, and advanced fabrication techniques are required [8–12].

On the other hand, the field of nanophotonics has seen rapid progress in recent years, and various applications have been actively developed [13]. Nanophotonics exploits the local interactions between nanometer-scale particles via optical near fields induced by incident light. Several characteristics of optical near fields can be described by the behavior of a dressed photon (DP), which is a quasi-particle representing the coupled state of a photon and an electron in a nanometric space [14]. A DP excites a multi-mode coherent phonon in a nanometric material, and the DP state is coupled with the excited coherent phonon state [15–18]. Because the coupled state can be regarded as an intermediate state during the excitation and relaxation process of the material, multistep excitation and relaxation, and corresponding optical functions, are allowed. By utilizing such a phenomenon, called a phonon-assisted transition, some experimental demonstrations on high-yield emission of upper-converted

Received 7 Mar 2014; revised 11 Apr 2014; accepted 14 Apr 2014; published 21 Apr 2014

optical energy by using organic dye grains [16,19] and high-intensity emission from indirect transition type semiconductors [17,18,20] have been reported.

Previously, we have proposed a novel method of coupling heterogeneous QDs in a photo-curable polymer solution by utilizing a phonon-assisted photo-curing process [21–23]. We call such coupled-QDs, when they are encapsulated by locally cured polymer, a nanophotonic droplet (ND). All we have to do to form NDs is to mix all components together and irradiate the mixture with light. Here, the irradiated energy must be *lower* than the curable energy of the polymer. The formation process is induced only when heterogeneous QDs encounter each other at the optimum distance to induce appropriate optical near field interactions between the two. Therefore, their relative spatial positions and corresponding optical functions are autonomously determined, which is a strongly desired property of wavelength conversion.

In this paper, we focus on the implementation of wavelength conversion utilizing the characteristics of NDs. First, we briefly review the principles of the phonon-assisted photo-curing process and our method of forming NDs. Here, we assume the use of a thermo-curable polymer that is transparent to the incident and emitted light, instead of a photo-curable polymer. Then, we describe experimental demonstrations on forming NDs and their quantitative evaluation as wavelength conversion elements. We embedded a large number of NDs into a transparent material and compared a figure-of-merit for wavelength conversion with a corresponding sample in which we embedded randomly dispersed QDs.

2. Principles

An ND is formed of coupled heterogeneous QDs encapsulated by locally cured polymer [21–23]. During the process of fabricating NDs, incident light having a lower photon energy than the curable energy of the polymer is radiated into a polymer solution that contains a number of nanometric components to be coupled. The incident light induces a phonon-assisted process [16–19], namely, multistep photo-curing, which locally cures the polymer with transitions via activated phonon levels. In particular, a thermo-curable polymers that is transparent over a wide range of wavelengths is used instead of a photo-curable polymer, so that light is losslessly input to and output from the sample. Moreover, in this case, the conventional photo-curing process due to the absorption of incident optical energy cannot be expected to occur. A detailed description of the formation process of NDs is given below.

The principle of our method is schematically shown in Fig. 1. Here we assume a mixture containing two types of QDs, namely, QD_A and QD_B, and a thermo-curable polymer. The mixture is irradiated with incident light, what we call assisting light, having photon energy $h\nu_{assist}$. The excitation energies of QD_A and QD_B are $E_{A:bg}$ and $E_{B:bg}$, respectively, and the curable energy of the thermo-curable polymer is $E_{poly:act}$. In the case where these energies satisfy the condition $E_{A:bg}<h\nu_{assist}<E_{poly:act}<E_{B:bg}$, the following process can be induced by radiating the assisting light. If the numbers of QDs, or in other words, their volume densities, in the mixture are not sufficiently high and they rarely encounter each other, only QD_A spontaneously emits light by absorbing the optical energy of the assisting light due to the energy condition $E_{A:bg}<h\nu_{assist}<E_{B:bg}$. In this case, no subsequent physical or chemical reaction occurs. On the other hand, if the density is sufficiently high that the QDs can frequently encounter each other, multistep photo-curing occurs due to induction of DPs and corresponding optical near-field interactions between neighboring QD_A and QD_B. Because the activated phonon-levels are real states, the excitation rate is expected to be much higher than any other multi-step excitation, such as conventional second harmonic generation [24] and phosphorescence using a multi-step transition [25]. As a result, the thermo-curable polymer is locally cured, and the spatial alignment of the encountered QDs is physically fixed by the cured polymer. The electronic transitions via such a coupled state induced by the assisting light have been described in a previous report by the authors [21].

Received 7 Mar 2014; revised 11 Apr 2014; accepted 14 Apr 2014; published 21 Apr 2014

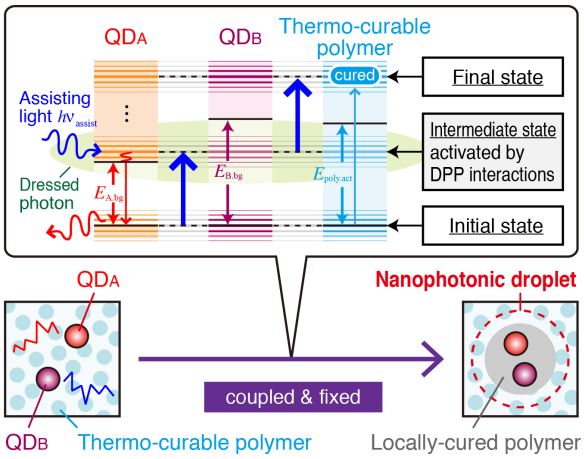

Fig. 1. Schematic diagram of process of forming a thermo-curable polymer-based ND via the phonon-assisted photo-curing process.

Since the spatial distribution of the DPs generated on the surface of the QDs is expressed by a Yukawa function [26], the separation between the two QDs in each ND is theoretically defined also by the Yukawa function. Moreover, because the above process occurs only when heterogeneous components encounter each other, the cured polymer necessarily contains coupled heterogeneous components. Such accuracy and homogeneity of their alignment and combinations of QDs ensure efficient induction of optical near-field interactions and the resulting wavelength conversion process, where QD_A and QD_B act as *emitters* and *absorbers* of light in each ND, respectively. A schematic diagram of wavelength conversion from a higher optical energy $h\nu_{IN}$ to a lower optical energy $h\nu_{OUT\text{-}A}$ is shown in Fig. 2.

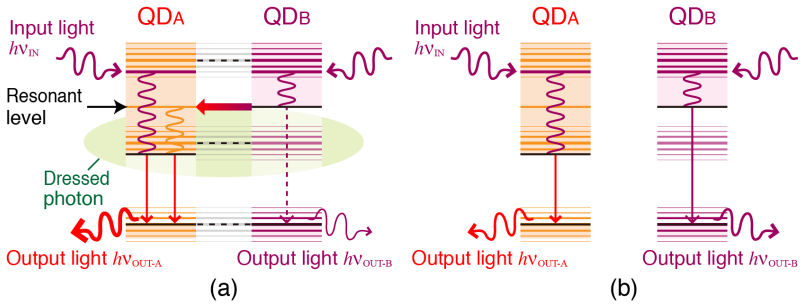

Fig. 2. (a) Schematic diagram of enhanced emission from a CdSe-QD via optical energy transfer from a CdS-QD to the CdSe-QD, and (b) individual emissions from the CdSe-QD and the CdS-QD.

As shown in Fig. 2(a), in the case of coupled CdSe-QDs, because the rate of an optically forbidden transition between neighboring QDs induced by optical near-field interactions is much higher than the relaxation rate in each QD, the optical energy absorbed by QD_B is preferably transferred to the neighboring QD_A. As a result, enhanced spontaneous emission is observed from QD_A. In this case, the emission intensity from QD_B is necessarily decreased. On the other hand, in the case of emission from isolated QDs, as shown in Fig. 2(b), each QD emits individually, and enhanced emission cannot occur. Therefore, though similar wavelength conversion occurs in both cases, the yield in the case of Fig. 2(b) is much lower than that in the case of Fig. 2(a). Besides, the time of such a transition between coupled QDs, which is a few hundred femtoseconds, has been theoretically and experimentally verified to be at least ten times faster than the relaxation rate of each QD, which is a few nanoseconds, in the case where specific QDs are assumed [27]. Furthermore, the processing time of the wavelength conversion is fundamentally limited by the transition rate between coupled QDs.

Received 7 Mar 2014; revised 11 Apr 2014; accepted 14 Apr 2014; published 21 Apr 2014

3. Experimental demonstration

In order to experimentally verify the proposed process of forming NDs with a thermo-curable polymer, as well as the mechanism of wavelength conversion using the formed NDs, as QD_A and QD_B in Fig. 1, we used commercially available CdSe-QDs (Sigma-Aldrich, Lumidots) and CdS-QDs (NN-Labs, Nanocrystals), respectively, which emit visible light with emission wavelengths of 560 nm and 420 nm, in toluene solutions. In this case, wavelength conversion from ultraviolet (UV) light to visible light is expected. The QD solutions were dispersed in a thermo-curable polymer (Dow Corning Toray, Sylgard 184), which consists of polydimethylsiloxane (PDMS). To form the NDs, the mixture was irradiated with assisting light emitted from a 200 mW laser diode with a wavelength of 457 nm for 30 minutes. These experimental conditions surely fulfilled the previously described energy conditions for inducing the sequential process of the phonon-assisted photo-curing method, as schematically shown in Fig. 1. The total amount of the mixture was limited to 1.0 mL to maintain spatially uniform illumination in our experimental setup. This volume contains about 10^{18} of each QD. Under these experimental conditions, the QDs can be assumed to encounter each other at a sufficiently high frequency to induce the photo-curing process. After irradiation with the assisting light, the mixture was separated into cured and uncured materials by centrifugation at 10,000 rpm for 5 min. The extracted cured material was assumed to contain a large number of NDs. Before demonstrating wavelength conversion using these NDs, they were dispersed in a toluene solution and uniformly dispersed on a Si substrate to observe their appearances with a fluorescence microscope. Figure 3 shows a fluorescence image of the formed NDs under UV light irradiation.

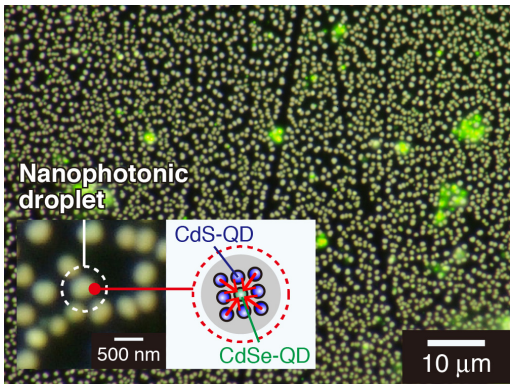

Fig. 3. Microscope fluorescence image of densely formed NDs under UV light irradiation and (inset) a magnified view.

As shown, a number of NDs with similar sizes and emission intensities were successfully obtained. In contrast to our previous NDs using a photo-curable polymer [21–23], which had diameters of a few micrometers, the diameters of the NDs in Fig. 3 are only a few hundred nanometers. This is due to suppression of the encapsulation process during formation of the NDs as a result of absorption of spontaneously emitted light from coupled QDs. Because the surrounding thermo-curable polymer does not absorb such emitted light, the NDs cannot grow as much as in the case where a photo-curable polymer is used. On the other hand, the distance between and the distribution of QDs in each ND are expected to be quite similar to those of our previous NDs because the QD coupling process during formation of NDs fundamentally depend on size of each QD and not on the types of polymers. Moreover, as schematically illustrated in the inset of Fig. 3, each ND is assumed to contain physically coupled QDs, which consist of CdSe-QDs as emitters and CdS-QDs as absorbers. By such alignment of the QDs, the optical energy absorbed by the CdS-QDs is preferentially transferred to the CdSe-QD before being emitting from it. Therefore, the emission from the CdSe-QD is expected to be enhanced. Related research that experimentally demonstrated

Received 7 Mar 2014; revised 11 Apr 2014; accepted 14 Apr 2014; published 21 Apr 2014

optical energy transfer between QDs and corresponding emission enhancement has been previously reported [28].

Next, the NDs were extracted and embedded in another pure PDMS solution. Then, the solution was cured for 2 hours by heating it at 150 °C after degasing to remove air bubbles in the mixture. We call this sample a w/-NDs (with NDs) sample in this paper. In order to discuss the effectiveness of embedding NDs, a corresponding sample without NDs, called a w/o-NDs sample, was prepared by embedding randomly dispersed QDs. The numbers of QDs in the w/-NDs and w/o-NDs samples were set to be equivalent. Figures 4(a) and 4(b) show the appearances of both samples under room light and their absorption spectra, respectively. As shown, it is quite difficult to discern a difference between the two. However, as shown in Fig. 4(c), their appearances under UV light seem quite different in terms of their color tones: the w/-NDs sample showed a more monochromatic green appearance than that of the w/o-NDs sample. Such appearances support the mechanism of the emission processes in both samples shown in Fig. 3, where the w/-NDs sample is expected to show enhanced light emission from the CdSe-QDs, whereas the w/o-NDs sample is expected to show individual emissions from both CdSe-QDs and the CdS-QDs.

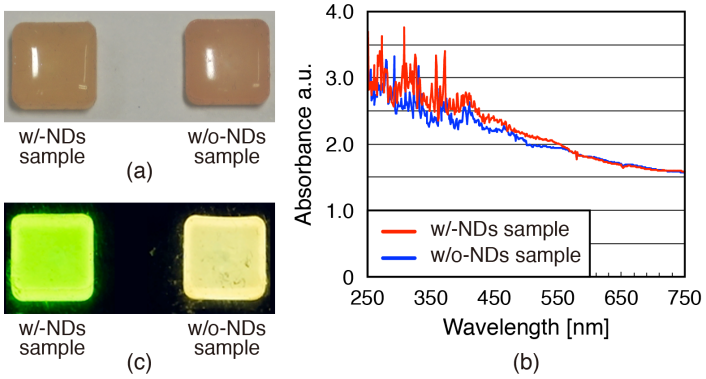

Fig. 4. Appearance of w/-NDs sample (left) and w/o-NDs sample (right) under (a) room light and (b) the absorption spectra of w/-NDs sample (red line) and w/o-NDs sample (blue line). (c) Appearance of w/-NDs sample (left) and w/o-NDs sample (right) under UV light.

For more quantitative evaluation of their optical properties, we measured the excitation spectra, which are shown in Figs. 5(a) and 5(b). Insets in each figure show schematic diagrams of the assumed QD arrangement in each sample. The emission and excitation wavelengths were scanned from 300 nm to 800 nm and from 300 nm to 600 nm, respectively.

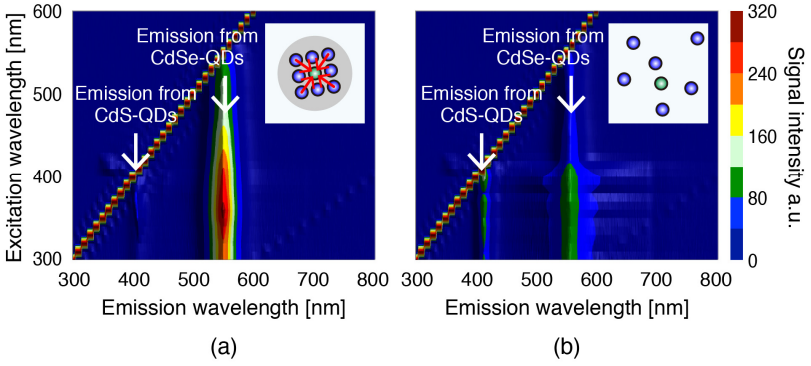

Fig. 5. Comparison of excitation spectra of (a) w/-NDs sample and (b) w/o-NDs sample.

Peaks at 420 nm and 560 nm in the spectra correspond to emission from the CdS-QDs and CdSe-QDs, respectively. As shown, a clear difference was revealed between the two samples.

Received 7 Mar 2014; revised 11 Apr 2014; accepted 14 Apr 2014; published 21 Apr 2014

Emission from the CdSe-QDs in the w/-NDs sample was enhanced, whereas the w/o-NDs sample revealed independent emissions from the CdSe-QDs and the CdS-QDs. Such spectra are the specific results of this research, and they indicate that NDs in the w/-NDs sample contained coupled CdS-QDs and CdSe-QDs, which exhibit optical energy transfer between them. As a result, the light emission from the CdSe-QDs was enhanced and that from the CdS-QDs was decreased, as we showed in Fig. 2(a). A quantitative difference on the yield of the wavelength conversion between the two samples was evaluated from the results of emission spectra with irradiation of 325 nm light. A result of comparison is shown in Fig. 6(a).

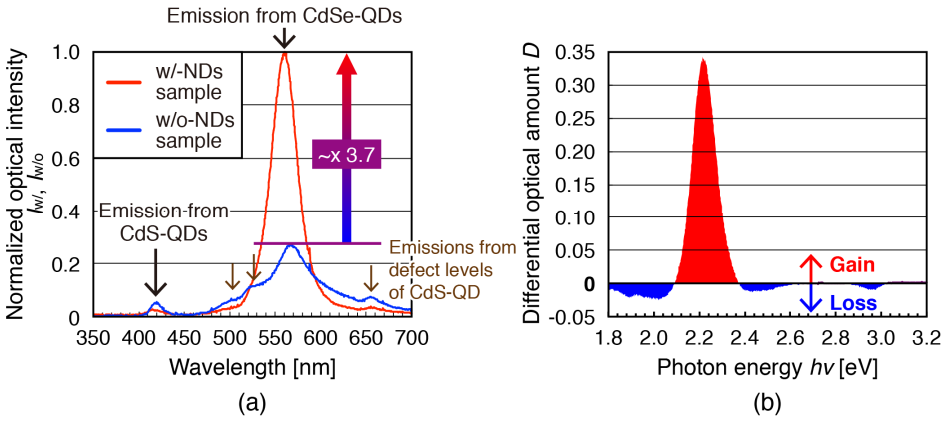

Fig. 6. (a) Comparison of emission spectra with 325 nm light irradiation, measured with w/-NDs sample (red line) and w/o-NDs sample (blue line), respectively. (b) Description of differential optical amount, D, calculated from the results in (a).

As shown, the w/-NDs sample showed a 3.7-times higher intensity of emission from the CdSe-QDs, whereas the intensity of emission from the CdS-QDs was decreased, which is evidence of the successful existence of NDs in the w/-NDs sample. Moreover, a sideband-like spectral feature from 500 nm to 650 nm, which is much more clearly recognized in Fig. 6 than in Fig. 5, was also decreased due to the existence of NDs. This spectral feature can be attributed to emission from defect levels of the CdS-QDs.

As we can confirm by the existence of emission spectra from the CdS-QDs in the w/-NDs sample in Fig. 6(a), not all QDs in the w/-NDs sample are coupled with each other, and the sample also includes isolated QDs. In order to directly discuss improvement of the energy effectiveness due to the existence of NDs and to compensate effect of the emission from isolated QDs in the w/-NDs sample, we defined a metric called the differential optical amount, $D = (I_{w/}-I_{w/o})/h\nu$, where $I_{w/}$ and $I_{w/o}$ represent the normalized optical intensities in Fig. 6(a), and $h\nu$ represents the photon energy of light at each wavelength. The calculated D is explained in Fig. 6(b). Regions filled with red and blue correspond to gain and loss caused by the existence of the NDs, respectively. As shown, the total gain due to the existence of the NDs was 4.2-times larger than that of the loss. The result is due to effective use of the incident optical energy by the induced energy transfer from the CdS-QDs to the CdSe-QDs. That is to say, while individual QDs necessarily reveal quenching of optical energy during their emission process, in the case of coupled QDs, optical energy transfer preferentially occurs before the quenching process. Therefore, the incident optical energy is utilized for wavelength conversion in NDs much more effectively than when using randomly dispersed QDs.

4. Summary

In this paper, we have reported the experimental demonstration of effective wavelength conversion based on novel optical functions of NDs due to the particular structural characteristics of their constituent elements. In order to verify the mechanism of wavelength

Received 7 Mar 2014; revised 11 Apr 2014; accepted 14 Apr 2014; published 21 Apr 2014

conversion from UV to visible light, to form NDs, we used a thermo-curable polymer that is transparent to input and output light, instead of a photo-curable polymer as in our previous experiments. As a result, NDs were successfully obtained, and a sample with NDs showed much more effective wavelength conversion than a corresponding sample without NDs, which contained randomly dispersed QDs. This effectiveness is due to the autonomously realized accuracy and homogeneity of the structured components in each ND and the resulting induced optical energy transfer between each component. Such optimized structures can also be realized by utilizing other components instead of CdSe-QDs and CdS-QDs and are therefore expected to achieve other optical functions with higher-efficiency than existing techniques.

Acknowledgment

A part of this work was supported by the "Development of next-generation high-performance technology for photovoltaic power generation system" program of the New Energy and Industrial Technology Development Organization (NEDO), Japan.

Received 7 Mar 2014; revised 11 Apr 2014; accepted 14 Apr 2014; published 21 Apr 2014

Analysis of optical near-field energy transfer by stochastic model unifying architectural dependencies

Makoto Naruse,[1,2,a)] Kouichi Akahane,[1] Naokatsu Yamamoto,[1] Petter Holmström,[3] Lars Thylén,[3,4] Serge Huant,[5] and Motoichi Ohtsu[2,6]
[1]*Photonic Network Research Institute, National Institute of Information and Communications Technology, 4-2-1 Nukui-kita, Koganei, Tokyo 184-8795, Japan*
[2]*Nanophotonics Research Center, Graduate School of Engineering, The University of Tokyo, 2-11-16 Yayoi, Bunkyo-ku, Tokyo 113-8656, Japan*
[3]*Laboratory of Photonics and Microwave Engineering, Royal Institute of Technology (KTH), SE-164 40 Kista, Sweden*
[4]*Hewlett-Packard Laboratories, Palo Alto, California 94304, USA*
[5]*Institut Néel, CNRS and Université Joseph Fourier, 25 rue des Martyrs BP 166, 38042 Grenoble Cedex 9, France*
[6]*Department of Electrical Engineering and Information Systems, Graduate School of Engineering, The University of Tokyo, 2-11-16 Yayoi, Bunkyo-ku, Tokyo 113-8656, Japan*

(Received 28 January 2014; accepted 5 April 2014; published online 17 April 2014)

We theoretically and experimentally demonstrate energy transfer mediated by optical near-field interactions in a multi-layer InAs quantum dot (QD) structure composed of a single layer of larger dots and N layers of smaller ones. We construct a stochastic model in which optical near-field interactions that follow a Yukawa potential, QD size fluctuations, and temperature-dependent energy level broadening are unified, enabling us to examine device-architecture-dependent energy transfer efficiencies. The model results are consistent with the experiments. This study provides an insight into optical energy transfer involving inherent disorders in materials and paves the way to systematic design principles of nanophotonic devices that will allow optimized performance and the realization of designated functions. © *2014 AIP Publishing LLC*. [http://dx.doi.org/10.1063/1.4871668]

I. INTRODUCTION

Optical energy transfer via optical near-field interactions is one of the most important and unique attributes of nanophotonics.[1,2] Its theoretical fundamentals have been explained by local optical near-field interactions,[3,4] which describe optical energy transfer involving conventionally dipole-forbidden transitions, and the model predictions are in agreement with experimental demonstrations based on CdSe quantum dots (QDs),[5] ZnO quantum wells (QWs),[6] and ZnO QDs[7] among others.[8] Energy transfer in hybrid systems has also been intensively studied.[9–11] Higher-order multipolar interactions due to localized near-fields that break electric-dipole selection rules have also been discussed in the literature.[4,12–16] Optical energy transfer on the nanoscale has been applied to a variety of applications, including energy concentration,[16] switching and logic circuits,[10,17] nanobiosensors,[9,11] engineered color rendering for solid state lighting,[18] and computing paradigms beyond the conventional von Neumann architecture,[19] thanks to its unique attributes, such as the ability to break through the diffraction limit of light, high energy efficiency,[20] and spatiotemporal dynamics.[19]

What is important is to regulate the size and the position of nanostructures so that optical near-field interactions are induced between them in order to obtain designated functions.[21] This gives rise to the importance of modeling of nanophotonic devices and systems composed of multiple nanostructures arranged in varying configurations in characterizing and designing designated functions, such as efficient energy concentration,[22] wavelength conversion,[23] sensing,[24] color rendering for lighting and displays,[18] and many others. Technologies such as droplet epitaxy[25] and light-assisted quantum-dot size formation[26] have been developed, enabling geometry-regulated fabrication of nanostructured matter. At the same time, however, fabricated experimental devices exhibit more or less unavoidable inherent disorder,[27] such as variation of the sizes or layout of the nanostructures.

With regard to all of these requirements related to applications and issues originating from technological concerns, this paper provides a theoretical approach that takes into account the architecture and inherent disorder of nanostructures in a comprehensive manner. More concretely, we constructed a stochastic model for studying energy transfer via optical near-field interactions in multi-layer quantum dot devices, and we demonstrated that the results obtained with the model are consistent with experimental observations.

The concrete device that we studied is composed of multi-layer InAs QDs.[22] Akahane *et al.* have developed an original molecular beam epitaxy (MBE) technology for realizing multi-layer QD structures, where the size of the QDs in each layer and the inter-layer distances are precisely and individually controlled. Even QD devices with more than 300 layers have been realized with this technology.[28] Moreover, they have developed multi-layer QD devices in which one layer contains larger-sized QDs that are sandwiched by multiple layers of smaller-sized QDs.[22] More precisely, N and $N+1$ layers (where N is an integer) of smaller-sized QDs

[a)]Electronic mail: naruse@nict.go.jp

were located, respectively, below and above the larger-QD layer, as schematically shown in Fig. 1(a). Thanks to the optical energy transfer from smaller to larger QDs, the resulting light emission spectra differ depending on the number of smaller-sized QDs; that is to say, an N-dependence emerges. They experimentally demonstrated that the efficiency of energy transfer was maximized at a specific number of smaller QD layers. The presumable physical reasons behind this were mentioned in Ref. 22, but no precise modeling or quantitative discussions were given; this is an immediate typical case where a theoretical approach unifying device architectures, inherent disorder, and optical near-field interactions is necessary. This paper also expands on the experimental results reported in Ref. 22 by demonstrating layer-dependent photoluminescence.

This paper is organized as follows. Section II presents experimental results of energy transfer in stacked quantum dot devices and describes a basic theory of energy transfer via near-field interactions. Section III describes stochastic modeling of stacked quantum-dot systems, the results of which are consistent with experiments. Section IV concludes the paper.

II. ENERGY TRANSFER IN STACKED QUANTUM DOTS

A. Context

We begin by briefly reviewing some related studies. In the literature, the Förster model is a widely known model used for explaining optical energy transfer.[29] However, the issue of discrepancies between experimentally observed data and dipole-based models like the Förster model has been raised.[30,31] As mentioned above, optical near-field interactions take into account transitions that are conventionally dipole-forbidden,[3,12,14] and we have previously proposed a theory of a network of optical near-fields to describe a mixture of smaller and larger quantum dots.[21] Also, this theory has been successfully applied to a cascaded energy transfer device fabricated by a layer-by-layer chemical assembly method.[16,32] In these former studies, an idealized model yields good agreement with the experiments. We assume that the good agreement reported in the former studies is a consequence of the relatively simple device architectures used, and thus it is sufficient to characterize the dominant physical processes, which are inter-dot optical near-field interactions.

In the case of much more complex devices, on the other hand, such as those composed of a large number of QDs, we need to take account of stochastic attributes inherent in the devices; for example, the model should satisfactorily explain fluctuations in quantum dot sizes, temperature-dependent energy level broadening, etc. At the same time, an exact theoretical treatment for large-scale systems, for example, with a density matrix formalism, results in an unnecessarily complex model, which will be computationally intractable in realistic computing environments. Therefore, keeping the model simple, while still extracting the essential physics, will be crucially important.[27]

B. Experiment

Now we describe the experimental devices demonstrated in Ref. 22 and some newly fabricated devices, followed by their photoluminescence analysis. A multi-layer InAs QD structure was formed on InP(311)B based on MBE with a strain-compensation scheme.[33] As schematically shown in Fig. 1(a), relatively large-diameter QDs (average diameter: 47.9 nm and average height: 4.5 nm) were formed in the middle layer, and $N+1$ and N layers of smaller-diameter QDs (average diameter: 42.8 nm and average height: 2.7 nm) were formed on the upper and lower sides, respectively. Six kinds of devices were fabricated, with N equal to 1, 3, 5, 10, 15, and 20. The average inter-layer distance was 15 nm. Figure 1(b) shows normalized photoluminescence spectra, with vertical offsets, obtained by exciting the device with the 532 nm line of a YVO laser with a power of 120 mW at 300 K for the six devices. The spectra of devices with $N=5$, 10, and 20 have already been reported in Ref. 22, and the others were newly obtained here. In order to evaluate these six data sets on an equal basis, the photoluminescence spectra were calibrated so that the minimum signal levels, or noise floors, were aligned, and the spectra were normalized.

Based on the spectra shown in Fig. 1(b), we evaluated the ratio of the photoluminescence from the larger QDs to that from the smaller QDs divided by the total number of such layers

$$R = \mathrm{PL(L)} \;/\; \big(\mathrm{PL(S)/per\,layer}\big), \tag{1}$$

where PL(L) and PL(S) respectively denote photoluminescence from the larger and smaller QDs. We used three metrics to characterize PL(S) and PL(L). The solid curve in Fig. 1(c) shows the photoluminescence spectrum of the $N=15$ device, as an example. The first metric is the spectral peak values in shorter and longer wavelength ranges, which are respectively denoted by $\mathrm{PL(S)}_p$ and $\mathrm{PL(L)}_p$. The second one is the integrated photoluminescence intensity around the spectral peaks; here, we integrate the intensities in the wavelength range ± 5 nm around the peaks, which are respectively denoted by PL(S) $p \pm 5$ nm and PL(L) $p \pm 5$ nm. The last one is based on decomposing the spectrum into two Gaussian distributions; the dashed and dotted curves in Fig. 1(c) respectively indicate Gaussian profiles corresponding to larger and smaller QDs, and the calculated peaks of these profiles are taken as the metrics denoted by $\mathrm{PL(L)}_f$ and $\mathrm{PL(S)}_f$. The dashed-dotted curve in Fig. 1(c) represents the summation of the two Gaussian profiles, whose root-mean-square error to the original spectrum is minimized. We consider that this metric R reflects the amount of optical energy transferred from the smaller dots to the larger ones. The circular, triangular, and square marks in Fig. 1(d) respectively show the metric R based on the above three metrics evaluated with an excitation power of 120 mW at 300 K, as a function of N. The three metrics exhibited similar tendencies, where the maximum R was obtained when N was 15. In addition, Fig. 1(e) summarizes the metric R as a function of the optical excitation power when N was 15. The circular and square marks in Fig. 1(e) correspond to the cases where the temperature was 150 K and 300 K, respectively. As introduced at the beginning, in Ref. 22, Akahane *et al.* gave a qualitative discussion of the possible physics behind this behavior, including the effect of energy level broadening due

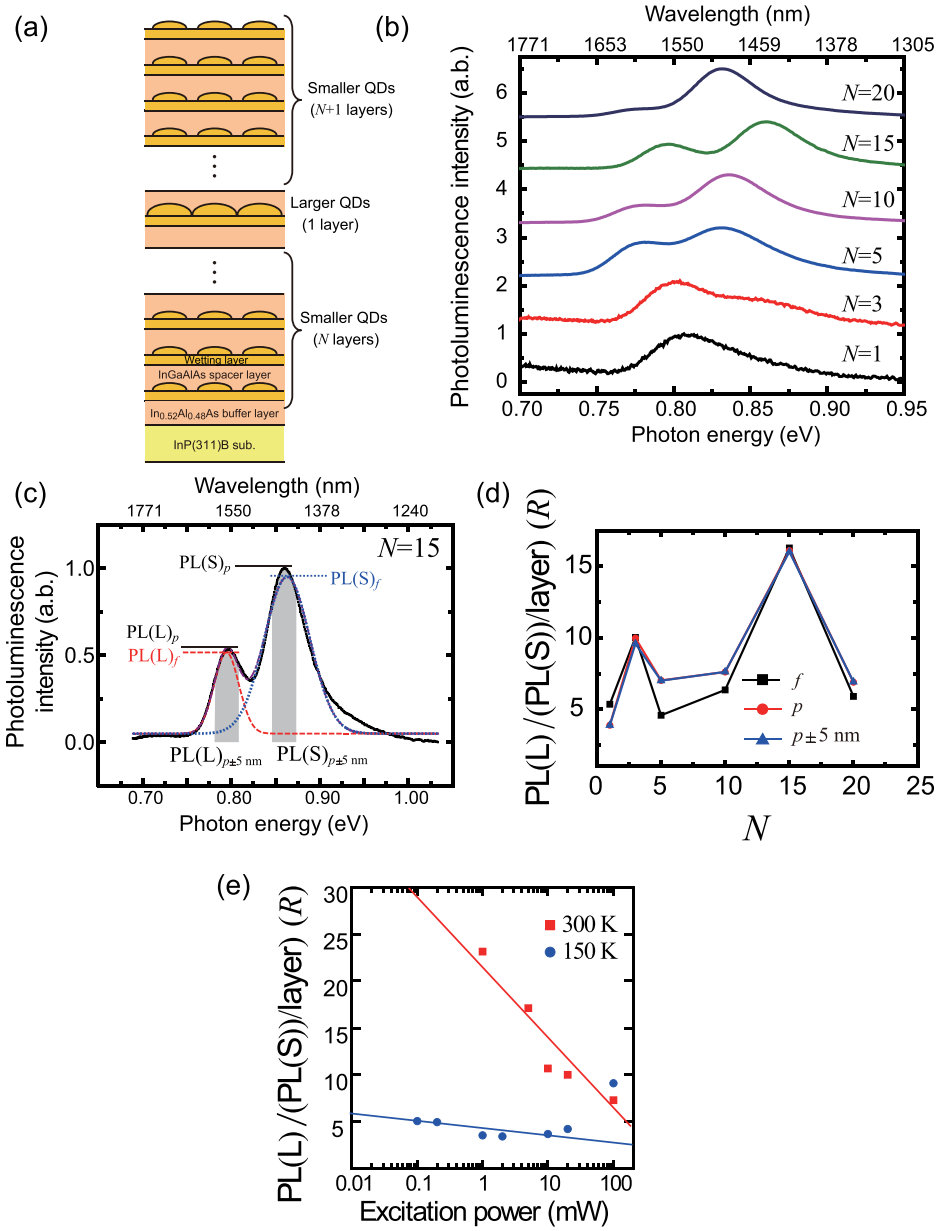

FIG. 1. (a) A stacked QD structure in which a large-sized QD layer is sandwiched by N and $N+1$ layers of smaller-sized QDs. (b) N-dependent photoluminescence spectra which differ due to energy transfer from smaller to larger QDs. (c) Photoluminescence spectrum of the device $N=15$ (solid curve) and two Gaussian profiles assumed for radiation from smaller QDs (dotted curve) and larger QDs (dashed curve). The dashed-dotted curve represents the summation of the two Gaussian profiles. (d) The metric R, which is the photoluminescence intensity from the larger-dot layer divided by that from the smaller-dot layers, per layer. The circular-, triangular-, and square-marks are based on different metrics defined in (c). See main text for detailed definitions. (e) The metric R evaluated at different temperatures and different excitation powers.

to the temperature increase, but no quantitative reasoning or an explanation of the N-dependence was given. The goal of the present work is to reproduce such a tendency quantitatively and to identify one of the fundamental attributes of nanophotonics, as well as to provide a systematic stochastic method for use in designing and implementing optimized nanophotonic devices.

C. Theoretical elements

Now we focus on some theoretical elements of optical energy transfer via optical near-field interactions. The interaction Hamiltonian between an electron–hole pair and an electric field is given by

$$\hat{H}_{\rm int} = -\int d^3r \sum_{i,j=e,h} \hat{\psi}_i^{\dagger}(\boldsymbol{r}) e\boldsymbol{r}\cdot\boldsymbol{E}(\boldsymbol{r})\hat{\psi}_j(\boldsymbol{r}), \qquad (2)$$

where e represents the electron charge, $\hat{\psi}_i^{\dagger}(\boldsymbol{r})$ and $\hat{\psi}_j(\boldsymbol{r})$ are respectively electronic wave operators corresponding to the creation and annihilation operators of either an electron $(i,j=e)$ or a hole $(i,j=h)$ at $\boldsymbol{r}$, and $\boldsymbol{E}(\boldsymbol{r})$ is the electric field.[21] We consider a quantum dot based on a semiconductor material with a bulk electric dipole moment on which a lightwave with a specific resonance frequency is incident. For the electronic system confined in a quantum dot, the electronic wave operator includes an envelope function of electronic waves in the quantum dot. In treating usual optical interactions of a quantum dot, the so-called long-wave approximation is employed, so that $\boldsymbol{E}(\boldsymbol{r})$ is considered to be constant over the size of the quantum dot since the electric field of propagating light wave is homogeneous on the nanometer scale. Depending on the symmetry of the electronic envelope function, numerical evaluation of the dipole transition matrix elements based on Eq. (2) results in selection rules for the optical transition for each excitonic state. For instance, in the case of spherical quantum dots, only optical transitions to the states specified by $l=m=0$ are allowed, where l and m are the orbital angular momentum quantum

number and magnetic quantum number for the envelope function, respectively. In the case of optical near-field interactions between a pair of resonant quantum dots separated by a sub-wavelength distance, on the other hand, due to the large spatial inhomogeneity of the optical near-fields of the source quantum dot, an optical transition that violates conventional optical selection rules becomes allowed, so that optical excitation transfer is possible between resonant states of quantum dots with different symmetries of the envelope functions via optical near-field interactions, regardless of the capability of each state to emit radiation into the optical far-field.[14,21] A physical model of near-field interactions is introduced at the beginning of Sec. III.

Here, we assume two spherical quantum dots whose radii are R_S and R_L, which we call QD_S and QD_L, respectively, as shown in Fig. 2(a). The energy eigenvalues of states specified by quantum numbers (n, l) are given by

$$E_{nl} = E_g + E_{ex} + \frac{\hbar^2 \alpha_{nl}^2}{2MR^2} \quad (n = 1, 2, 3, ...), \tag{3}$$

where E_g is the band gap energy of the bulk semiconductor, E_{ex} is the exciton binding energy in the bulk system, M is the effective mass of the exciton, and α_{nl} are determined from the boundary conditions, for example, $\alpha_{n0} = n\pi, \alpha_{11} = 4.49$. According to Eq. (3), there exists a resonance between the level of quantum number (1,0) in QD_S and that of quantum number (1,1) in QD_L if $R_L/R_S = 4.49/\pi \approx 1.43$. Note that optical excitation of the (1,1)-level in QD_L corresponds to an electric dipole-forbidden transition. However, an optical near-field, denoted by U in Fig. 2(a), allows this level to be

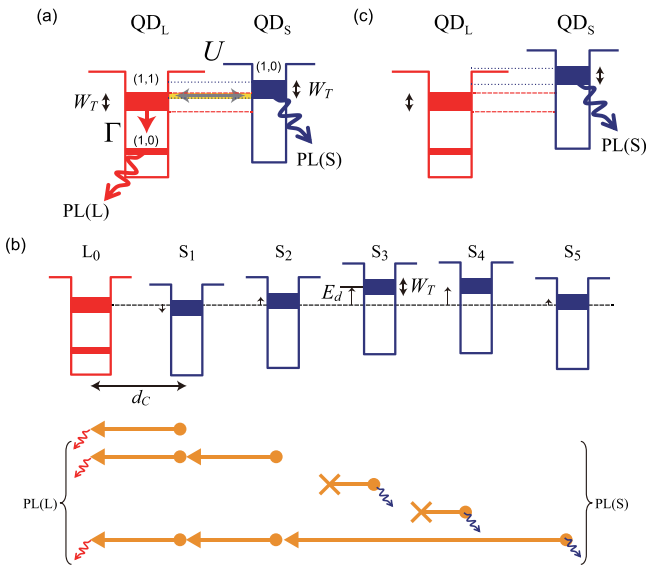

FIG. 2. (a) Schematic diagram of optical energy transfer from a smaller QD to a larger one via an optical near-field interaction (U). The energy levels are broadened to width W_T due to temperature. When there is an overlap between the energy bands, energy transfer is induced. (b) Schematic diagram of a larger dot (L_0) and an array of N cascaded smaller dots (S_1, S_2,…, S_N). The example shows the case where $N = 5$. The optical energy induced in "energy transfer allowable" bands, which are in S_1, S_2, and S_5, is transferred to L_0 by way of such dots and contributes to the photoluminescence from the larger dot (PL(L)). Photoluminescence from the smaller dots is represented by PL(S). (c) Optical energy induced in the smaller dots that are not resonant with the larger one is not delivered to the larger dot.

populated due to the steep electric field in the vicinity of QD_S. Therefore, an exciton in the (1,0)-level in QD_S could be transferred to the (1,1)-level in QD_L. In QD_L, the excitation undergoes intersublevel energy relaxation due to exciton–phonon coupling with a transition rate denoted by Γ, which is faster than the rate of the optical near-field interaction between the quantum dots,[32] and the excitation causes a transition to the (1,0)-level and radiation into the far-field. As a result, we find unidirectional optical excitation transfer from QD_S to QD_L.

III. STOCHSTIC MODELING

The optical near-field interaction between two nanoparticles is known to be expressed as a screened potential using a Yukawa function, given by

$$U = \frac{A \exp(-\mu r)}{r}, \tag{4}$$

where r is the distance between the two dots, and the coefficient μ can take either real or imaginary values, which respectively correspond to localized and propagating modes.[3,14] Here, we assume a real-valued μ since we consider a localized mode. In general, an effective field relevant to an interaction of finite range can be described by a Yukawa function by renormalizing long-range interactions.[34] In the case of optical near-field interactions, we can derive a Yukawa-type potential as the effective interaction between QDs by renormalizing the effects of surrounding matter. Furthermore, as a consequence of a steep spatial gradient due to this Yukawa-type potential, an optical transition that violates conventional optical selection rules becomes allowed, unlike the case of dipole–dipole interactions, as mentioned in Sec. II C. The detailed derivation of Eq. (4) is shown in Ref. 14.

In our stochastic modeling of the stacked QD devices, we take the following strategy. First, for the sake of simplicity while retaining the principal structure of the device, we assume that a larger dot, denoted by L_0, is located at the edge, and multiple smaller QD_S are cascaded at one side of L_0, as schematically shown in Fig. 2(b). The smaller QDs are labeled S_1, S_2,…, S_N, where N is the total number of smaller QDs. Also, due to variation of the size of the QDs and energy level broadening due to temperature, the energy levels fluctuate and exhibit a certain width. The width of the energy band is denoted by W_T. The energy level deviation of a smaller QD with respect to the larger dot is denoted by E_d.

Here, we consider that energy transfer from a smaller QD in the chain to the larger QD occurs when there exists an overlap between the resonant energy bands of the two QDs, as schematically shown in Fig. 2(a). We call such energy bands "energy-transfer-allowable" for the sake of later explanations. Note that we assume that the inter-dot energy transfer time is faster than the recombination time in individual dots. On the other hand, in the case where there is no energy band overlap, energy transfer does not take place; instead, the optical energy induced in the smaller dot contributes to the photoluminescence from the smaller dot, PL(S), as illustrated in Fig. 2(c). The optical energy transferred to

the upper energy level of the larger dot relaxes to its lower energy band and results in photoluminescence from the larger dot, PL(L).

We assume that the sizes of the smaller QDs in the chain exhibit fluctuations that follow Gaussian statistics, which affects the energy band overlap. Take the example shown in Fig. 2(b), where the number of smaller dots is five ($N = 5$), which are labeled S_1,…, S_5. The dots S_1, S_2, and S_5 have energy-transfer-allowable energy bands; that is to say, they are resonant with the larger dot, L_0. Now, recall that the inter-dot energy transfer follows the Yukawa potential given by Eq. (4). We assume that energy transfer occurs perfectly if two adjacent dots have resonant energy bands; we represent such a situation by rewriting Eq. (4) such that a unit of energy induced in a smaller dot denoted by i is transferred to the quantum dot denoted by j with an efficiency given by

$$t_{i,j} = \frac{A' \exp(-\mu(d_{i,j} - d_C))}{d_{i,j}}, \tag{5}$$

where d_C is the constant inter-layer distance between adjacent layers (which is about 15 nm, as mentioned above), and $d_{i,j}$ is the distance between QDs labeled i and j. A' is a constant so that the value $t_{i,j}$ becomes a dimensionless number, and is given by unity. This means, for example, that if two adjacent QDs have energy bands that are energy-transfer-allowable, $t_{i,j}$ is equal to 1 because $d_{i,j} = d_C$. Therefore, in the case shown in Fig. 2(b), the units of optical energy induced in S_1 and S_2 are both transferred to the larger dot, yielding radiation from the larger dot. Note that the optical energy induced in S_2 is first transferred to S_1 ($t_{S_2,S_1} = 1$), followed by a transfer from S_1 to L_0 ($t_{S_1,L_0} = 1$). The net amount of energy transferred to the larger dot from S_2 is $t_{S_2,S_1} \times t_{S_1,L_0} = 1$. The energy band of S_5 is also energy-transfer-allowable, meaning that a unit of optical energy induced in S_5 is transferred to L_0 by way of S_2 and S_1. Since the distance between S_5 and S_2 is $d_{S_5,S_2} = 3d_C$, the energy transferred from S_5 to S_2 is $t_{S_5,S_2} = \exp(-\mu(3d_C - d_C))/3d_C$, which is smaller than unity. The rest of the energy, $1 - t_{S_5,S_2}$, results in radiation from the smaller dot, which gives rise to PL(S). The energy t_{S_5,S_2} transferred to S_2 is then transferred to S_1 with an efficiency $t_{S_2,S_1} = 1$. Summing up, the amount of radiation from the larger dot originating from S_5 is given by $\exp(-\mu(3d_C - d_C))/3d_C$. In this manner, we calculate the total amount of optical energy transferred to the larger QD and the radiation from the smaller QDs, which provides a metric corresponding to Eq. (1), that is, the amount of radiation from the larger QD divided by that from the smaller QDs, per layer.

We performed a Monte Carlo calculation based on the above modeling with 50 000 iterations for each of the devices with N ranging from 1 to 20. We assumed that μ is unity and that the smaller QD size followed a Gaussian distribution with a standard deviation of unity, and we equated such a distribution with the energy level deviation from the larger QD. The energy band of the larger QD is represented by width W_T, with its center being equal to the mean of the normal distribution. The energy band of a smaller QD corresponds to a range whose width is also W_T, and its center is displaced from the mean of the normal distribution by E_d, as schematically shown in Fig. 3(a).

In our stochastic modeling, the width W_T is simply a constant that increases as the temperature T increases, corresponding to the linewidth broadening of the energy levels (1,1) in QD_L and (1,0) in QD_S, as shown in Fig. 2(a). Theoretically, Sangu *et al.* considered the finite temperature effect in energy transfer mediated by optical near-field interactions involving a finite number of phonons that are back-transferred from the heat-bath system, and this resulted

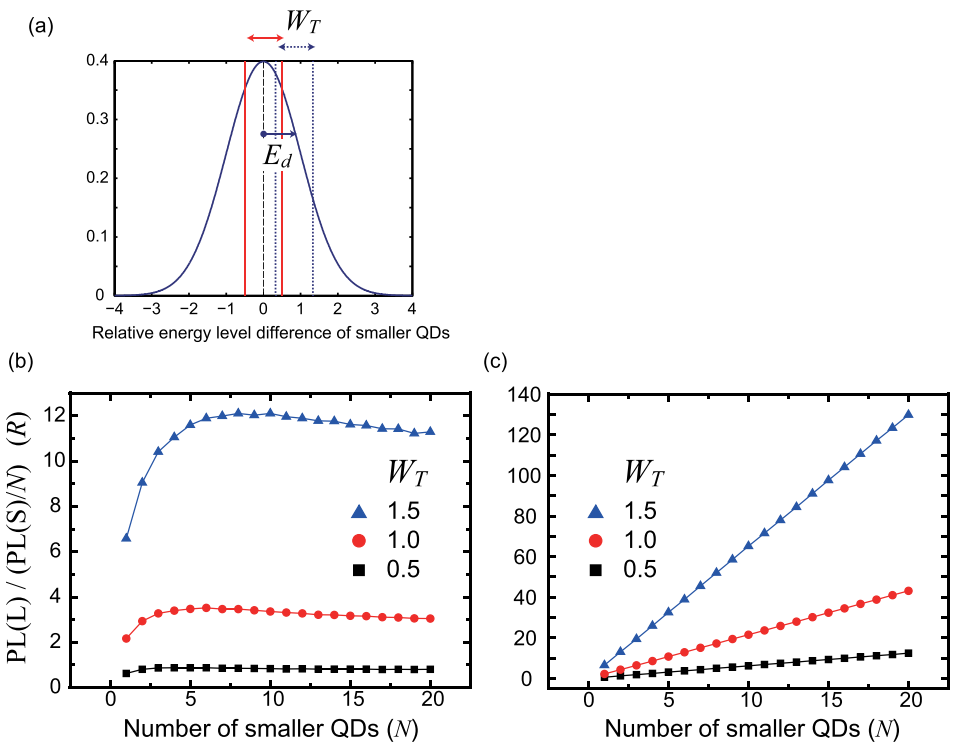

FIG. 3. (a) The size of the smaller QDs, that is, the relative energy level difference with respect to the larger QD, is assumed to follow a normal distribution. The energy level broadening and the relative difference with respect to the larger dot are respectively denoted by W_T and E_d. (b) The metric R as a function of the number of smaller QDs provided in the stochastic model. In the case where W_T is 1.5, the profile and the maximum R give results consistent with the experimental demonstration summarized in Fig. 1(d). Also, we observed that as W_T increases, the metric R increases; this is consistent with the temperature dependence experimentally observed in Fig. 1(e). (c) When the inter-dot optical near-field is assumed not to follow the Yukawa potential, R simply linearly increases as N increases, which is not consistent with the experiment.

in linewidth broadening.[14] Meanwhile, detailed experimental investigations of homogeneous linewidth broadening of QDs as a function of temperature have been reported, for example, by Matsuda *et al.*[35] and Bayer *et al.*,[36] where acoustic and optical phonons have been introduced. For this paper, on the other hand, the major interest is to investigate stochastic modeling concerning inherent disorder, and hence we consider that representing the linewidth broadening simply by W_T is reasonable, without explicitly showing its temperature dependency.

The square, circular, and triangular marks shown in Fig. 3(b) represent the ratio R as a function of the number of smaller QD layers (N) when W_T was 0.5, 1, and 1.5, respectively. The profile corresponding to the case where W_T was 1.5 exhibits a similar tendency to the experimental results shown in Fig. 1(d), which were obtained at 300 K. In the experiment, there exists a maximum value R of around 16 when N is 15, whereas in the calculation, the maximum R is 12.1 when N is 10. We consider that these results show consistency between the experiment and the stochastic model. Furthermore, from the experimental results shown in Fig. 1(c), the inhomogeneous linewidth due to variation of QD sizes is about 30 meV, which corresponds to the normal distribution with a standard deviation of unity, denoted by $\sigma = 1$, in the stochastic modeling shown in Fig. 3(a). Meanwhile, the homogeneous linewidth of our QD is considered to have characteristics similar to those of our former study reported in Ref. 37, where the full width at half maximum (FWHM) width was about 16 meV at room temperature, which corresponds to W_T in the stochastic model. By considering that 2σ corresponds to 30 meV, $W_T = 1.5$ corresponds to 22.5 meV, which is consistent with the reported homogeneous linewidth of QDs at room temperature.

To further evaluate the validity of the model, assume that the inter-dot interaction does *not* follow the Yukawa potential; specifically, suppose that the energy transfer efficiency does not depend on the inter-dot distance. All of the other assumptions are the same as the previous ones. In such a case, the energy transfer performance depending on the number of layers results in the profiles shown in Fig. 3(c), where the ratio R monotonically increases as a function of N, which is not consistent with the experiment. This is another indication that the inter-layer-distance–dependent near-field interactions, as well as the inherent stochastic distributions, are the origin of the optimized energy transfer observed in the multi-layer QD device.

The temperature- and excitation-power–dependent energy transfer experimentally demonstrated in Fig. 1(e) are not completely manageable in the proposed stochastic model. The temperature-dependence, however, is partially reproduced by the model. In the modeling results demonstrated in Fig. 3(b), the ratio R exhibits a larger value when W_T, that is, the temperature, increases. This is consistent with the experimental results shown in Fig. 1(e), where the energy transfer efficiencies at the higher temperature (300 K) are larger than those at the lower temperature (150 K). This is also consistent from the viewpoint that the homogeneous linewidth of QDs at 150 K is about half of that at 300 K.[35] That is to say, by reducing the W_T value from 1.5 to 0.5, the ratio R in the modeling results is reduced by about an order of magnitude, as shown in Fig. 3(b), and the ratio R in the experiment is also reduced by about an order of magnitude. There was an exception in Fig. 1(e) when the excitation power was high (100 mW), where the low-temperature experiment yielded a larger value than the high-temperature one. More detailed modeling will be needed to fully explain this, for example, by including state filling effects, which may occur in cases where the excitation power is high.[21] This will be one of the topics of future work.

IV. SUMMARY

In summary, we demonstrated energy transfer mediated by optical near-field interactions in a multi-layer InAs QD structure composed of a single layer of smaller dots and N layers of larger ones and examined its basic principles by using a stochastic model in which optical near-field interactions that follow a Yukawa function, QD size fluctuations, and temperature-dependent energy level broadening are unified. The properties of experimentally observed energy transfer and the results calculated from the model were in good agreement. This study provides an insight into optical energy transfer while taking account of inherent disorder and paves the way to systematic design principles of nanophotonic devices for achieving optimized performance and realizing designated functionalities.

ACKNOWLEDGMENTS

This work was supported in part by the Japan–Sweden Bilateral Joint Project and the Core-to-Core Program of the Japan Society for the Promotion of Science (JSPS). This work was also supported in part by the Strategic Information and Communications R&D Promotion Programme (SCOPE) of the Ministry of Internal Affairs and Communications, and by Grants-in-Aid for Scientific Research from the JSPS.

[1]M. Ohtsu, K. Kobayashi, T. Kawazoe, S. Sangu, and T. Yatsui, IEEE J. Sel. Top. Quantum Electron. **8**, 839 (2002).
[2]*Semiconductor and Metal Nanocrystals*, edited by V. I. Klimov (Marcel Dekker, New York, 2003).
[3]K. Kobayashi, S. Sangu, H. Ito, and M. Ohtsu, Phys. Rev. A **63**, 013806 (2000).
[4]R. Filter, S. Mühlig, T. Eichelkraut, C. Rockstuhl, and F. Lederer, Phys. Rev. B **86**, 035404 (2012).
[5]R. C. Somers, P. T. Snee, M. G. Bawendi, and D. G. Nocera, J. Photochem. Photobiol. A **248**, 24 (2012).
[6]T. Yatsui, S. Sangu, T. Kawazoe, M. Ohtsu, S. J. An, J. Yoo, and G.-C. Yi, Appl. Phys. Lett. **90**, 223110 (2007).
[7]T. Yatsui, H. Jeong, and M. Ohtsu, Appl. Phys. B **93**, 199 (2008).
[8]P. Vasa, R. Pomraenke, S. Schwieger, Yu. I. Mazur, Vas. Kunets, P. Srinivasan, E. Johnson, J. E. Kihm, D. S. Kim, E. Runge, G. Salamo, and C. Lienau, Phys. Rev. Lett. **101**, 116801 (2008).
[9]J. D. Cox, M. R. Singh, G. Gumbs, M. A. Anton, and F. Carreno, Phys. Rev. B **86**, 125452 (2012).
[10]J. D. Cox, M. R. Singh, C. von Bilderling, and A. V. Bragas, Adv. Opt. Mater. **1**, 460 (2013).
[11]C. Racknor, M. R Singh, Y. Zhang, D. J. S. Birch, and Y. Chen, Methods Appl. Fluoresc. **2**, 015002 (2014).
[12]J. R. Zurita-Sánchez and L. Novotny, J. Opt. Soc. Am. B **19**, 1355–1362 (2002).
[13]J. R. Zurita-Sánchez and L. Novotny, J. Opt. Soc. Am. B **19**, 2722–2726 (2002).

[14]S. Sangu, K. Kobayashi, A. Shojiguchi, T. Kawazoe, and M. Ohtsu, J. Appl. Phys. **93**, 2937 (2003).
[15]O. Mauritz, G. Goldoni, F. Rossi, and E. Molinari, Phys. Rev. Lett. **82**, 847 (1999).
[16]T. Franzl, T. A. Klar, S. Schietinger, A. L. Rogach, and J. Feldmann, Nano Lett. **4**, 1599–1603 (2004).
[17]C. Pistol, C. Dwyer, and A. R. Lebeck, IEEE Micro **28**, 7–18 (2008).
[18]B. A. Akins, G. Medina, T. A. Memon, A. C. Rivera, G. A. Smolyakov, and M. Osinski, "Nanophosphors based on CdSe/ZnS and CdSe/SiO^2 colloidal quantum dots for daylight-quality white LEDs," in *Conference on Lasers and Electro-Optics 2010, OSA Technical Digest (CD)* (Optical Society of America, 2010), paper CTuNN7.
[19]M. Aono, M. Naruse, S.-J. Kim, M. Wakabayashi, H. Hori, M. Ohtsu, and M. Hara, Langmuir **29**, 7557–7564 (2013).
[20]M. Naruse, H. Hori, K. Kobayashi, P. Holmström, L. Thylén, and M. Ohtsu, Opt. Express **18**, A544 (2010).
[21]M. Naruse, N. Tate, M. Aono, and M. Ohtsu, Rep. Prog. Phys. **76**, 056401 (2013).
[22]K. Akahane, N. Yamamoto, M. Naruse, T. Kawazoe, T. Yatsui, and M. Ohtsu, Jpn. J. Appl. Phys., Part 1 **50**, 04DH05 (2011).
[23]I. Robel, V. Subramanian, M. Kuno, and P. V. Kamat, J. Am. Chem. Soc. **128**, 2385 (2006).
[24]V. Bagalkot, L. Zhang, E. Levy-Nissenbaum, S. Jon, P. W. Kantoff, R. Langer, and O. C. Farokhzad, Nano Lett. **7**, 3065–3070 (2007).
[25]T. Mano, T. Kuroda, K. Mitsuishi, Y. Nakayama, T. Noda, and K. Sakoda, Appl. Phys. Lett. **93**, 203110 (2008).
[26]H. Koyama and N. Koshida, J. Appl. Phys. **74**, 6365 (1993).
[27]S. E. Skipetrov, Phys. Rev. E **67**, 036621 (2003).
[28]K. Akahane, N. Yamamoto, and T. Kawanishi, Phys. Status Solidi A **208**, 425 (2011).
[29]T. Förster, Ann. Phys. **437**, 55 (1948).
[30]G. D. Scholes and G. R. Fleming, J. Phys. Chem. B **104**, 1854 (2000).
[31]M. Kubo, Y. Mori, M. Otani, M. Murakami, Y. Ishibashi, M. Yasuda, K. Hosomizu, H. Miyasaka, H. Imahori, and S. Nakashima, J. Phys. Chem. A **111**, 5136 (2007).
[32]M. Naruse, E. Runge, K. Kobayashi, and M. Ohtsu, Phys. Rev. B **82**, 125417 (2010).
[33]K. Akahane, N. Ohtani, Y. Okada, and M. Kawabe, J. Cryst. Growth **245**, 31 (2002).
[34]M. Ohtsu and H. Hori, *Near-Field Nano-Optics* (Kluwer Academic/Plenum Publishers, New York, 1999).
[35]K. Matsuda, K. Ikeda, T. Saiki, H. Tsuchiya, H. Saito, and K. Nishi, Phys. Rev. B **63**, 121304(R) (2001).
[36]M. Bayer and A. Forchel, Phys. Rev. B **65**, 041308(R) (2002).
[37]T. Kawazoe, M. Ohtsu, S. Aso, Y. Sawado, Y. Hosoda, K. Yoshizawa, K. Akahane, N. Yamamoto, and M. Naruse, Appl. Phys. B **103**, 537 (2011).

Appl Phys A (2014) 115:127–133
DOI 10.1007/s00339-013-7930-x

Applied Physics A
Materials Science & Processing

INVITED PAPER

Bulk crystal SiC blue LED with p–n homojunction structure fabricated by dressed-photon-phonon–assisted annealing

Tadashi Kawazoe · Motoichi Ohtsu

Received: 9 August 2013 / Accepted: 11 August 2013 / Published online: 24 August 2013

Abstract To fabricate a high-efficiency light emitting diode using indirect-transition-type bulk crystal SiC having a p–n homojunction structure, annealing was performed using stimulated emission via dressed photons generated at the inhomogeneous domain boundaries of Al dopant sites. This device emitted electroluminescence (EL) due to a two-step transition process via dressed-photon–phonons generated at the inhomogeneous domain boundaries of the Al dopant sites. The EL emission peak wavelength was 480–515 nm when the device was driven by a direct current and 390 nm when driven by a pulsed current. The external quantum efficiency of the EL emission was 1 %, and the internal quantum efficiency was as high as 10 %.

1 Introduction

To fabricate high-efficiency light emitting diodes (LEDs), direct-transition-type semiconductors, which have a high probability of electron–hole radiative recombination, have conventionally been used. The emission wavelength of these devices is determined by the bandgap energy, E_g, of the semiconductor used. For example, InGaN has been used in LEDs with wavelengths of 400–495 nm (bandgap energies 3.099–2.504 eV) [1, 2]. However, these devices have some shortcomings, such as the need for a double heterostructure, and the use of In, which is a scarce resource. Silicon carbide (SiC), on the other hand, is a semiconductor that has no issues concerning depletion of resources, and research has been conducted on blue LEDs using this material. However, since SiC is an indirect-transition-type semiconductor, the external quantum efficiency of the light emission is low, at 0.1 % or less, and it has not been easy to fabricate practical devices [3, 4]. Recently, SiC has been considered as a suitable material for use in power devices, rather than LEDs, because of its high electrical breakdown strength, thermal conductivity, and heat tolerance [5].

We have previously succeeded in developing an LED using p–n homojunction-structured bulk crystal silicon (Si), which is an indirect-transition-type semiconductor, by using dressed photons (DPs) [6]. A DP is a quasi-particle representing the coupled state between a photon and an electron–hole pair in a nano-scale region [7]. A Si laser [8], an optical and electrical relaxation oscillator [9], and an infrared Si photodiode [10] have been successfully developed by utilizing DPs. In addition, a blue LED using ZnO, which is a direct-transition-type semiconductor, has also been successfully fabricated [11]. These devices were realized by using a unique annealing technique involving a dressed-photon-phonon–assisted process induced by DPs generated at the dopant sites [6]. A dressed-photon–phonon (DPP) is a quasi-particle representing the coupled state between a DP and a multimode coherent phonon in a nano-scale region [7, 12, 13].

In the research reported here, we employed a DPP-assisted process in bulk crystal 4H-SiC having a homojunction structure to modify the spatial distribution of the Al dopant sites in SiC, and fabricated a blue LED with high light-emission efficiency. In Si-based visible LEDs fabri-

T. Kawazoe (✉) · M. Ohtsu
Department of Electrical Engineering and Information Systems,
Graduate School of Engineering, The University of Tokyo,
2-11-16 Yayoi, Bunkyo-ku, Tokyo 113-8656, Japan
e-mail: kawazoe@ee.t.u-tokyo.ac.jp
Fax: +81-3-58411140

T. Kawazoe · M. Ohtsu
Nanophotonics Research Center,
Graduate School of Engineering, The University of Tokyo,
2-11-16 Yayoi, Bunkyo-ku, Tokyo 113-8656, Japan

cated via a DPP-assisted process, because Si has a bandgap that corresponds to infrared wavelengths, visible light is absorbed by the Si; therefore, to fabricate high-efficiency LEDs, a device structure for extracting the light is necessary. SiC, on the other hand, has a bandgap corresponding to blue to near-ultraviolet wavelengths; therefore, ultraviolet to visible SiC LEDs fabricated via the DPP-assisted process can avoid a drop in efficiency due to light absorption by SiC. In other words, the suitability of the DPP-assisted process for SiC makes it easy to fabricate LEDs in the ultraviolet to visible region. In addition, in the present study, by confirming the applicability of the DPP-assisted process to SiC, we were also able to show the generality of this technique, which can be used more widely in indirect-transition type semiconductors.

2 Principles of light emission

The DPP-assisted process [6] we used here originates from the nature of the coupling between the DP and the phonon: by using this process, an electron–hole pair is created even when light having a photon energy $h\nu$ smaller than the bandgap energy E_g of the semiconductor is incident. The reason for this is that, since the DPP field is localized, the wavenumber conservation law and the angular-momentum conservation law can be relaxed, enabling electrons in the valence band to be excited to the conduction band via an electric-dipole forbidden transition to a phonon level. This excitation, which is a two-step transition, has been applied to photochemical vapor deposition [12], organic thin-film photovoltaic cells [14], photolithography [15], subnanometer polishing of glass surfaces [16], and frequency upconversion [17], among others. This two-step transition is explained below (see Fig. 1) [6, 12].

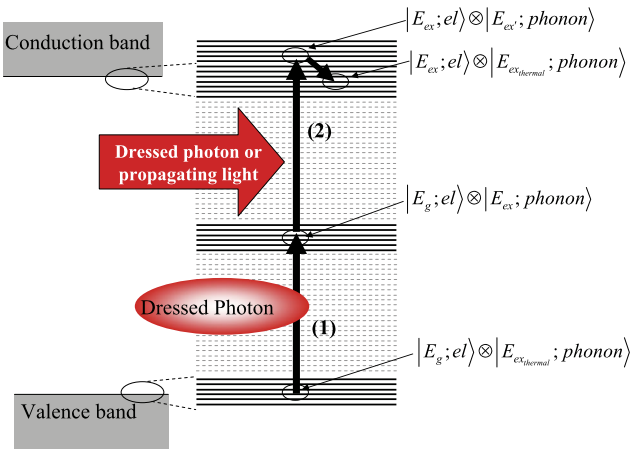

Fig. 1 Two-step transition via a dressed-photon–phonon level. The *horizontal solid lines* show dressed-photon–phonon levels

(1) First step: Excitation from the initial ground state $|E_g;el\rangle\otimes|E_{ex_{thermal}};phonon\rangle$ to an intermediate state $|E_g;el\rangle\otimes|E_{ex};phonon\rangle$. Here, $|E_g;el\rangle$ represents the electronic ground state, and $|E_{ex_{thermal}};phonon\rangle$ and $|E_{ex};phonon\rangle$ respectively represent the phonon excited state determined by the crystal lattice temperature and the phonon excited state determined by the DP energy. The symbol $\otimes$ is the direct product of the ket vectors representing these two states. Since this is an electric-dipole forbidden transition, the DP is essential in this excitation process. Also, since the intermediate state $|E_g;el\rangle\otimes|E_{ex};phonon\rangle$ possesses the energy of the DPP, it is called the DPP level.

(2) Second step: Excitation from the intermediate state $|E_g;el\rangle\otimes|E_{ex};phonon\rangle$ to the final state $|E_{ex};el\rangle\otimes|E_{ex'};phonon\rangle$. Here, $|E_{ex};el\rangle$ represents the electronic excited state, and $|E_{ex'};phonon\rangle$ represents the phonon excited state. Since this is an electric-dipole allowed transition, excitation occurs not only via a DP but also via propagating light. After this excitation, the phonon excited state relaxes to a thermal equilibrium state having an occupation probability determined by the lattice temperature, which completes the excitation to the electronic excited state $|E_{ex};el\rangle\otimes|E_{ex_{thermal}};phonon\rangle$.

There is an inverse process to this two-step process, namely, two-step spontaneous emission [6, 8], which is explained below. This inverse process is a transition from an initial state $|E_{ex};el\rangle\otimes|E_{ex_{thermal}};phonon\rangle$ of electrons in the conduction band to the ground state $|E_g;el\rangle\otimes|E_{ex'};phonon\rangle$ via the intermediate state $|E_g;el\rangle\otimes|E_{ex};phonon\rangle$. During this transition, a DP or propagating light having the same energy as the transition energy is radiated. After this transition, the phonon excited state relaxes to the thermal equilibrium state determined by the crystal lattice temperature, which completes the transition to the electronic ground state $|E_g;el\rangle\otimes|E_{ex_{thermal}};phonon\rangle$. Some of the spontaneously emitted DPs are converted to propagating light and are observed as normal photons [6]. Therefore, an LED can be realized if electrons injected into the conduction band are transported to the region where DPs are generated. Also, the emission wavelength of this device depends not on the bandgap energy E_g but on the energy of the DPs generated in the vicinity of the p–n junction.

It is well-known that phonons are necessary for an indirect-transition-type semiconductor to spontaneously emit propagating light. The reason why is that, in this spontaneous emission process, the wave number must be conserved (this is known as the wavenumber conservation law). However, in the nano-size spaces where DPs that are localized at dopant sites spread out, due to the individual properties of electrons and holes in the electron–hole pairs forming the DPs in these spaces, the DPs strongly couple with lattice vibrations [18]. As a result, in the DP, a photon strongly

couples with a multi-mode coherent phonon, forming a DPP, and this DPP has multiple modes that can contribute to satisfying the wavenumber conservation law [7, 12, 13]. Therefore, the probability of spontaneous emission via a DP becomes extremely high. This DPP, which is a quasi-particle, has been used in photochemical reactions [12, 15] and optical frequency up-conversion [17, 19], and lifetime measurements of this level have also been performed [19].

A two-step stimulated emission process is also made possible by the DP, similarly to the spontaneous emission process described above: when the oscillating electromagnetic field formed by the DP irradiates electrons in the conduction band, the electrons transition from the initial state $|E_{\mathrm{ex}}; el\rangle \otimes |E_{\mathrm{ex}_{\mathrm{thermal}}}; phonon\rangle$ to the intermediate state $|E_{\mathrm{g}}; el\rangle \otimes |E_{\mathrm{ex}}; phonon\rangle$, emitting light via stimulated emission. Then, a transition from the intermediate state $|E_{\mathrm{g}}; el\rangle \otimes |E_{\mathrm{ex}}; phonon\rangle$ to the final state $|E_{\mathrm{g}}; el\rangle \otimes |E_{\mathrm{ex}'}; phonon\rangle$ also occurs, emitting light due to stimulated emission. After this transition, the phonon excited state relaxes to the thermal equilibrium state determined by the crystal lattice temperature, which completes the transition to the electronic ground state $|E_{\mathrm{g}}; el\rangle \otimes |E_{\mathrm{ex}_{\mathrm{thermal}}}; phonon\rangle$.

3 Device fabrication

To realize the SiC-LED proposed in this paper, we used the two-step DPP-assisted process involving DPs two times. The first time was to activate the device so as to obtain spontaneously emitted light, as described in the previous section. The second time was to fabricate the device, in other words, to control the spatial distribution of the dopant density in a self-organized manner to achieve a spatial distribution suitable for high-efficiency spontaneous emission [6–8]. In order to explain the second use, in this section we explain the device fabrication procedure.

Using a CVD process, a 500 nm-thick n-type buffer layer (dopant density 1×10^{18} cm^{-3}) was deposited on an n-type SiC substrate (4H type) with a thickness of 360 μm, a diameter of 100 mm, a resistivity of 25 mΩ cm, and a surface orientation of (0001), after which a 10 μm-thick n-type epilayer (dopant density 1×10^{16} cm^{-3}) was deposited. The substrate was then implanted with a p-type dopant (Al ions) by ion implantation. During this process, the implantation energy was changed in multiple steps in the range 30–700 keV, and by adjusting the ion dose in the range 3.0×10^{13} cm^{-2} to 2.5×10^{14} cm^{-2} for each implantation energy, we fabricated a structure in which the dopant density was modulated between 2.2×10^{19} cm^{-3} and 1.8×10^{19} cm^{-3} in seven periods in the depth direction. After this, thermal annealing was performed for 5 minutes at 1800 °C to activate the Al ions, forming a p–n junction. A 150 nm-thick ITO film formed on the front surface (the p-type ion implantation surface) of the SiC substrate by sputtering was used as an anode. Similarly, a layer composed of Cr (100 nm), Pt (100 nm), and Au (200 nm), deposited on the back surface (n-type side) of the SiC substrate in this order from the substrate side, was used as a cathode. After this, a 500 μm × 500 μm chip was cut from the wafer by dicing, and the device was mounted in a package by soldering the cathode. The anode side was connected to the anode of the package by wire bonding.

Next, the DPP-assisted annealing will be described. A forward bias voltage of 12 V (current density 45 A/cm^2) was applied to the device fabricated as described above to bring about annealing due to Joule heating, which caused the Al dopant to diffuse, modifying the spatial distribution of the dopant density. During this process, the device was irradiated from the ITO electrode side with laser light (optical power density 2 W/cm^2) having a photon energy $h\nu_{\mathrm{anneal}}$ (= 2.33 eV; wavelength 532 nm) smaller than E_{g} of the 4H-SiC (= 3.26 eV) [20]. This induced the DPP-assisted process, which modified the Al diffusion due to annealing, leading to the self-organized formation of unique minute inhomogeneous domain boundaries in which sites of the dopant (Al) formed. The reasons for this are threefold:

(1) Since the potential energy difference between injected electrons and holes by forward bias voltage (12 V) is much higher than E_{g} (= 3.26 eV), the energy difference ($E_{\mathrm{Fc}} - E_{\mathrm{Fv}}$) between the quasi-Fermi energies of the conduction band, E_{Fc} in n-type layer, and the valence band, E_{Fv} in p-type layer, is much higher than E_{g}. Therefore, the population inversion condition is satisfied. Also, when light having a photon energy $h\nu_{\mathrm{anneal}}$ lower than E_{g} is radiated, this light propagates in the SiC substrate without being absorbed, and reaches the domain boundaries of the Al dopant sites, which are inhomogeneously distributed [21], thus generating DPs at the surfaces of the Al dopant sites. These DPs excite multimode coherent phonons in the vicinity of the p–n junction [12, 13], forming DPPs [7, 12, 13]. Since the density of states of these DPPs is much higher than the density of states of conduction electrons, a population inversion is formed. Therefore, stimulated emission is generated by the two-step transition driven by the incident light (the electric-dipole forbidden transition from the excited state to the DPP level, followed by the transition from the DPP level to the ground state).

(2) Since part of the Joule heat due to the forward bias is spent for stimulated emission of photons, the annealing progress is controlled. In other words, it becomes more difficult to change the shape and sizes of the inhomogeneous domain boundaries of the Al dopant sites in regions where the stimulated emission process in (1) above easily occurs via DPPs. In the stationary state, the sizes of the dopant sites eventually reach a constant value determined by the light intensity and the cur-

rent [6]. This stimulated emission occurs at the domain boundaries of all of the Al dopant sites in the device.

(3) Because the stimulated emission probability and spontaneous emission probability are proportional to each other [22], in regions where the DPP-mediated stimulated emission process easily occurs, DPP-mediated spontaneous emission also easily occurs. Therefore, as the process in (2) proceeds, the simulated emission light irradiates the entire device, and thus, the process in (2) does not stop in the light irradiation regions, but spreads throughout the entire device in a self-organized manner. It is expected that the shape and distribution of the domain boundaries formed in this way will be optimal for efficiently inducing the DPP-assisted process during device operation.

4 Device operation

We used a spectrometer and a cooled Si-CCD (Roper Scientific Inc.) to observe the emission spectra of the fabricated device. For driving the device, we used a high-speed power supply (Matsusada Precision: POP60-2.5) with a maximum rated capacity of 60 V–2.5 A, and for pulsed driving, we used an oscillator (Agilent Technologies, Inc., model 55321A) in conjunction with this power supply. The response time constant of the power supply was 2 μs, and the temporal resolution of the measurement equipment was 50 ns.

The measurement results of the EL emission spectra from the device during DPP-assisted annealing are shown in Fig. 2(a). The surface temperature during annealing was 120–150 °C. The wavelength of the light irradiated onto the device during DPP-assisted annealing is indicated by the downward long arrow in the figure. While measuring the spectra, the current was reduced to 0.2 A/cm^2 during annealing to arrest the progress of annealing, and the device was not irradiated with light. Figure 2(b) shows the dependency of the total EL emission power on the DPP-assisted annealing time (the area surrounded by the curves and horizontal axis in Fig. 2(a)). The EL emission increases approximately in proportion to the logarithm of the annealing time because the dopant diffusion rate due to annealing has an extremely large distribution, as has been described for 2-level systems [23].

After 8 hours of annealing, the total EL emission power was five-times greater than the value immediately after starting annealing. The total EL emission power saturated when annealing was conducted for 8 hours or more. As shown in Fig. 2(a), the peak emission wavelength was red shifted from 480 nm (upward arrow A) to 490 nm (downward arrow B). Figure 2(c) shows EL emission spectra observed after 8 hours of annealing. As shown by the blue curve, when

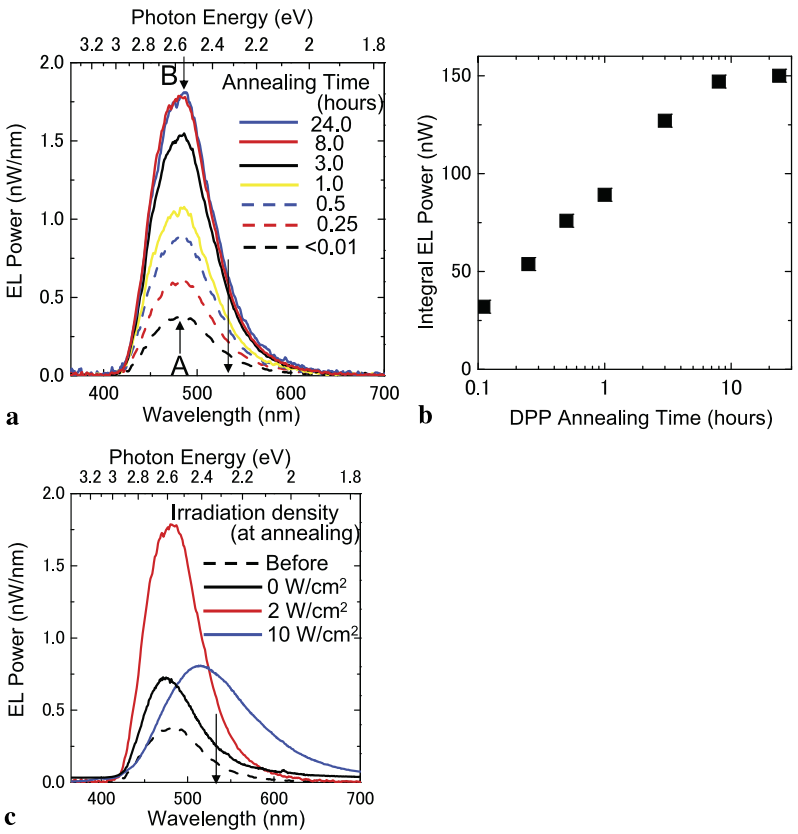

Fig. 2 Temporal change in EL emission characteristics of SiC-LED during dressed-photon-phonon–assisted annealing. (**a**) Spectra obtained when dressed-photon-phonon–assisted annealing was performed while irradiating the device with 523 nm laser light at a power density of 2 W/cm^2 and applying a voltage of 12 V and a current density of 45 A/cm^2. The EL emission peak wavelength before annealing was 480 nm (*upward arrow* A), and that after annealing was 490 nm (*downward arrow* B). (**b**) Temporal change in total EL emission power in (**a**). (**c**) Relationship between EL emission spectra and irradiation intensity during dressed-photon–assisted annealing

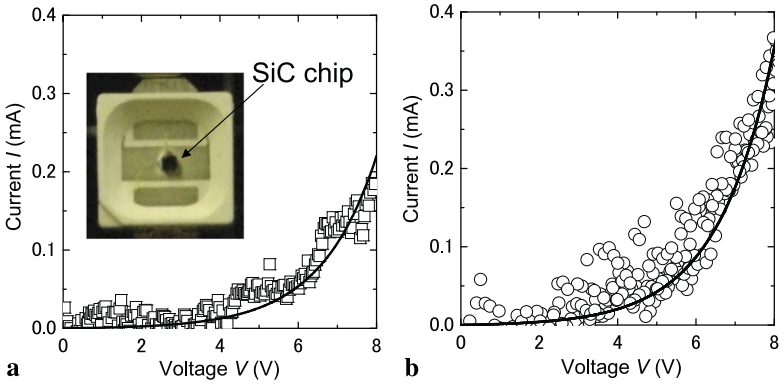

Fig. 3 Relationship between forward bias voltage V and injection current I. (**a**) Before and (**b**) after dressed-photon-phonon–assisted annealing. Solid line is the result of least-squares fitting using the Shockley equation. *Inset* in (**a**) is image of fabricated SiC-LED (chip size 500 μm × 500 μm)

the irradiation intensity during annealing was 10 W/cm^2, the wavelength had red-shifted to 515 nm after annealing. On the other hand, the emission power was reduced to about half that in the case of the red curve (irradiation intensity of 2 W/cm^2 during annealing). This was because the progress of the DPP-assisted annealing was not sufficiently controlled by the light irradiation since the SiC substrate that was used absorbed 532 nm-wavelength light, generating heat. Compared with the red curve, the reason for the greater wavelength shift and lower EL emission intensity in the case of the blue curve (irradiation intensity of 10 W/cm^2 during annealing) was because the intrinsic energy of the DPP level was close to the photon energy of the light irradiated during annealing, which counteracted the heat generation due to absorption. On the other hand, when annealing was performed using only current, without irradiating any light (black curve in Fig. 2(c); current density 45 A/cm^2), the electrodes were degraded due to heat generation in about 1 hour, and the EL emission power decreased.

Figures 3(a) and (b) show measurement results of the relationship between the forward bias voltage V and the injection current I before and after annealing, respectively. The image in the inset in Fig. 3(a) shows the SiC-LED chip mounted in the package. During the measurements, the current was limited to 0.5 mA or less in order to reduce the effects of annealing due to current alone. The solid line in Fig. 3 is the result of least-squares fitting to the measured values using the Shockley diode equation $I = I_0\{\exp(e(V - I \cdot R)/nkT) - 1\}$ for a p–n junction [24]. Here, I_0 is the reverse saturation current, e is the electronic charge, k is Boltzmann's constant, T is the device temperature, R is parasitic resistance, and n is the ideality factor, which is 1 in the case of an ideal p–n junction. Assuming $T = 300$ K, the value of n was estimated to be 51. Since this value is much larger than 1, it means that the SiC crystal surface and the electrode surface do not form an Ohmic contact. Also, the value of R was 100 Ω. Although the values of n and R did not change between before and after annealing, the value of I_0 increased by 0.5×10^{-6} A from 0.8×10^{-6} A to 1.3×10^{-6} A, a value 1.6-times greater. Since I_0 is proportional to the recombination current, this means that the recombination current was increased by a factor of 1.6 by the DPP-assisted annealing. This corresponds to a higher number of electron–hole pairs that radiatively recombine via DPs due to the DPP-assisted annealing; however, this value of 1.6 is small compared with the fivefold increase in the emission power. This is because the majority of the value of I_0 before DPP-assisted annealing is due to non-radiative recombination. For the 0.5×10^{-6} A increase in I_0, the corresponding increase in EL emission power was 0.12×10^{-6} W. Since it is not difficult to achieve $n = 1$ by improving the electrodes [25], if we assume that the increase in I_0 is entirely due to the recombination process via DPs, we will obtain a quantum efficiency of $(0.12 \times 10^{-6}/2.5 \times 0.5 \times 10^{-6}) = 0.096$ (at a photon energy of 2.5 eV corresponding to the center emission wavelength).

Figure 4 shows the measurement results of the injection current dependency of the EL emission power of the fabricated SiC-LED. The SiC-LED was driven with both direct current (●) and pulsed current (■). The images of the SiC-LED shown in the insets were taken under fluorescent room lights while driving the device. The relationship between V and I in Fig. 3 indicates that a Schottky barrier effect at the electrodes reduced the light emission efficiency; however, this can be eliminated by applying a voltage sufficiently higher than the potential gap of the Schottky barrier. Therefore, first we increased the injected direct current, which caused the voltage applied to the device to rise. In this case, as shown by the circles (●) and the black curve in the figure, at injection currents below 0.3 mA, the EL emission power increased nonlinearly due to the two-step transition, and at injection currents of 0.3 mA or higher, it saturated.

The major cause of this saturation is probably heat generation due to the injection current. Therefore, to avoid this, we injected a pulsed current with a pulse width of 50 μs and a repetition frequency of 100 Hz. In this case, an instantaneous current of 780–1300 mA flowed in the SiC-LED, and the instantaneous voltage was 23.0–23.6 V. By driving the device with a pulsed current, the problem of heat generation was eliminated. As a result, the EL emission power was ob-

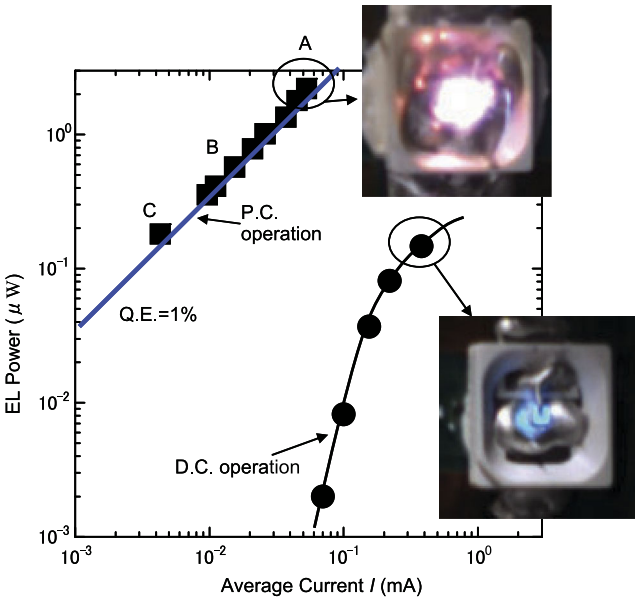

Fig. 4 Injection current dependency of EL emission power of fabricated SiC-LED. *Insets* are images showing light emission during LED operation. Circles (●) are measured values of EL emission power when device was driven by direct current, and square (■) are measured values when device was driven by pulsed current

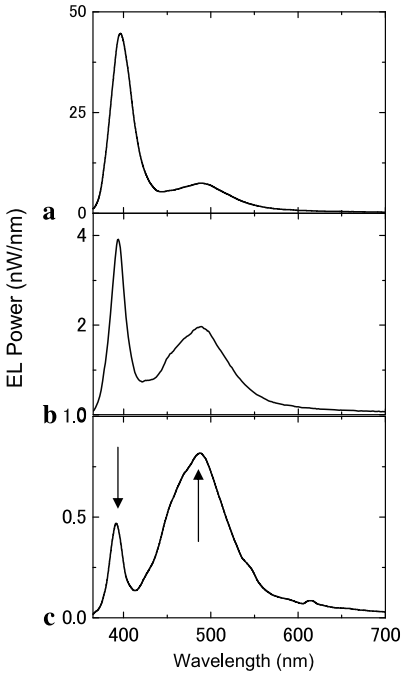

Fig. 5 EL spectra of SiC-LED during pulsed current operation. (**a**), (**b**), and (**c**) correspond to points A, B, and C among the squares (■) in Fig. 4

served to increase linearly and did not saturate, as shown by the squares (■) and the blue curve in the figure. The reasons for this are as follows: (1) The driving voltage was sufficiently high, making the number of carriers that nonradiatively recombine at the Schottky barrier at the electrode negligibly small. (2) The injected pulsed current density reached 320–520 A/cm^2; therefore, there were insufficient Al sites serving as the origin of the DPs required to form DPP levels, making the two-step transition impossible. As a result, electrons and holes accumulated at the bottom of the bands, where they soon formed DPPs, and the one-step transition due to phonon scattering was dominant.

Reason (1) above is well-known in electronic devices having a normal Schottky barrier. The basis for reason (2) is as follows. Figure 5 shows measurement results of the EL emission spectra of the SiC-LED when driven by pulsed current. Figures 5(a), (b), and (c) correspond to points A, B, and C among the squares (■) in Fig. 4, respectively. When the pulsed current was small (Fig. 5(c)), the temperature of the device was low, and a separate phonon level was observed (the peak at the wavelength of 390 nm in the figure: downward arrow). This peak appeared for the first time due to pulsed current operation, but the photon energy of this peak is lower than E_g of 4H-SiC by an amount corresponding to the energy of LO-mode phonons (95 meV) or the energy of TO-mode phonons (110 meV) [26]. From a comparison of Figs. 5(a), (b), and (c), it is clear that what governs the EL emission intensity while driving the device with pulsed current is the intensity of this emission peak. Since the energy of this emission level (DPP level) is close to E_g, recombination luminescence is possible via a one-step transition involving only phonon emission. Of course, an emission peak and sidebands corresponding to the DPP level, which were strongly emitted when driving the device with a direct current, are also present (upward arrow); however, comparing Figs. 5(a), (b), and (c), the height of these is saturated. From the reasons given above, when the device was driven by a pulsed current, it is likely that the one-step transition was dominant, and therefore, the EL emission intensity increased linearly with current. The gradient of the blue line in Fig. 4 corresponds to an external quantum efficiency of 1 %. Using the light extraction efficiency (<30 %) and the light absorptance (>70 %), we estimated the internal quantum efficiency to be 10 %. This value is large enough to rank alongside the efficiency of conventional LEDs using direct-transition-type semiconductors. It will be possible to further increase this efficiency by controlling the thickness and dopant density of the epilayer on the substrate.

5 Conclusion

We fabricated a SiC LED with high light emission efficiency by an annealing process brought about by current injection, using stimulated emission via dressed photons (DPs) generated at the inhomogeneous domain boundaries of Al dopant sites in indirect-transition-type bulk crystal SiC having a

homojunction structure. In the DPP-assisted annealing process, we used a forward current density of 45 A/cm^2 and a light source with an optical power density of 2 W/cm^2 and a wavelength of 532 nm. As a result, the emission peak wavelength of the fabricated device was 480–515 nm (when driven by direct current) and 390 nm (when driven by pulsed current). The external quantum efficiency of the EL emission was 1 %, and the internal quantum efficiency was as high as 10 %.

Acknowledgements The authors thank A. Mizushima and K. Matsue for their assistance in conducting the experiments. A part of this study has been supported by "Development of Next-generation High-performance Technology for Photovoltaic Power Generation System Project" of The New Energy and Industrial Technology Development Organization (NEDO) since 2012.

References

1. W.S. Wong , T. Sands, N.W. Cheung, M. Kneissl, D.P. Bour, P. Mei, L.T. Romano, N.M. Johnson, Appl. Phys. Lett. **75**, 1360 (1999)
2. F.A. Ponce, D.P. Bour, Nature **386**, 354 (1997)
3. G. Ziegler, P. Lanig, D. Theis, C. Weyrich, IEEE Trans. Electron Devices **30**, 277 (1983)
4. J.A. Edmond, H.-S. Kong, C.H. Carter Jr., Physica B **185**, 453 (1993)
5. M. Bhatnagar, B.J. Baliga, IEEE Trans. Electron Devices **40**, 645 (1993)
6. T. Kawazoe, M.A. Mueed, M. Ohtsu, Appl. Phys. B **104**, 747 (2012)
7. M. Ohtsu, J. Nanophotonics **1**, 83 (2012)
8. T. Kawazoe, M. Ohtsu, K. Akahane, N. Yamamoto, Appl. Phys. B **107**, 659 (2012)
9. N. Wada, T. Kawazoe, M. Ohtsu, Appl. Phys. B **108**, 25 (2012)
10. H. Tanaka, T. Kawazoe, M. Ohtsu, Appl. Phys. B **108**, 51 (2012)
11. K. Kitamura, T. Kawazoe, M. Ohtsu, Appl. Phys. B **107**, 293 (2012)
12. T. Kawazoe, K. Kobayashi, S. Takubo, M. Ohtsu, J. Chem. Phys. **122**, 024715 (2005)
13. Y. Tanaka, K. Kobayashi, Physica E **40**, 297 (2007)
14. S. Yukutake, T. Kawazoe, T. Yatsui, W. Nomura, K. Kitamura, M. Ohtsu, Appl. Phys. B, Lasers Opt. **99**, 415 (2010)
15. T. Kawazoe, M. Ohtsu, Y. Inao, R. Kuroda, J. Nanophotonics **1**, 011595 (2007)
16. T. Yatsui, K. Hirata, W. Nomura, Y. Tabata, M. Ohtsu, Appl. Phys. B **93**, 55 (2008)
17. T. Kawazoe, H. Fujiwara, K. Kobayashi, M. Ohtsu, IEEE J. Sel. Top. Quantum Electron. **15**, 1380 (2009)
18. T. Itoh, M. Nishijima, A.I. Ekimov, C. Gourdon, Al.L. Efros, M. Rosen, Phys. Rev. Lett. **74**, 1645 (1995)
19. H. Fujiwara, T. Kawazoe, M. Ohtsu, Appl. Phys. B, Lasers Opt. **100**, 85 (2010)
20. C. Persson, U. Lindefelt, Phys. Rev. B **54**, 10257 (1996)
21. J.A. Van den Berg, D.G. Armour, S. Zhang, S. Whelan, H. Ohno, T.-S. Wang, A.G. Cullis, E.H.J. Collart, R.D. Goldberg, P. Bailey, T.C.Q. Noakes, J. Vac. Sci. Technol. B **20**, 974 (2002)
22. A. Einstein, P. Ehrenfest, Z. Phys. **19**, 301 (1923)
23. W. Breinl, J. Friedrich, D. Haarer, Chem. Phys. Lett. **106**, 487 (1984)
24. W. Shockley, H.J. Queisser, J. Appl. Phys. **32**, 501 (1961)
25. D. Defives, O. Noblanc, C. Dua, C. Brylinski, M. Barthula, V. Aubry-Fortuna, F. Meyer, IEEE Trans. Electron Devices **46**, 449 (1999)
26. H. Nienhaus, T.U. Kampen, W. Monch, Surf. Sci. **324**, L328 (1995)

Appl Phys A (2014) 115:119–125
DOI 10.1007/s00339-013-7904-z

Applied Physics A
Materials Science & Processing

INVITED PAPER

Evaluating the coupling strength of electron–hole pairs and phonons in a 0.9 μm-wavelength silicon light emitting diode using dressed-photon–phonons

M. Yamaguchi · T. Kawazoe · M. Ohtsu

Received: 30 July 2013 / Accepted: 1 August 2013 / Published online: 9 August 2013

Abstract We investigated the coupling strength between electron–hole pairs and phonons in a silicon light emitting diode (Si-LED) fabricated by dressed-photon-assisted annealing. This Si-LED emitted light in the 1.4 eV photon energy (0.9 μm wavelength) band, and phonon sidebands were observed in the emission spectrum. From a comparison with simulation results, these sidebands were found to be due to coupling of electron–hole pairs with LO-mode and TO-mode coherent phonons via dressed-photon–phonons. The value of the Huang–Rhys factor, S, representing the coupling strength between the electron–hole pairs and the phonons was estimated to be 4.08 ± 0.02.

1 Introduction

Si is an indirect band gap semiconductor and has therefore been considered to be an unsuitable material for light-emitting devices such as LEDs and lasers. Nevertheless, there has been a great deal of research on Si light-emitting devices because of Si's advantages, including its high compatibility with integrated circuits and its abundance in the Earth's crust. Studies reported in the literature include research on the quantum confinement effect in nanostructures, such as quantum dots [1] and porous Si [2], core electron transitions in a Si crystal doped with rare earth elements [3], dislocation loops due to high dopant concentrations [4], and the plasmonic effect [5]. However, the devices fabricated in this research have low light emission efficiency, and current injection is difficult. Moreover, the device structures and fabrication processes are complex, which hinders their practical utilization.

To overcome these issues, we recently succeeded in fabricating a high-efficiency Si-LED with an external quantum efficiency as high as 15 % by exploiting dressed photons (DPs) [6, 7], which are quasi-particles created when photons couple with electron–hole pairs, in nano-regions inside a bulk Si crystal [8]. This method has also been used to realize a Si laser [9], a Si optical and electrical relaxation oscillator [10], and a wideband Si photodiode [11]. Furthermore, the method has also been applied to ZnO, which is a direct band gap semiconductor, to fabricate a short-wavelength LED [12].

A Si-LED using DPs was fabricated by a method known as dressed-photon-assisted annealing. In this method, a forward current is injected into a bulk Si crystal having a p–n junction structure while simultaneously irradiating it with light to bring about annealing due to heating caused by light absorption. A feature of the Si-LED fabricated by this method is that the photon energy of the emitted light does not depend on the band gap energy (E_g); it emits light having approximately the same photon energy as the photon energy of the light radiated during annealing. Also, phonon sidebands are found in the emission spectrum, and these are caused by the creation of quasi-particles called dressed-photon–phonons (DPPs) when DPs generated in the Si crystal couple with phonons. The phonons constituting these DPPs have been theoretically shown to be multi-mode coherent phonons [13]. The parameter representing the cou-

M. Yamaguchi (✉) · T. Kawazoe · M. Ohtsu
Department of Electrical Engineering and Information Systems, Graduate School of Engineering, The University of Tokyo, 2-11-16 Yayoi, Bunkyo-ku, Tokyo 113-8656, Japan
e-mail: yamaguchi@nanophotonics.t.u-tokyo.ac.jp
Fax: +81-3-58411140

T. Kawazoe · M. Ohtsu
Nanophotonics Research Center, Graduate School of Engineering, The University of Tokyo, 2-11-16 Yayoi, Bunkyo-ku, Tokyo 113-8656, Japan

pling strength between electron–hole pairs and phonons is called the Huang–Rhys factor, S [14], and its value can be obtained experimentally from the intensities of the phonon sidebands [15, 16]. When a DPP is created, an increase in the value of S is expected, but its magnitude has remained unknown.

In the research described here, in order to evaluate the increase in the value of S in Si-LEDs using DPPs, we fabricated a Si-LED that emitted light in the 1.4 eV (0.9 μm wavelength) band and measured the emission intensities of the phonon sidebands found in its emission spectrum. In addition to these experiments, we performed a simulation of the light emission process taking account of the DPP-mediated coupling between electron–hole pairs and phonons, and we estimated the value of S by comparing the simulation and experimental results.

The above-mentioned photon energy of 1.4 eV is larger than E_g of Si (the energy difference between the top of the valence band at the Γ point and the bottom of the conduction band close to the X point; 1.1 eV). We investigated light emission with such a large photon energy because it is easy to evaluate the involvement of phonons in the light emission process due to the following two reasons: (1) The influence of the electron density on the emission intensity is low because the band structure is simple and there are no singular points in this band. (2) Light emission is based on a simple process involving a single-step radiative relaxation. (Reference [8] reports light emission with a photon energy smaller than E_g, but this emission is based on a complex two-step radiative relaxation.)

The rest of this paper is organized as follows. In Sect. 2, we describe the Si-LED fabrication and the principle of the light emission process. In Sect. 3, we present measurement results of the emission characteristics of the fabricated Si-LED. In Sect. 4, we compare the experimental results with simulation results. Finally, in Sect. 5, we conclude with a summary of our findings.

2 Operating principle and fabrication of an LED using dressed photons

The principle of light emission and the fabrication method of the Si-LED fabricated in this study are essentially the same as in our previous study [8]. In our previous study, however, the photon energy of the emitted light was less than the value of E_g mentioned above. In contrast, in the present study, the photon energy of the emitted light is higher than E_g. The principle of light emission and the fabrication method will be described in this section while focusing on this difference.

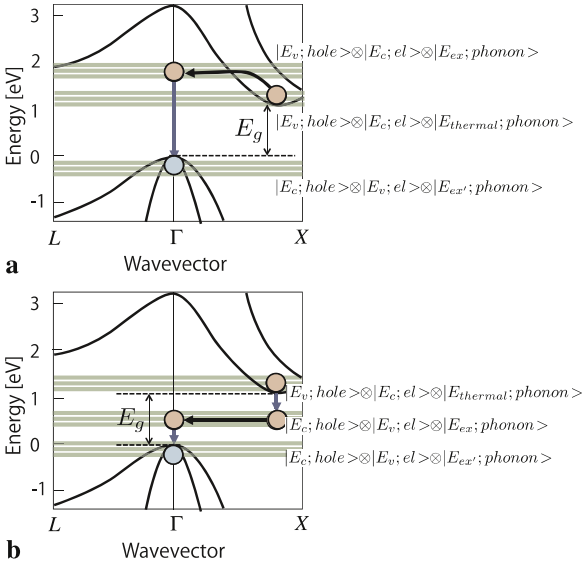

Fig. 1 Band structure of Si. (**a**) One-step radiative relaxation between phonon levels in the Si-LED reported in this paper. (**b**) Two-step radiative relaxation between phonon levels in the Si-LED reported in the previous study

2.1 Principle of light emission

With the Si-LED reported in this paper, as a result of fabricating a device using a processing method called dressed-photon-assisted annealing [8], we realized conditions in which DPs are easily generated in the active layer. These DPs couple with phonons to form quasi-particles called dressed-photon–phonons (DPPs). It is considered that the coupling between electron–hole pairs and phonons in the active layer by means of these DPPs is stronger than in a p–n junction in normal bulk Si. Such strong coupling between electron–hole pairs and phonons via dressed photons has been theoretically shown [12] and experimentally observed [17]. As a result, the wavenumber required for radiative relaxation of the electron–hole pairs is supplied from the phonons, thereby realizing an LED having a light-emission efficiency as high as that of an LED formed of a direct band gap semiconductor.

This principle can be more intuitively understood by considering a picture in which the electron–hole pair radiatively relaxes via the DPP energy level. Since the wavenumber is supplied by multimode phonons, the dispersion relation of the DPP is represented by multiple straight lines parallel to the wavenumber axis, as shown by the green solid lines in Fig. 1. Therefore, a radiative relaxation that is not restricted by the wavenumber conservation law becomes possible. The energy eigenvalue of the DPP is equal to the energy eigenvalue of the coupled state of the electron–hole pair and the phonon, and the state function of the DPP is represented by the direct product of the state function of the hole (conduction band: $|E_c; hole\rangle$, valence band:

$|E_v; hole\rangle$), the state function of the electron (valence band: $|E_v; el\rangle$, conduction band: $|E_c; el\rangle$), and the state function of the phonon (thermal equilibrium state: $|E_{\text{thermal}}; phonon\rangle$, excited state: $|E_{\text{ex}}; phonon\rangle$). With the Si-LED fabricated in this study, as shown in Fig. 1(a), the excited electron–hole pair $|E_v; hole\rangle \otimes |E_c; el\rangle \otimes |E_{\text{thermal}}; phonon\rangle$ couples with a phonon and transitions to $|E_c; hole\rangle \otimes |E_v; el\rangle \otimes |E_{\text{ex}}; phonon\rangle$, and subsequently relaxes to $|E_c; hole\rangle \otimes |E_v; el\rangle \otimes |E_{\text{ex}'}; phonon\rangle$, during which light emission is observed. Since the probability of generating DPPs in normal bulk Si is low, such DPP-mediated transitions have been overlooked.

In this study, we observed light emission due to the simple one-step transition shown in Fig. 1(a). On the other hand, with the Si-LED fabricated in the previous study [8], the photon energy of the emitted light is smaller than E_g. More specifically, light emission is observed due to a complex two-step transition via a phonon level $|E_c; hole\rangle \otimes |E_v; el\rangle \otimes |E_{\text{ex}}; phonon\rangle$ in the band gap, as shown in Fig. 1(b).

2.2 Fabrication method

In order to form a spatial distribution of a p-type dopant (boron, B) concentration suitable for generating DPPs, we injected a forward current into the device while irradiating it with light (photon energy $h\nu_{\text{anneal}}$) to perform annealing. This annealing method is called dressed-photon-assisted annealing [8]. The spatial distribution of the B concentration is modified by the dressed-photon-assisted annealing, forming a distribution that is suitable for generating DPPs. For the LED fabricated here, $h\nu_{\text{anneal}} > E_g$, and therefore, the mechanism by which the distribution is modified differs from that in the case where $h\nu_{\text{anneal}} < E_g$ [8]. The mechanism is explained as follows, by considering regions where DPPs are hardly generated and regions where DPPs are easily generated.

(i) Regions where DPPs are hardly generated: If the device is irradiated with light satisfying $h\nu_{\text{anneal}} > E_g$, as shown in Fig. 2, when an electron in the valence band absorbs a photon (generating an electron–hole pair), it is simultaneously scattered by a phonon (indicated by the upward blue arrow and the red wavy arrow in Fig. 2(a), respectively). As a result, the electron is excited to the conduction band and quickly relaxes to the bottom of the conduction band. After this relaxation, the electron–hole pair cannot radiatively relax because it has a different wavenumber, and therefore it eventually relaxes non-radiatively. This non-radiative relaxation generates heat in the Si crystal, causing the B to diffuse, and thus changing the spatial distribution of the B concentration.

(ii) Regions where DPPs are easily generated: When the B diffuses as in (i), it is considered that the B concentration changes to a spatial distribution suitable for generating DPPs with a fairly high probability. Here we consider the case where DPPs are generated at the surfaces of the B domains. In that case, as shown in Fig. 2(b), an electron and a hole injected by the forward current recombine via the DPP energy level, producing a photon generated by stimulated emission. Since this photon generated by stimulated emission is radiated outside the device, part of the light energy that the device absorbs is dissipated outside the device in the form of light energy, and therefore, the thermal diffusion rate of the B becomes smaller than in (i).

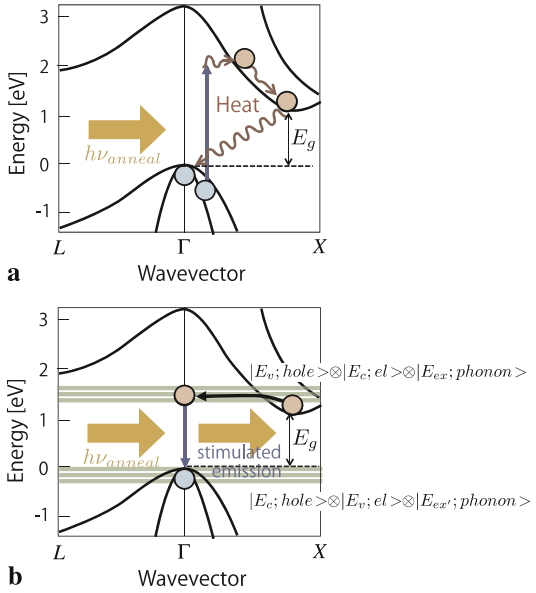

Fig. 2 Principle of dressed-photon-assisted annealing. (**a**) In the region where dressed photons are hardly generated, the B is thermally diffused due to light absorption. (**b**) In the region where dressed photons are easily generated, the energy is dissipated outside the device by stimulated emission via the phonon level, and the thermal diffusion rate is low

Due to the difference in the thermal diffusion rates between (i) and (ii), after the B has diffused throughout the entire device in a self-organized manner as annealing proceeds, it reaches an equilibrium state in which the spatial distribution of the B concentration has been modified, like region (ii), and the annealing process is thus completed. Although region (ii) is in a state where stimulated emission with photon energy $h\nu_{\text{anneal}}$ is easily generated via the DPPs, since the stimulated emission probability is proportional to the spontaneous emission probability [18], after annealing, the device should become an LED that exhibits spontaneous emission with the photon energy $h\nu_{\text{anneal}}$ of the irradiation light.

For the annealing to proceed based on the above process, it is necessary for the irradiation light to be efficiently absorbed in the depletion layer. However, since light having a large photon energy excites electron–hole pairs via a direct

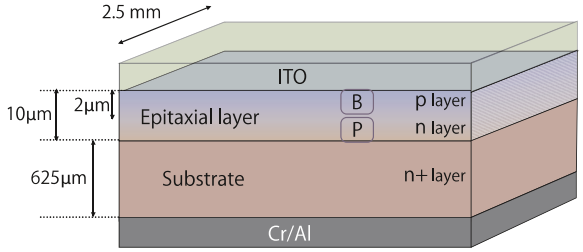

Fig. 3 Schematic diagram of fabricated Si-LED

Fig. 4 Photograph of the device. The device shown in Fig. 3 is mounted on a wiring substrate

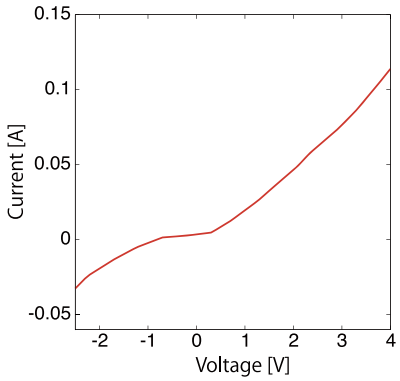

Fig. 5 I–V characteristic of the Si-LED

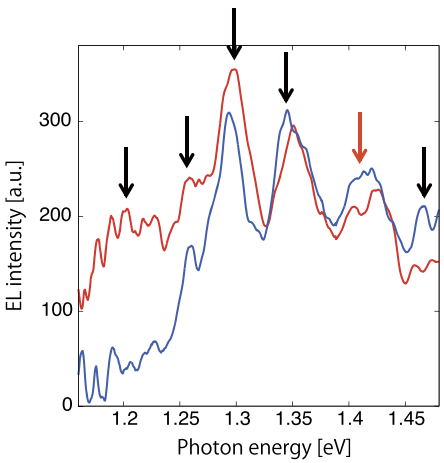

Fig. 6 Emission spectra of the Si-LED. The *blue* and *red curves* show the spectra obtained 1 hour and 3 hours after starting annealing, respectively. *Red arrow*: Peak corresponding to photon energy $h\nu_{\mathrm{anneal}}$. *Black arrows*: Phonon sideband peaks

transition, it is absorbed in the Si bulk crystal before it can reach the depletion layer. In the case of the device used in this study, the photon energy of the light absorbed in the depletion layer is 1.2–3.0 eV (estimated based on the depletion layer depth and thickness obtained from the B doping conditions). In this range, there is no singular point at an energy level corresponding to the emission of light with a photon energy close to 1.4 eV in the Si band structure; thus, this region is suitable for evaluating the involvement of phonons in the light emission process. In this study, therefore, we irradiated the surface of the device with light having a photon energy of 1.4 eV during annealing.

We fabricated a Si-LED with the following annealing method: We grew a 10 μm phosphorus (P)-doped n-type epitaxial layer on a commercially available n^+-type Si substrate with a thickness of 625 μm and a resistivity of 0.09 Ω · cm, and doped it with boron (B) using ion implantation to form a p-type layer, thus fabricating a p–n junction. The maximum B ion implantation energy was 700 keV, the concentration was 1×10^{19} cm^{-3}, and the thickness of the p-type layer was 2 μm. After dicing this substrate into a 2.5 mm × 2.5 mm area, an indium tin oxide (ITO) layer with a thickness of 300 μm and a chromium/aluminum (Cr/Al) layer with a thickness of 150 μm were, respectively, deposited, by RF sputtering, on the surfaces of the p-type and n-type layers to serve as an anode and a cathode. A schematic diagram of the device is shown in Fig. 3.

We applied a forward-bias voltage of 2 V to the device (current density 0.96 $\mathrm{A/cm}^2$) while simultaneously irradiating it with 1.4 eV photon energy light emitted from a Ti:sapphire laser to perform dressed-photon-assisted annealing for 3 hours. We measured the surface temperature of the device during annealing using thermography and found it to be approximately 150 °C. This value is approximately the same as the value measured in the previous study [8].

3 I–V characteristic and EL emission spectrum of fabricated LED

A photograph of the fabricated Si-LED is shown in Fig. 4. Looking at the I–V characteristic shown in Fig. 5, we do not see the unusual negative resistance exhibited by the Si-LED fabricated in the previous study [8]. This is because the device in this study had a lower resistance and smaller area, succeeding in suppressing the generation of a filament current.

The EL emission spectra measured when a forward current (current density 3.2 $\mathrm{A/cm}^2$) was injected into the Si-LED are shown in Fig. 6. The blue curve shows the spec-

trum obtained one hour after starting annealing, and the red curve shows the spectrum obtained three hours after starting annealing. Even before annealing, the device emitted extremely low-intensity light having a photon energy corresponding to E_g. This was because, although only slightly, the electrons at the bottom of the conduction band radiatively relaxed by being scattered by phonons. This weak emission intensity was removed from the intensity curve shown in Fig. 6. Also, the effect of reabsorption of the emitted light was corrected for by using the absorption coefficient of Si [19]. From Fig. 6 we can see that, when comparing the spectra obtained 1 hour after and 3 hours after starting annealing, the emission intensity showed almost no change at photon energies of 1.25 eV and above, whereas at photon energies below 1.25 eV, the emission intensity was considerably increased. A possible reason for this is that, in the regions where low-energy photons are easily generated, the energy dissipation level due to stimulated emission produced in regions like those discussed in (ii) in Sect. 2.2 is also small, thus exhibiting a small difference in thermal diffusion rate compared with region (i), and therefore, annealing proceeds slowly. This phenomenon suggests the validity of the annealing principle discussed in Sect. 2.2. In Fig. 6, the photon energy $h\nu_{\mathrm{anneal}}$ (=1.4 eV) of the light radiated during annealing is indicated by the downward red arrow. From this spectrum, we found that this Si-LED emitted light with a photon energy approximately equal to $h\nu_{\mathrm{anneal}}$. Furthermore, multiple sidebands are observed in the spectrum (indicated by the downward black arrows). The spacing between these peaks is approximately constant at 60 meV, which substantially agrees with the energy of optical phonons in Si [20], and therefore these sidebands likely originate from phonons.

Similarly, peaks were also observed at $h\nu_{\mathrm{anneal}}$ in the emission spectrum of the Si-LED reported in the previous study [8]. Multiple peaks thought to be phonon sidebands were also found. Therefore, the features in the spectrum shown in Fig. 6 are probably phenomena common to Si-LEDs using DPPs. However, the cause of the peaks seen in the light emission spectrum observed in the previous study [8] is not clear. Possible reasons for this are that two photons due to the complex two-step transition based on the state-to-state transition $|E_v; hole\rangle \otimes |E_c; el\rangle \otimes |E_{\mathrm{thermal}}; phonon\rangle \rightarrow |E_c; hole\rangle \otimes |E_v; el\rangle \otimes |E_{\mathrm{ex}}; phonon\rangle \rightarrow |E_c; hole\rangle \otimes |E_v; el\rangle \otimes |E_{\mathrm{ex}'}; phonon\rangle$ are observed simultaneously, and that multiple intermediate states $|E_c; hole\rangle \otimes |E_v; el\rangle \otimes |E_{\mathrm{ex}}; phonon\rangle$ exist.

In contrast, in the Si-LED fabricated in this study, since it involves a simple single-step transition based on the state-to-state transition $|E_v; hole\rangle \otimes |E_c; el\rangle \otimes |E_{\mathrm{ex}}; phonon\rangle \rightarrow |E_c; hole\rangle \otimes |E_v; el\rangle \otimes |E_{\mathrm{ex}'}; phonon\rangle$ as shown in Fig. 1(a), only one photon is emitted due to the radiative relaxation of a single electron–hole pair. In addition, it has been reported

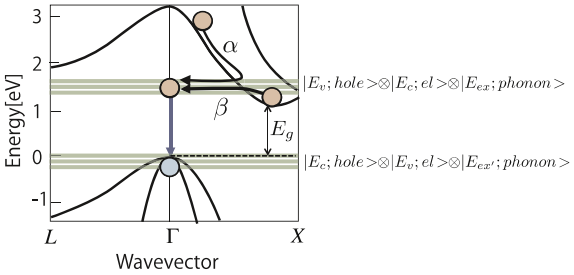

Fig. 7 Emission process via DPP energy levels. α: Light emission during relaxation of electron. β: Light emission after relaxation of electron

that the emission lifetime of a Si-LED using DPPs is on the order of 1 ns [10], which is considerably shorter than the lifetime of the weak emission from a normal Si bulk crystal, but is as much as three to four orders of magnitude larger than the 0.1–1 ps intraband relaxation time of electrons in Si [21, 22]. Therefore, it is reasonable to assume that the injected electrons do not radiatively relax during the relaxation process α in Fig. 7, but instead radiatively relax by coupling with phonons after they have relaxed to the bottom of the conduction band, as shown by process β. This indicates the electron–hole pairs forming the DPPs that contribute to light emission have energy identical to E_g. Therefore, it can be concluded that the difference between the photon energy of the emitted light and E_g is the energy of the phonons that have coupled to the electron–hole pairs.

4 Comparison of experimental and simulation results

We obtained the emission spectrum via simulation and examined the coupling strength between electron–hole pairs and phonons by comparing the simulation results with the measured spectrum. We made the following four assumptions in the simulation:

(1) The electron and hole forming the DPP are at the bottom of the conduction band and at the top of the valence band, respectively, and the wavenumber and energy of the phonon are imparted to this electron–hole pair. We made this assumption based on the fact that the electron and hole intraband relaxation time is shorter than the emission lifetime via the phonon level, as described in Sect. 3.

(2) The electron–hole pair is coupled with coherent phonons including all optical modes. This was decided based on experimental results [17] and theoretical considerations [13] regarding DPPs.

(3) The probability distribution of the number of phonons that couple with an electron–hole pair follows a Poisson distribution. In other words, the probability of n_p phonons coupling with an electron–hole pair is proportional to $S^{n_p}/n!$ for Huang–Rhys factor S. This means

that coupling of electron–hole pairs and phonons via DPPs occurs randomly.

(4) Radiative relaxation occurs only when the sum of the wave vector of an electron at the bottom of the conduction band and the wave vector of a phonon that is coupled with it matches the wave vector of a hole at the Γ point. This assumption was made on the basis of the wavenumber conservation law between the initial state and the final state.

Although the spectral shape can be analytically obtained based on these assumptions, the computational complexity is huge because it involves multiple integrals and infinite sums. Therefore, we obtained the spectrum based on the above assumptions by performing a simulation using random numbers, and by comparing the results with the experimentally obtained spectrum, we estimated the Huang–Rhys factor S, which is an indicator representing the coupling strength between the electron–hole pairs and the phonons in the Si-LED. The simulation procedure was as follows:

(I) Based on assumption (3), we determined the number of phonons coupling with an electron–hole pair.

(II) Based on assumption (2), from among all of the optical phonons, we randomly selected phonons whose number was determined in (I). From this number and the dispersion relation of phonons in Si [23], we determined the wavenumber and energy of the coupling phonons.

(III) As the electron state at the bottom of the conduction band, from among the energy states of the electrons between the Γ point and the X point, we selected those having the lowest energy and obtained the sum of their wave vectors and the wave vectors of the phonons selected in (II). If this value and the value of the wave vector at the Γ point do not match, no light emission occurs, and the procedure returns to (I). On the other hand, if they do match, light with a photon energy corresponding to the sum of the electron–hole pair and the energy of the phonons, which are coupled via a DPP, is emitted, and therefore the value of this photon energy is calculated. Then the procedure returns to (I).

(IV) The number of individual photons obtained by repeating (I) to (III) above is determined, and the simulation ends.

Figure 8(a) shows the emission spectrum obtained by performing the simulation using both longitudinal optical mode (LO mode) and transverse optical mode (TO mode) phonons as the phonons that couple with the electron–hole pair. The parameter n_p in the figure is the number of phonons that coupled with an electron–hole pair via a DPP. Multiple peaks corresponding to each n_p are observed in this spectrum, similarly to the measured results (Fig. 6). For ease of viewing the spectral shape, the heights of all peaks are

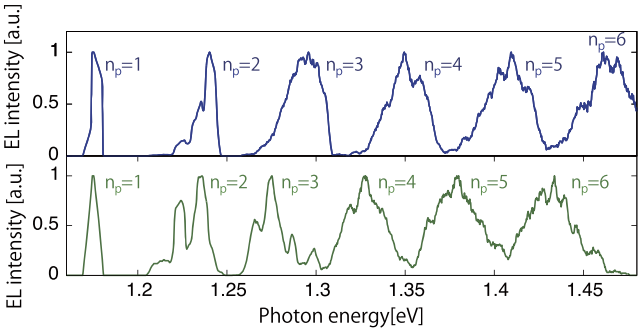

Fig. 8 Emission spectra obtained from the simulation. (**a**) When both LO-mode and TO-mode phonons were used. (**b**) When only LO-mode phonons were used

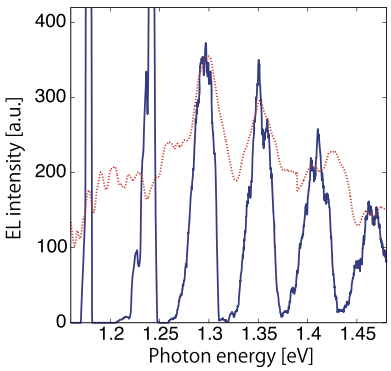

Fig. 9 Least squares fitting for comparing simulation and measurement results

normalized. By comparing the curve in this figure with the curve shown in Fig. 6, since the photon energies at the peaks match, and since the spectral shapes resemble each other, we can conclude that the phonons that couple with the electron–hole pair are composed of both LO-mode and TO-mode phonons. For the sake of comparison, Fig. 8(b) shows an emission spectrum obtained by performing the simulation using only longitudinal optical mode (LO-mode) phonons as the optical phonons. The positions of the peaks on the curve in Fig. 8(b) differ from the positions of the peaks in Figs. 8(a) and 6. Therefore, this shows that both LO-mode and TO-mode phonons are involved in the coupling with the electron–hole pair.

Next, to determine the value of the Huang–Rhys factor, S, we considered the intensity of the emission peaks. As described in assumption (III) above, since the distribution of the number of phonons, n_p, that couple with an electron–hole pair follows a Poisson distribution which depends on the value of S, the height of each spectral peak in Fig. 8(a) also depends on the value of S. Hence, the value of S in the case where the height of each peak in Fig. 8(a) best matches the height of each peak on the red curve in Fig. 6 was determined by the least squares method. The results of this fitting are shown in Fig. 9. The curve in Fig. 6 is also over-

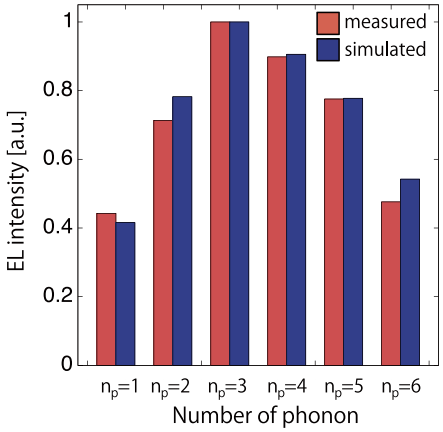

Fig. 10 Comparison of intensity of each sideband

laid on this figure. The resulting value of S was found to be 4.08 ± 0.02. In a normal bulk Si crystal, S is from 0.001 to 0.01 [24], and therefore, the DPP-mediated coupling between the electron–hole pair and phonons is two to three orders of magnitude stronger. From Fig. 9, we can see that the peak widths in the EL spectrum of the actual device differ from those in the simulated spectrum. This is because coupling between the electron–hole pair and acoustic-mode phonons was not taken into account in the simulation.

For this value of S, Fig. 10 represents the emission intensity of each sideband obtained by the simulation and experiments as a function of the number of phonons, n_p, that couple with an electron–hole pair. In this figure, the intensity is normalized to the value at $n_p = 4$. Thus, we can see that, when $S = 4.08$, the intensity ratios of the sidebands are in good agreement with the experimental results.

5 Conclusion

We investigated the coupling strength between electron–hole pairs and phonons in a Si-LED fabricated by dressed-photon-assisted annealing. This Si-LED emitted light in the 1.4 eV photon energy (0.9 μm wavelength) band, and phonon sidebands were observed in the emission spectrum. From a comparison with the results of a simulation, these sidebands were found to be due to coupling between electron–hole pairs and both LO-mode and TO-mode coherent phonons, mediated by dressed-photon–phonons (DPPs). The value of the Huang–Rhys factor, S, representing the coupling strength between the electron–hole pairs and the phonons, was estimated to be 4.08 ± 0.02, which is two to three orders of magnitude greater than in the case of conventional bulk Si. From these results, we were able to quantitatively evaluate the increase in coupling between the electron–hole pairs and the phonons mediated by DPPs in the Si-LED.

References

1. N.M. Park, T.S. Kim, S.J. Park, Appl. Phys. Lett. **78**, 2575 (2001)
2. L.T. Canham, Appl. Phys. Lett. **57**, 1046 (1990)
3. H. Ennen, G. Pomrenke, A. Axmann, K. Eisele, W. Haydl, J. Schneider, Appl. Phys. Lett. **43**, 943 (1983)
4. W.L. Ng, M.A. Lourenco, R.M. Gwilliam, S. Ledain, G. Shao, K.P. Homewood, Nature **410**, 192 (2001)
5. C.H. Cho, C.O. Aspetti, J. Park, R. Agarwal, Nat. Photonics **7**, 285 (2013)
6. M. Ohtsu, J. Nanophotonics **1**, 83 (2012)
7. M. Ohtsu, *Progress in Nanophotonics*, vol. 1 (Springer, Berlin, 2011)
8. T. Kawazoe, M.A. Mueed, M. Ohtsu, Appl. Phys. B **104**, 747 (2012)
9. T. Kawazoe, M. Ohtsu, K. Akahane, N. Yamamoto, Appl. Phys. B **107**, 659 (2012)
10. N. Wada, T. Kawazoe, M. Ohtsu, Appl. Phys. B **108**, 25 (2012)
11. H. Tanaka, T. Kawazoe, M. Ohtsu, Appl. Phys. B **108**, 51 (2012)
12. K. Kitamura, T. Kawazoe, M. Ohtsu, Appl. Phys. B **107**, 293 (2012)
13. Y. Tanaka, K. Kobayashi, J. Microsc. **229**, 228 (2008)
14. K. Huang, A. Rhys, Proc. R. Soc. Lond. Ser. A, Math. Phys. Sci. **204**, 406 (1950)
15. H. Zhao, H. Kalt, Phys. Rev. B **68**, 125309 (2003)
16. T.W. Hagler, K. Pakbaz, K.F. Voss, A.J. Heeger, Phys. Rev. B **44**, 8652 (1991)
17. T. Kawazoe, K. Kobayashi, S. Takubo, M. Ohtsu, J. Chem. Phys. **122**, 024715 (2005)
18. A. Einstein, P. Ehrenfest, Z. Phys. **19**, 301 (1923)
19. M.A. Green, M.J. Keevers, Prog. Photovolt. **3**, 189 (1995)
20. H. Palevsky, D.J. Hughes, W. Kley, E. Tunkelo, Phys. Rev. Lett. **2**, 258 (1959)
21. J.R. Goldman, J.A. Prybyla, Phys. Rev. Lett. **72**, 1364 (1994)
22. A.J. Sabbah, D.M. Riffe, Phys. Rev. B **66**, 165217 (2002)
23. P. Giannozzi, S. Gironcoli, P. Pavone, S. Baroni, Phys. Rev. B **43**, 7231 (1991)
24. S. Nomura, T. Kobayashi, Phys. Rev. B **45**, 1305 (1992)

Appl Phys A (2014) 115:113–118
DOI 10.1007/s00339-013-7906-x

Applied Physics A
Materials Science & Processing

INVITED PAPER

Measurement of multimode coherent phonons in nanometric spaces in a homojunction-structured silicon light emitting diode

Naoki Wada · Minh Anh Tran · Tadashi Kawazoe · Motoichi Ohtsu

Received: 31 July 2013 / Accepted: 1 August 2013 / Published online: 14 August 2013

Abstract This paper reports the results of measuring the sidebands in the emitted visible spectrum of a novel homojunction-structured silicon (Si) light emitting diode (LED), which was fabricated by Joule annealing assisted by dressed-photon–phonons. Using pump–probe spectroscopy, both the fundamentals and higher-order harmonics of the longitudinal optical (LO) phonon were observed for the first time. These fundamentals and harmonics are the constituent components of the multimode coherent phonons generated in the nanometric spaces around the inhomogeneous domain boundaries of boron doped in the Si LED. Furthermore, it was confirmed that the fourth-order harmonics of the LO phonon are the origin of the sidebands in the emission spectrum of the Si LED.

1 Introduction

The spectral properties of phonons have been experimentally studied by high-resolution Raman spectroscopy [1], Fourier transform infrared spectroscopy [2], and so on. Furthermore, coherent phonons (CPs) have been generated by irradiating macroscopic materials with short optical pulses, and their spectral properties have been studied by measuring CP-induced temporal variations in macroscopic physical quantities of the materials, such as the optical reflectivity [3, 4]. Theoretical studies have also been carried out to explain several phenomena caused by these CPs [5].

Unlike these conventional studies of phonons, in order to construct a novel silicon (Si) light emitting diode (LED), the authors have carried out experimental and theoretical studies of dressed photons (DPs), which are quasi-particles representing the coupled state of photons and electron–hole pairs in nanometric spaces in a material. These studies have revealed that DPs are accompanied by multimode coherent phonons [6], resulting in the creation of dressed-photon–phonons (DPPs), which are quasi-particles representing the coupled state of DPs and multimode coherent phonons. In contrast to the conventionally studied CPs generated in a super-wavelength macroscopic space in a macroscopic material, these multimode coherent phonons are excited by the DPs in nanometric spaces. Furthermore, these multimode coherent phonons in the nanometric spaces (MCP-NSs) have large uncertainties in their wavenumber and momentum because of the sub-wavelength size of the nanometric spaces in which they are generated.

A broad wavenumber spectrum of the MCP-NSs, due to the large uncertainty in the wavenumber, has allowed the fabrication of a Si LED with high light emission efficiency by using a novel DPP-assisted Joule annealing process, even though Si is an indirect transition-type semiconductor [7, 8]. The fabrication and operation principles of this Si LED have been applied to realize a room-temperature continuous-wave (CW) Si laser [9], an optical and electrical Si relaxation oscillator [10], and an infrared Si photodetector with optical gain [11]. They have been applied also to a direct transition-type ZnO semiconductor crystal in order to construct a visible LED [12].

N. Wada (✉) · M.A. Tran · T. Kawazoe · M. Ohtsu
Department of Electrical Engineering and Information Systems, Graduate School of Engineering, The University of Tokyo, 2-11-16 Yayoi, Bunkyo-ku, Tokyo 113-8656, Japan
e-mail: wada@nanophotonics.t.u-tokyo.ac.jp
Fax: +81-3-58411140

T. Kawazoe · M. Ohtsu
Nanophotonics Research Center, Graduate School of Engineering, The University of Tokyo, 2-11-16 Yayoi, Bunkyo-ku, Tokyo 113-8656, Japan

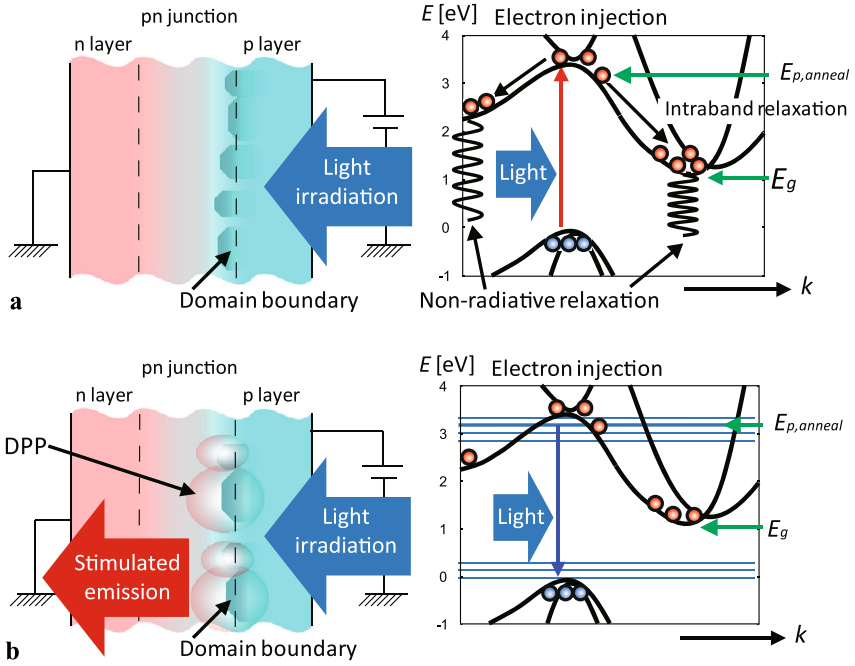

Fig. 1 Cross-sectional profile of the pn junction and the energy diagram of the homojunction-structured Si LED. (**a**) and (**b**) represent cases where DPPs are hardly generated and easily generated at the domain boundaries, respectively. The *red upward arrow* in (**a**) and the *blue downward arrow* in (**b**) represent the absorption and stimulated emission of light, respectively. The *horizontal parallel blue lines* in (**b**) represent the energy levels of the coherent phonons

In one previous study by the authors of DPP-assisted Joule annealing, a Si crystal was illuminated by light whose photon energy, $E_{\mathrm{p,anneal}}$, was lower than the band gap energy ($E_{\mathrm{g}} = 1.12$ eV) of a homojunction-structured Si crystal [7]. As a result, the fabricated Si LED emitted near-infrared light whose photon energy was equivalent to $E_{\mathrm{p,anneal}}$ ($<E_{\mathrm{g}}$). Several spectral sidebands were found in the emission spectrum (refer to Fig. 6d of Ref. [7]). In another study by the authors, a Si crystal was irradiated with visible light (photon energy $E_{\mathrm{p,anneal}} > E_{\mathrm{g}}$) in the process of DPP-assisted Joule annealing. This allowed fabrication of a novel Si LED that emitted visible light whose photon energy is equivalent to $E_{\mathrm{p,anneal}}$ ($>E_{\mathrm{g}}$) [8]. However, phonon sidebands observed in its emission spectrum have not yet been explained. In the work described in the present paper, the sidebands observed in the emission spectrum of this visible Si LED were investigated. Furthermore, the origin of these sidebands was studied experimentally through measurement of optical phonons in the MCP-NSs by using pump–probe spectroscopy.

2 Device fabrication

As the first step in fabricating a visible Si LED, a P-doped n-type layer with a thickness of 10 μm was epitaxially grown on an As-doped n-type Si crystal with a thickness of 625 μm and a sheet resistance of 0.1 Ω cm. To realize a homo-structured pn junction, boron (B) was doped into the P-doped layer by ion implantation with an acceleration energy as high as 700 keV. The doped B concentration and the thickness of the formed p-type layer were 1×10^{19} cm^{-3} and 2 μm, respectively. The purpose of this high-concentration B doping was to form domain boundaries with an inhomogeneous spatial distribution of B at the pn junction, around which the DPPs are generated by irradiating the substrate with light in the process of Joule annealing. As the second step, a 150-nm-thick transparent indium tin oxide (ITO) film was formed on the surface of the p-type layer and was used as a positive electrode. For a negative electrode, Cr and Al films with a total thickness of 150 nm were formed on the surface of the n-type layer. The coated Si crystal was cut into an area of 25 mm^2. As the last step, DPP-assisted Joule annealing of the cut Si crystal was carried out by applying a forward-bias voltage while the crystal surface was illuminated with laser light having a photon energy $E_{\mathrm{p,anneal}}$ ($>E_{\mathrm{g}}$). The forward-bias voltage was set higher than $E_{\mathrm{p,anneal}}/e$, where e represents the electron charge.

In this annealing process, the domain boundaries of the inhomogeneous distribution of B at the pn junction vary from moment to moment autonomously, as confirmed by previous experimental studies [7, 9–12]. This process is explained as follows:

(1) At the domain boundaries where DPPs are hardly generated (the left-hand part of Fig. 1a): electrons injected by applying the forward-bias voltage generate electron–hole pairs at the pn junction by absorbing the light with photon energy $E_{\mathrm{p,anneal}}$ ($>E_{\mathrm{g}}$) (see the right-hand part of Fig. 1a). Here, the non-absorbed excess energy, $E_{\mathrm{p,anneal}} - E_{\mathrm{g}}$, is converted to thermal energy via the intraband relaxation of electrons. Moreover, since the Si crystal remains as an indirect-transition type in the

early stage of the annealing, electron–hole recombination is not possible, resulting in intraband relaxation and non-radiative interband relaxation of electrons, so that the energies applied by the forward-bias voltage and by light irradiation are converted to thermal energy. As a result of this thermal energy, the domain boundaries are heated, causing the B to diffuse, and resulting in variation of its spatial distribution.

(2) At the domain boundaries where DPPs are easily generated (the left-hand part of Fig. 1b): the DPPs trigger stimulated emission when the electrons injected by the forward-bias voltage reach the domain boundaries (see the right-hand part of Fig. 1b). This emission is possible because the injected electrons have an energy higher than $E_{\mathrm{p,anneal}}$. Due to the decrease in the carrier density caused by this stimulated emission, the amount of absorbed optical energy decreases, and part of the applied electrical energy is converted to the energy of propagating light, which is radiated from the Si crystal. As a result of the decrease in absorption and dissipation of energy, the shape and dimensions of the inhomogeneous domain boundaries of the B become more difficult to change. Furthermore, as this diffusion process progresses, the stimulated emission propagates through the whole Si crystal and, as a result, this diffusion process progresses autonomously in the entire volume of the Si crystal to increase the number of domain boundaries at which the DPPs are easily generated.

By the balance of the diffusions in processes (1) and (2), characteristic minute inhomogeneous domain boundaries of B are autonomously formed, asymptotically reaching a stationary profile. As a result, the domain boundaries become optimum for efficiently generating DPPs over the entire pn junction.

Using these processes, a Si LED was fabricated by applying a forward-bias voltage of 3.5 V (injected current: 240 mA) while irradiating the Si crystal with pulsed laser light for 1 h. The laser light had a wavelength of 400 nm (photon energy 3.1 eV), a pulse width of 100 fs, a repetition frequency of 80 MHz, a pulse energy density of 5×10^{-8}J/cm^2, and an average power density of 4 W/cm^2. Since the pulse energy used during this process was seven orders of magnitude smaller than the ablation threshold for a pulsed laser with a center wavelength of 800 nm, for example, ablation did not occur [13, 14]. The reason for using a pulsed laser, not a CW laser, was to maintain a sufficiently high peak power for efficient annealing by light absorption.

Figure 2 shows the main part of the spectrum of the light emitted from the fabricated Si LED with an injected current of 450 mA. The curve in this figure clearly shows three peaks in the visible range. The spectral component at 3.1 eV ($=E_{\mathrm{p,anneal}}$), which originated from the light irradiated in the annealing process, is not displayed due to the low efficiency of the diffraction grating in the monochromator used for the spectral measurement. The separations between adjacent peaks were about 60 THz, from which these peaks can be identified as phonon sidebands originating from the strong coupling between DPs and MCP-NSs in the Si crystal, as will be discussed in the next section.

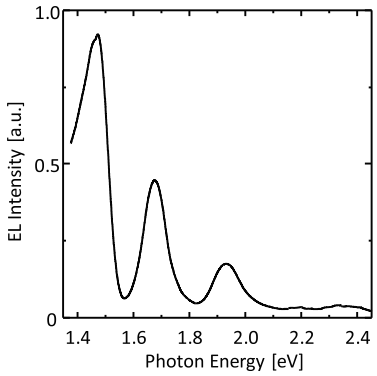

Fig. 2 Spectrum of the light emitted from the fabricated Si LED. The applied voltage and injected current were 4 V and 450 mA, respectively

3 Measurement of optical phonons of multimode coherent phonons in nanometric spaces

In order to generate and evaluate the MCP-NSs for studying the origin of the sidebands in Fig. 2, pump–probe laser spectroscopy was employed based on the principle of impulsive stimulated Raman scattering (ISRS) [15]. If the spectral width of the optical pulse (carrier frequency ν) from the light source is wider than the eigen-frequency of the phonon, ν_{p}, the intensity of the frequency components $\nu - \nu_{\mathrm{p}}$ in the optical pulse can be maintained sufficiently high for generating the MCP-NSs efficiently.

Since the generated MCP-NSs, i.e. the coherent collective motion of atoms, temporally modulate the Coulomb potential of the interaction with electrons, the energy band structure of the electrons is modulated, resulting in modulation of the optical reflectivity of the Si crystal [4, 16]. Among the coherent and incoherent phonons, this modulation enables selective detection of the MCP-NSs because the thermally excited incoherent phonons do not induce any variations in the optical reflectivity due to incoherent motions of the atoms. The temporal variation of the optical reflectivity can be acquired by plotting the reflected probe beam intensity as a function of the difference, t, between the arrival times of the incident probe and pump optical beams at the Si crystal surface.

The experimental setup is shown in Fig. 3. A Ti:sapphire laser was used as a light source. The center wavelength was 780–805 nm, the photon energy was 1.54–1.59 eV, and the

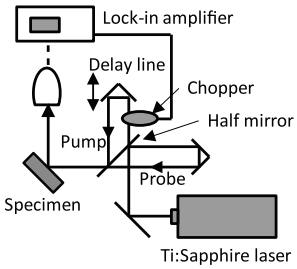

Fig. 3 Experimental setup for pump–probe laser spectroscopy

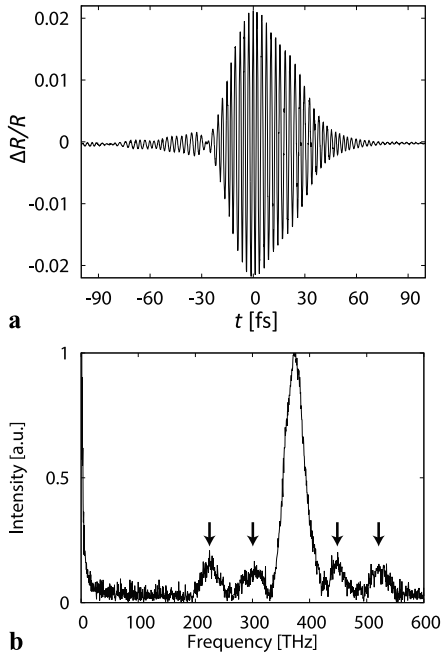

Fig. 4 Measurement results of pump–probe laser spectroscopy. (**a**) Typical normalized fractional variation, $\Delta R/R$, of the optical reflectivity measured as a function of the time difference, t, between the pump and probe beams. (**b**) Fourier transform spectrum obtained when the average powers of the pump and probe beams were 120 mW and 20 mW, respectively

pulse width was 15 fs. The temporal variation of the optical reflectivity was measured by lock-in detection of the intensity of the reflected probe beam from the Si crystal surface. The specimen used for the measurement was a Si crystal before it was processed by DPP-assisted Joule annealing. Even before the annealing, efficient DPP generation is expected around the nanometric-sized inhomogeneous domain boundaries of B because the acceleration energy for ion implantation was maintained sufficiently high in order to dope the crystal with a high concentration of B. The amount of these generated DPPs is expected to be sufficiently high to generate MCP-NSs around these domain boundaries of B.

Figure 4a shows a typical normalized fractional variation of the optical reflectivity measured as a function of the time difference t defined above. The curve in this figure represents a rapidly oscillating, amplitude-modulated optical interference signal between the pump and probe beams. Figure 4b shows the spectrum obtained by Fourier transforming the fractional variation of the optical reflectivity when the average powers of the pump and probe beams were 120 mW and 20 mW, respectively. Their beam spot diameters were 1 mm. As represented by the four downward arrows, the spectral curve shows several sidebands on both sides of the high spectral peak of the optical interference signal at 385 THz. These sidebands originate from the amplitude and phase modulations of the reflected probe beam intensity, i.e. the modulation of the optical reflectivity of the Si crystal. These results suggest that there is strong coupling between the MCP-NSs and the pump-beam photons.

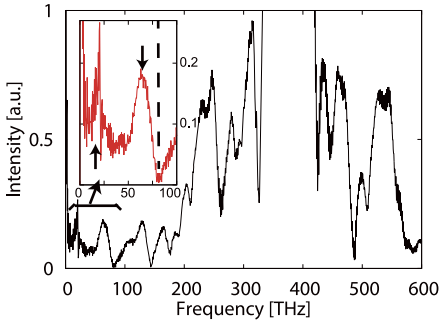

Fig. 5 Fourier transform spectrum. The probe beam average power was increased to 120 mW. The inset shows a magnified view of the spectral curve in the frequency range 0–100 THz.

In order to evaluate the spectral properties in Fig. 4b more quantitatively, the average power of the probe beam was increased to 120 mW to increase the measurement sensitivity. Figure 5 shows the measured Fourier-transformed spectrum. In this curve, the interference signal peak at 385 THz is much higher than the maximum on the vertical axis. On both sides of this over-scaled peak, many more sidebands are seen, as compared with Fig. 4b. In addition to the optical interference signal and the sidebands in Fig. 4b, Fig. 5 also reveals the unique signals originating from the MCP-NSs. The spectral curve of these signals is magnified and shown in the inset of Fig. 5. These signals are manifested by spectral peaks at frequencies lower than 80 THz, as represented by the two arrows, and were successfully detected because the ISRS efficiently generated the MCP-NSs due to the sufficiently high intensity of the frequency components $\nu - \nu_p$ in the pump beam. The high-frequency cut-off, which is governed by the value $\nu - \nu_p$, was confirmed to be 80 THz because the spectral intensity of the curve in the inset decreased to zero at 80 THz (represented by a vertical broken line in the inset). The curve in the region higher than 80 THz represents tails of the sidebands of the optical interference signal.

The spectral peaks shown by the two arrows on the curve in the inset are at the frequencies of 18 THz and 64 THz (74 meV and 265 meV). It is easily seen that the spectral intensity at 64 THz, which is defined by the area under the

bell-shaped spectral curve, is larger than that at 18 THz. As a result of these comparisons between the spectral intensities, it was found that the sidebands with a separation of about 60 THz in Fig. 2 originated from the spectral peak at 64 THz in this magnified curve.

For a more detailed evaluation of the curve in the inset, it was fitted by the superposition of the Lorentzian spectral curves of the fundamentals and harmonics of the longitudinal optical (LO) phonon, which can contribute to forming the MCP-NSs. Each Lorentzian spectral curve is represented by $S_n(\nu) = A/\{(\nu - n\nu_p)^2 + (\Delta\nu/2)^2\} + B$, where the first term is the Lorentzian spectral function and the second term, B, represents the noise intensity in the measurements. The integer n represents the order of the harmonics, where $n = 1$ represents the fundamental. The quantities A and B were used as parameters to be adjusted for the curve fitting. The center frequency ν_p was set to 15.6 THz for the LO phonon by referring to previous experimental and theoretical studies. (The CPs of the LO mode in a Si crystal have been studied, and the eigen-frequency of the LO mode has been measured to be 15.6 THz [3, 4]. Since TO phonons can also contribute to forming the MCP-NSs, these could also be measured; however, with pump–probe spectroscopy, only phonons with a wavenumber of 0 (the Γ point in wavenumber space) are measured and, since the natural frequencies of the LO phonons and TO phonons at the Γ point are approximately equal [17], it is not possible to distinguish between them.) The full width at half maximum (FWHM), $\Delta\nu$, was fixed at around 10 THz (41 meV) by referring to the average phonon energy (30 meV) and additional scattering by incoherent phonons at room temperature [3, 18].

The result of the fitting is represented by the blue broken curve in Fig. 6, where the red solid curve is a copy of the curve in the inset of Fig. 5. The green broken curves represent the Lorentzian spectral curves of the fundamentals and harmonics of the LO phonon whose superposition yields the blue broken curve. As a result of this accurate fitting of the blue broken curve to the red curve, the spectral peak at 64 THz in the inset of Fig. 5 was found to be composed of the fourth-order harmonics of the LO phonon. The spectral peak at 18 THz is composed of the fundamentals of the LO phonon. The second- and third-order harmonics of the LO phonon contribute to the lower signal. Since the spectral intensity of the 64 THz peak was the largest, it was found that the fourth-order harmonics of the LO phonon couple most strongly with the pump-beam photons. The reason for this strong coupling is not yet fully understood and is still under investigation. Furthermore, it was confirmed that these fourth-order harmonics are the origin of the sidebands in the emission spectrum in Fig. 2.

By curve fitting to the measured spectra of a Si crystal, in which tiny sources for generating DPPs were efficiently formed as a result of doping with a high concentration of B,

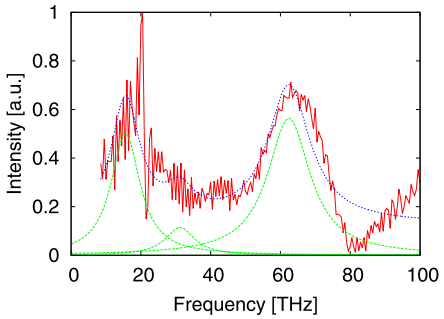

Fig. 6 Results of curve fitting. *Red solid curve*: experimental curve in the inset of Fig. 5. *Blue broken curve*: superposition of Lorentzian curves fitted to the *red solid curve*. *Green broken curves*: Lorentzian curves of the fundamental and harmonics of the LO phonons, which are constituent components of the fitted *blue broken curve*

we were able to successfully measure the LO phonon, whose fundamental and harmonics were the constituent elements of the MCP-NSs.

4 Summary

By fabricating a novel visible Si LED using DPP-assisted Joule annealing, the sidebands originating from the multimode coherent phonons in nanometric spaces were observed in the emitted spectrum. By using pump–probe spectroscopy, higher-order harmonics of the LO phonon were observed for the first time, and those were revealed to be the constituent components of the multimode coherent phonons generated in the nanometric spaces around the domain boundaries of B in the homojunction-structured Si LED. Furthermore, it was confirmed that the fourth-order harmonics of the LO phonon are the origin of the sidebands observed in the emission spectrum of the Si LED.

References

1. D. Bermejo, M. Cardona, J. Non-Cryst. Solids **32**, 405 (1979)
2. T. Prokofyeva, M. Seon, J. Vanbuskirk, M. Holtz, S.A. Nikishin, N.N. Faleev, H. Temkin, S. Zollner, Phys. Rev. B **63**, 125313 (2001)
3. D.M. Riffe, A.J. Sabbah, Phys. Rev. B **76**, 085207 (2007)
4. M. Hase, M. Katsuragawa, A.M. Constantinescu, H. Petek, Nat. Photonics **6**, 243 (2012)
5. A.V. Kuznetsov, C.J. Stanton, Phys. Rev. Lett. **73**, 3243 (1994)
6. Y. Tanaka, K. Kobayashi, J. Microsc. **229**, 228 (2008)
7. T. Kawazoe, M.A. Mueed, M. Ohtsu, Appl. Phys. B **104**, 747 (2011)
8. A.M. Tran, M. Yamaguchi, T. Kawazoe, M. Ohtsu, Silicon blue light emitting diode, in *Int. Congr. Optics & Photonics*, Tokyo, Japan, October 2012
9. T. Kawazoe, M. Ohtsu, K. Akahane, N. Yamamoto, Appl. Phys. B **107**, 659 (2012)
10. N. Wada, T. Kawazoe, M. Ohtsu, Appl. Phys. B **108**, 25 (2012)
11. H. Tanaka, T. Kawazoe, M. Ohtsu, Appl. Phys. B **108**, 51 (2012)

12. K. Kitamura, T. Kawazoe, M. Ohtsu, Appl. Phys. B **107**, 293 (2012)
13. J. Bonse, S. Baudach, J. Krüger, W. Kautek, M. Lenzner, Appl. Phys. A **74**, 19 (2002)
14. H.O. Jeschke, M.E. Garcia, M. Lenzner, J. Bonse, J. Krüger, W. Kautek, Appl. Surf. Sci. **197–198**, 839 (2002)
15. Y.-X. Yan, E.B. Gamble Jr., K.A. Nelson, J. Chem. Phys. **83**, 5391 (1985)
16. S.I. Kudryashov, M. Kandyla, C.A.D. Roeser, E. Mazur, Phys. Rev. B **75**, 085207 (2007)
17. T. Soma, Phys. Status Solidi B **99**, 701 (1980)
18. T.R. Hart, R.L. Aggarwal, B. Lax, Phys. Rev. B **1**, 638 (1970)

Appl Phys A (2014) 115:105–111
DOI 10.1007/s00339-013-7907-9

Applied Physics A
Materials Science & Processing

INVITED PAPER

Fabrication of a bulk silicon p–n homojunction-structured light-emitting diode showing visible electroluminescence at room temperature

Minh Anh Tran · Tadashi Kawazoe · Motoichi Ohtsu

Received: 31 July 2013 / Accepted: 1 August 2013 / Published online: 14 August 2013

Abstract We have developed a novel dressed-photon-assisted annealing process, in which the distribution of dopant (boron) domains is modified in a self-organized manner based on the absorption of light having a photon energy higher than the band gap and subsequent stimulated emission. Using this process, we were able to fabricate a bulk silicon p–n homojunction-structured light-emitting diode that showed electroluminescence emission in the visible region at room temperature. A broadband spectrum with three emission peaks at 400 nm, 590 nm, and 620 nm was clearly observed.

1 Introduction

The possibility of achieving light emission from silicon (Si) has been receiving much attention for many years because of the numerous advantages of Si. One major advantage is the ability to produce high-quality Si from silica, the second most abundant material in the surface of the Earth, using a well-developed conventional electric arc furnace process without any toxic emissions [1]. Thus, Si light-emitting diodes (LEDs) have a greater ease of processing and lower cost and will be more environmentally friendly than conventional LEDs made from exotic and often toxic chemical compounds, e.g., InGaAsP. However, because Si is an indirect band gap material, electrons and holes cannot recombine easily due to the momentum conservation law; this results in an extremely low efficiency of spontaneous emission in silicon [2]. Despite the many efforts, over decades, that researchers have been making to achieve light emission from Si, there still remains a significant demand for an efficient solution that can address the so-called "indirect band gap dilemma" [3].

One promising method for achieving light emission from Si is to generate dressed photons (DPs) by forming a suitable dopant density distribution inside a Si crystal [4]. A DP is a quasi-particle representing the coupled state of a photon and an electron–hole pair. It has been found that the DP excites a multi-mode coherent phonon, forming a quasi-particle representing the coupled state of a DP and a multi-mode coherent phonon, called a dressed-photon–phonon (DPP) [5]. A DPP can efficiently provide the necessary momentum for the radiative recombination of the electron–hole pair. In recent research by the authors, we succeeded in fabricating such a structure in Si by employing a technique known as DP-assisted annealing, which allowed us to realize a high-efficiency p–n homojunction-structured LED using a bulk Si crystal [4]. This annealing process has also been applied not only to a Si infrared LED but also to a Si infrared laser [6], a Si photodetector [7], a Si optical and electrical relaxation oscillator [8], and a ZnO LED [9]. However, the light emitted from the devices fabricated using this annealing principle resulted from a two-step transition of an electron in the conduction band to the valence band; hence, the photon energy of the light cannot exceed the band gap energy of the material. For example, the Si LED fabricated by using this annealing method could only emit light in the infrared region (0.75–0.95 eV) [4], which is lower than the Si band gap energy ($E_g = 1.12$ eV).

The purpose of this study was to develop a new annealing technique that can transcend the above limitation. We describe the principle of a new DP-assisted annealing method that enables the emission of light with a photon energy higher than the band gap energy. Instead of using

M.A. Tran · T. Kawazoe (✉) · M. Ohtsu
Graduate School of Engineering, The University of Tokyo,
2-11-16 Yayoi, Bunkyo-ku, Tokyo 113-8656, Japan
e-mail: kawazoe@ee.t.u-tokyo.ac.jp

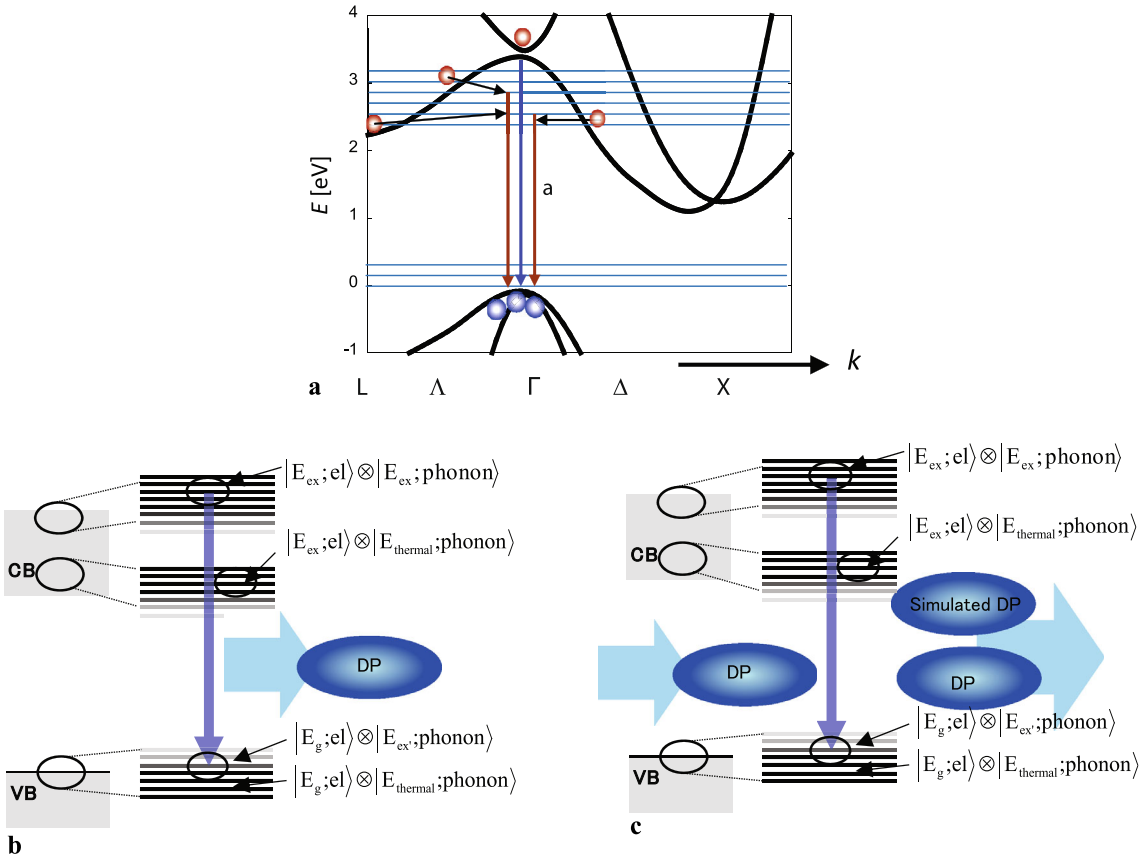

Fig. 1 (**a**) Schematic diagram of the radiative relaxation of an electron from a high-energy excited state via a DPP-assisted process. *Blue horizontal blue lines* represent the phonon-coupled electronic states. (**b**), (**c**) DPP models for energy transitions via DPP-assisted process in radiative relaxation of high-excited state electron from high energy level. The *vertical arrows* represent the relaxation process of electron. (**b**) shows the spontaneous emission process when a DP is emitted. (**c**) shows the stimulated emission process when a DP stimulates the emission of one more identical DP

a two-step transition as in the previous research, the photon is emitted in a relaxation transition of the electron from its excited high-energy state; hence, the photon energy of the emitted light can be higher than the band gap energy of the material. By applying this new DP-assisted annealing technique, we successfully fabricated a Si bulk p–n homojunction-structured LED that emitted light in the visible region (whose photon energy is two times higher than the band gap energy of Si) at room temperature. The principle of light emission, the annealing technique, the fabrication process, and characteristics of the Si visible LED are described in detail.

2 Principle of light emission with photon energy higher than band gap

In this section, we explain the operating principle of our Si visible LED. The fabrication will be described later because the operating principle will also be used in the fabrication process. As was pointed out in the previous section, a DPP can provide a certain momentum for the recombination of an electron and hole because the phonon in the DPP is a multimode phonon. This characteristic was used in our previous research to accomplish infrared light emission from a bulk Si crystal [4, 6, 8]. Although the lowest point of the conduction band (X-point) and the highest point of the valence band (Γ-point) correspond to different momenta, an electron in the conduction band efficiently relaxes to the ground state and emits a photon thanks to the assistance of the phonon in the DPP. Furthermore, radiative transition from a high-energy excited electron can also easily occur via the DPP (Fig. 1(a)). For example, due to the existence of the DPP at a high energy (e.g., level *a* in Fig. 1(a)), an excited-state electron nearby can quickly couple with the coherent phonon and then directly relax to the ground state; thus, a radiative relaxation shown by the red arrow occurs and results in emission with a photon energy higher than the band gap energy. Recall that, without the DP, an electron in an excited state at high energy quickly transitions to the lowest point in the conduction band due to fast intra-band relaxation; there-

fore, the probability of a transition from a high-energy excited state is extremely low in conventional methods.

In the DPP model shown in Fig. 1(b) and (c), since the electron–hole pair strongly couples with the photon and phonon, the energy state is expressed as the direct product of the ket vectors of the electronic state and the phonon state. For example, $|E_g; el\rangle \otimes |E_{thermal}; phonon\rangle$ includes the ground state of the electron and the thermal equilibrium state of the phonon. The spontaneous emission of a DP (Fig. 1(b)) is the result of the radiative transition from the initial state $|E_{ex}; el\rangle \otimes |E_{ex}; phonon\rangle$ to the ground state $|E_g; el\rangle \otimes |E_{ex'}; phonon\rangle$. After the transition, the phonon excited state relaxes to the thermal equilibrium state determined by the crystal lattice temperature and ends with a transition to the electronic ground state $|E_g; el\rangle \otimes |E_{thermal}; phonon\rangle$. In addition, the stimulated emission process (Fig. 1(c)) is explained as follows. When an electron in the conduction band is irradiated with a DP, the electron transitions from the initial state $|E_{ex}; el\rangle \otimes |E_{ex}; phonon\rangle$ to the ground state $|E_g; el\rangle \otimes |E_{ex'}; phonon\rangle$, and emits light. When the electron number densities of occupation in the initial state $|E_{ex}; el\rangle \otimes |E_{ex}; phonon\rangle$ and the intermediate state $|E_g; el\rangle \otimes |E_{ex'}; phonon\rangle$, denoted by n_{ex} and n_g, satisfy the Bernard–Duraffourg inversion condition ($n_{ex} > n_g$) [10], the number of photons created by stimulated emission exceeds the number of photons annihilated by absorption. Like spontaneous emission, the phonon then relaxes to a thermal equilibrium state determined by the crystal lattice temperature, and ends with a transition to the electronic ground state $|E_g; el\rangle \otimes |E_{thermal}; phonon\rangle$.

In order to realize a Si p–n homojunction-structured LED that emits light in the visible region, the two emission processes described above were used two times. The first was for fabrication of the device, more specifically, for the self-organization of the spatial distribution of the dopant suitable for the emission of high-energy photons. The second was for the operation of the device, to obtain spontaneously emitted light with a photon energy higher than the band gap energy. These are described in the following sections.

3 Dressed-photon-assisted annealing process

In order to form a suitable nanostructure for generating DPPs to assist the radiative transition of electrons from a high energy level, we used a DP-assisted annealing technique. As a preparation before annealing, a dopant (boron: B) is implanted into a low-electrical-resistivity n-type wafer, forming a p-layer with an inhomogeneous dopant distribution. Then, the annealing process is carried out by applying a forward bias voltage to the crystal while irradiating it with a laser beam from the p-layer side. The laser light has a photon energy E_{anneal} which is higher than the band gap energy E_g ($E_{anneal} > E_g$), and the forward bias voltage is set to be higher than E_{anneal}/e, where e represents the electron charge. During this annealing process, the dopant distribution at the p–n junction is continuously modified in a self-organized manner until reaching the desirable shape via the following mechanisms.

(1) At dopant domains where DPPs are hardly generated: The incoming photon excites an electron from the ground state in the valence band to an excited state in the conduction band. The non-absorbed excess energy, $E_{anneal} - E_g$, is quickly converted to thermal energy via fast intra-band relaxation of electrons. Moreover, because of the indirect band gap, the electron will relax to the ground state via a non-radiative process, and the energy of the electron is converted to thermal energy. Thus, as a whole, the optical energy of the laser beam is converted to the heat in crystal. It is this heat that causes the dopant to diffuse; as a result, the spatial distribution of the dopant domains changes.
(2) At the dopant domains where DPPs are easily generated: Since electrons having energy higher than E_{anneal} are injected sufficiently by the forward bias current to satisfy the Bernard–Duraffourg inversion condition, stimulated emission via the DPPs is triggered. Due to this stimulated emission, the energy of the laser beam is converted to optical energy, instead of heat, as in the domains where DPPs are not generated. Thus, it becomes more difficult to bring about heat-induced changes in the dopant distribution.

At the domains where stimulated emission via DPPs strongly occurs, the shape and dimension of the inhomogeneous dopant distribution become stable, whereas at the other domains where the conditions are unsuitable for DPP generation, the dopant distribution keeps changing due to the annealing heat. Furthermore, since the probability of spontaneous emission is proportional to that of stimulated emission, spontaneous emission via DPPs also tends to occur in regions where stimulated emission tends to occur. Therefore, as the annealing advances, together with temporal evolution of the dopant distribution, the stimulated emitted light spreads through the whole device. After a sufficient DP assisted annealing, all of the dopant domains reach a stable profile, in which the probability of stimulated emission via DPPs becomes significantly high. It can be expected that the spatial distribution of the dopant formed after this annealing process will be optimized for the spontaneous emission of light having high photon energy.

4 Device fabrication

The fabrication of the device can be divided into two steps. The first step is to prepare a Si p–n homojunction structure

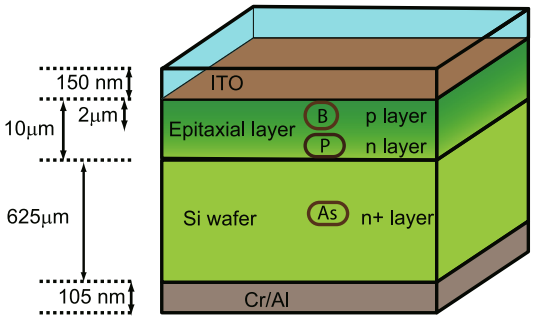

Fig. 2 Structure of Si LED with a p–n homojunction

having a modifiable dopant distribution. The second step is to modify the shape of the dopant domains through the DP-assisted annealing process described above.

In the first step, we used an As-doped n-type Si single crystal on which we deposited an epitaxial layer of phosphorus (P). This Si crystal was doped with boron (B) by an ion implantation method, with seven different levels of accelerating energy of 30, 70, 130, 215, 330, 480, and 700 keV, to form dopant domains with a dose density of 10^{19} cm^{-3}. A p-type region was successfully formed in Si, and as a result, a p–n homojunction structure was constructed. Furthermore, with such a high energy and high-concentration B-doping profile, the distribution of B at the p–n junction was spatially inhomogeneous; this was to increase the probability of producing a dopant distribution favorable for generating DPs. The crystal was then diced into a 5 mm × 5 mm area. A 150 nm-thick indium tin oxide (ITO) film was deposited on the surface of the p-type layer, whereas a 5 nm-thick Cr film and a 100 nm-thick Al film were deposited on the back surface of the n-type Si to serve as electrodes, by using RF sputtering. The layer structure of the device is shown in Fig. 2.

In the second step, the DP-assisted annealing was performed by causing a forward bias current to flow through the device while irradiating the p-type side of the device with a laser beam. The experimental setup is illustrated in Fig. 3. To connect the electric power supply to the device, Dotite paste was used to attach a Cu film on the p-type surface. Another Cu film was also attached to the n-type side of the device. The forward bias current density used for the annealing was 1.44 A/cm^2, and the optical power of the laser beam irradiation was 75 mW. At the surface of the device, the laser beam radius was 1.5 mm, and so the irradiation light density was approximately 3.33 W/cm^2, which is high enough for inducing the DP-assisted annealing. The wavelength of the laser light was 400 nm; in other words, the photon energy was 3.1 eV, which is 2.5 times higher than the band gap energy of Si. After one hour of annealing, the fabrication of our Si homojunction-structured LED was completed.

To confirm the stimulated emission, Fig. 4 shows the results of measuring the change in surface temperature difference between the irradiated area and the non-irradiated area. The Si crystal was continuously irradiated with light, and current injection was started after 7 minutes. At the beginning, when only the laser beam was radiated, the temperature difference dramatically increased due to the heat generated by light absorption. After a few minutes, the heat gradually diffused into the whole device, and the temperature difference reached a stable state. This agreed with our hypothesis of how the annealing process advances with laser irradiation, which was described in (1) and (2) in the previous section. Next, after 7 minutes, a forward bias voltage was applied to the device, while continuing to radiate the laser beam. This led to an obvious decrease in the temperature difference. This decrease was a result of stimulated emission in the area where DPs were generated: The irradiation light was not converted into heat, but induced light emission due to the stimulated emission process. In other words, the decrease in temperature difference when an electrical bias was applied has confirmed the occurrence of stimulated emission of DPPs.

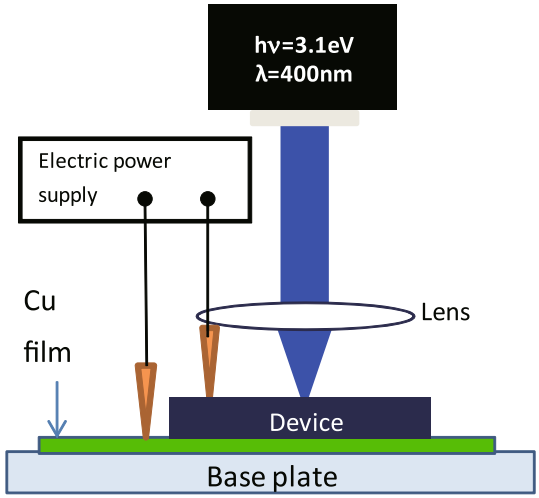

Fig. 3 Experimental setup for dressed-photon-assisted annealing process

5 Device characterization

In this section, we present the electroluminescence (EL) characteristics and electrical characteristics of the fabricated device. We also discuss the physical mechanism of the device operation.

5.1 Electroluminescence spectrum at room temperature

Figure 5 shows photographs of the external appearance of the non-biased and forward-biased (voltage 7 V, current density 2 A/cm^2) device taken with a band-filtered visible CCD

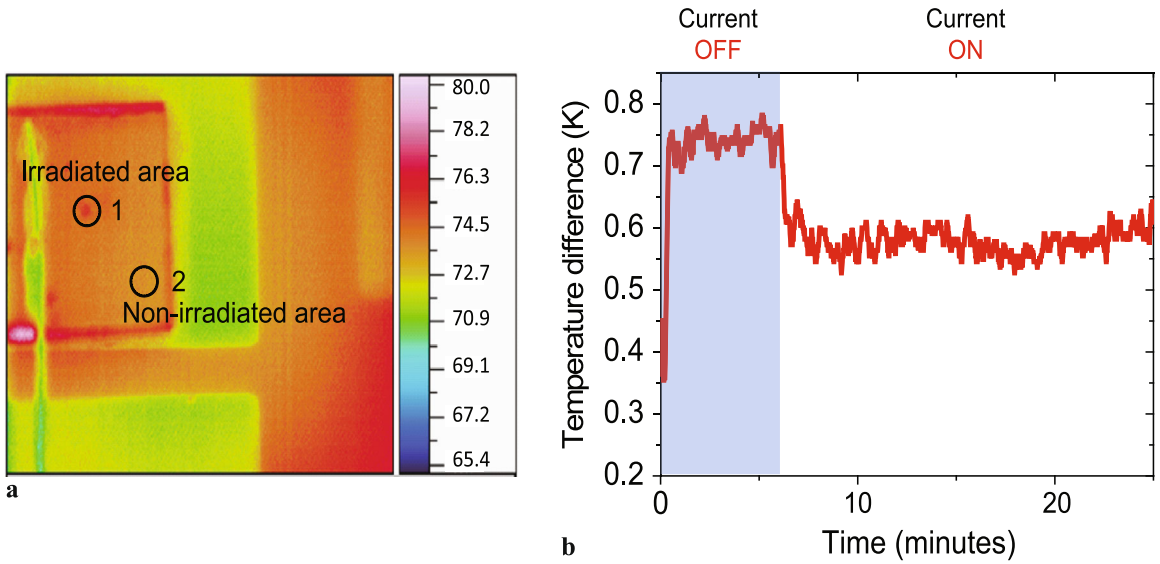

Fig. 4 Surface temperature variation due to DPP stimulated emission. (**a**) Thermography image of the device surface temperature. (**b**) The vertical axis shows the temperature difference between an area irradiated by the laser beam (*area 1*) and a non-irradiated area (*area 2*). The device was continuously irradiated with laser, while current was injected only after seventh minute

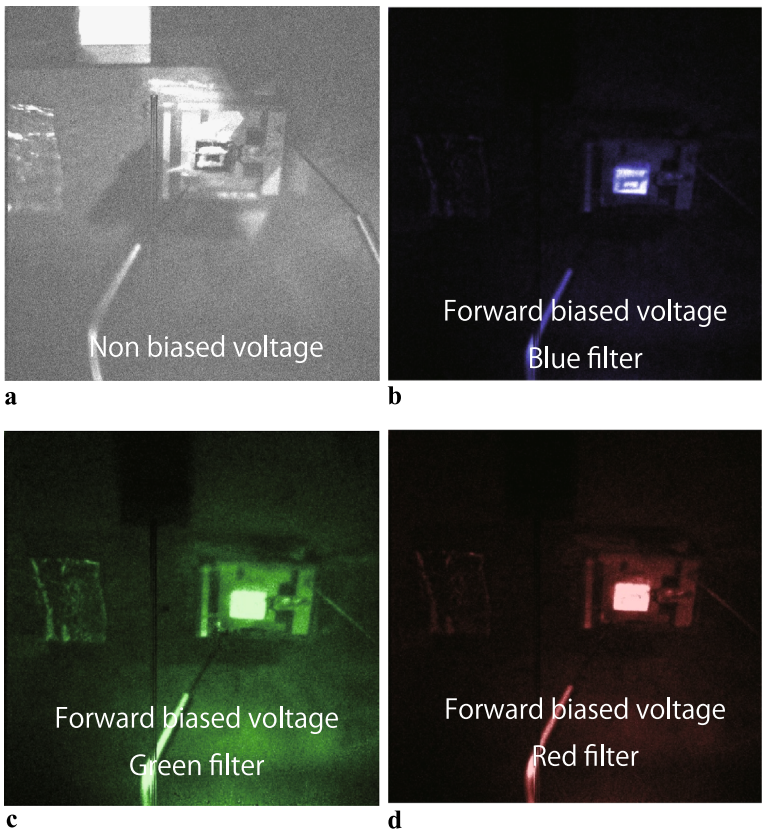

Fig. 5 Photographs of device emitting light at room temperature, captured with a CCD camera. (**a**) No forward-bias voltage. (**b**), (**c**), (**d**) A forward-bias voltage of 4.5 V was applied. Blue, green, and red band pass filters (center wavelengths of 450 nm, 550 nm, and 650 nm, respectively) were used

camera at room temperature. Figure 5(b)–(d) clearly reveal that the light emission spectrum from our Si LED contained all three primary colors: blue, green, and red. This confirms that the fabricated Si LED showed EL emission in the visible region when a forward-bias voltage was applied.

We studied the EL spectrum of the Si LED when a forward-bias voltage was applied. The curves in Fig. 6 are visible-region EL spectra of our device at room temperature before and after the DP-assisted annealing process. As we can see, no EL emission was observed before the anneal-

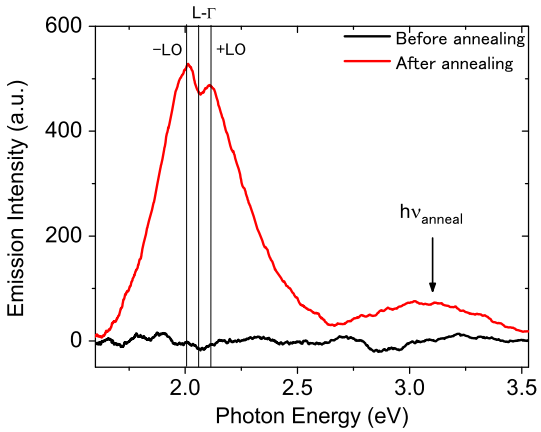

Fig. 6 EL spectra of the Si LED. *Black* and *red curves* show emission before and after the dressed-photon-assisted annealing, respectively. The *vertical lines* (shown as −LO, L-Γ and +LO) represent specific values of $E_{L-\Gamma} - E_{1\ \mathrm{LO\ phonon}}$, $E_{L-\Gamma}$, and $E_{L-\Gamma} + E_{1\ \mathrm{LO\ phonon}}$ respectively

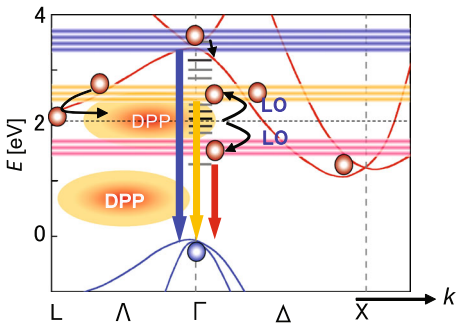

Fig. 7 Schematic diagram of light emission in visible region from Si. *Red* and *blue curves* represent the energy levels of the conduction and valence bands. *Blue*, *orange*, and *gray thick horizontal lines* represent the phonon levels corresponding to 3.1 eV, 2.1 eV, and 2.0 eV, respectively. Via phonon levels, electrons in high-energy excited states at the Γ-point and L-point of the conduction band can radiatively relax to the ground state with a high probability. Interactions with longitudinal optical phonons (LO) result in two split energy levels from which excited electrons at the L-point of the conduction band transition to the ground state

ing. After the annealing, a broad EL spectrum appeared. Noticeably, there exist three dominant peaks in the EL spectra: the first one at 3.1 eV (wavelength 400 nm), which corresponds to blue, and the other two close peaks at photon energies 2.0 eV (wavelength 620 nm) and 2.1 eV (wavelength 590 nm), which correspond to red and green.

The above EL emission characteristics of our Si LED agree with the light emission principle we proposed in Sect. 2 and will be explained in detail here. Figure 7 shows the band structure of Si (red and blue curves) and the phonon-coupled electronic levels (in particular, the blue, orange, and gray thick horizontal lines represent phonon levels involved in the light emission in the visible region). Since a DP strongly couples with phonons, a transition between the phonon-coupled electronic levels appears if the probability of a DP that is resonant with the transition energy is high. After the annealing process, almost all the B domains in Si become suitable for generating DPs whose photon energy corresponds to the light radiated during annealing. Because the photon energy of the annealing light was 3.1 eV ($\lambda = 400$ nm), high-energy excited electrons at the Γ-point of the conduction band likely relaxed to the ground state via those 3.1 eV photon levels, resulting in the spectral peak at 3.1 eV in the EL spectrum. Moreover, the injected electrons also tend to relax to the lower energy level via intra-band relaxation, i.e., the L- and X-points in the conduction band. Therefore, the density of electrons at those points in the conduction band is considerably high. Because the emission intensity is also proportional to the number of electrons, the radiative transition of electrons from the L-point results in light emission in the proximity of 2.0 eV.

The broad spectrum of the observed EL emission resulted from the interaction of electrons with phonons. Since the probability of phonon interaction is inversely proportional to the number of phonons involved (phonon absorption or emission), the EL spectrum is symmetric with respect to the peak emission values at energies of 2.0 eV, 2.1 eV, and 3.1 eV. Furthermore, the existence of the two peaks in Fig. 6 with photon energies close to the energy level of the L-point indicates the interaction with one longitudinal optical (LO) phonon in the light emission process. The radiative relaxation process of electrons from the L-point to the ground state is also illustrated in Fig. 7. Since there is a large difference in momentum between an electron at the L-point of the conduction band and a hole at the Γ-point of the valence band, according to the momentum conservation law, in order to emit a photon, the electron at the L-point needs to interact with a phonon to lose the excess momentum (or to gain momentum in the case of insufficient momentum). As a result, photons are emitted from two separated energy levels. This explains the existence of two peaks in the vicinity of the L-point, at 2.0 eV and 2.1 eV, as we observed in the EL spectrum in Fig. 6. The energy difference between the two peaks is 100 meV, approximately equivalent to twice the LO phonon energy [11]. The dip between the two peaks corresponds to the zero-phonon line. On the other hand, no similar peaks appear in the spectrum at 3.1 eV. This is because the electrons with an energy of 3.1 eV nearly directly relaxed to the valence band, and thus, the interactions with phonons were weaker.

5.2 Voltage dependence of EL emission intensity

As discussed above, the visible EL emission resulted from the high-energy excited electrons, which are provided by the electrical power source when operating the device as an LED. Therefore, it is necessary to study the dependence of

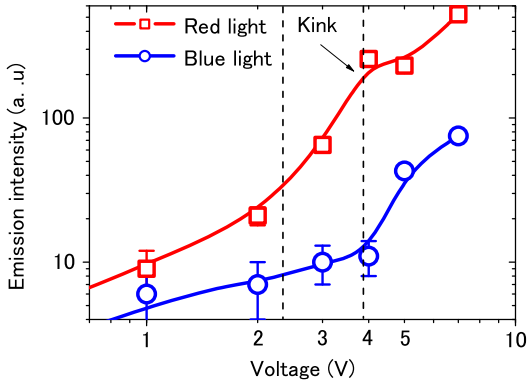

Fig. 8 Relation between the forward-bias voltage and the light emission intensity. *Blue* and *red curves* represent the heights of the peaks in the EL spectrum at 3.1 eV and 2.0 eV in Fig. 6

EL emission performance of the LED on the forward bias voltage. We investigated the dependence of the height of the peak at 3.1 eV (blue light) and the peak at 2.0 eV (red light) in Fig. 6 on the applied voltage. The results are represented by the blue and red curves in Fig. 8. The peak at 2.1 eV (green light) showed behavior similar to the peak at 2.0 eV and is therefore omitted here.

Figure 8 shows that, at a voltage of 2.5 V, the red curve started rising with a higher slope. This corresponds to the threshold for red light emission. Furthermore, at a voltage of about 4 V, the blue curve changed its slope. This kink corresponds to the start of blue light emission. Interestingly, a kink in the red curve is also observed at the kink in the blue curve. This characteristic relation between emission intensity and voltage is well explained by the emission mechanism we discussed above. Assume that the voltage loss due to the Schottky barrier and parasitic circuit resistance is about 1 V. Therefore, when a voltage of 3 V is applied, the highest energy of injected electrons is about 2 eV. Thus, the number density of electrons that have relaxed to the L-point in the conduction band (energy level of about 2 eV) starts rising; therefore, the emission with photon energies of 2.0 and 2.1 eV appears. This transition corresponds to the change in slope of the red curve in Fig. 8. When a sufficiently high forward bias is applied, the energy of injected electrons becomes larger than 3.1 eV, and the density of electrons at the Γ-point increases, resulting in the appearance of emission from a transition with a photon energy corresponding to blue light. This threshold voltage corresponds to the kink in the slope of the blue curve. Here, the appearance of a kink in the red curve is evidence for the fact that some of the injected electrons recombine for the blue light emission, and so the density of electrons that have relaxed to the L-point becomes relatively lower and results in the decreased emission intensity of the red light.

6 Summary

We succeeded in fabricating a light-emitting diode having a p–n homojunction structure by applying a novel dressed-photon-assisted annealing process to an n-type P epitaxial layer on an n-type Si crystal doped with As. The p-type layer was formed by doping B. The device showed a broad EL spectrum in the visible region at room temperature when a forward bias voltage was applied. The emission peak wavelengths of the fabricated device were 400 nm, 590 nm, and 620 nm (photon energies of 3.1 eV, 2.1 eV, and 2.0 eV, respectively). The EL emission and voltage dependence characteristics of the device confirmed that the probability of a radiative relaxation process of electrons from a high-energy excited state was significantly increased due to the assistance of DPPs generated in the Si crystal. This is the world's first demonstration of a bulk Si p–n homojunction-structured LED that shows EL emission in the visible region.

References

1. A. Schei, J.Kr. Tuset, H. Tveit, *Production of High Silicon Alloys* (Tapir Forlag, Trondheim, 1997)
2. D. Liang, J.E. Bowers, Nat. Photonics **4**, 511 (2010)
3. European Commission, *Technology Roadmap: Optoelectronics Interconnects for Integrated Circuits* (Office for Official Publications of the European Communities, Luxembourg, 1998)
4. T. Kawazoe, M. Mueed, M. Ohtsu, Appl. Phys. B **104**, 747 (2011)
5. Y. Tanaka, K. Kobayashi, J. Microsc. **229**, 228 (2008)
6. T. Kawazoe, M. Ohtsu, K. Akahane, N. Yamamoto, Appl. Phys. B **107**, 659 (2012)
7. H. Tanaka, T. Kawazoe, M. Ohtsu, Appl. Phys. B **108**, 51 (2012)
8. N. Wada, T. Kawazoe, M. Ohtsu, Appl. Phys. B **108**, 25 (2012)
9. K. Kitamura, T. Kawazoe, M. Ohtsu, Appl. Phys. B **107**, 637 (2012)
10. M.G.A. Bernald, G. Duraffourg, Phys. Status Solidi **1**, 699 (1961)
11. W. Goldammer, W. Ludwig, W. Zierau, Phys. Rev. B **36**, 4624 (1987)

Appl Phys A (2014) 115:1–4
DOI 10.1007/s00339-013-7905-y

Applied Physics A
Materials Science & Processing

INVITED PAPER

Emission from a dipole-forbidden energy state in a GaAs quantum-ring induced by dressed photon

T. Yatsui · W. Nomura · T. Mano · H.T. Miyazaki · K. Sakoda · T. Kawazoe · M. Ohtsu

Received: 31 July 2013 / Accepted: 1 August 2013 / Published online: 13 August 2013

Abstract The emission intensity from the dipole-forbidden state in a GaAs quantum-ring was increased via close proximity with an aperture fiber probe to induce a near-field interaction between the probe apex and the quantum-ring. As a result, a significant decrease was observed in the decay time of the emission from a dipole-forbidden energy state.

To reduce the size of photonic devices below the diffraction limit, we have previously proposed nanoscale photonic devices (i.e., nanophotonic devices) [1] that consist of semiconductor quantum structures, including quantum cubes [2], quantum dots [3], and quantum wells [4]. In a nanophotonic device, specifically, the dipole-forbidden energy transition can be exploited to reduce the device size beyond the diffraction limit of light and achieve unidirectional energy transfer, which is unattainable in conventional photonic devices [5]. This transition originates from the near-field interaction by exchanging virtual photons between resonant energy states. This virtual photon, also referred to as a dressed photon [6], is distinguished from the free photon because it carries a material excitation energy. The use of dressed photon activates dipole-forbidden energy states. In nanophotonic devices, the energy transfer occurs more efficiently in comparison with conventional photonic devices, in which energy transfer occurs via emission and absorption from one quantum structure to another.

T. Yatsui (✉) · W. Nomura · T. Kawazoe · M. Ohtsu
School of Engineering, University of Tokyo, 2-11-16 Yayoi, Bunkyo-ku, Tokyo 113-8656, Japan
e-mail: yatsui@ee.t.u-tokyo.ac.jp

T. Mano · H.T. Miyazaki · K. Sakoda
National Institute for Materials Science, 1-2-1 Sengen, Tsukuba, Ibaraki 305-0047, Japan

Among various quantum structures investigated for nanophotonic device, the quantum-ring structure [7] shows a unique property in a comparison with the quantum cubes, quantum spheres, and quantum wells, in that the lowest energy level of the quantum-ring is a dipole-forbidden energy state. Unlike in a quantum cube structure (Fig. 1(a)), in a quantum-ring structure (Fig. 1(b)), the magnitude of the exciton wave-function should take a value of zero at the center of the structure, because the quantum-ring structure has a barrier layer at the center. Thus, the mode of $|x, y, z\rangle = |1, 1, 1\rangle$, which corresponds to the (1, 1, 1) mode in a quantum cube, cannot be excited. In turn, the cross-sectional profile of the exciton wave-function of the lowest mode ($|x, y, z\rangle = |2, 1, 1\rangle$, corresponding to the (2, 1, 1) mode in a quantum cube) should take a value of zero, as indicated by the solid sine curve in Fig. 1(b). Because the lowest mode is a dipole-forbidden energy state, the quantum-ring structure can be utilized as optical buffer memory. Such a system can be observed in the light-harvesting antenna complex of photosynthetic purple bacteria, in which the lowest ring of bacteriochlorophyll molecules, called B850, is a dipole-forbidden energy state [8]. As a result, the light-harvesting antenna acts as a highly efficient optical buffer system.

Although an emission from the dipole-forbidden energy state cannot be detected in the far field (FF), it can be utilized when the nanostructure and detector are in close proximity [9]. In this study, we report the direct observation of emission from a dipole-forbidden energy state in a GaAs quantum-ring using the near-field (NF) interaction induced by a fiber probe.

The GaAs quantum-ring structure was fabricated using the droplet epitaxy technique [7]. To form the ring structure, a 100-nm-thick AlGaAs buffer layer was grown on a GaAs buffer layer. First, 1.8 monolayer (ML) of Ga was deposited

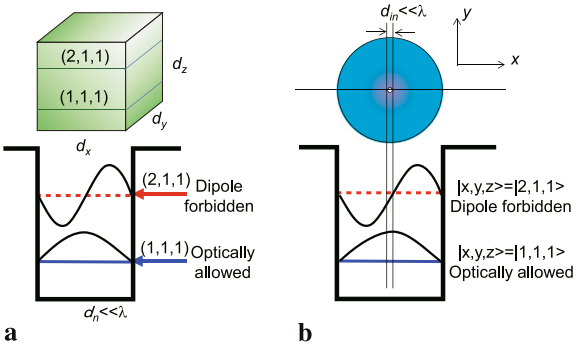

Fig. 1 Schematic diagram of discrete energy state of (**a**) quantum cube and (**b**) quantum ring. d_n $(n = x, y, z)$ represents each side length of the quantum cube. d_{in} represents the inner diameter of the quantum ring

at 250 °C. Second, As was deposited under 1.0×10^{-5} Torr at 200 °C. Then, the substrate was annealed at 350 °C for 10 min. After the emitting GaAs quantum-ring structure was deposited, it was capped with 20-nm-thick AlGaAs, 10-nm-thick GaAs, and 2-ML AlGaAs. Finally, the same GaAs quantum-ring structure was repeated on the top of the substrate to form GaAs quantum-ring. For optical characterization, we performed rapid thermal annealing (RTA) at 800 °C after the growth of the entire structure. During capping and RTA, the structure of the GaAs quantum-ring remained the same because it was deposited using droplet epitaxy so as to maintain the shapes of the GaAs quantum-ring structure despite inter-diffusion among GaAs quantum-ring structure [10]. As shown in Figs. 2(a), an emitting GaAs quantum-ring is located below the 10-nm-thick GaAs cap layer, and the top GaAs quantum-ring layer is inactive to confirm the shape of quantum-ring structure (Fig. 2(b)). From an atomic force microscopic (AFM) image (Fig. 2(b)) and cross-sectional profile (Fig. 2(c)), the diameter and height of the quantum-ring was found to be in the range of 30–50 nm and 23 nm, respectively. The quantum-ring structures were slightly elongated along the [1-10] orientation.

We evaluated the optical properties using propagating FF light. Figure 3(a) shows the FF photoluminescence (PL) spectrum with 400-nm light (repetition rate; 80 MHz, pulse width; 25 ps) excitation obtained at 7 K. A single spectral peak corresponding to the GaAs quantum-ring was observed at wavelength of 725 nm, in which no difference between *p*- (parallel along the crystal orientation [1-10]) and *s*- (parallel along the crystal orientation [110]) polarized light was observed. The time-resolved PL intensity profile (Fig. 3(b)) revealed the decay time to be 580 ps.

Based on the above results, we performed low-temperature (15 K) NF PL spectroscopy using an aperture fiber probe (aperture diameter; 300 nm) [9]. Figure 4(a) shows a comparison of the PL spectra in the FF (black solid curve

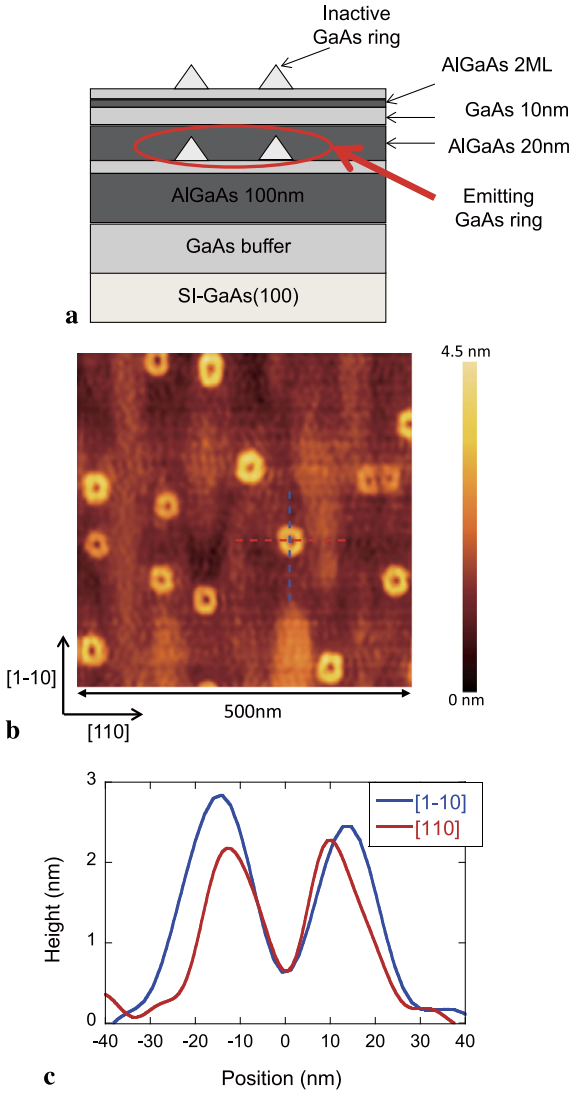

Fig. 2 (**a**) Schematic diagram of GaAs ring structure. (**b**) AFM image of fabricated GaAs ring. (**c**) Cross-sectional image of (**b**)

PL_{FF}, same as Fig. 3(a)) and NF (blue solid curve PL_{NF1} and red solid curve PL_{NF2}). The difference in the peak wavelength between PL_{NF1} and PL_{NF2} caused by the shape difference of the quantum ring. The similarity of PL spectra between far-field and near-field indicated the spectral peak around 725 nm was originated from the lowest energy state, that is, dipole-forbidden energy state. The observation of the emission from dipole-forbidden energy state in the far-field spectrum should be originated from the imperfection of ring shape. Figure 4(b) shows the spatial distribution of the NF PL intensity integrated for a wavelength of 700–740 nm. From this result, the hot spots indicated by the red circles corresponded to the position of the quantum-ring structure.

To evaluate the optical properties of the quantum-ring structure in greater detail, we performed time-resolved PL spectroscopy at 15 K. Figure 5(a) shows the time-resolved PL spectra obtained at a 725-nm wavelength for the ground

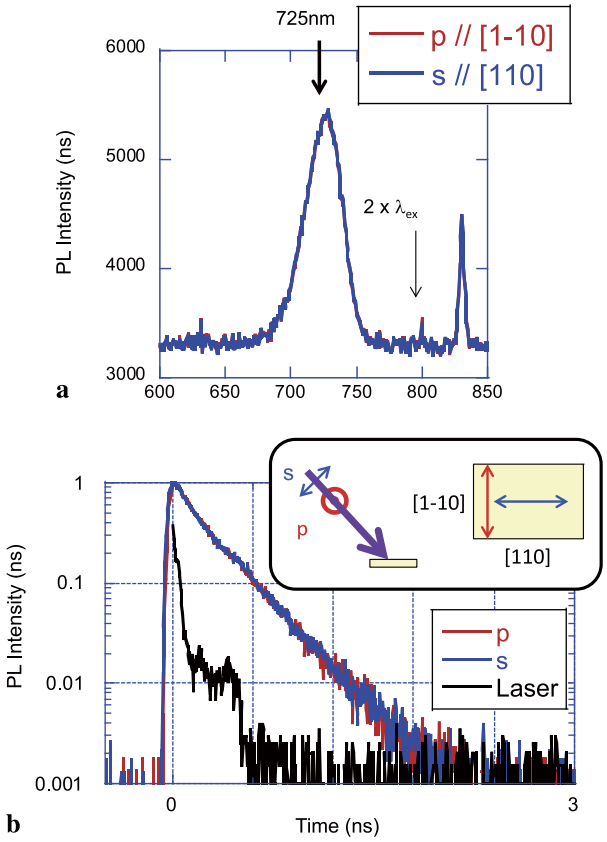

Fig. 3 (**a**) Incident polarization dependence of PL spectra. *p* and *s* represent the incident polarization parallel to [1-10] and [110], respectively (see the *inset* of (**b**)). (**b**) Time-resolved PL intensity

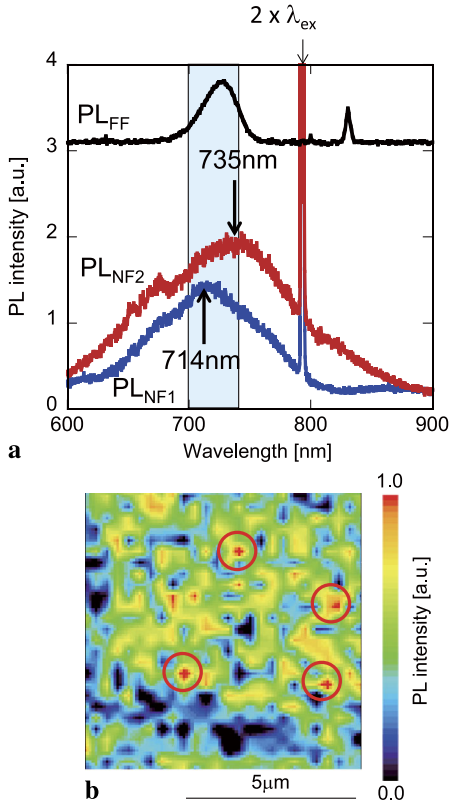

Fig. 4 (**a**) Comparison of PL spectra of FF (*black-solid curve*, PL_{FF}) and NF (*blue-solid curve* PL_{NF1} and red solid curve PL_{NF2}). (**b**) NF PL intensity distribution for 700 nm $< \lambda <$ 740 nm

Table 1 Decay time τ of time-resolved PL spectra shown in Fig. 5(a), those values were determined by fitting curves in Figs. 5(b)–5(d)

	τ (ps)
NF_1 ($d \sim 5$ nm)	305
NF_2 ($d \sim 10$ nm)	305
FF ($d > 1$ μm)	330
FF′	580

state of the GaAs quantum ring; the curves correspond to the spectra obtained with probe-to-sample distances of $d >$ 1 μm (curve FF, solid black line), $d \sim 5$ nm (curve NF_1, solid red line), $d \sim 10$ nm (curve NF_2, solid blue line), and conventional FF (curve FF′, dashed black line). The results indicated that the PL intensity increased drastically as the fiber probe approached the GaAs quantum-ring. We fitted the each spectra in Fig. 5(a) and found that all spectra can be fitted well with single exponential curves (see Figs. 5(b)–5(d)). From those results we obtained the decay time (Table 1). Although the emission peak at 725 nm originated from the dipole-forbidden energy state, the decay time τ decreased to almost half that of the FF spectrum owing to the close proximity of the fiber probe to the quantum ring. These results were attributed to NF interaction between the probe tip and the quantum ring to activate the dipole-forbidden energy state [9]. The time-resolved PL intensity profile was obtained at different positions as taken in Fig. 5(a). The green solid curve (curve NF′) in Fig. 6(a) was taken at a different hot spot from that shown in Fig. 4(b). The decay time of curve NF′ was fitted by single exponential curve and found to be 260 ps (see Fig. 6(b); this was comparable to that of curve NF_1 (305 ps). The difference between NF′ and NF_1 might originate from the different d arising from the surface of the aperture not being flat (see Figs. 6(c) and 6(d)).

In conclusion, we observed a significant increase in the PL intensity and consequent decrease in the decay time of the emission from a dipole-forbidden energy state in a GaAs quantum-ring, by using the NF interaction induced by the close proximity of an apertured fiber probe tip. Because the decay time of the dipole-forbidden energy state is 10^6 times longer than that of the dipole-active state [11], the former can be used to realize novel devices such as optical buffer memory and signal-transmission devices.

Acknowledgements This work was partially supported by a Grant-in-Aid for Young Scientists (A) and Challenging Exploratory Research, Grants-in-Aid for Scientific Research, Japan Society for the Promotion of Science (JSPS) and The New Energy and Industrial Technology Development Organization (NEDO) Project "Develop-

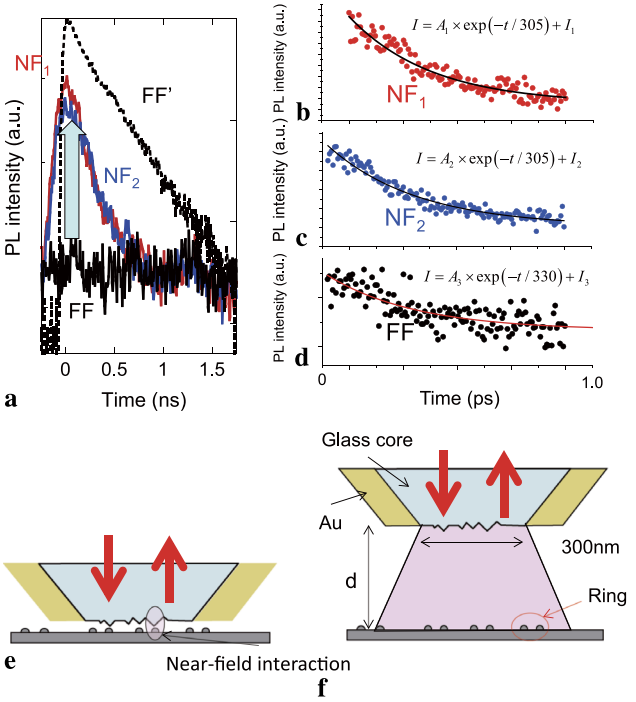

Fig. 5 (**a**) Time-resolved PL intensity profile. NF_1 and NF_2: near-field PL spectra using NF spectroscopy with $d \sim 5$ nm and $d \sim 10$ nm, respectively (corresponding to (**e**)). FF: Far-field spectra using NF spectroscopy with $d > 1$ μm (corresponding to (**f**)). FF′: FF spectra using conventional spectroscopy (same as blue solid curve in Fig. 3(b)). (**b**)–(**d**) *Solid circles* correspond to the curves NF_1, NF_2, and FF, respectively. (**e**) and (**f**) Schematic of probe-to-sample distances dependence

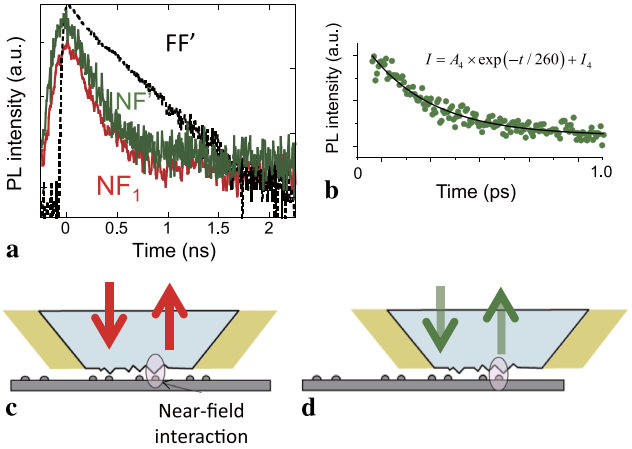

Fig. 6 (**a**) Position dependent time-resolved PL intensity profile. NF_1 and NF′: NF PL spectra using NF spectroscopy with $d \sim 5$ nm taken at different hot spot from that shown in Fig. 4(b). FF′: FF spectra using conventional spectroscopy (same as blue solid curve in Fig. 3(b)). (**b**) *Solid circles* correspond to the curves NF′. (**c**) and (**d**) Schematic of probe position dependence

ment of Next-generation High-performance Technology for Photovoltaic Power Generation System."

References

1. M. Ohtsu, T. Kawazoe, T. Yatsui, M. Naruse, IEEE J. Sel. Top. Quantum Electron. **14**(6), 1404 (2008)
2. T. Kawazoe, K. Kobayashi, M. Ohtsu, Appl. Phys. Lett. **86**(10), 103102 (2005)
3. T. Kawazoe, M. Ohtsu, S. Aso, Y. Sawado, Y. Hosoda, K. Yoshizawa, K. Akahane, N. Yamamoto, M. Naruse, Appl. Phys. B, Lasers Opt. **103**(3), 537 (2011)
4. T. Yatsui, S. Sangu, T. Kawazoe, M. Ohtsu, S.J. An, J. Yoo, G.-C. Yi, Appl. Phys. Lett. **90**(22), 223110 (2007)
5. T. Kawazoe, K. Kobayashi, S. Sangu, M. Ohtsu, Appl. Phys. Lett. **82**(18), 2957 (2003)
6. M. Ohtsu, Nanophotonics **1**(1), 83 (2012)
7. T. Mano, T. Kuroda, S. Sanguinetti, T. Ochiai, T. Tateno, J. Kim, T. Noda, M. Kawabe, K. Sakoda, G. Kido, N. Koguchi, Nano Lett. **5**(3), 425 (2005)
8. K. Mukai, S. Abe, H. Sumi, J. Phys. Chem. B **103**(29), 6096 (1999)
9. T. Yatsui, M. Tsuji, Y. Liu, T. Kawazoe, M. Ohtsu, Appl. Phys. Lett. **100**(22), 223110 (2012)
10. T. Mano, T. Kuroda, K. Mitsuishi, M. Yamagiwa, X.J. Guo, K. Furuya, K. Sakoda, N. Koguchi, J. Cryst. Growth **301**, 740 (2007)
11. C. Garcia, B. Garrido, P. Pellegrino, R. Ferre, J.A. Moreno, J.R. Morante, L. Pavesi, M. Cazzanelli, Appl. Phys. Lett. **82**(10), 1595 (2003)

Optical near-field–mediated polarization asymmetry induced by two-layer nanostructures

Makoto Naruse,[1,*] Naoya Tate,[2] Yasuyuki Ohyagi,[3] Morihisa Hoga,[3] Tsutomu Matsumoto,[4] Hirokazu Hori,[5] Aurélien Drezet,[6] Serge Huant,[6] and Motoichi Ohtsu[2]

[1]*Photonic Network Research Institute, National Institute of Information and Communications Technology, 4-2-1 Nukui-kita, Koganei, Tokyo 184-8795, Japan*
[2]*Department of Electrical Engineering and Information Systems and Nanophotonics Research Center, Graduate School of Engineering, The University of Tokyo, 2-11-16 Yayoi, Bunkyo-ku, Tokyo 113-8656, Japan*
[3]*Dai Nippon Printing Co. Ltd., 250-1 Wakashiba, Kashiwa, Chiba 277-0871, Japan*
[4]*Yokohama National University, Hodogaya, Yokohama, Kanagawa 240-8501, Japan*
[5]*University of Yamanashi, Takeda, Kofu, Yamanashi 400-8511, Japan*
[6]*Institut Néel, CNRS and University of Joseph Fourier, 25 rue des Martyrs BP 166, 38042 Grenoble cedex 9, France*
[*]*naruse@nict.go.jp*

Abstract: We demonstrate that a two-layer shape-engineered nanostructure exhibits asymmetric polarization conversion efficiency thanks to near-field interactions. We present a rigorous theoretical foundation based on an angular-spectrum representation of optical near-fields that takes account of the geometrical features of the proposed device architecture and gives results that agree well with electromagnetic numerical simulations. The principle used here exploits the unique intrinsic optical near-field processes associated with nanostructured matter, while eliminating the need for conventional scanning optical fiber probing tips, paving the way to novel nanophotonic devices and systems.

OCIS codes: (260.5430) Polarization; (180.4243) Near-field microscopy; (160.4236) Nanomaterials.

References and links

1. M. Ohtsu, K. Kobayashi, T. Kawazoe, S. Sangu, and T. Yatsui, "Nanophotonics: design, fabrication, and operation of nanometric devices using optical near fields," IEEE J. Sel. Top. Quantum Electron. **8**(4), 839–862 (2002).
2. A. Cuche, A. Drezet, Y. Sonnefraud, O. Faklaris, F. Treussart, J.-F. Roch, and S. Huant, "Near-field optical microscopy with a nanodiamond-based single-photon tip," Opt. Express **17**(22), 19969–19980 (2009).
3. M. Aeschlimann, M. Bauer, D. Bayer, T. Brixner, F. J. García de Abajo, W. Pfeiffer, M. Rohmer, C. Spindler, and F. Steeb, "Adaptive subwavelength control of nano-optical fields," Nature **446**(7133), 301–304 (2007).
4. K. Akahane, N. Yamamoto, and M. Tsuchiya, "Highly stacked quantum-dot laser fabricated using a strain compensation technique," Appl. Phys. Lett. **93**(4), 041121 (2008).
5. M. Naruse, N. Tate, M. Aono, and M. Ohtsu, "Information physics fundamentals of nanophotonics," Rep. Prog. Phys. **76**(5), 056401 (2013).
6. T. Yatsui, S. Sangu, T. Kawazoe, M. Ohtsu, S. J. An, J. Yoo, and G.-C. Yi, "Nanophotonic switch using ZnO nanorod double-quantum-well structures," Appl. Phys. Lett. **90**(22), 223110 (2007).
7. C. Pistol, C. Dwyer, and A. R. Lebeck, "Nanoscale optical computing using resonance energy transfer logic," IEEE Micro **28**(6), 7–18 (2008).
8. M. Naruse, M. Aono, S.-J. Kim, T. Kawazoe, W. Nomura, H. Hori, M. Hara, and M. Ohtsu, "Spatiotemporal dynamics in optical energy transfer on the nanoscale and its application to constraint satisfaction problems," Phys. Rev. B **86**(12), 125407 (2012).
9. M. Aono, M. Naruse, S.-J. Kim, M. Wakabayashi, H. Hori, M. Ohtsu, and M. Hara, "Amoeba-inspired nanoarchitectonic computing: solving intractable computational problems using nanoscale photoexcitation transfer dynamics," Langmuir **29**(24), 7557–7564 (2013).
10. M. Naruse, N. Tate, and M. Ohtsu, "Optical security based on near-field processes at the nanoscale," J. Opt. **14**(9), 094002 (2012).
11. N. Tate, H. Sugiyama, M. Naruse, W. Nomura, T. Yatsui, T. Kawazoe, and M. Ohtsu, "Quadrupole-dipole transform based on optical near-field interactions in engineered nanostructures," Opt. Express **17**(13), 11113–11121 (2009).
12. N. Tate, M. Naruse, T. Yatsui, T. Kawazoe, M. Hoga, Y. Ohyagi, T. Fukuyama, M. Kitamura, and M. Ohtsu, "Nanophotonic code embedded in embossed hologram for hierarchical information retrieval," Opt. Express **18**(7), 7497–7505 (2010).

Received 12 Jun 2013; revised 3 Aug 2013; accepted 3 Sep 2013; published 10 Sep 2013

13. A. Drezet, C. Genet, J. Y. Laluet, and T. W. Ebbesen, "Optical chirality without optical activity: How surface plasmons give a twist to light," Opt. Express **16**(17), 12559–12570 (2008).
14. K. L. Kelly, E. Coronado, L. L. Zhao, and G. C. Schatz, "The optical properties of metal nanoparticles: the influence of size, shape, and dielectric environment," J. Phys. Chem. B **107**(3), 668–677 (2003).
15. N. Tate, W. Nomura, T. Yatsui, M. Naruse, and M. Ohtsu, "Hierarchical hologram based on optical near- and far-field responses," Opt. Express **16**(2), 607–612 (2008).
16. G. L. J. A. Rikken and E. Raupach, "Observation of magneto-chiral dichroism," Nature **390**(6659), 493–494 (1997).
17. A. Papakostas, A. Potts, D. M. Bagnall, S. L. Prosvirnin, H. J. Coles, and N. I. Zheludev, "Optical manifestations of planar chirality," Phys. Rev. Lett. **90**(10), 107404 (2003).
18. T. Vallius, K. Jeffimovs, J. Turunen, P. Vahimaa, and Y. Svirko, "Optical activity in subwavelength-period arrays of chiral metallic particles," Appl. Phys. Lett. **83**(2), 234–236 (2003).
19. W. Zhang, A. Potts, A. Papakostas, and D. M. Bagnall, "Intensity modulation and polarization rotation of visible light by dielectric planar chiral materials," Appl. Phys. Lett. **86**(23), 231905 (2005).
20. V. A. Fedotov, P. L. Mladyonov, S. L. Prosvirnin, A. V. Rogacheva, Y. Chen, and N. I. Zheludev, "Asymmetric propagation of electromagnetic waves through a planar chiral structure," Phys. Rev. Lett. **97**(16), 167401 (2006).
21. J. K. Gansel, M. Thiel, M. S. Rill, M. Decker, K. Bade, V. Saile, G. von Freymann, S. Linden, and M. Wegener, "Gold helix photonic metamaterial as broadband circular polarizer," Science **325**(5947), 1513–1515 (2009).
22. C. Menzel, C. Helgert, C. Rockstuhl, E.-B. Kley, A. Tünnermann, T. Pertsch, and F. Lederer, "Asymmetric transmission of linearly polarized light at optical metamaterials," Phys. Rev. Lett. **104**(25), 253902 (2010).
23. D. W. Pohl and D. Courjon, *Near Field Optics*, (Kluwer Academic, 1993).
24. E. Wolf and M. Nieto-Vesperinas, "Analyticity of the angular spectrum amplitude of scattered fields and some of its consequences," J. Opt. Soc. Am. A **2**(6), 886–889 (1985).
25. T. Inoue and H. Hori, "Quantum theory of radiation in optical near field based on quantization of evanescent electromagnetic waves using detector mode," in *Progress in Nano-Electro-Optics IV*, M. Ohtsu ed. (Springer, 2005), pp. 127–199.
26. M. Naruse, T. Inoue, and H. Hori, "Analysis and synthesis of hierarchy in optical near-field interactions at the nanoscale based on angular spectrum," Jpn. J. Appl. Phys. **46**(9A), 6095–6103 (2007).
27. M. Brun, A. Drezet, H. Mariette, N. Chevalier, J. C. Woehl, and S. Huant, "Remote optical addressing of single nano-objects," Europhys. Lett. **64**(5), 634–640 (2003).
28. A. Drezet, A. Cuche, and S. Huant, "Near-field microscopy with a single-photon point-like emitter: Resolution versus the aperture tip?" Opt. Commun. **284**(5), 1444–1450 (2011).
29. D. W. Lynch and W. R. Hunter, "Comments on the optical constants of metals and an introduction to the data for several metals," in *Handbook of Optical Constants of Solids*, E. D. Palik ed. (Academic, 1985), pp. 275–367.
30. M. Naruse, T. Yatsui, H. Hori, M. Yasui, and M. Ohtsu, "Polarization in optical near- and far-field and its relation to shape and layout of nanostructures," J. Appl. Phys. **103**(11), 113525 (2008).
31. C. Menzel, C. Rockstuhl, and F. Lederer, "Advanced Jones calculus for the classification of periodic metamaterials," Phys. Rev. A **82**(5), 053811 (2010).
32. G. R. Fowles, *Introduction to Modern Optics* (Dover Publications, 1989).
33. A. Drezet and C. Genet, "Reciprocity and optical chirality," in *Singular and Chiral Nanoplasmonics*, N. Zheludev and S. V. Boriskina, eds. (Pan Stanford Publishing), in press.
34. J. A. Schuller, E. S. Barnard, W. Cai, Y. C. Jun, J. S. White, and M. L. Brongersma, "Plasmonics for extreme light concentration and manipulation," Nat. Mater. **9**(3), 193–204 (2010).
35. M. Kauranen and A. V. Zayats, "Nonlinear plasmonics," Nat. Photonics **6**(11), 737–748 (2012).
36. S. V. Zhukovsky, C. Kremers, and D. N. Chigrin, "Plasmonic rod dimers as elementary planar chiral meta-atoms," Opt. Lett. **36**(12), 2278–2280 (2011).
37. D. N. Chigrin, C. Kremers, and S. V. Zhukovsky, "Plasmonic nanoparticle monomers and dimers: from nanoantennas to chiral metamaterials," Appl. Phys. B **105**(1), 81–97 (2011).
38. H. Matsumoto and T. Matsumoto, "Clone match rate evaluation for an artifact-metric system," IPSJ J. **44**, 1991–2001 (2003).
39. T. Matsumoto, K. Hanaki, R. Suzuki, D. Sekiguchi, M. Hoga, Y. Ohyagi, M. Naruse, N. Tate, and M. Ohtsu, "A nano artifact-metric system leveraging resist collapsing in electron beam lithography," submitted.
40. N. Guth, B. Gallas, J. Rivory, J. Grand, A. Ourir, G. Guida, R. Abdeddaim, C. Jouvaud, and J. de Rosny, "Optical properties of metamaterials: influence of electric multipoles, magnetoelectric coupling, and spatial dispersion," Phys. Rev. B **85**(11), 115138 (2012).
41. Y. Tomaru, S. Hakuta, T. Tani, and M. Naya, "Optical properties of nano silver pavement," in *Extended Abstracts of the 73rd Autumn Meeting, 2012* (The Japan Society of Applied Physics, 2012), p. 03–152.
42. C. Enkrich, M. Wegener, S. Linden, S. Burger, L. Zschiedrich, F. Schmidt, J. F. Zhou, Th. Koschny, and C. M. Soukoulis, "Magnetic metamaterials at telecommunication and visible frequencies," Phys. Rev. Lett. **95**(20), 203901 (2005).

1. Introduction

Nanophotonics has been extensively studied with the aim of unveiling and exploiting optical near-field interactions associated with nanostructured matter [1]. The technologies used for characterizing optical near-field processes [2,3] and related materials technologies [4] have been rapidly advancing. In addition, investigations based on information physics have been

Received 12 Jun 2013; revised 3 Aug 2013; accepted 3 Sep 2013; published 10 Sep 2013

revealing some unique and emergent attributes of nanophotonics that are useful for various applications [5]; examples include, but are not limited to, basic logic circuits [6,7], computing paradigms that go beyond the von Neumann architecture [8,9], and applications related to information security [10].

What we particularly address in this paper stems from advancements in shape-engineered nanostructures and some technological concerns in conventional near-field optics that necessitate precision mechanical control, for example, in controlling optical fiber probing tips. Advances in electron-beam lithography, nano-imprinting, and other areas allow the fabrication of well-controlled reliable nanostructures [11–14], and interesting information applications, such as information security, have been made possible. For instance, we have demonstrated a "*hierarchical hologram*" that works in both optical far-fields and near-fields, the former being associated with conventional holographic images, and the latter being associated with the optical intensity distribution originating from a nanometric structure embedded in the hologram, which is accessible only via optical near-fields [12,15]. In other words, information hiding can be realized by using optical near-fields and nanofabrication technologies. Also, authentication functions can be implemented by using two shape-engineered nanostructures and their associated optical near-fields [11]. In this system, the two nanostructures respectively work as a *lock* and *key*, where authenticity is guaranteed by the nanoscale-precision shapes of the structures.

The physical principles of nano-optics can contribute to the development of novel functionalities. The common feature across these demonstrations is that they are based on high-precision mutual relations between nanostructured matter, mediated by optical near-fields. Technologically, in turn, they require high-precision alignment between nanostructured matter, such as an optical near-field fiber probe tip and the device under study. Although this attribute is one fundamentally superior aspect in terms of increased security, at the same time it is a severe technological difficulty in terms of stability and practical use.

Therefore, in this paper, we demonstrate a two-layer united nanostructure in which the layers interact via optical near-fields and which exhibits unique optical properties that are observable in the optical far-field. More concretely, the proposed device architecture exhibits "asymmetry" in its associated polarization properties; specifically, the polarization conversion efficiency from *x*-polarized input light to *y*-polarized output light ($X \rightarrow Y$) and that from *y*-polarized input light to *x*-polarized output light ($Y \rightarrow X$) results in different values. We demonstrate its rigorous theoretical foundation based on an angular spectrum representation of optical near-fields that takes account of the geometries of the two-layer nanostructure, and in which representative features are characterized by electromagnetic numerical calculations. With such an architecture, we are able to exploit optical near-field processes occurring at the subwavelength scale, while at the same time allowing them to be retrieved by a macro-scale optical measurement, thus considerably relaxing the stringent requirements of precision alignment in conventional optical near-field setups.

The asymmetric polarization property discussed in this paper, defined as described above, is *not* related to the magneto-optical chiral effects [16], chiral plasmonic structures [13,17–21]. Although it may be possible to achieve equivalent asymmetric optical responses by combinations of conventional optical elements or anisotropic materials, the focus of this paper is to accomplish the asymmetric polarization properties defined above by using shape-engineered two-layer nanostructures formed of isotropic matter via their associated optical near-fields. We consider that such an approach will pave the way to new functional nanophotonic devices and optical security applications based on near-field processes, without the need for technologically difficult demands, such as those required in scanning probe-based measurements. That is to say, the asymmetric polarization properties, which can be associated with *information*, are implemented with the built-in shape of the nanostructures themselves. The asymmetric transmission of linearly polarized light in optical metamaterials was demonstrated by Menzel et al. [22]. The findings of our study, emphasizing the role of optical near-fields associated with nanostructures, will give greater physical insights regarding

Received 12 Jun 2013; revised 3 Aug 2013; accepted 3 Sep 2013; published 10 Sep 2013

asymmetric polarization, provide a systematic approach for designing designated functions, and offer fundamentals for novel applications, such as information security.

This paper is organized as follows. First, Section 2 characterizes one fundamental feature of precision alignment requirements involving optical near-field processes via a rigorous theory based on an angular-spectrum representation of electromagnetic fields on the nanoscale. Section 3 introduces asymmetry of polarization conversion efficiency in a two-layer nanostructure. Section 4 describes the theoretical background based on the angular spectrum framework introduced in Section 2. Section 5 demonstrates some representative features based on electromagnetic calculations and presents methods of characterizing devices via some figures-of-merit that correspond to the theoretical framework discussed in Section 4. Section 6 concludes the paper.

2. Theoretical foundations for describing precision mutual relations via optical near-fields

First, we characterize the fundamental properties of precision mutual relations required in order to retrieve a proper signal via optical near-fields with a simple but rigorous theoretical approach. These theoretical elements will be used in discussing the asymmetry of polarization conversion to be discussed in Section 3 and later sections.

Optical near-fields are the localized, non-propagating components of electromagnetic fields in the vicinity of materials [23]. We need to locate certain kinds of *reader* to induce interactions with the device under study. In order to characterize the structure of the system, we denote the entities of the system as follows. Let the device under study be denoted by D, and the reader by R. One of the characteristic consequences of nano-optical systems is that the output signal depends precisely on both D and R, a relationship which is represented by $v = g(D,R)$. In order to theoretically represent the fundamental characters of the output signal we take the following approach.

The device under study is regarded as an oscillating electric dipole $\boldsymbol{D}$ with frequency K placed in a vacuum at the origin of a Cartesian space in which the velocity of light is taken as unity ($c = 1$). To deal with scattering problems based on assumed planar boundary conditions, as well as offering a physically intuitive understanding, it is convenient to represent the complex amplitude $\boldsymbol{E}$ of the electric dipole radiation as a superposition of plane waves having complex wave vectors—an approach called the angular spectrum representation [24–26]. In this representation, $\boldsymbol{E}$ is defined by

$$\mathbf{E}(\mathbf{r}) = \left(\frac{iK^3}{8\pi^2 \varepsilon_0} \right) \sum_{\mu=TE}^{TM} \int_0^{2\pi} d\beta \int_0^{\infty} ds_{\parallel} \frac{s_{\parallel}}{s_z} \left[\boldsymbol{\varepsilon}(\mathbf{s}^{(\pm)}, \mu) \bullet \mathbf{D} \right] \boldsymbol{\varepsilon}(\mathbf{s}^{(\pm)}, \mu) \exp(iK\mathbf{s}^{(\pm)} \bullet \mathbf{r}), \quad (1)$$

where the unit wavevector and the TE- and TM-polarization vectors are respectively given by

$$\begin{aligned} \mathbf{s}^{(\pm)} &= \left(s_{\parallel} \cos\beta, s_{\parallel} \sin\beta, \pm s_z \right) \\ \boldsymbol{\varepsilon}(\mathbf{s}^{(+)}, TE) &= \left(-\sin\beta, \cos\beta, 0 \right) \\ \boldsymbol{\varepsilon}(\mathbf{s}^{(+)}, TM) &= \left(\pm s_z \cos\beta, \pm s_z \sin\beta, -s_{\parallel} \right), \end{aligned} \quad (2)$$

and the parameter s_z of the unit wavevector $\mathbf{s}^{(\pm)}$, which satisfies $s_{\parallel}^2 + s_z^2 = 1$, is represented by

$$s_z = \begin{cases} \sqrt{1 - s_{\parallel}^2} & \text{for } 0 \le s_{\parallel} < 1 \\ i\sqrt{s_{\parallel}^2 - 1} & \text{for } 1 \le s_{\parallel} < +\infty. \end{cases} \quad (3)$$

Received 12 Jun 2013; revised 3 Aug 2013; accepted 3 Sep 2013; published 10 Sep 2013

We denote the complex wavevector as $\mathbf{s}^{(+)}$ for $z>0$ and $\mathbf{s}^{(-)}$ for $z<0$. One of the remarkable attributes of the angular spectrum representation is that the value of $s_{\parallel}$ specifies the property of a plane wave as a homogeneous wave ($0 \le s_{\parallel} < 1$) or an evanescent wave ($1 \le s_{\parallel} < +\infty$). Since we wish to investigate optical interactions in the subwavelength regime where evanescent components dominate and homogeneous ones are negligible, in this paper, we focus on the region $1 \le s_{\parallel} < +\infty$, where $s_{\parallel}$ indicates the spatial frequency of an evanescent wave propagating in the assumed planar boundary plane, namely, the *xy* plane.

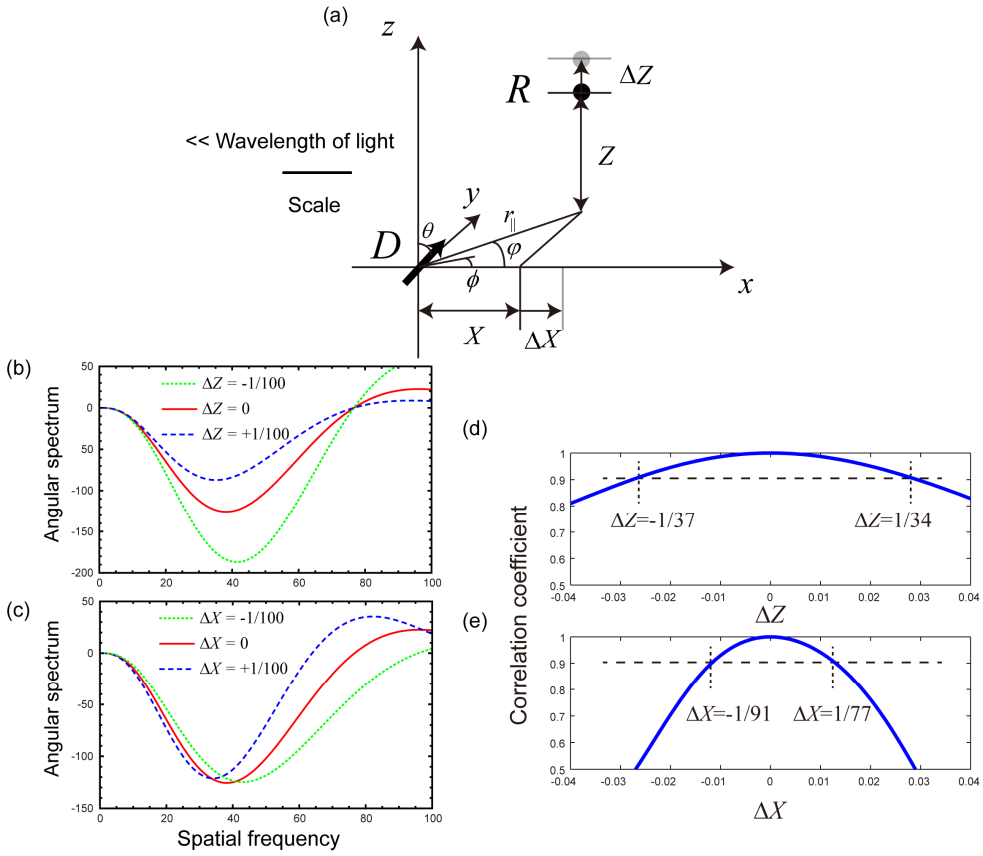

Fig. 1. Fundamental characterization of mutual relation between a device (*D*) and a reader (*R*) via optical near-fields based on angular-spectrum representation. (a) Schematic illustration of a point dipole (***D***) and an evaluation point (***R***). (b,c) The "output signal" is equated with the angular spectrum, which is the near-field component of the electromagnetic field in the subwavelength regime. The *Z*- and *X*-dependent signals are respectively shown in (b) and (c). (d,e) Correlation coefficient of the output signal as a function of minute differences in *Z* and *X*. A tiny difference strongly affects the output signal, which is a manifestation of the precision dependence of nanostructured matter via optical near-fields.

Suppose that the dipole ***D*** is oriented at an angle θ with respect to the *z* axis and at an angle ϕ in the *xy* plane, that is, $\mathbf{D} = d(\sin\theta\cos\phi, \sin\theta\sin\phi, \cos\theta)$, as schematically shown in Fig. 1(a). Suppose also that we observe the radiation from the electric dipole at a position displaced from the dipole by $\mathbf{R} = (r_{\parallel}\cos\varphi, r_{\parallel}\sin\varphi, Z)$; that is to say, we assume that the reader is placed at ***R***. The angular spectrum representation of the *z* component of the electric field for evanescent waves (namely, $1 \le s_{\parallel} < +\infty$) from the dipole ***D*** is given by

Received 12 Jun 2013; revised 3 Aug 2013; accepted 3 Sep 2013; published 10 Sep 2013

$$E_z(\mathbf{R}) = \left(\frac{iK^3}{4\pi\varepsilon_0}\right)\int_1^\infty ds_\parallel \frac{s_\parallel}{s_z} f_z(s_\parallel, \mathbf{D}, \mathbf{R}), \tag{4}$$

where

$$\begin{aligned} f_z(s_\parallel, \mathbf{D}, \mathbf{R}) = {} & ds_\parallel \sqrt{s_\parallel^2 - 1} \sin\theta \cos(\phi - \varphi) J_1\left(Kr_\parallel s_\parallel\right) \exp\left(-KZ\sqrt{s_\parallel^2 - 1}\right) \\ & + ds_\parallel^2 \cos\theta J_0\left(Kr_\parallel s_\parallel\right) \exp\left(-KZ\sqrt{s_\parallel^2 - 1}\right). \end{aligned} \tag{5}$$

Here, $J_n(x)$ represents a Bessel function of the first kind, where n is an integer, and the term $f_z(s_\parallel, \mathbf{D}, \mathbf{R})$ is called the angular spectrum of the electric field.

Now, we consider that $f_z(s_\parallel, \mathbf{D}, \mathbf{R})$ is equivalent to the signal $v = g(D,R)$ characterized in the system model. Assuming that the dipole is oriented parallel to the x-axis, we have $\phi = 0$ and $\theta = \pi/2$. Also, assuming that the reader R is located on the xz-plane, we have $\varphi = 0$. In such a model, letting $r_\parallel$ be denoted by X, we characterize the horizontal (X) and vertical (Z) dependences. Note that X and Z are given in units of wavelength.

The solid curve in Fig. 1(b) shows the angular spectrum when $X = 1/20$ and $Z = 1/20$. We consider that this corresponds to a *genuine* device ***D*** and a *genuine* reader ***R***. Differences of the reader ***R*** are equivalent to differences of Z; for instance, when Z is shifted by distance $\Delta Z = -1/100$, the angular spectrum is given by the dotted curve in Fig. 1(b). Similarly, when $\Delta Z = 1/100$, the angular spectrum is given by the dashed curve in Fig. 1(b). (As described below, Fig. 1(c) is for the horizontal (X) direction.) As shown by the changes of the curve in Fig. 1(b), a slight difference with respect to Z results in a different output signal from the system. In order to quantitatively evaluate the Z-dependence, the correlation coefficient of the angular spectrum is calculated as a function of ΔZ, as summarized in Fig. 1(d). More specifically, let the angular spectrum of the genuine device D and genuine reader R be given by $f_a(s_\parallel)$, and let the angular spectrum of the genuine device D and a reader displaced from the genuine reader by an amount of ΔZ be given by $f_{\Delta Z}(s_\parallel)$; hence, the correlation coefficient is defined by $\int (f_{\Delta Z}(s_\parallel) - \overline{f_{\Delta Z}(s_\parallel)})(f_a(s_\parallel) - \overline{f_a(s_\parallel)}) ds_\parallel \Big/ \sqrt{\int \left(f_{\Delta Z}(s_\parallel) - \overline{f_{\Delta Z}(s_\parallel)}\right)^2 ds_\parallel \int \left(f_a(s_\parallel) - \overline{f_a(s_\parallel)}\right)^2 ds_\parallel}$, where $\overline{f(s_\parallel)}$ indicates the average value of $f(s_\parallel)$. If we determine that a genuine signal should yield a correlation coefficient larger than 0.9, ΔZ should be between $-1/37$ and $1/34$, which would be an extremely small absolute value in real dimensions. This indicates that nano-optics exhibits a strong reader-dependence, in agreement with reports on near-field scanning optical microscopy [27,28]. Similarly, by considering the horizontal position of the dipole as the identity of the device, a different X provides a different angular spectrum. The solid, dotted, and dashed curves in Fig. 1(c) indicate the angular spectra when ΔX is given by 0, $-1/100$, and $+1/100$, respectively. The correlation coefficient is evaluated as shown in Fig. 1(e); it is larger than 0.9 when ΔX is between $-1/77$ and $1/91$, indicating that the output signal is sensitive to subtle differences of the device ***D***.

3. Polarization asymmetry induced by a two-layer nanostructure

As demonstrated in the simple model shown Section 2, tiny mutual differences between ***D*** and ***R*** result in large differences in the output signal via optical near-fields. The fundamental idea of this paper is to combine, or unite, ***D*** and ***R*** in the first place; that is to say, we consider a device architecture where two nanostructures are located in close proximity.

The basic architecture of the proposed structure is schematically shown in Fig. 2(a), where the first layer is composed of square shapes, whereas the second layer is composed of rectangular shapes located at the lower right corners of the square shapes in the first layer. In

Received 12 Jun 2013; revised 3 Aug 2013; accepted 3 Sep 2013; published 10 Sep 2013

other words, the first layer has a symmetric shape, and the second layer has an asymmetric shape and is placed at an asymmetric position with respect to the first layer.

The square and circular marks in Fig. 2(b) respectively denote the polarization conversion efficiency from *x*-polarized input light to *y*-polarized output light (denoted by $E_{X\to Y}$) and from *y*-polarized input light to *x*-polarized output light ($E_{Y\to X}$), calculated by a finite-difference time-domain (FDTD) simulation. The absolute value of the difference between the polarization conversion efficiencies is denoted by triangular marks in Fig. 2(c). The horizontal axes in Figs. 2(b) and 2(c) are accompanied by schematic illustrations of the elemental nanostructures to be evaluated.

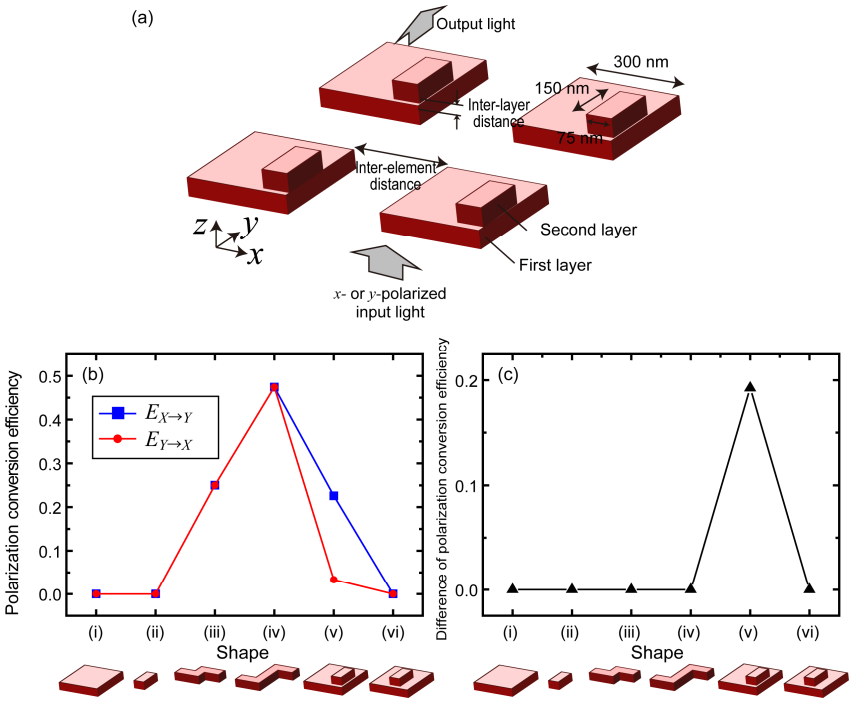

Fig. 2. (a) Two-layer nanostructure: the first layer is composed of an array of square-shaped structures, and the second layer is an array of rectangular-shaped structures which is aligned at the lower right corner with respect to the first layer. (b) This structure yields differences in polarization conversion efficiencies between *x*-polarized input light to *y*-polarized output and *y*-polarized input light to *x*-polarized output light, what is defined as "asymmetry" discussed in this paper (v). Other representative shapes (i–iv and vi) do not provide such asymmetric polarization conversion efficiencies. (c) Difference of polarization conversion efficiency in (b).

The operating wavelength used was 688 nm. As the material, we assumed gold, which has a refractive index of 0.16 and an extinction ratio of 3.8 at a wavelength of 688 nm [29]. The dimensions of each square in the first layer were 300 nm × 300 nm, and the dimensions of each rectangle in the second layer were 75 nm (*x*) × 150 nm (*y*), which are respectively 1/4 and 1/2 the sizes of the squares in the first layer. These shapes are periodically arranged at regular intervals. (In the calculation, the interval between the neighboring units was 200 nm.) The thicknesses of the first and second layers were 100 nm. The gap between the two layers was 10 nm.

The nanostructures shown in Figs. 2(b,i) and 2(b,ii) were used to evaluate the polarization conversion efficiency of the first layer only and the second layer only, respectively, resulting in nearly no asymmetry. The nanostructures shown in Figs. 2(b,iii) and 2(b,iv) have a single-layer shape that mimics the letter "Z". With such a shape, although polarization conversion efficiencies ($E_{X\to Y}$ and $E_{Y\to X}$) appeared [30], these efficiencies had almost the same value,

Received 12 Jun 2013; revised 3 Aug 2013; accepted 3 Sep 2013; published 10 Sep 2013

and so the difference of the polarization conversion efficiency, which is the definition of polarization asymmetry in this paper, as summarized in Fig. 2(c), was negligible.

The nanostructure shown in Fig. 2(a), corresponding to Fig. 2(b,v), exhibits asymmetry in the polarization conversion efficiencies. The nanostructure shown in Fig. 2(b,vi) consisted of the same-sized elements and the same inter-layer gap as those in Fig. 2(b,v), but the second-layer rectangles were placed at the *centers* with respect to the first-layer squares. This led to significantly reduced polarization conversion efficiencies, and the corresponding difference was calculated to be nearly zero; that is, there was no asymmetry.

Before discussing the theoretical background behind such asymmetry in Section 4 based on optical near-fields, here we make a few remarks on related work in the literature. Regarding the Jones matrix of a polarization rotation θ, the polarization conversion efficiencies $E_{X\to Y}$ and $E_{Y\to X}$ are respectively given by the (2,1) and (1,2) elements of the Jones matrix, which are sin θ and -sin θ, respectively. The difference of their absolute values results in zero, meaning that the polarization asymmetry discussed in this paper, i.e., $E_{X\to Y} \neq E_{Y\to X}$, does not appear. A polarizer extracting polarized light oriented at angle θ with respect to the *x*-axis exhibits polarization conversion efficiencies $E_{X\to Y}$ and $E_{Y\to X}$ having the same value, given by sin θ cos θ; that is to say, there is no asymmetry, as defined in this paper.

In the field of metamaterials, classification of periodic metamaterials regarding their polarization properties has been studied [31]. The asymmetric polarization conversion efficiencies discussed in this paper correspond to the "fifth" group in the context discussed in [31]. In a more general context, the relevance to general optical activity [32,33] could be considered. Optical activity is described in its most general form by a Jones matrix, given by

$$J_{o.a.} = \begin{pmatrix} A + B\cos\theta & B\sin\theta \\ B\sin\theta & A - B\cos\theta \end{pmatrix} + \begin{pmatrix} 0 & i\gamma \\ -i\gamma & 0 \end{pmatrix} \tag{6}$$

where γ is called the gyromagnetic coefficient [33]. The first term is related to a mirror symmetry, and the second is related to pure optical rotation. A difference in the absolute value of the non-diagonal elements of the matrix $J_{o.a.}$, corresponding to the "asymmetry" discussed in this paper, could give a non-zero result if B and γ are given by non-zero, complex numbers. Further insights regarding the relation between these generalized schemes [31,33] and the effects offered by near-field interactions may be interesting topics of future work.

4. Theory of asymmetry by two-layer nanostructures based on angular spectrum representation

Here we give a theoretical description of the asymmetry induced by a two-layer nanostructure based on the angular spectrum representation of optical near-fields introduced in Section 2. With *x*-polarized input light irradiating the square-shaped first-layer nanostructure, we consider that electron charges are concentrated in the corners of the nanostructure due to the so-called plasmon resonance effect [34,35]. Also, the phases of the oscillating electron charges differ by π between the right-hand and left-hand sides. In Fig. 3(a), this is represented by four dipoles, two on the right and two on the left, with opposite orientations. The side length of the first-layer shape is assumed to be $\lambda/4$, where λ is the operating wavelength.

Received 12 Jun 2013; revised 3 Aug 2013; accepted 3 Sep 2013; published 10 Sep 2013

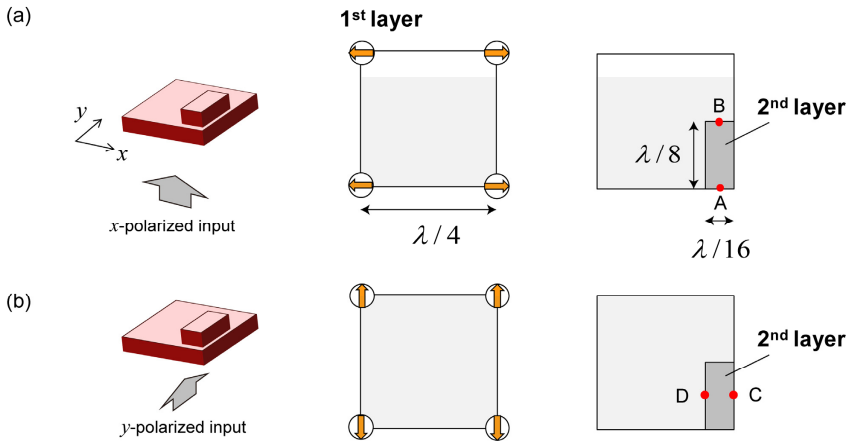

Fig. 3. Theoretical model for the polarization conversion asymmetry in the two-layer nanostructure, (a) with *x*-polarized input light, and (b) *y*-polarized input light.

Now we turn our attention to the induced electric fields and their associated induced electron charges in the second layer. Since the *y*-polarized component is of primary concern, we focus our attention on points A and B in Fig. 3(a), which correspond to the upper and lower center edges of the second layer, respectively. Note that the side length of the second-layer structure is λ/16 along the *x*-axis and λ/8 along the *y*-axis, and the second layer is located at the bottom right corner with respect to the first layer. Also, the inter-layer distance between the first and the second layer is assumed to be λ/20.

Similarly, with *y*-polarized input light, we assume that four oscillating dipoles are induced in the corners of the first layer, with the upper two and lower two being reversed in phase. In order to characterize the *x*-to-*y* polarization conversion, this time we focus on points C and D in Fig. 3(b), which are the centers of the right and left edges of the second layer, respectively.

Concerning the relative phase arrangements of the dipoles, we derive the angular spectrum corresponding to points A, B, C, and D, as shown in Fig. 4(a,i), based on Eq. (5). We observe that the difference of the angular spectrum at points A and B is more significant compared with that at points C and D.

Second, we locate the second layer at the center with respect to the first layer. In this case, as demonstrated in Fig. 4(a,ii), the angular spectra at points A and B exhibit exactly the same profile, as do those at points C and D. That is, via Eq. (5), the geometrical features of an array of dipoles and the relative evaluation positions give rise to identical angular spectra. Therefore, the difference between points A and B (and also points C and D) is zero, which indicates that such a configuration exhibits no polarization conversion from *x* to *y* or *y* to *x*. This agrees with the numerical calculations shown in Fig. 2(b,vi).

Third, we assume a square shape, that is, a symmetric structure, in the second layer, located at the lower right corner with respect to the first layer, as schematically shown in Fig. 4(a,iii). The side length of the second-layer squares is half that of the first-layer squares, namely, λ/8. The angular spectra at points A, B, C, and D behave differently; however, the "difference" of the curves between points A and B and between points C and D is not as significant as in the case of Fig. 4(a,i), as will be evaluated numerically below. Finally, we assume the same rectangular second-layer structure as in Fig. 4(a,i) but with an increased inter-layer distance of λ/2 (Fig. 4(a,iv)). The angular spectra at points A and B, as well as those at points C and D, exhibit nearly the same profiles, and the high-frequency components disappear. This is purely due to the increased inter-layer distance, causing the spectra to exponentially decay from the first layer, which is a manifestation of Eq. (5).

Received 12 Jun 2013; revised 3 Aug 2013; accepted 3 Sep 2013; published 10 Sep 2013

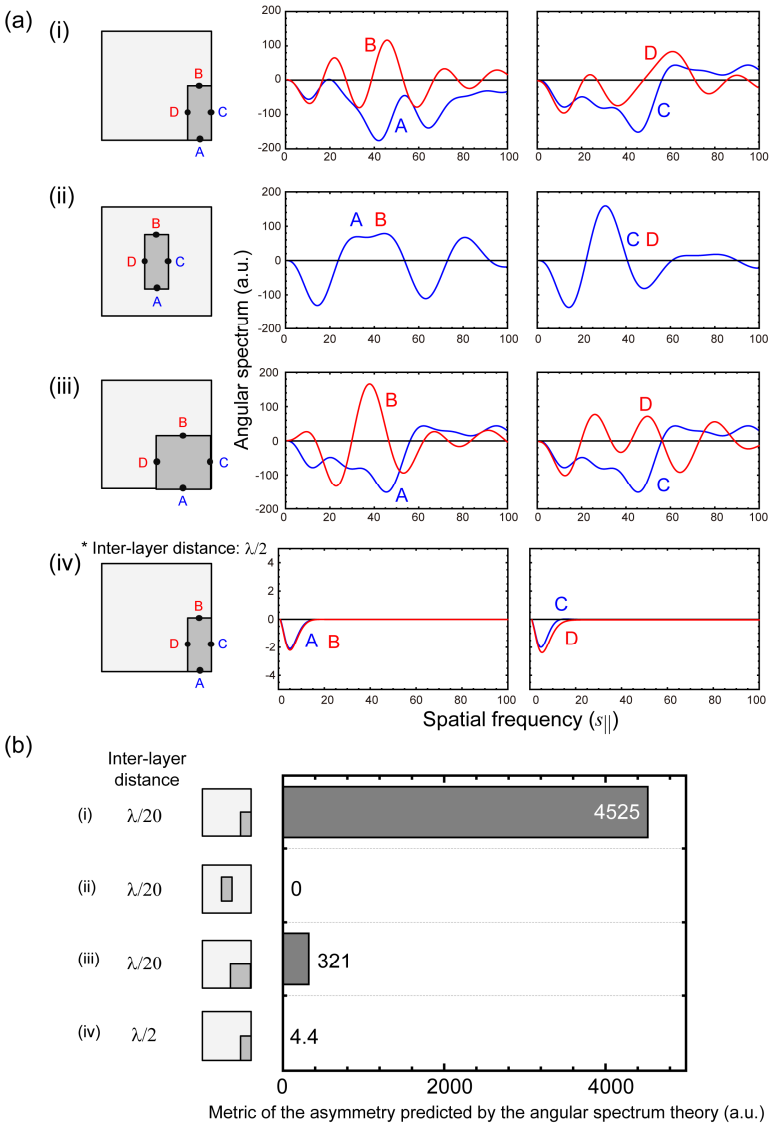

Fig. 4. (a) Angular spectra corresponding to different device architectures. The first layer is composed of square shapes. (i) The second layer is composed of rectangles placed at the lower right corners with respect to the squares in the first layer. The inter-layer distance is λ/20. (ii) The second-layer rectangles are placed in the centers with respect to the squares in the first layer. (iii) The second layer is composed of squares placed at the lower right corners of those in the first layer. (iv) The second-layer structure is the same as that in (i) but the inter-layer distance is λ/2. (b) The structure in (i) exhibits significant asymmetric properties.

Here, we define the following metric for the asymmetry of polarization conversion predicted by the theory based on the angular spectrum representation:

$$\left|\int [f(s_{\|}, A, X_{IN}) - f(s_{\|}, B, X_{IN})]ds_{\|}\right| - \left|\int [f(s_{\|}, C, Y_{IN}) - f(s_{\|}, D, Y_{IN})]ds_{\|}\right| \qquad (7)$$

where $f(s_{\|}, P, X_{IN})$ and $f(s_{\|}, P, Y_{IN})$ denote the angular spectra with x- and y-polarized input light evaluated at point P, respectively. The first term of Eq. (7) represents the X to Y polarization conversion, and the second describes the Y to X conversion; we consider that the difference between the two represents the asymmetry of the polarization conversion. As

Received 12 Jun 2013; revised 3 Aug 2013; accepted 3 Sep 2013; published 10 Sep 2013

summarized in Fig. 4(b), which contains the numerical values based on Eq. (7), the two-layer nanostructure in which the asymmetric second layer is placed at an asymmetric position with respect to the first layer and in close proximity to it yields a significantly larger value. This is a clear manifestation that the asymmetric polarization conversion stems from the two-layer shape-engineered nanostructure in which the layers interact via optical near-fields.

5. Electromagnetic calculation and multi-polar analysis

In order to characterize some basic features, we first evaluate the inter-layer-distance dependences. Figures 5(a) and 5(b) show cross-sectional profiles of the electric field intensity $|E_y|^2$ when two-layer nanostructures with inter-layer distances of 10 nm and 50 nm, respectively, are irradiated with *x*-polarized input light. As is clearly observed from the images, the increased inter-layer distance decreases the inter-layer interactions. The square and circular marks in Fig. 5(c) represent the calculated polarization conversion efficiencies $E_{X\to Y}$ and $E_{Y\to X}$, respectively, whose difference diminishes as the inter-layer distance increases.

Based on the theory discussed in Section 4, for instance with *x*-polarized input light, we focus on the differences of the angular spectrum of the second layer in the vertical direction through an analytical scheme concerning the geometries. Numerically, we can discuss the induced charge distribution by calculating the divergence of the electric fields in the numerical simulations. As schematically shown in Fig. 5(d), we can decompose the induced charge distribution in the second layer into representative components corresponding to a constant value, a vertically different component, a horizontally different component, and higher-order components. In other words, we can factorize the charge distribution on an orthogonal basis, like a multi-polar expansion. We consider that the vertically different component corresponds to *y*-polarized output light (denoted by "$X\to Y$" in Fig. 5(d)), and the horizontally different component corresponds to *x*-polarized output light (denoted by "$Y\to X$"). More specifically, let the difference between the sum of the induced charge in the upper half and the sum of the induced charge in the lower half of the surface of the second layer facing the first layer with the *x*-polarized input light be $p_{X\to Y}$. Also, with the *y*-polarized input light, the difference between the sum of the induced charge in the left-hand half and the sum of the induced charge in the right-hand half of the surface of the second layer facing the first layer is $p_{Y\to X}$. Here we consider that the figure-of-merit (FoM) representing the asymmetric polarization conversion originating from the charge induced in individual elements is given by

$$\mathrm{FoM}_{\mathrm{intrinsic}} = \| p_{X\to Y} | - | p_{Y\to X} \|. \tag{8}$$

The triangular marks in Fig. 5(e) indicate calculated value of the $\mathrm{FoM}_{intrinsic}$ for the charge distribution in the second layer, which show good agreement with the calculated polarization conversion efficiencies.

Additionally, we discuss some related concerns regarding structural attributes and asymmetry in polarization conversion. The first is related to the dependencies on inter-element-distances or the arrangement of elemental two-layer structures. (This is also referred to as the coupling between meta-atoms or the meta-atom arrangement [36,37].) While keeping the dimensions of the elemental two-layer structure the same as the one shown in Fig. 2(b,v), the circular marks in Fig. 6(a) represent the difference of the polarization conversion efficiencies as a function of the inter-element distance. The inter-element distances are the same for both vertical and horizontal directions. The asymmetry is maximized with an inter-element distance of 200 nm, which is actually the case shown in Fig. 2(b,v), indicating that inter-element distances that are too small or too large eliminate the asymmetry.

Received 12 Jun 2013; revised 3 Aug 2013; accepted 3 Sep 2013; published 10 Sep 2013

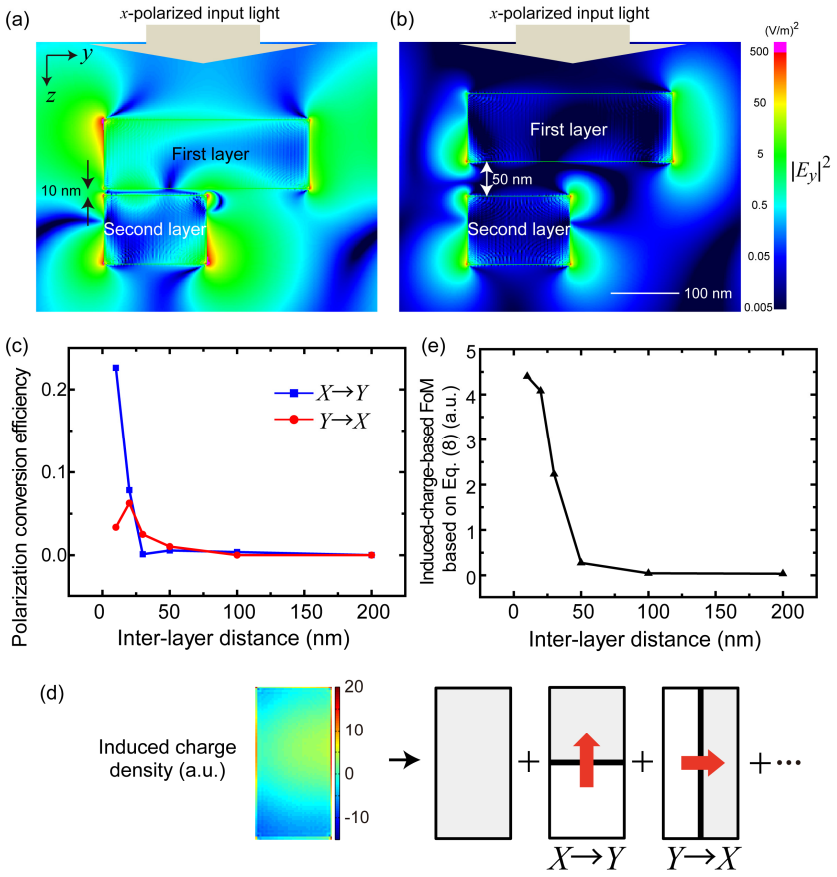

Fig. 5. (a,b) Electromagnetic simulations for the inter-layer distance dependence. (c) Inter-layer-distance-dependent polarization conversion efficiencies. (d) Induced charge distributions in the second layer and their decomposition, representing the vertical and horizontal non-uniformity corresponding to the *x*-to-*y* polarization conversion efficiency and the *y*-to-*x* polarization conversion efficiency. (e) Induced-charge-based figure-of-merit (FoM) for the asymmetry in polarization conversion. The disappearance of asymmetry with larger inter-layer distances agrees with (c).

A presumable physical reason for this is as follows. With *x*-polarized input light, a vertically uniform charge distribution is induced in each of the second-layer rectangular elements, which is introduced above as $p_{X\to Y}$. The effect originating from vertically adjacent elements can be represented by $-p_{X\to Y}\times L_y/(L_y+L_y^{(G)})$, where L_y is the vertical length of the second-layer rectangular elements (150 nm), and $L_y^{(G)}$ is the distance between the vertically adjacent second-layer elements (Fig. 6(a)). The coefficient $-L_y/(L_y+L_y^{(G)})$ indicates that the greater the inter-element distance, manifested by $L_y^{(G)}$, the lower the impact on the polarization, and the minus sign means that the electron charge density in the upper half of an element and that in the lower half of an element located above and adjacent to the former are in an opposite relation with respect to the polarity of the element-intrinsic attribute ($p_{X\to Y}$), as schematically shown in Fig. 6(a). Similarly, the inter-element-dependent *x*-polarization with *y*-polarized input light is represented by $-p_{Y\to X}\times L_x/(L_x+L_x^{(G)})$, where L_x is the horizontal length of the second-layer rectangular element (75 nm), and $L_x^{(G)}$ is the distance between the horizontally adjacent second-layer elements. The net figure-of-merit

Received 12 Jun 2013; revised 3 Aug 2013; accepted 3 Sep 2013; published 10 Sep 2013

concerning both the element-intrinsic attribute and the inter-element-distance-dependent component is given by

$$\mathrm{FoM}_{\mathrm{intrinsic+inter}} = \left| \left| p_{X\to Y}(1-L_y/(L_y+L_y^{(G)})) \right| - \left| p_{Y\to X}(1-L_x/(L_x+L_x^{(G)})) \right| \right| \quad (9)$$

which is shown by the triangular marks in Fig. 6(a), exhibiting a similar tendency to the electromagnetic simulations, and the inter-element distances that provide the maximum asymmetry agree with each other.

Another concern is the spectral dependency and the thickness dependency. The solid and dashed blue curves in Fig. 6(b) show the spectrum of the *y*-polarized output light with *x*-polarized input light and that of the *x*-polarized output light with *y*-polarized input light, respectively. Here, we assume an input optical pulse with a differential Gaussian form whose width is 0.9 fs, corresponding to a bandwidth of around 200–1300 THz. The conversion efficiency is given by calculating the Fourier transform of the output electric field evaluated at a point 2 μm away from the output surface of the second layer. Similarly, the solid and dashed red curves show the spectra for the nanostructures whose thicknesses and inter-layer gap are reduced by half (50%). The solid and dashed green curves, on the other hand, are the spectra for the nanostructure whose thicknesses and inter-layer gap are doubled (200%). The particular nanostructures investigated in earlier sections (blue curves) exhibit larger polarization conversion efficiencies (and strong asymmetric properties) around 680 nm. In any case, the asymmetric property exhibits wavelength and thickness dependencies. Detailed studies regarding these inter-element couplings (or meta-atom couplings) and spectra will be interesting topics of future work.

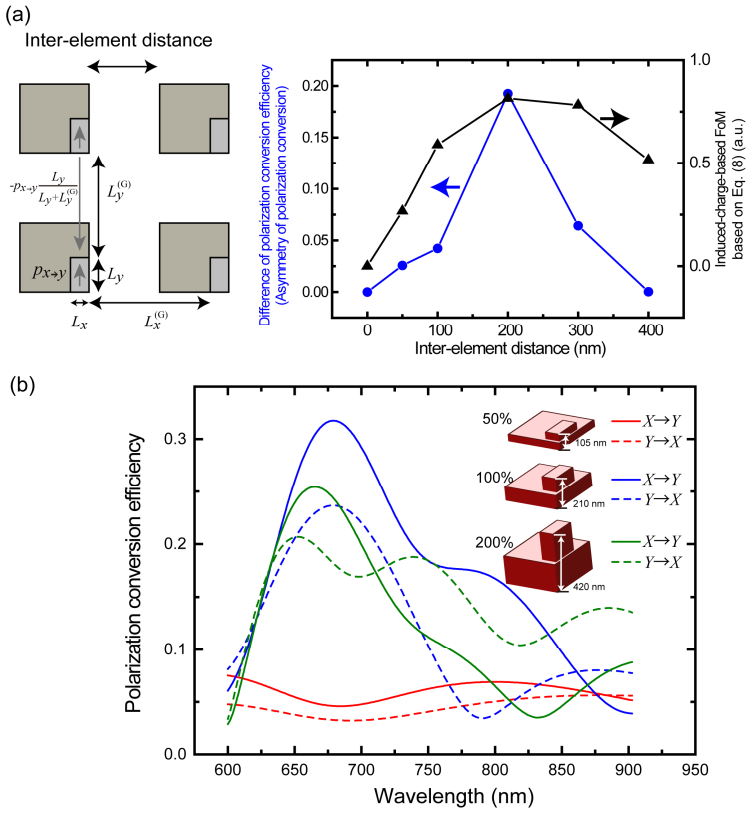

Fig. 6. (a) Inter-element-distance dependent asymmetry in polarization conversion. The asymmetry calculated by electromagnetic simulations and induced-charge-based FoM based on an intuitive physical picture exhibit similar behavior. (b) The spectra of polarization conversion efficiencies. The dependencies on the thicknesses of elemental structures are also shown.

Received 12 Jun 2013; revised 3 Aug 2013; accepted 3 Sep 2013; published 10 Sep 2013

6. Conclusion

In summary, we demonstrate an asymmetry in polarization conversion induced by a two-layer shape-engineered nanostructure formed of isotropic materials that interact via optical near-fields. By using an angular spectrum representation of electric fields in the subwavelength regime, we first characterize the stringent alignment requirements in the conventional setup in which the device and reader are separated. With a view to achieving responses that can be detected in the far-field while at the same time exploiting the intrinsic optical near-fields associated with nanostructured matter, we propose a two-layer unified device architecture consisting of a square-shaped (or symmetric) first layer and a rectangular-shaped (or asymmetric) second layer located in an asymmetric position with respect to the first layer. The geometrical features of the nanostructure are systematically taken into account in a theoretical framework based on the angular-spectrum representation of optical near-fields, giving an asymmetric polarization conversion which agrees well with numerical calculations. The dependence on the inter-layer distance also clearly indicates the involvement of near-field interactions between the two layers.

Finally, we make a few additional remarks about future work regarding applications. In Sections 1 and 2, we addressed the precision alignment requirements required between the "device" and the "reader". With the two-layer unified nanostructures, the inter-layer precisions are still important, as indicated for instance in Figs. 4(a,i) and 4(a,ii). We have to emphasize that the stringent alignment requirements addressed in the introduction are for the case where optical near-field probing tips are used. On the other hand, while alignment is indeed crucial in the manufacturing process in the case of the two-layer nanostructures proposed here, the device can be implemented in a fixed configuration, without any further alignment needed, in the form of a module together with some other optical elements, such as emitters and detectors. We should note that the intrinsic optical near-field processes associated with nanostructured matter are still utilized. The precision shape- and layout-dependencies of the polarization properties can then be exploited, for example, as the identity of the devices, as in the application known as "artifact-metrics" for anti-counterfeit technologies proposed by Matsumoto et al. [38]. Indeed, Matsumoto et al. succeeded in demonstrating "nano artifact-metrics" by utilizing randomly formed silicon nanostructures by leveraging resist collapse in electron beam lithography [39]. A discussion of such applications, as well as physical insights into the optical properties made possible by nanostructures [40], is an interesting topic for future work. Also, the theoretical approach based on optical near-field processes demonstrated in Section 4 will be applicable to various metamaterial structures aimed at, for instance, environmental applications [41] and telecommunications [42], among others.

Acknowledgments

The authors would like to thank many collaborators for illuminating discussions over several years, in particular T. Kawazoe, T. Yatsui, and W. Nomura. This work was supported in part by Grants-in-Aid for Scientific Research from the Japan Society for the Promotion of Science (JSPS) and the Strategic Information and Communications R&D Promotion Programme (SCOPE) of the Ministry of Internal Affairs and Communications.

Received 12 Jun 2013; revised 3 Aug 2013; accepted 3 Sep 2013; published 10 Sep 2013

SCIENTIFIC REPORTS

OPEN

SUBJECT AREAS:
THEORETICAL PHYSICS
COMPUTATIONAL SCIENCE
NANOPHOTONICS AND PLASMONICS
QUANTUM DOTS

Received
18 March 2013

Accepted
19 July 2013

Published
9 August 2013

Correspondence and requests for materials should be addressed to S.-J.K. (KIM.Songju@nims.go.jp)

Decision Maker based on Nanoscale Photo-excitation Transfer

Song-Ju Kim[1], Makoto Naruse[2], Masashi Aono[3], Motoichi Ohtsu[4] & Masahiko Hara[5]

[1]WPI Center for Materials Nanoarchitectonics (MANA), National Institute for Materials Science (NIMS), 1-1 Namiki, Tsukuba, Ibaraki 305-0044, Japan, [2]Photonic Network Research Institute, National Institute of Information and Communications Technology, 4-2-1 Nukui-kita, Koganei, Tokyo 184-8795, Japan, [3]Earth-Life Science Institute, Tokyo Institute of Technology, 2-12-1 Ookayama, Meguro-ku, Tokyo 152-8550, Japan, [4]Department of Electrical Engineering and Information Systems / Nanophotonics Research Center, Graduate School of Engineering, The University of Tokyo, 2-11-16 Yayoi, Bunkyo-ku, Tokyo 113-8656, Japan, [5]Department of Electronic Chemistry, Interdisciplinary Graduate School of Science and Engineering, Tokyo Institute of Technology, 4259 Nagatsuta, Midori-ku, Yokohama 226-8503, Japan.

Decision-making is one of the most important intellectual abilities of the human brain. Here we propose an efficient decision-making system which uses optical energy transfer between quantum dots (QDs) mediated by optical near-field interactions occurring at scales far below the wavelength of light. The simulation results indicate that our system outperforms the softmax rule, which is known as the best-fitting algorithm for human decision-making behaviour. This suggests that we can produce a nano-system which makes decisions efficiently and adaptively by exploiting the intrinsic spatiotemporal dynamics involving QDs mediated by optical near-field interactions.

Which clothes should I wear? Which restaurant should we choose for lunch? Which article should I read first? We make many decisions in our daily lives. Can we look to nature to find a method for 'efficient decision-making'? For formal discussion, let us focus on the multi-armed bandit problem (BP), stated as follows. Consider a number of slot machines. Each machine when pulled, rewards the player with a coin at a certain probability P_k ($k \in \{1, 2, \ldots, N\}$). For simplicity, we assume that the reward from one machine is the same as that from another machine. To maximise the total amount of reward, it is necessary to make a quick and accurate judgment of which machine has the highest probability of giving a reward. To accomplish this, the player should gather information about many machines in an effort to determine which machine is the best; however, in this process, the player should not fail to exploit the reward from the known best machine. These requirements are not easily met simultaneously, because there is a trade-off between 'exploration' and 'exploitation'. The BP is used to determine the optimal strategy for maximising the total reward with incompatible demands, either by exploiting rewards obtained owing to already collected information or by exploring new information to acquire higher pay-offs in risk taking. Living organisms commonly encounter this 'exploration-exploitation dilemma' in their struggle to survive in the unknown world.

This dilemma has no known generally optimal solution. What strategies do humans and animals exploit to resolve this dilemma? Daw et al. found that the softmax rule is the best-fitting algorithm for human decision-making behaviour in the BP task[1]. The softmax rule uses the randomness of the selection specified by a parameter analogous to the temperature in the Boltzmann distribution (see Methods). The findings of Daw et al. raised many exciting questions for future brain research[2]. How humans and animals respond to the dilemma and the underlying neural mechanisms still remain important and open questions.

The BP was originally described by Robbins[3], although the same problem in essence was also studied by Thompson[4]. However, the optimal strategy is known only for a limited class of problems in which the reward distributions are assumed to be 'known' to the players, and an index called 'the Gittins index' is computed[5,6]. Furthermore, computing the Gittins index in practice is not tractable for many problems. Auer et al. proposed another index expressed as a simple function of the total reward obtained from a machine[7]. This upper confidence bound (UCB) algorithm is used worldwide for many applications, such as Monte-Carlo tree searches[8,9], web content optimization[10] and information and communications technology (ICT)[11–14].

Kim et al. proposed a decision-making algorithm called the 'tug-of-war model' (TOW); it was inspired by the true slime mold *Physarum*[15,16], which maintains a constant intracellular resource volume while collecting environmental information by concurrently expanding and shrinking its branches. The conservation law entails a 'nonlocal correlation' among the branches, that is, the volume increment in one branch is immediately

compensated for by volume decrement(s) in the other branch(es). This nonlocal correlation was shown to be useful for decision-making. Thus, the TOW is a dynamical system which describes spatio-temporal dynamics of a physical object (i.e. an amoeboid organism). The TOW connected 'natural phenomena' to 'decision-making' for the first time. This approach enables us to realise an 'efficient decision maker'–an object which can make decisions efficiently.

Here we demonstrate the physical implementation of the TOW with quantum dots (QDs) and optical near-field interactions by using numerical simulations. Semiconductor QDs have been used for innovative nanophotonic devices[17,18] and optical near-field interactions have been successfully applied to solar cells[19], LEDs[20], diode lasers[21] etc. We have already proposed QD systems for computing applications, such as the constraint satisfaction problem (CSP) and the satisfiability problem (SAT)[22,23]. We introduce a new application for decision-making by making use of optical energy transfer between QDs mediated by optical near-field interactions.

We use three types of cubic QDs with side lengths of a, $\sqrt{2}a$ and $2a$, which are respectively represented by $\mathbf{QD}_S$, $\mathbf{QD}_M$ and $\mathbf{QD}_L$ [Fig. 1(a)]. We assume that five QDs are one-dimensionally arranged in '**L-M-S-M-L**' or '**M-L-S-L-M**' as shown in Fig. 1(b), where **S**, **M** and **L** are simplified representations of $\mathbf{QD}_S$, $\mathbf{QD}_M$ and $\mathbf{QD}_L$, respectively. Owing to the steep electric fields in the vicinity of these QDs, an optical excitation can be transferred between QDs through resonant energy levels mediated by optical near-field interactions[24–28]. Here we should note that an optical excitation is usually transferred from smaller QDs to larger ones owing to energy dissipation processes occurring at larger QDs (details are described in Supplementary Information). In addition, an optical near-field interaction follows Yukawa-type potential, meaning that it could be engineered by inter-dot distances,

$$U(r) = Aexp(-r/a)/r, \tag{1}$$

where r is the inter-dot distance, and A and a are constants[29].

When an optical excitation is generated at $\mathbf{QD}_S$, it is transferred to the lowest energy levels in $\mathbf{QD}_L$s; we observe negligible radiation from $\mathbf{QD}_M$s. However, when the lowest energy levels of $\mathbf{QD}_L$s are occupied by control lights, which induce state-filling effects, the optical excitation at $\mathbf{QD}_S$ is more likely to be radiated from $\mathbf{QD}_M$s[30].

Here we consider the photon radiation from either left $\mathbf{QD}_{ML}$ or right $\mathbf{QD}_{MR}$ as the decision of selecting slot machine A and B, respectively. The intensity of the control light to induce state-filling at the left and right $\mathbf{QD}_L$s is respectively modulated on the basis of the resultant rewards obtained from the chosen slot machine. We call such a decision-making system the 'QD-based decision maker (QDM)'. The QDM can be easily extended to N-armed ($N > 2$) cases, although we demonstrate only the two-armed case in this study.

It should be noted that the optical excitation transfer between QDs mediated by optical near-field interactions is fundamentally probabilistic; this is described below in detail on the basis of density matrix formalism. Until energy dissipation is induced, an optical excitation simultaneously interacts with potentially transferable destination QDs in the resonant energy level. We exploit such probabilistic behaviour for the function of exploration for decision-making.

It also should be emphasised that conventionally, propagating light is assumed to interact with nanostructured matter in a spatially uniform manner (by a well-known principle referred to as long-wavelength approximation) from which state transition rules for optical transitions are derived, including dipole-forbidden transitions. However, such an approximation is not valid for optical near-field interactions in the subwavelength vicinity of an optical source; the inhomogeneity of optical near-fields of a rapidly decaying nature makes even conventionally dipole-forbidden transitions allowable[17,22,23].

We introduce quantum mechanical modelling of the total system based on a density matrix formalism. For simplicity, we assume one excitation system. There are in total 11 energy levels in the system: S_1 in $\mathbf{QD}_S$; ML_1 and ML_2 in $\mathbf{QD}_{ML}$; LL_1, LL_2 and LL_3 in $\mathbf{QD}_{LL}$; MR_1 and MR_2 in $\mathbf{QD}_{MR}$; LR_1, LR_2 and LR_3 in $\mathbf{QD}_{LR}$. Therefore the number of different states occupying these energy levels is 12 including the vacancy state, as schematically shown in Fig. 1(b). Because a fast inter-sublevel transition in $\mathbf{QD}_L$s and $\mathbf{QD}_M$s is assumed, it is useful to establish theoretical treatments on the basis of the exciton population in the system composed of $\mathbf{QD}_S$, $\mathbf{QD}_M$s and $\mathbf{QD}_L$s, where 11 basis states are assumed, as schematically illustrated in Fig. 1(c).

Results

Here we propose the QDM that is based on the five QD system, as shown in Fig. 1(b). Through optical near-field interactions, an optical excitation generated at $\mathbf{QD}_S$ is transferred to the lowest energy levels in the largest-size QD, namely the energy level LL_1 or LR_1. However, when LL_1 and LR_1 are occupied by other excitations, the input excitation generated at S_1 should be relaxed from the middle-sized QD, that is, ML_1 and MR_1. The idea of the QDM is to induce state-filling at LL_1 and/or LR_1 while observing radiations from ML_1 and MR_1. If radiation occurs in ML_1 (MR_1), then we consider that the system selects machine A (B). We can modulate these radiation probabilities by changing the intensity of the incident light.

We adopt the intensity adjuster (IA) to modulate the intensity of incident light to large QDs, as shown at the bottom of Fig. 2. The initial position of the IA is zero. In this case, the same intensity of light is applied to both LL_1 and LR_1. If we move the IA to the right, the intensity of the right increases and that of the left decreases. In contrast, if we move the IA to the left, the intensity of the left increases and that of the right decreases. This situation can be described by the following relaxation rate parameters as functions of the IA position j: $\Gamma_{LR_2} = \frac{1}{100} - \frac{1}{10000}j + \frac{1}{100000}$, and $\Gamma_{LL_2} = \frac{1}{100} + \frac{1}{10000}j + \frac{1}{100000}$.

In advance, we calculated two (right and left) radiation probabilities from ML_1 and MR_1, namely $S_A(j)$ and $S_B(j)$, in each of the 201 states ($-100 \leq j \leq 100$) by using the quantum master equation of the total system (see Supplementary Information). There are 101 independent values. Results are shown in Fig. 2 as the solid red line. If $j > 0$, the intensity of incident light to the LR_1 increases (the Γ_{LR_2} decreases by the amount of j/10, 000), while that to the LL_1 decreases (the Γ_{LL_2} increases by the amount of j/10, 000). Correspondingly, the radiation probability $S_B(j)$ is larger than $S_A(j)$ for $j > 0$, while the radiation probability $S_A(j)$ is larger than $S_B(j)$ for $j < 0$. For $j < -100$, we used probabilities $S_A(-100)$ and $S_B(-100)$. Similarly, we used $S_A(100)$ and $S_B(100)$ for $j > 100$.

The dynamics of the IA is set up as follows. The IA position is moved according to the reward from a slot machine. Here the parameter D is a unit of the move.

1. Set the IA position j to 0.
2. Select machine A or B by using $S_A(j)$ and $S_B(j)$.
3. Play on the selected machine.
4. If a coin is dispensed, then move the IA to the selected machine's direction, that is, $j = j - D$ for A, and $j = j + D$ for B.
5. If no coin is dispensed, then move the IA to the inverse direction of the selected machine, that is, $j = j + D$ for A, and $j = j - D$ for B.
6. Repeat step (2).

In this way, the system selects A or B, and the IA moves to the right or left according to the reward.

Figures 3(a) and (b) demonstrates the efficiency (cumulative rate of correct selections) for the QDM (solid red line) and the softmax rule with optimised parameter τ (dashed line) in the case where the reward probabilities of the slot machines are (a) $P_A = 0.2$ and $P_B =$

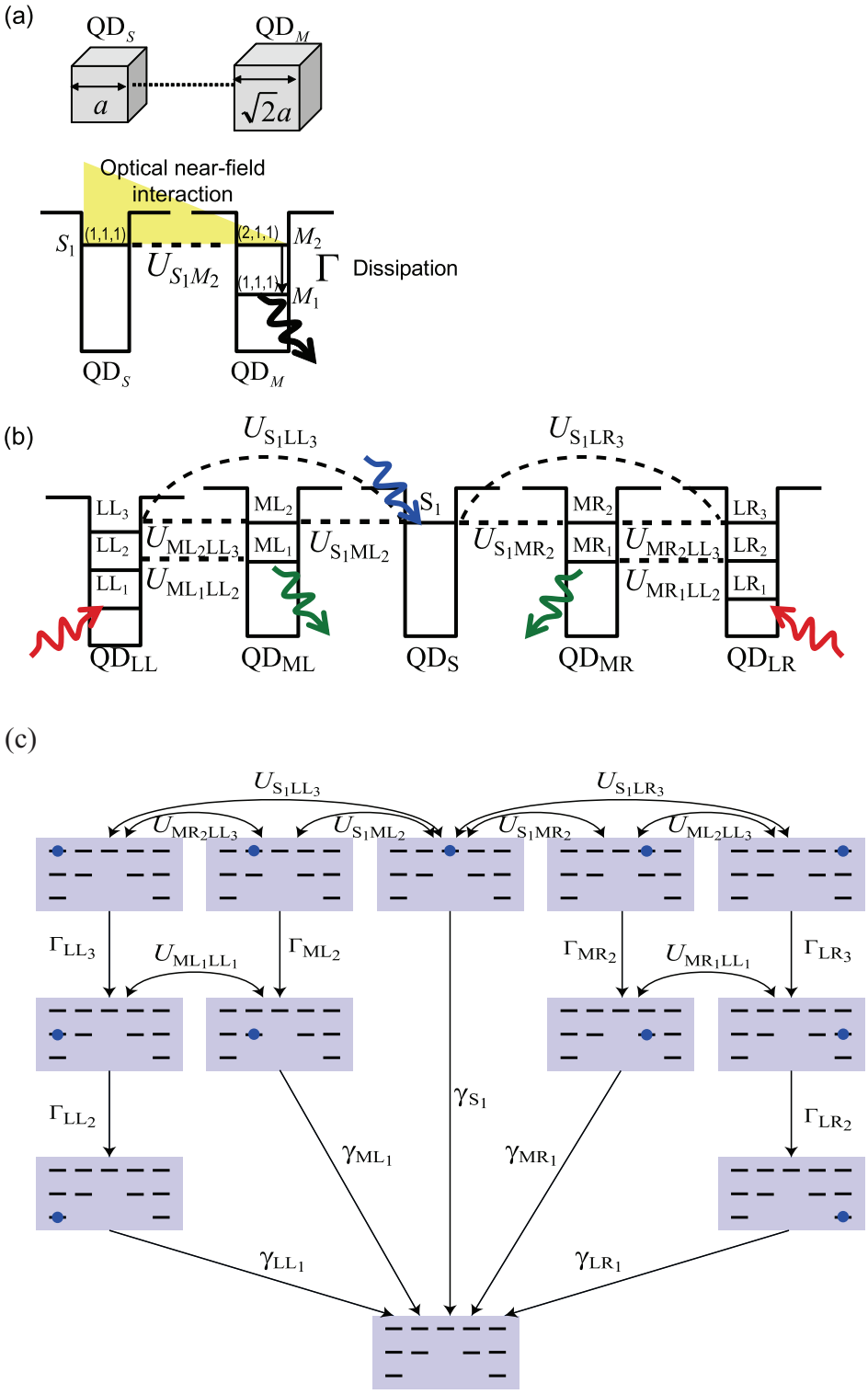

Figure 1 | (a) Energy transfer between quantum dots (QDs). Two cubic quantum dots $\mathbf{QD}_S$ and $\mathbf{QD}_M$, whose side lengths are a and $\sqrt{2}a$, respectively, are located close to each other. Optical excitations in $\mathbf{QD}_S$ can be transferred to neighbouring structures $\mathbf{QD}_M$ via optical near-field interactions, denoted by $U_{S_1M_2}$ [29], because there exists a resonance between the level of quantum number (1, 1, 1) for $\mathbf{QD}_S$ (denoted by S_1) and that of quantum number (2, 1, 1) for $\mathbf{QD}_M$ (M_2). (b) QD-based decision maker. The system consists of five QDs denoted $\mathbf{QD}_{LL}$, $\mathbf{QD}_{ML}$, $\mathbf{QD}_S$, $\mathbf{QD}_{MR}$ and $\mathbf{QD}_{LR}$. The energy levels in the system are summarised as follows. The (2, 1, 1)-level of $\mathbf{QD}_{ML}$, $\mathbf{QD}_{MR}$, $\mathbf{QD}_{LL}$ and $\mathbf{QD}_{LR}$ is respectively denoted by ML_2, MR_2, LL_2 and LR_2. The (1, 1, 1)-level of $\mathbf{QD}_{ML}$, $\mathbf{QD}_{MR}$, $\mathbf{QD}_{LL}$ and $\mathbf{QD}_{LR}$ is respectively denoted by ML_1, MR_1, LL_1 and LR_1. The (2, 2, 2)-level of $\mathbf{QD}_{LL}$ and $\mathbf{QD}_{LR}$ is respectively denoted by LL_3 and LR_3. The optical near-field interactions are $U_{S_1Mi_2}$, $U_{S_1Li_3}$, $U_{Mi_2Li_3}$ and $U_{Mi_1Li_2}$ ($i = L, R$). (c) Schematic summary of the state transitions. Shown are the relaxation rates Γ_{LL_3}, Γ_{LL_2}, Γ_{ML_2}, Γ_{MR_2}, Γ_{LR_3} and Γ_{LR_2}, and the radiative decay rates γ_{LL_1}, γ_{ML_1}, γ_{S_1}, γ_{MR_1} and γ_{LR_1}.

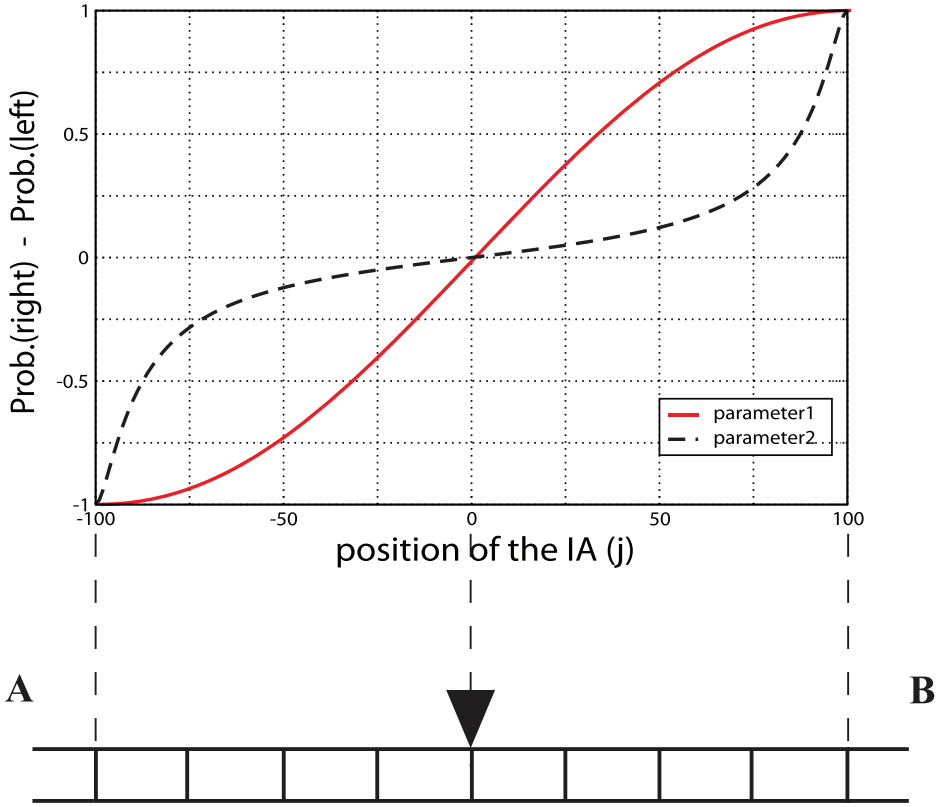

Figure 2 | Intensity adjuster (IA) and difference between radiation probabilities from ML_1 and MR_1. The difference between radiation probabilities $S_B(j) - S_A(j)$ as a function of the IA position j, which are calculated from the quantum master equation of the total system, is denoted by the solid red line. Here we used the parameters $\Gamma_{LR_2} = \frac{1}{100} - \frac{1}{10000}\, j + \frac{1}{100000}$, and $\Gamma_{LL_2} = \frac{1}{100} + \frac{1}{10000}\, j + \frac{1}{100000}$. As supporting information, the dashed line denotes the case where $\Gamma_{LR_2} = \frac{1}{10 + 500(100 + j)}$, and $\Gamma_{LL_2} = \frac{1}{10 - 500(100 - j)}$.

0.8 and (b) $P_A = 0.4$ and $P_B = 0.6$. In these cases, the correct selection is 'B' because P_B is larger than P_A. These cumulative rates of correct selections are average values for each 1, 000 samples. Hence, each value corresponds to the average number of coins acquired from the slot machines. Even with a non-optimised parameter D, the performance of the QDM is higher than that of the softmax rule with optimised parameter τ, in a wide parameter range of $D = 10$–100 although we show only the $D = 50$ case in Figs. 3(a) and (b).

Figure 3(c) shows the adaptability (percentage of correct selections) for the QDM (red line) and the softmax rule (black line). The parameter τ of the softmax rule was optimised to obtain the fastest adaptation. The switching occurs at time steps $t = 3, 000$ and 6, 000. Up to $t = 3, 000$, the systems adapt to the initial environment ($P_A = 0.4$ and $P_B = 0.6$). Between $t = 3, 000$ and 6, 000, the systems adapt to the new environment ($P_A = 0.6$ and $P_B = 0.4$). Beyond $t = 6, 000$, the systems adapt to the first environment again ($P_A = 0.4$ and $P_B = 0.6$). It is noted that we set $\beta = 0$ at the switching points because the softmax rule cannot detect the environmental change. Nevertheless, the adaptation (slope) of the QDM was found to be faster (steeper) than that of the softmax rule to the initial environment ($P_A = 0.4$ and $P_B = 0.6$) as well as to the new environment ($P_A = 0.6$ and $P_B = 0.4$). Thus, we can conclude that the QDM has better adaptability than the softmax rule.

Discussion

In summary, we have demonstrated a QDM on the basis of the optical energy transfer occurring far below the wavelength of light by using computer simulations. This paves a new way for utilising quantum nanostructures and inherent spatiotemporal dynamics of optical near-field interactions for totally new application, that is, 'efficient decision-making'. Surprisingly, the performance of the QDM is better than that of the softmax rule in our simulation studies. Moreover, the QDM exhibits superior flexibility in adapting to environmental changes, which is an essential property for living organisms to survive in uncertain environments.

Finally, there are a few additional remarks. First, it has been demonstrated that the optical energy transfer is about 10^4 times more energy efficient as compared with the bit-flip energy of conventional electrical devices[31]. Furthermore, nanophotonic devices based on optical energy transfer with such energy efficiency have been experimentally demonstrated, including input and output interfaces with the optical far-field[32]. These studies indicate that the QDM is highly energy efficient. The second remark is about the experimental implementation of size- and position-controlled quantum nanostructures. Kawazoe et al. successfully demonstrated a room-temperature-operated two-layer QD device by utilising highly sophisticated molecular beam epitaxy (MBE)[17]. In addition, Akahane et al. succeeded in realising more than 100 layers of size-controlled QDs[33]. Besides, DNA-based self-assembly technology can also be a solution in realising controlled nanostructures[34]. Other nanomaterial systems, such as nanodiamonds[35], nanowires[36], nanostructures formed by droplet epitaxy[37], have also been showing rapid progress. These technologies provide feasible solutions. Finally, in the demonstration of decision-making in this study, for simplicity, we dealt with restricted problems, namely, $P_A + P_B = 1$. However, general problems can also be solved by the extended QDM although the IA dynamics becomes a bit more complicated. The IA and its dynamics can also be implemented by using QDs.

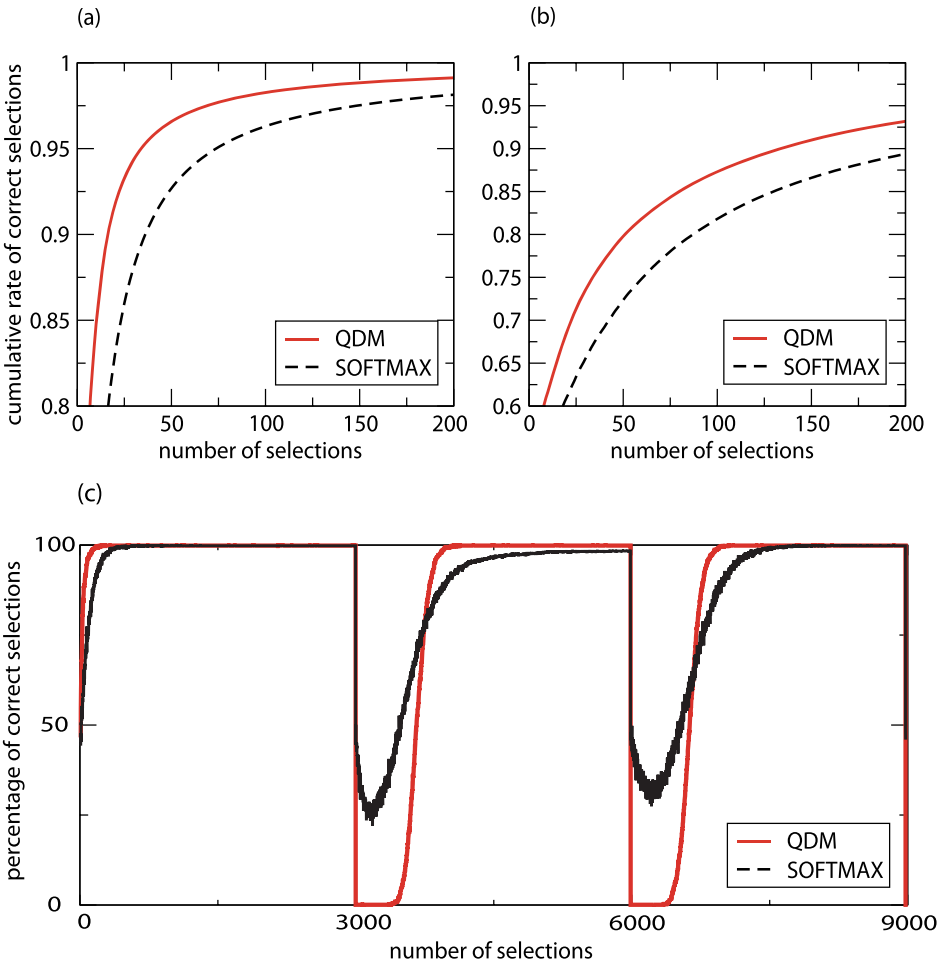

Figure 3 | (a) Efficiency comparison 1. The efficiency comparison between the QDM and the softmax rule is for slot machine reward probabilities of $P_A = 0.2$ and $P_B = 0.8$. The cumulative rate of correct selections for the QDM with fixed parameter $D = 50$ (solid red line) and the softmax rule with optimised parameter $\tau = 0.40$ (dashed line) are shown. (b) Efficiency comparison 2. The efficiency comparison between the QDM and the softmax rule for $P_A = 0.4$ and $P_B = 0.6$. The cumulative rate of correct selections for the QDM with fixed parameter $D = 50$ (solid red line) and the softmax rule with optimised parameter $\tau = 0.25$ (dashed line) are shown. (c) Adaptability comparison. The adaptability comparison between the QDM and the softmax rule for $P_A = 0.4$ and $P_B = 0.6$. In every 3,000 steps, two reward probabilities switch. The percentage of correct selections for the QDM with fixed parameter $D = 50$ (red line), and the softmax rule with the optimised parameter $\tau = 0.08$ (black line) are shown. In this simulation, we used the forgetting parameter $\alpha = 0.999$ (see Methods).

Methods

Calculation of radiation probabilities $S_A(j)$ and $S_B(j)$. Using the quantum Liouville equation (see Supplementary Information), we can calculate the probabilities of radiation from ML_1 and MR_1. We used the following relaxation rate and radiative decay parameters as shown in Fig. 1(c), $\gamma_{S_1} = \frac{1}{(2)^3 1{,}000}$, $\gamma_{MR_1} = \frac{1}{(\sqrt{2})^3 1{,}000}$, $\gamma_{ML_1} = \frac{1}{(\sqrt{2})^3 1{,}000}$, $\gamma_{LR_1} = \frac{1}{1{,}000}$, $\gamma_{LL_1} = \frac{1}{1{,}000}$, $\Gamma_{MR_2} = \frac{1}{10}$, $\Gamma_{LR_3} = \frac{1}{10}$, $\Gamma_{LR_2} = \frac{1}{100} - \frac{1}{10{,}000}j + \frac{1}{100{,}000}$, $\Gamma_{ML_2} = \frac{1}{10}$, $\Gamma_{LL_3} = \frac{1}{10}$ and $\Gamma_{LL_2} = \frac{1}{100} + \frac{1}{10{,}000}j + \frac{1}{100{,}000}$, where j represents the position of the intensity adjuster (IA).

Note that we used the following optical near-field interaction parameters so that the QDs are one-dimensionally arranged in "**M-L-S-L-M**" order for this calculation: $U_{S_1MR_2} = \frac{1}{10{,}000{,}000}$, $U_{S_1LR_3} = \frac{1}{100}$, $U_{MR_2LR_3} = \frac{1}{10{,}000}$, $U_{MR_1LR_2} = \frac{1}{10{,}000}$, $U_{S_1ML_2} = \frac{1}{10{,}000{,}000}$, $U_{S_1LL_3} = \frac{1}{100}$, $U_{ML_2LL_3} = \frac{1}{10{,}000}$ and $U_{ML_1LL_2} = \frac{1}{10{,}000}$. Here we used $A = 0.1$ and $a = 10^{-9}$ for the parameters in eq.(1). Then, the distance between $\mathbf{QD}_S$ and $\mathbf{QD}_L$ (r_1) is 20 nm, and the distance between $\mathbf{QD}_L$ and $\mathbf{QD}_M$ (r_2) is 24.5 nm, such that $U(r_1) = \frac{1}{100}$ and $U(r_2) = \frac{1}{10{,}000}$. Finally, we obtained two radiation probabilities whose maximum ratio is 8520.82. The difference between radiation probabilities, $S_B(j) - S_A(j)$, is shown by the solid red line in Fig. 2.

Algorithms. *Softmax rule.* In the softmax rule, the probability of selecting A or B, $P'_A(t)$ or $P'_B(t)$, is given by the following Boltzmann distributions:

$$P'_A(t) = \frac{\exp[\beta Q'_A(t)]}{\exp[\beta Q'_A(t)] + \exp[\beta Q'_B(t)]}, \tag{2}$$

$$P'_B(t) = \frac{\exp[\beta Q'_B(t)]}{\exp[\beta Q'_A(t)] + \exp[\beta Q'_B(t)]}, \tag{3}$$

where $Q'_k(k \in \{A,B\})$ is the estimated reward probability of slot machines k, denoted by P_k, and 'temperature' β is a parameter. These estimates are given as,

$$Q'_k(t) = \frac{W_k(t)}{M_k(t)}, \tag{4}$$

$$W_k(t) = w_k(t) + \alpha W_k(t-1), \tag{5}$$

$$M_k(t) = m_k(t) + \alpha M_k(t-1). \tag{6}$$

Here $w_k(t)$ ($k \in \{A, B\}$) is 1 if a reward is dispensed from machine k at time t, otherwise 0, and $m_k(t)$ ($k \in \{A, B\}$) is 1 if machine k is selected at time t, otherwise 0. α is a parameter that can control the forgetting of past information. We used $\alpha = 1$ for Figs. 3(a) and (b), and $\alpha = 0.999$ for (c).

In our study, the 'temperature' β was modified to a time-dependent form as follows:

$$\beta(t) = \tau \cdot t. \tag{7}$$

Here, τ is a parameter that determines the growth rate. $\beta = 0$ corresponds to a random selection, and $\beta \to \infty$ corresponds to a greedy action. Greedy action means that the player selects A if $Q'_A > Q'_B$, or selects B if $Q'_A < Q'_B$.

Dynamics of the intensity adjuster. We adopt the IA to modulate the intensity of incident light to large QDs as shown at the bottom of Fig. 2. The dynamics of the IA also uses estimates Q_k ($k \in \{A, B\}$) which are different from those of the softmax rule. The IA position j is determined by

$$j = floor(Q_B - Q_A), \tag{8}$$

$$Q_k(t) = r_k(t) + \alpha Q_k(t-1), \tag{9}$$

where the function $floor(x)$ truncates the decimal point. $r_k(t)$ ($k \in \{A, B\}$) is D if a reward is dispensed from the machine k at time t, $-D$ if a reward is not dispensed from the machine k and 0 if the system does not select the machine k. Here D is a parameter and α is also a parameter that can control forgetting of past information. We used $\alpha = 1$ for Figs. 3(a) and (b), and $\alpha = 0.999$ for (c).

If we set $\alpha = 1$, the dynamics can be stated by the following rules.

1. If a coin is dispensed, then move the IA to the selected machine's direction, that is, $j = j - D$ for A and $j = j + D$ for B.
2. If a coin is not dispensed, then move the IA to the inverse direction of the selected machine, that is, $j = j + D$ for A and $j = j - D$ for B.

1. Daw, N., O'Doherty, J., Dayan, P., Seymour, B. & Dolan, R. Cortical substrates for exploratory decisions in humans. *Nature* **441**, 876–879 (2006).
2. Cohen, J., McClure, S. & Yu, A. Should I stay or should I go? How the human brain manages the trade-off between exploitation and exploration. *Phil. Trans. R. Soc. B* **362**(1481), 933–942 (2007).
3. Robbins, H. Some aspects of the sequential design of experiments. *Bull. Amer. Math. Soc.* **58**, 527–536 (1952).
4. Thompson, W. On the likelihood that one unknown probability exceeds another in view of the evidence of two samples. *Biometrika* **25**, 285–294 (1933).
5. Gittins, J. & Jones, D. A dynamic allocation index for the sequential design of experiments. In: Gans, J. (Eds.), *Progress in Statistics* North Holland, 241–266 (1974).
6. Gittins, J. Bandit processes and dynamic allocation indices. *J. R. Stat. Soc. B* **41**, 148–177 (1979).
7. Auer, P., Cesa-Bianchi, N. & Fischer, P. Finite-time analysis of the multiarmed bandit problem. *Machine Learning* **47**, 235–256 (2002).
8. Kocsis, L. & Szepesvári, C. Bandit based monte-carlo planning. *ECML2006, LNAI 4212,* Springer, 282–293 (2006).
9. Gelly, S., Wang, Y., Munos, R. & Teytaud, O. Modification of UCT with patterns in Monte-Carlo Go. *RR-6062-INRIA,* 1–19 (2006).
10. Agarwal, D., Chen, B.-C. & Elango, P. Explore/exploit schemes for web content optimization. *Proc. of ICDM2009,* http://dx.doi.org/10.1109/ICDM.2009.52 (2009).
11. Gai, Y., Krishnamachari, B. & Jain, R. Learning multiuser channel allocations in cognitive radio networks: A combinatorial multi-armed bandit formulation. *Proc. of DySPAN2010,* http://dx.doi.org/10.1109/DYSPAN.2010.5457857 (2010).
12. Lai, L., Gamal, H., Jiang, H. & Poor, V. Cognitive medium access: Exploration, exploitation, and competition. *IEEE Trans. on Mobile Computing* **10**, 239–253 (2011).
13. Kim, S.-J., Aono, M., Nameda, E. & Hara, M. Tug-of-war model for competitive multi-armed bandit problem: Amoeba-inspired algorithm for cognitive medium access. *Proc. of NOLTA2012,* 590–593 (2012).
14. Lazaar, N., Hamadi, Y., Jabbour, S. & Sebag, M. Cooperation control in parallel SAT solving: A multi-armed bandit approach. *RR-8070-INRIA,* 1–15 (2012).
15. Kim, S.-J., Aono, M. & Hara, M. Tug-of-war model for multi-armed bandit problem. *UC2010, LNCS 6079,* Springer, 69–80 (2010).
16. Kim, S.-J., Aono, M. & Hara, M. Tug-of-war model for the two-bandit problem: Nonlocally-correlated parallel exploration via resource conservation. *BioSystems* **101**, 29–36 (2010).
17. Kawazoe, T. *et al*. Two-dimensional array of room-temperature nanophotonic logic gates using InAs quantum dots in mesa structures. *Appl. Phys. B* **103**, 537–546 (2011).
18. Crooker, S. A., Hollingworth, J. A., Tretiak, S. & Klimov, V. I. Spectrally resolved dynamics of energy transfer in quantum-dot assemblies: Towards engineered energy flows in artificial materials. *Phys. Rev. Lett.* **89**, 186802 (2002).
19. Yukutake, S., Kawazoe, T., Yatsui, T., Nomura, W., Kitamura, K. & Ohtsu, M. Selective photocurrent generation in the transparent wavelength range of a semiconductor photovoltaic device using a phonon-assisted optical near-field process. *Appl. Phys. B* **99**, 415–422 (2010).
20. Kawazoe, T., Mueed, M. A. & Ohtsu, M. Highly efficient and broadband Si homojunction structured near-infrared light emitting diodes based on the phonon-assisted optical near-field process. *Appl. Phys. B* **104**, 747–754 (2011).
21. Kawazoe, T., Ohtsu, M., Akahane, K. & Yamamoto, N. Si homojunction structured near-infrared laser based on a phonon-assisted process. *Appl. Phys. B* **107**, 659–663 (2012).
22. Naruse, M. *et al*. Spatiotemporal dynamics in optical energy transfer on the nanoscale and its application to constraint satisfaction problems. *Physical Review B* **86**, 125407 (2012).
23. Aono, M. *et al*. Amoeba-inspired nanoarchitectonic computing: Solving intractable computational problems using nanoscale photoexcitation transfer dynamics. *Langmuir* **29**, 7557–7564 (2013).
24. Ohtsu, M., Kawazoe, T., Yatsui, T. & Naruse, M. Nanophotonics: Application of dressed photons to novel photonic devices and systems. *IEEE JSTQE* **14**, 1404–1417 (2008).
25. Nomura, W., Yatsui, Y., Kawazoe, T., Naruse, M. & Ohtsu, M. Structural dependency of optical excitation transfer via optical near-field interactions between semiconductor quantum dots. *Appl. Phys. B* **100**, 181–187 (2010).
26. Unold, I. T., Mueller, K., Lienau, C., Elsaesser, T. & Wiek, A. D. Optical control of excitons in a pair of quantum dots coupled by the dipole-dipole interaction. *Phys. Rev. Lett.* **94**, 137404 (2005).
27. Vasa, I. P. *et al*. Coherent excitonsurface-plasmon-polariton interaction in hybrid metal-semiconductor nanostructures. *Phys. Rev. Lett.* **101**, 116801 (2008).
28. Franzl, T., Klar, T. A., Schietinger, S., Rogach, A. L. & Feldmann, J. Exciton recycling in graded gap nanocrystal structures. *Nano Lett.* **4**, 1599–1603 (2004).
29. Ohtsu, M., Kobayashi, K., Kawazoe, T., Yatsui, T. & Naruse, M. *Principles of Nanophotonics.* Taylor and Francis (2008).
30. Naruse, M. *et al*. Skew Dependence of Nanophotonic Devices based on Optical Near-Field Interactions. *ACM JETC* **8**, 4:1–4:12 (2012).
31. Naruse, M., Hori, H., Kobayashi, K., Holmstrom, P., Thylen, L. & Ohtsu, M. Lower bound of energy dissipation in optical excitation transfer via optical near-field interactions. *Optics Express* **18**, A544–A553 (2010).
32. Naruse, M. *et al*. Energy dissipation in energy transfer mediated by optical near-field interactions and their interfaces with optical far-fields. *Appl. Phys. Lett.* **100**, 241102 (2012).
33. Akahane, K., Yamamoto, N. & Tsuchiya, M. Highly stacked quantum-dot laser fabricated using a strain compensation technique. *Appl. Phys. Lett.* **93**, 041121 (2008).
34. Pistol, C., Dwyer, C. & Lebeck, A. R. Nanoscale Optical Computing Using Resonance Energy Transfer Logic. *IEEE Micro.* **28**, 7–18 (2008).
35. Cuche, A. *et al*. Near-field optical microscopy with a nanodiamond-based single-photon tip. *Opt. Express* **17**, 19969–19980 (2009).
36. Benson, O. Assembly of hybrid photonic architectures from nanophotonic constituents. *Nature* **480**, 193–199 (2011).
37. Mano, T. & Koguchi, N. Nanometer-scale GaAs ring structure grown by droplet epitaxy. *J. Cryst. Growth* **278**, 108–112 (2005).

Acknowledgements

This work was done when S.-J. K., M. A. and M. H. belonged to RIKEN Advanced Science Institute, which was reorganized and was integrated into RIKEN as of the end of March, 2013. This work was supported in part by the Strategic Information and Communications R&D Promotion Program (SCOPE) of the Ministry of Internal Affairs and Communications, and Grant-in-Aid for Scientific Research from the Japan Society of the Promotion of Science.

Author contributions

S.-J.K., M.N. and M.A. designed research, S.-J.K. performed the computer simulations and analysed the data, M.N. and M.A. helped with the modelling. M.O. and M.H. helped with the analysis. S.-J.K. and M.N. wrote the manuscript. All atuthors reviewed the manuscript.

Additional information

Supplementary information accompanies this paper at http://www.nature.com/scientificreports

Competing financial interests: All authors along with others, have filed a patent application on the technology described here.

How to cite this article: Kim, S.-J., Naruse, M., Aono, M., Ohtsu, M. & Hara, M. Decision Maker based on Nanoscale Photo-excitation Transfer. *Sci. Rep.* **3**, 2370; DOI:10.1038/srep02370 (2013).

nature photonics

LETTERS

PUBLISHED ONLINE: 7 JULY 2013 | DOI: 10.1038/NPHOTON.2013.179

Brightening of excitons in carbon nanotubes on dimensionality modification

Yuhei Miyauchi[1,2]*, Munechiyo Iwamura[1], Shinichiro Mouri[1], Tadashi Kawazoe[3], Motoichi Ohtsu[3] and Kazunari Matsuda[1]

Despite the attractive one-dimensional characteristics of carbon nanotubes[1], their typically low luminescence quantum yield, restricted because of their one-dimensional nature[2–9], has limited the performance of nanotube-based light-emitting devices[10,11]. Here, we report the striking brightening of excitons (bound electron–hole pairs)[12,13] in carbon nanotubes through an artificial modification of their effective dimensionality from one dimension to zero dimensions. Exciton dynamics in carbon nanotubes with luminescent, local zero-dimension-like states generated by oxygen doping[14] were studied as model systems. We found that the luminescence quantum yield of the excitons confined in the zero-dimension-like states can be more than at least one order larger (∼18%) than that of the intrinsic one-dimensional excitons (typically ∼1%), not only because of the reduced non-radiative decay pathways but also due to an enhanced radiative recombination probability beyond that of intrinsic one-dimensional excitons. Our findings are extendable to the realization of future nanoscale photonic devices including a near-infrared single-photon emitter operable at room temperature.

The low luminescence quantum yield of semiconducting carbon nanotubes (hereafter, termed (carbon) nanotubes), which is typically, at most, only a few percent for dispersed nanotubes[7,8,15–17], is deeply related to their one-dimensional nature. The balance between radiative and non-radiative relaxation rates (that is, the probability) of electron–hole bound states, termed excitons[12,13], determines the nanotube luminescence quantum yield. Fast non-radiative decay, which dominates exciton recombination in nanotubes and results in their low luminescence quantum yield, is mainly caused by the quenching of one-dimensional mobile excitons due to the rapid collision between these excitons and local quencher states, which include nanotube defects and end sites[4–6,8,9]. Moreover, the temperature-limited radiative relaxation rate ($\propto T^{-1/2}$), characteristic of one-dimensional excitons, substantially reduces the quantum yield at room temperature[2,3,7]. Efforts to improve the luminescence quantum yield by reducing the defect quenching of excitons[18,19] have been reported. Conversely, if a local defect is not an exciton quencher[18–20] but is luminescent by virtue of appropriate local electronic structures[14,21–25], the local state may function as a zero-dimension-like quantum state that captures mobile excitons and converts them to photons (as shown in Fig. 1) with a radiative relaxation rate possibly lying beyond that of intrinsic one-dimensional excitons. Therefore, one-dimensional nanotubes with luminescent, local zero-dimension-like states offer a unique opportunity for photophysical investigation of nearly ideal zero-dimensional–one-dimensional hybrid systems. Moreover, understanding the excitonic properties of these states can lead to the development of novel strategies for brightening nanotube excitons beyond the intrinsic limit for future photonics applications.

We examined the excitonic characteristics of luminescent, local zero-dimension-like states embedded in one-dimensional carbon nanotubes. Figure 2a shows photoluminescence excitation maps of carbon nanotubes with and without the doping of oxygen atoms that generate these local states[14]. The distinct luminescence peak at E_{11}^* (∼1.07 eV) appears after oxygen-doping treatment[14] (see Methods and Supplementary Section S1), while the change in the intrinsic luminescence feature at E_{11} (∼1.25 eV) is small. The luminescence peak at E_{11}^* has been attributed to light emission from the zero-dimension-like local states generated by oxygen doping in carbon nanotubes[14]. The excitation maxima at E_{11} and E_{11}^* are coincident with the second sub-band exciton energy E_{22} of (6,5) nanotubes, indicating that the photogenerated intrinsic excitons are converted into local excitons with energy E_{11}^*.

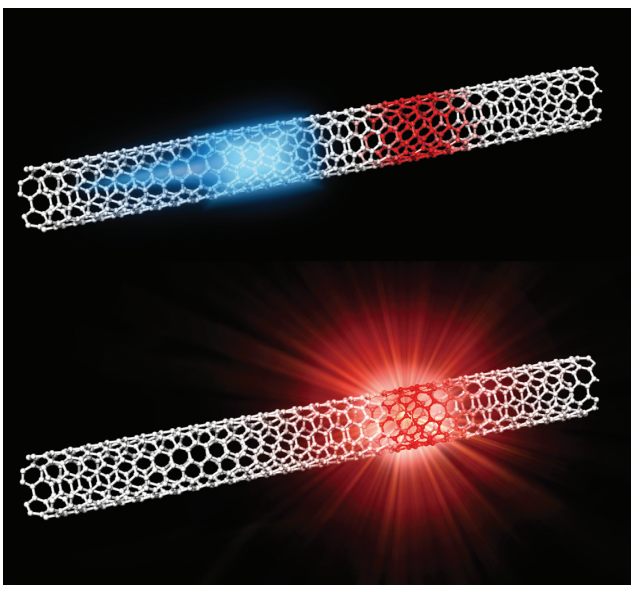

Figure 1 | Schematic of a carbon nanotube with a luminescent local state. A photoexcited intrinsic exciton is mobile along the nanotube axis (blue spot). When the mobile exciton collides with a local state (red spot), where the exciton energy becomes lower than that of the intrinsic state, the mobile exciton can be trapped by the local state. If the local state has no efficient non-radiative decay paths, it should work as a luminescence centre, and the exciton can decay radiatively by emitting a photon.

[1]Institute of Advanced Energy, Kyoto University, Uji, Kyoto 611-0011, Japan, [2]PRESTO, Japan Science and Technology Agency, 4-1-8 Honcho Kawaguchi, Saitama 332-0012, Japan, [3]Department of Electrical Engineering and Information Systems, Graduate School of Engineering, The University of Tokyo, Hongo 7-3-1, Bunkyo-ku, Tokyo 113-8656, Japan. *e-mail: miyauchi@iae.kyoto-u.ac.jp

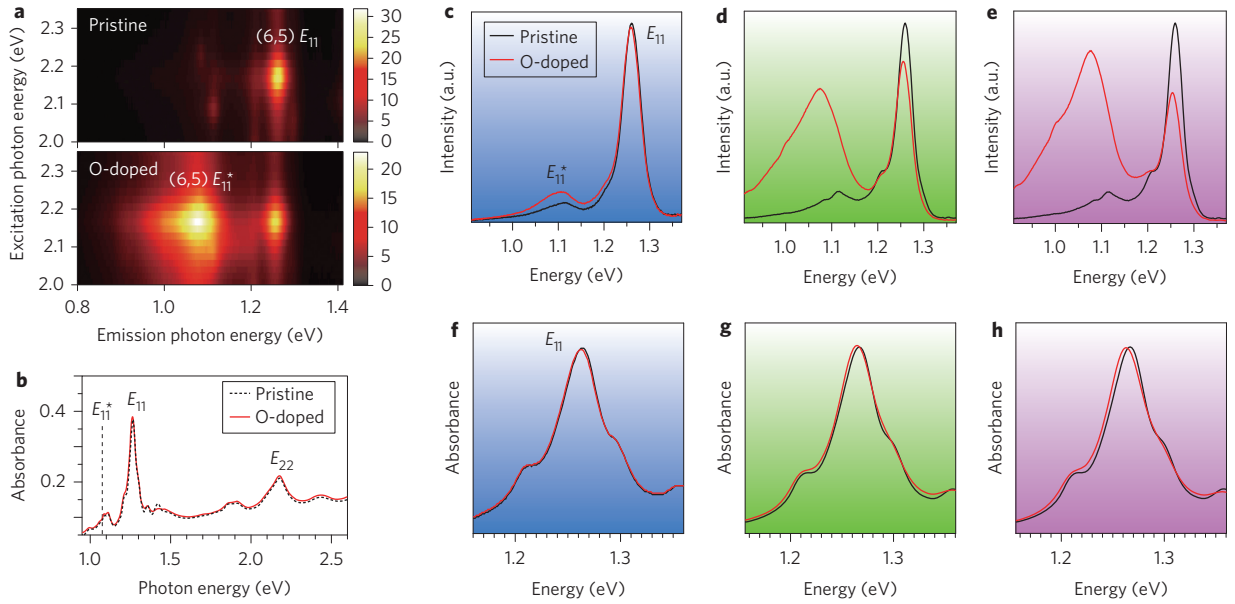

Figure 2 | Optical spectra of carbon nanotubes with luminescent local states. a, Photoluminescence excitation maps of nanotubes before (pristine) and after (O-doped) oxygen-doping treatment. Vertical and horizontal axes correspond to the excitation and emission photon energies, respectively. Colours in the map correspond to the photoluminescence intensity (white being the highest and black the lowest). **b**, Optical absorption spectra of the pristine (black dotted curve) and oxygen-doped (red solid curve) nanotubes. The vertical dotted line indicates energy E_{11}^* (~1.07 eV). **c**–**e**, Photoluminescence spectra of the various nanotubes with variable oxygen-doping measured under E_{22} energy excitation (2.175 eV). The slight differences observed for the pristine spectra are due to the use of different batches of starting material. **f**–**h**, Optical absorption spectra of various nanotubes around the E_{11} energy. The photoluminescence and absorption spectra with the same background colours [(**c**,**f**), (**d**,**g**), (**e**,**h**)] were taken from the same nanotubes. In **c**–**h**, the black and red solid curves correspond to optical spectra of pristine and oxygen-doped carbon nanotubes, respectively.

Hereafter, we denote the intrinsic exciton state with energy E_{ii} as X_{ii}, and the oxygen-derived local states with energy E_{11}^* as X_{11}^*. Figure 2b compares the absorption spectra of pristine (non-doped) and oxygen-doped nanotubes. The distinct absorption peaks of intrinsic X_{11} and X_{22} excitons of (6,5) nanotubes are almost unchanged, and there are no prominent absorption features originating from the X_{11}^* excitons around E_{11}^*. The small changes in the absorption spectra indicate that the number density of the X_{11}^* sites is very small (deduced to be on the order of one X_{11}^* site per micrometre; Supplementary Section S4), and most parts of the nanotubes, except for the oxygen-doped sites, remain unchanged.

Figure 2c–h compares the photoluminescence and absorption spectra of various oxygen-doped nanotubes with different X_{11}^* peak intensities, which reflect the variable density of the local X_{11}^* states. We see a considerable change in the photoluminescence spectra of the pristine nanotubes, as shown in Fig. 2c–e. As the integrated photoluminescence intensity of the X_{11} peak at E_{11} (I_{11}) decreases slightly, that of the X_{11}^* peak at E_{11}^* (I_{11}^*) appears and increases drastically.

In Fig. 3a we plot the integrated photoluminescence intensity of the X_{11}^* state, I_{11}^*, as a function of the decreasing X_{11} photoluminescence intensity ΔI_{11}. Here, ΔI_{11} is defined as $\Delta I_{11} = |I_{11} - I_0|$, where I_0 is the X_{11} photoluminescence intensity of the pristine nanotubes. A linear relationship was found to exist between the change in I_{11} (ΔI_{11}) and the value of I_{11}^*, as indicated by the dotted, straight line in Fig. 3a, where the slope of the line, $I_{11}^*/\Delta I_{11}$, is 7.5 ± 0.6. This linear relation contains rich information on the photophysical parameters of the zero-dimension-like X_{11}^* states.

In this study, as shown in Fig. 3b, we consider the migration (diffusion) of the intrinsic one-dimensional excitons along the nanotube and the successive trapping at extrinsic local quenching sites (defect sites), with a density of n_q, or at local luminescent sites (X_{11}^* sites), with a density of n_x. Based on a one-dimensional diffusion-limited exciton contact-quenching mechanism[8,9] that predicts the luminescence quantum yield η of one-dimensional excitons, where $\eta \propto (n_q + n_x)^{-2}$, the ratio of I_{11}^* to ΔI_{11} (for $\Delta I_{11} \ll I_0$) is evaluated as (Supplementary Section S2)

$$\frac{I_{11}^*}{\Delta I_{11}} \leq \frac{1}{2}\left(\frac{\eta^*}{\eta_0}\right)\left(\frac{E_{11}^*}{E_{11}}\right) \quad (1)$$

where η_0 and η^* are the luminescence quantum yields of an exciton in the X_{11} (non-doped) and X_{11}^* states, respectively. Hence, a linear relationship between I_{11}^* and ΔI_{11} is expected for small ΔI_{11}. From equation (1), a value of $\eta^*/\eta_0 \geq 18 \pm 1$ is derived from the experimental results in Fig. 3a. That is, the quantum yield of a single X_{11}^* site is at least ~18 times larger than that obtained from a X_{11} state. Thus, at room temperature, the luminescence quantum yield of the X_{11}^* state, η^*, is estimated to be $\eta^* \geq 18 \pm 6\%$, given that the quantum yield of the X_{11} excitons is $\eta_0 = 1.0 \pm 0.3\%$, as calculated from the reported radiative lifetime of 1.6 ± 0.3 ns (ref. 8) and the observed photoluminescence decay of X_{11} excitons, described in the following (Supplementary Section S3).

To clarify the mechanism of the large quantum yield enhancement of the X_{11}^* states discussed above, we examined photoluminescence decay in pristine and oxygen-doped nanotubes (Fig. 4a,b). Clearly, the photoluminescence decay of the X_{11}^* excitons at E_{11}^* (red filled circles in Fig. 4b) is much slower than that of the X_{11} excitons at E_{11}. We conducted a numerical fitting procedure of the intensity decay $I_{11}^{(*)}(t)$ using the stretched exponential function $\exp[-(t/\tau_0)^{1/2}]$ with a characteristic timescale τ_0 for the E_{11} photoluminescence decay based on a kinetic model of the diffusion-limited one-dimensional exciton contact quenching[8], and using the double exponential functions for the decay of the one-dimension-like X_{11}^* excitons at E_{11}^* (Supplementary Section S3).

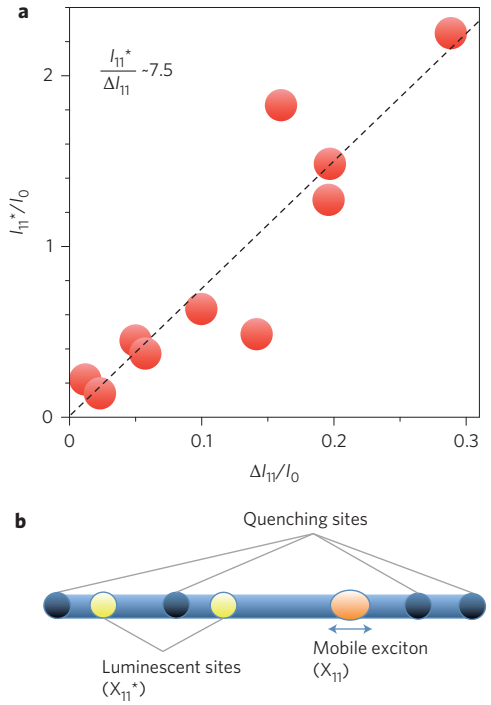

Figure 3 | Relationship of luminescence intensities from mobile and local excitons. a, Integrated photoluminescence intensity of the X_{11}^* peak (I_{11}^*) as a function of the absolute value of the change in photoluminescence intensity of the X_{11} peak ΔI_{11}. I_{11}^* and ΔI_{11} are normalized by the photoluminescence intensity of the X_{11} peak (I_0) of pristine (non-doped) nanotubes. The integrated photoluminescence intensities are evaluated by peak decomposition procedures, where the X_{11}^* peak is fit by a Voigt function, and where the weak and broad intensity tail of the lower energy side is not included as I_{11}^*. **b**, Schematic of exciton migration and successive trapping by local quenching sites (including the end sites of nanotubes) with density n_q or by local luminescent (X_{11}^*) sites with density n_x.

Here, we define a quantity $\langle\tau^{(*)}\rangle = \int_0^\infty I_{11}^{(*)}(t)/I_{11}^{(*)}(0)\mathrm{d}t$, which corresponds to the time-integrated exciton number normalized by the initial exciton number and related to η_0 and η^* as $\eta_0 = \tau_R^{-1}\langle\tau\rangle$ and $\eta^* = \tau_R^{*-1}\langle\tau^*\rangle$, respectively, where τ_R and τ_R^* are the radiative lifetimes of the X_{11} and X_{11}^* states, respectively. From the fitting procedure (Supplementary Section S3), the values $\langle\tau\rangle = 16 \pm 4$ ps and $\langle\tau^*\rangle = 95 \pm 7$ ps are obtained. This contributes to an enhancement of the quantum yield of the X_{11}^* excitons equivalent to approximately six times that of the intrinsic X_{11} excitons.

The further quantum yield enhancement necessary to account for the net 18× quantum yield enhancement is attributed to the shortened radiative lifetime. Considering the experimentally estimated values of $\eta^*/\eta_0 \geq 18 \pm 1$ and $\langle\tau\rangle/\langle\tau^*\rangle = 0.17 \pm 0.04 \approx 1/6$, the ratio of the radiative lifetimes can be evaluated through the relation $\tau_R/\tau_R^* = (\eta^*/\eta_0)(\langle\tau\rangle/\langle\tau^*\rangle)$ as $\tau_R/\tau_R^* \geq 3.0 \pm 0.8$, which indicates that the radiative decay rate of the X_{11}^* exciton ($1/\tau_R^*$) is more than approximately three times that of the intrinsic X_{11} excitons ($1/\tau_R$).

Let us now discuss the mechanisms of the reduced non-radiative decay rate, given as a factor of 1/6× (the extended exciton lifetime), and the enhanced radiative decay rate, given as a factor of ≥3× (the shortened radiative lifetime), of the X_{11}^* excitons relative to the X_{11} excitons. First, the reduced non-radiative exciton decay is mainly attributed to exciton immobilization by the localization effect. Once the mobile exciton is stopped at a local X_{11}^* state, the exciton can avoid collision with quenching sites and live longer, which contributes to the ~6× quantum yield enhancement. If only this 6× enhancement is considered, the quantum yield is evaluated to be 6 ± 2%, which is close to the quantum yield of ~7% estimated for a clean air suspended nanotube[26].

The dimensionality modification of the excitons is more critical for understanding the further quantum yield enhancement than recovering the original quantum yield of intrinsic one-dimensional excitons. Because of the one-dimensional nature of the intrinsic X_{11} excitons, their effective radiative decay rates are limited by the momentum mismatch between photons and thermally excited excitons in the one-dimensional band dispersion[2,3,7]. This restriction is responsible for the characteristic one-dimensional radiative decay rate that is proportional to $T^{-1/2}$. In contrast, the spatially localized zero-dimension-like states should be free from this momentum restriction, which could lead to enhancement of the radiative decay rate. Considering the possible E_{11} homogeneous line width of at least 10 meV at room temperature[7], however, the enhancement factor due to this effect is at most 1.6. Hence, to fully explain the enhancement of the radiative decay rate by a factor of 3 ± 0.8, an additional enhancement mechanism of a factor of at least 1.9 ± 0.5 is required.

The remaining issue that should be addressed before we further discuss the enhancement mechanism is whether there is a lower-lying dark (optically forbidden) X_{11}^* exciton state. If a lower-lying dark state exists, the effective radiative decay rate of excitons can be reduced due to the accumulation of excitons in this dark state, as is actually the case for the intrinsic X_{11} excitons[2,3]. In contrast, if there is no X_{11}^* dark state, excitons in the X_{11}^* sites can be free from the restriction caused by the dark state and may achieve a larger effective radiative decay rate. To examine this issue, we conducted temperature-dependent photoluminescence studies (Fig. 4c–e). The major findings are summarized as follows. The temperature-dependent variations of both I_{11} and I_{11}^* in the low-temperature range shown in Fig. 4d,e are reproduced well by considering exciton diffusional transport and reduction of the bright exciton population due to the existence of lower-lying dark states, not only in the X_{11} states, but also in the X_{11}^* states, which is consistent with a theoretical prediction of an impurity-bound exciton in carbon nanotubes[27] (Supplementary Sections S5, S6). From the numerical fitting results, we infer the existence of the X_{11}^* dark state, eventually leading to no significant change in the X_{11}^* effective radiative decay rate compared to that of the X_{11} excitons at room temperature (Supplementary Section S6).

Given the negligible change related to the existence of the dark state, we attribute the remaining enhancement of the radiative decay rate by a factor of ~2 to the increased oscillator strength due to the squeezing of an exciton in the zero-dimension-like X_{11}^* state, which is known as the 'giant-oscillator-strength effect' of a localized exciton[28]. The radiative decay rate τ_R^{-1} and the oscillator strength f of an exciton follow the relation $\tau_R^{-1} \propto E^2 f$, where E is the exciton energy and f is approximately inversely proportional to the average electron–hole separation, that is, the exciton size in a one-dimensional nanotube. Hence, the radiative decay rate can be enhanced by a factor of ~2 for an exciton squeezed to be ~40% of its original size, considering the different exciton energies E_{11} and E_{11}^*. From the size of the X_{11} exciton[29] (~2 nm in (6,5) nanotubes), the size of the X_{11}^* exciton is deduced to be ~0.8 nm.

Our findings regarding the strongly enhanced luminescence properties of sparsely distributed, zero-dimension-like excitonic states beyond the intrinsic properties in one-dimensional carbon nanotubes will stimulate research on the physics of zero-dimensional–one-dimensional hybrid systems. Furthermore, the findings presented here will allow the development of nanotube-based novel optoelectronic devices while utilizing the advantages of both zero-dimensional and one-dimensional electronic systems, such as a near-infrared single-photon emitter[21] driven by direct carrier-injection[30] that can be operated even at room temperature.

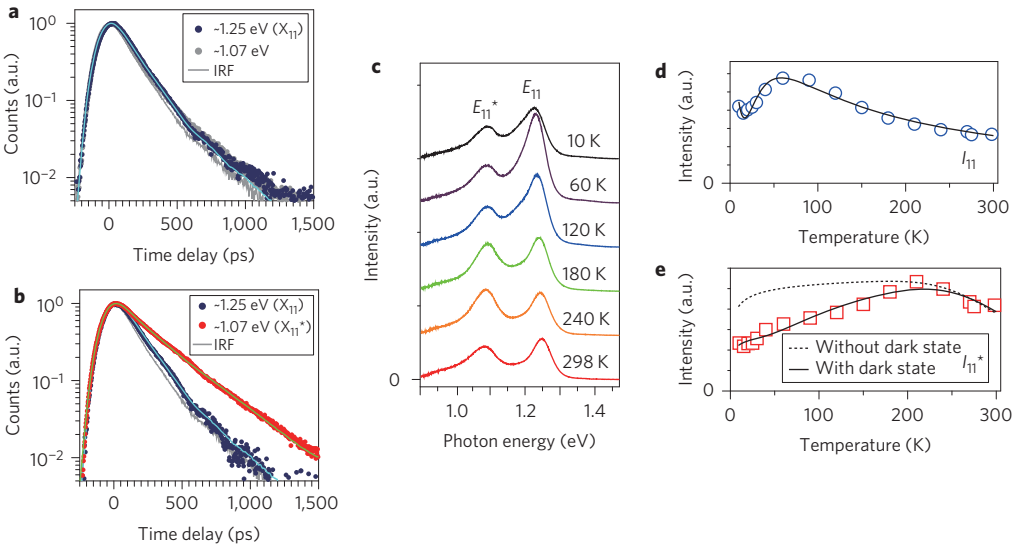

Figure 4 | Time-resolved and temperature-dependent luminescence studies. a,**b**, Time-resolved photoluminescence decay profiles of pristine (non-doped) (**a**) and oxygen-doped (**b**) nanotubes. Blue circles in **a** and **b** indicate the photoluminescence decay of X_{11} excitons taken at E_{11} (~1.25 eV), and the red circles in **b** indicate the photoluminescence decay at E_{11}^* that corresponds to the decay of local X_{11}^* states. The grey solid curve is the IRF. **c**, Photoluminescence spectra of moderately oxygen-doped nanotubes measured at various temperatures. **d**,**e**, Temperature-dependent variation of I_{11} (blue circles, **d**) and I_{11}^* (red squares, **e**). The solid curves in **d** and **e** are reproduced by numerical fitting considering the diffusional transport of X_{11} excitons, exciton trapping at the X_{11}^* sites, and the probability that the X_{11} (**d**) and X_{11}^* (**e**) excitons are in their bright states (calculated by taking into account the lower-lying dark states that reside 6.6 meV (**d**) and 15 meV (**e**) below the bright states). The dotted curve in **e** is calculated without taking the existence of the lower-lying dark state into account (Supplementary Sections S5 and S6).

Methods

Sample preparation. The oxygen-doped (6,5) carbon nanotubes dispersed in a D_2O solution used in this work were prepared with ozone using the procedure reported by Ghosh *et al.*[14], but the experimental conditions and parameters were considerably modified so that the broadening of the absorption peak[14], indicating the degradation of the intrinsic part of the nanotubes, could be minimized. Details of the sample preparation procedure are described in Supplementary Section S1. In short, (6,5)-rich CoMoCAT nanotubes were isolated by dispersion in D_2O with 0.2% (wt/vol) sodium dodecyl benzene sulphonate (SDBS), 60 min of moderate bath sonication, 40 min of vigorous sonication with a tip-type sonicator, and centrifugation at 130,000*g* for 4 h. A 0.75 ml volume of D_2O, containing dissolved ozone with variable density, was added to the resulting 2 ml of isolated nanotube dispersion. For the control samples that were denoted as 'pristine' (non-doped) nanotubes, 0.75 ml of D_2O was added without dissolved ozone. The samples were left under a lighted desk lamp (~5 mW cm^{-2}), typically overnight, before conducting the optical measurements. In our protocol, the relative oxygen-doping level (number density of the X_{11}^* site) was mainly controlled by the density of ozone dissolved in the D_2O solution. The relation between I_{11}^* and the estimated absorbance of ozone at 260 nm in the added D_2O solution is presented in Supplementary Fig. S2. The moderately oxygen-doped nanotubes utilized for the temperature-dependent photoluminescence measurements were deposited on a membrane filter and dried in vacuum before the measurements. Further details of the sample preparation protocols and parameters are presented in Supplementary Section S1.

Optical measurements and data analysis. Continuous-wave absorption and photoluminescence spectra of dispersed nanotubes in D_2O were measured at room temperature using a near-infrared spectrometer with monochromated incident light. All the optical measurements at room temperature were conducted on the liquid samples in optical quartz cells. The time-resolved photoluminescence decay profiles of the dispersed nanotubes in D_2O were recorded at room temperature using a time-correlated, single-photon counting technique under pulsed laser excitation (80 MHz, ~6 ps pulse duration with a photon energy of 1.378 eV) with a liquid-nitrogen-cooled near-infrared photomultiplier attached with a microchannel plate. The photoluminescence from each peak feature (E_{11} or E_{11}^*) was separated using optical filters with a bandpass of ~0.1 eV. The time-resolved measurements were conducted on the same nanotubes for which the photoluminescence excitation maps shown in Fig. 2a were taken. We fitted the data using the convolution of the instrumental response function (IRF) with model functions to obtain the original photoluminescence decay profiles (Supplementary Section S3). Temperature-dependent photoluminescence measurements were performed on the as-deposited samples attached to the cold finger of a liquid-helium-cooled microscopy cryostat, with monochromated light from a broadband light source (Fianium, SC450) used for photoexcitation. The measurements were conducted with an excitation energy of 2.175 eV (570 nm), corresponding to the second sub-band exciton energy E_{22} of (6,5) nanotubes. The photoluminescence peaks of the nanotubes cast on a membrane filter were broadened, suggesting a more inhomogeneous environment for the cast nanotubes than that of the micelle-suspended nanotubes. We confirmed that the temperature-dependent variation of the E_{22} exciton energy is sufficiently small by observing the photoluminescence excitation spectra at 5 K and 298 K.

Received 1 October 2012; accepted 7 June 2013; published online 7 July 2013

References

1. Saito, R., Dresselhaus, G. & Dresselhaus, M. S. *Physical Properties of Carbon Nanotubes* (Imperial College Press, 1998).
2. Perebeinos, V., Tersoff, J. & Avouris, P. Radiative lifetime of excitons in carbon nanotubes. *Nano Lett.* **5,** 2495–2499 (2005).
3. Spataru, C. D., Ismail-Beigi, S., Capaz, R. B. & Louie, S. G. Theory and *ab initio* calculation of radiative lifetime of excitons in semiconducting carbon nanotubes. *Phys. Rev. Lett.* **95,** 247402 (2005).
4. Cognet, L. *et al.* Stepwise quenching of exciton fluorescence in carbon nanotubes by single-molecule reactions. *Science* **316,** 1465–1468 (2007).
5. Rajan, A., Strano, M. S., Heller, D. A., Hertel, T. & Schulten, K. Length-dependent optical effects in single walled carbon nanotubes. *J. Phys. Chem. B* **112,** 6211–6213 (2008).
6. Miyauchi, Y., Matsuda, K., Yamamoto, Y., Nakashima, N. & Kanemitsu, Y. Length-dependent photoluminescence lifetimes in single-walled carbon nanotubes. *J. Phys. Chem. C* **114,** 12905–12908 (2010).
7. Miyauchi, Y., Hirori, H., Matsuda, K. & Kanemitsu, Y. Radiative lifetimes and coherence lengths of one-dimensional excitons in single-walled carbon nanotubes. *Phys. Rev. B* **80,** 081410(R) (2009).
8. Hertel, T., Himmelein, S., Ackermann, T., Stich, D. & Crochet, J. Diffusion limited photoluminescence quantum yields in 1-D semiconductors: single-wall carbon nanotubes. *ACS Nano* **4,** 7161–7168 (2010).
9. Harrah, D. M. & Swan, A. K. The role of length and defects on optical quantum efficiency and exciton decay dynamics in single-walled carbon nanotubes. *ACS Nano* **5,** 647–655 (2011).
10. Mueller, T. *et al.* Efficient narrow-band light emission from a single carbon nanotube p–n diode. *Nature Nanotech.* **5,** 27–31 (2010).
11. Hertel, T. Carbon nanotubes: a brighter future. *Nature Photon.* **4,** 77–78 (2010).
12. Ando, T. Excitons in carbon nanotubes. *J. Phys. Soc. Jpn* **66,** 1066–1073 (1997).
13. Wang, F., Dukovic, G., Brus, L. E. & Heinz, T. F. The optical resonances in carbon nanotubes arise from excitons. *Science* **308,** 838–841 (2005).
14. Ghosh, S., Bachilo, S. M., Simonette, R. A., Beckingham, K. M. & Weisman, R. B. Oxygen doping modifies near-infrared band gaps in fluorescent single-walled carbon nanotubes. *Science* **330,** 1656–1659 (2010).

15. O'Connell, M. J. *et al.* Band gap fluorescence from individual single-walled carbon nanotubes. *Science* **297,** 593–596 (2002).
16. Lebedkin, S. *et al.* FTIR-luminescence mapping of dispersed single-walled carbon nanotubes. *New J. Phys.* **5,** 140 (2003).
17. Crochet, J., Clemens, M. & Hertel, T. Quantum yield heterogeneities of aqueous single-wall carbon nanotube suspensions. *J. Am. Chem. Soc.* **129,** 8058–8059 (2007).
18. Ju, S.-Y., Kopcha, W. P. & Papadimitrakopoulos, F. Brightly fluorescent single-walled carbon nanotubes via an oxygen-excluding surfactant organization. *Science* **323,** 1319–1323 (2009).
19. Lee, A. J. *et al.* Bright fluorescence from individual single-walled carbon nanotubes. *Nano Lett.* **11,** 1636–1640 (2011).
20. Crochet, J. J., Duque, J. G., Werner, J. H. & Doorn, S. K. Photoluminescence imaging of electronic-impurity-induced exciton quenching in single-walled carbon nanotubes. *Nature Nanotech.* **7,** 126–132 (2012).
21. Högele, A., Galland, C., Winger, M. & Imamoğlu, A. Photon antibunching in the photoluminescence spectra of a single carbon nanotube. *Phys. Rev. Lett.* **100,** 217401 (2008).
22. Hirori, H., Matsuda, K., Miyauchi, Y., Maruyama, S. & Kanemitsu, Y. Exciton localization of single-walled carbon nanotubes revealed by femtosecond excitation correlation spectroscopy. *Phys. Rev. Lett.* **97,** 257401 (2006).
23. Kilina, S., Ramirez, J. & Tretiak, S. Brightening of the lowest exciton in carbon nanotubes via chemical functionalization. *Nano Lett.* **12,** 2306–2312 (2012).
24. Nagatsu, K., Chiashi, S., Konabe, S. & Homma, Y. Brightening of triplet dark excitons by atomic hydrogen adsorption in single-walled carbon nanotubes observed by photoluminescence spectroscopy. *Phys. Rev. Lett.* **105,** 157403 (2010).
25. Iakoubovskii, K. *et al.* Midgap luminescence centers in single-wall carbon nanotubes created by ultraviolet illumination. *Appl. Phys. Lett.* **89,** 173108 (2006).
26. Lefebvre, J., Austing, D. G., Bond, J. & Finnie, P. Photoluminescence imaging of suspended single-walled carbon nanotubes. *Nano Lett.* **6,** 1603–1608 (2006).
27. Tomio, Y. & Suzuura, H. Aharonov–Bohm effect on impurity-bound excitons in semiconducting carbon nanotubes. *J. Phys. Conf. Ser.* **302,** 012005 (2011).
28. Takagahara, T. & Hanamura, E. Giant-oscillator-strength effect on excitonic optical nonlinearities due to localization. *Phys. Rev. Lett.* **56,** 2533–2536 (1986).
29. Lüer, L. *et al.* Size and mobility of excitons in (6, 5) carbon nanotubes. *Nature Phys.* **5,** 54–58 (2009).
30. Mizuochi, N. *et al.* Electrically driven single-photon source at room temperature in diamond. *Nature Photon.* **6,** 299–303 (2012).

Acknowledgements

This research was supported by Precursory Research for Embryonic Science and Technology (PRESTO) programme (no. 3538 from the Japan Science and Technology Agency (JST)), by Grants-in-Aid for Scientific Research (nos 24681031, 22740195 and 23340085 from the Japan Society for the Promotion of Science (JSPS); no. 22016007 from the Ministry of Education, Culture, Sports, Science and Technology, Japan (MEXT)), and by Asahi Glass Foundation. The authors thank Y. Kawazoe, M. Uesugi, N. Tokitoh, T. Murakami, T. Umeyama and H. Imahori for experimental equipment and T. F. Heinz for discussions.

Author contributions

Y.M. developed the concept, designed the experiment and prepared the manuscript. Y.M. and M.I. performed the optical measurements. T.K. and M.O. contributed to the time-resolved photoluminescence measurements. M.I. prepared the samples. Y.M., M.I., S.M. and K.M. contributed to interpreting the results and writing the manuscript. All authors discussed the results and commented on the manuscript.

Additional information

Supplementary information is available in the online version of the paper. Reprints and permissions information is available online at www.nature.com/reprints. Correspondence and requests for materials should be addressed to Y.M.

Competing financial interests

The authors declare no competing financial interests.

Appl. Phys. B (2013) 112:587–592
DOI 10.1007/s00340-013-5442-1

Applied Physics B
Lasers and Optics

Experimental demonstration and stochastic modeling of autonomous formation of nanophotonic droplets

Naoya Tate · Makoto Naruse · Yang Liu · Tadashi Kawazoe · Takashi Yatsui · Motoichi Ohtsu

Received: 18 January 2013 / Accepted: 1 April 2013 / Published online: 16 April 2013

Abstract We have previously demonstrated a novel technique for autonomously forming a nanophotonic droplet, which is micro-scale spherical polymer structure that contains paired heterogeneous nanometric components. The sort-selectivity and alignment accuracy of the nanometric components in each nanophotonic droplet, and the related homogeneity of the optical function, are due to a characteristic pairing process based on a phonon-assisted photo-curing method. The proposed method requires irradiating a mixture of components with light to induce optical near-field interactions between each component, and subsequent processes based on these interactions. The pairing yield of components via the interactions is considered to mainly depend on the frequency of their encounters and the size-resonance effect between encountered components. In this paper, we model these two factors by individual stochastic procedures and construct a numerical model to describe the pairing process. Agreement between the results of numerical and experimental demonstrations shows the validity of our stochastic modeling.

1 Introduction

Nanophotonic devices utilize local interactions between nanometric components via dressed photon (DP), which have been proposed to meet the requirements of future optical technologies [1]. A DP is a quasi-particle representing the coupled state of a photon and an electron in a nanometric space [2]. DPs can excite multi-mode coherent phonons in the components during the interactions, and the DPs and phonons can electrically couple with each other [3–6]. The quasi-particle representing this coupled state has been named a dressed-photon–phonon (DPP). In particular, utilization of the energy transfer between semiconductor quantum dots (QDs) based on such interactions has been experimentally demonstrated, and novel functions and characteristic features have been realized [7–10]. One of the fundamental problems faced in using micro- and nano-scale physics to realize practicable nanophotonic devices and systems is the difficulty of establishing appropriate mechanisms for inducing the intended optical functions, which can be directly applied to macro-scale applications. At the same time, mass-production and uniform quality are also essential.

Self-assembly is one promising method of resolving such difficulties [11–14]. Also, several self-assembly methods for constructing nanophotonic devices have been developed [3,15–17]. Previously, the authors reported an autonomous technique for producing nanophotonic droplets [18]. A nanophotonic droplet is a micro-scale spherical structure that contains coupled QDs encapsulated by a locally cured photocurable polymer. As has been experimentally verified [19], the produced nanophotonic droplets exhibit homogeneous sizes, shapes, and optical properties due to their autonomous formation process. During the process, a mixed solution of heterogeneous QDs and polymer is continuously irradiated with incident light having a lower photon energy than the activation energy of the polymer to induce DPP-mediated optical near-field interactions between the components and a subsequent phonon-assisted process [3–6]. The process

N. Tate (✉) · Y. Liu · T. Kawazoe · T. Yatsui · M. Ohtsu
The University of Tokyo, 2-11-16 Yayoi, Bunkyo-ku, Tokyo 113-8656, Japan
e-mail: tate@nanophotonics.t.u-tokyo.ac.jp

M. Naruse
National Institute of Information and Communications Technology, 4-2-1 Nukui-kita, Koganei, Tokyo 184-8795, Japan

realizes multistep excitation via excited phonon levels, allowing the polymer to be cured by such low-photon-energy light. The essential point is that this process occurs only when heterogeneous QDs possess appropriate sizes, which has been called a size-resonance, and also electronic energy conditions.

The efficiency of the phonon-assisted process depends on the velocity-fluctuation of components in the mixed solution in addition to the size-resonance effect [20]. As theoretically reported in [20], the energy of the DPP-mediated optical near-field interactions between two nanometric structures is expected to be maximized when the sizes of the two components are similar. Because the phonon-assisted process for the coupling of QDs is fundamentally based on the DPP-mediated optical near-field interactions between the QDs, QDs with similar sizes are preferably coupled with each other due to the size-resonance effect. Therefore, if the sizes of the encountered QDs are quite similar so that they exhibit size-resonance, the phonon-assisted process is induced, and the encountered QDs are successfully coupled with each other.

In this paper, we focus on fluctuating behaviors of components in the mixed solution during the coupling process. In order to discuss fundamentals of the behaviors, we constructed a numerical model that consists of two individual stochastic procedures corresponding to the fluctuation and the size-resonance. Here, we considered thermal equilibrium state of the mixed solution in a finite temperature in which velocities of its components are distributed along Maxwell–Boltzmann distribution law. In such case, fluctuating behavior of each component is often simply described by using random walk model. First, we briefly review the basics of our phonon-assisted coupling process for forming a nanophotonic droplet. Then, we describe some experimental demonstrations. Finally, we propose a stochastic model of the coupling process and verify the validity of our model by comparison with the results of experimental demonstrations.

2 Basics of forming nanophotonic droplet

In our proposed method for producing nanophotonic droplets, a mixed solution of QDs and photo-curable polymer is illuminated by the light to generate DPP around each QD for fixing and coupling QDs by local-curing of the polymer via the phonon-assisted process based on DPP-mediated optical near-field interactions.

An overview of our proposed method is schematically shown in Fig. 1a. The sequence of forming a nanophotonic droplet is divided into two steps: coupling and encapsulating. We assume a mixed solution of two sorts of heterogeneous QDs, called QD_A and QD_B, and a photo-curable

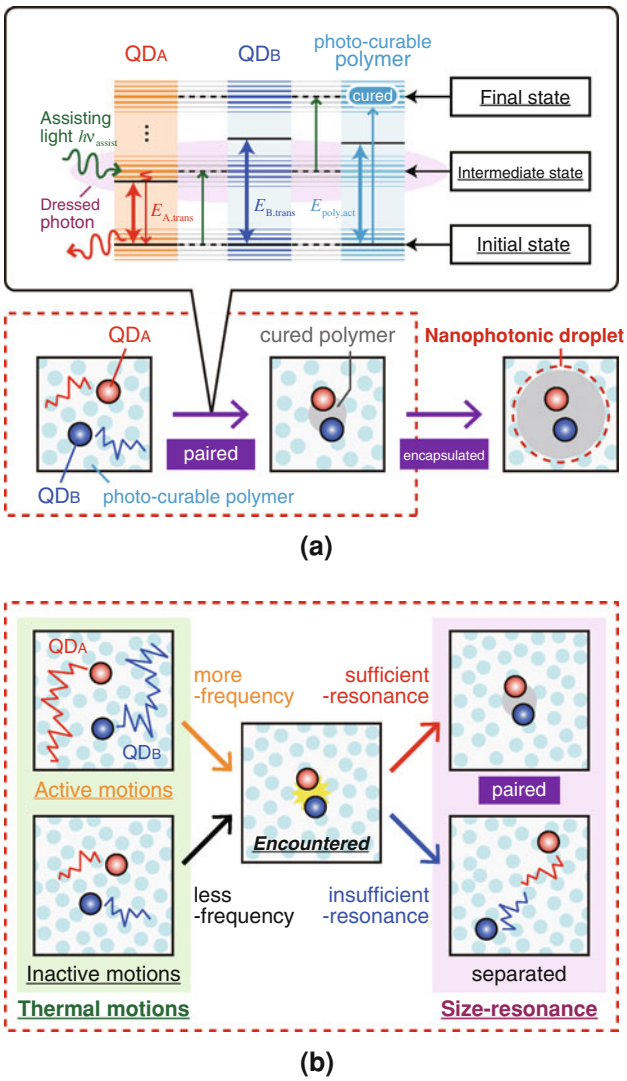

Fig. 1 **a** Schematic diagram of nanophotonic droplet formation, consisting of pairing and encapsulating processes based on a phonon-assisted photo-curing method. **b** Detailed diagram of the pairing process, considering the effects of velocity-fluctuation and size-resonance between QD_A and QD_B

polymer. In order to induce the sequence, the mixed solution is illuminated by assisting light having photon energy $h\nu_{assist}$. The transition energies of QD_A and QD_B are represented by $E_{A.trans}$ and $E_{B.trans}$, respectively, and the activation energy of the photo-curable polymer is represented by $E_{poly.act}$. The following process is induced only when their energy conditions fulfill $E_{A.trans} < h\nu_{assist} < E_{poly.act} < E_{B.trans}$. If the volume densities of the QDs are low, resulting in the long separation between both QDs, only QD_As spontaneously emit light with the appropriate energy upon absorbing the assisting light. In this case, no physical or chemical reactions occur. However, if the volume densities of the QDs are sufficiently high, resulting in a sufficiently short separation between each other, multistep energy excitation of the photo-

curable polymer occurs due to DPP-mediated optical near-field interactions with neighboring QD_As and QD_Bs, and the photo-curable polymer is subsequently cured. Although there is a subsequent process of encapsulating the coupled QDs by the spontaneous emission of optical energy from the QDs, we focus only on the coupling process in this paper, because the actual electronic transitions involved in the encapsulating process has been described in the authors' previous paper [18].

The detailed coupling process is schematically shown in Fig. 1b. As shown, two factors are considered before and after an encounter, namely, the velocity-fluctuation of QDs for encountering each other and the size-resonance between the encountered QDs, respectively. The former mainly depends on the temperature, i.e., the energy of the fluctuation in the mixed solution. Because higher mobility causes higher frequency of encounter, the temperature of the mixed solution directly affects the pairing process. Then, if the QDs encounter, the size-resonance must govern the efficient induction of the DPP-mediated optical near-field interactions between encountered QDs [19].

3 Experimental formation of nanophotonic droplet

In order to verify the size-resonance in the pairing process, three kinds of CdSe QDs (QD_A) ($CdSe_{546}$, $CdSe_{557}$, and $CdSe_{578}$; Ocean Optics, Inc., *Evidot*) were individually used for coupling with the CdS QDs (QD_B) (CdS_{415}; NN-Labs, LLC., *Nanocrystals*). The QDs exhibited evidently different emission spectra, as shown in Fig. 2b. A mixed solution of the QD solutions and a UV-curable polymer (Tesk Co., Ltd.; *A1527*) was illuminated assisting light emitted from a 120 mW laser diode having a photon energy of 2.33 eV. Figure 2a shows the relevant energy levels of QDs and UV-curable polymer molecule in the following experiment. These experimental conditions fulfill the previously described energy conditions for inducing the phonon-assisted photo-curing to form nanophotonic droplets. The total amount of mixed solution was limited to 50 µL to maintain spatially uniform illumination by the assisting light. This volume contained about 10^{14} CdSe QDs and about 10^{15} CdS QDs. Under these experimental conditions, the QDs can be assumed to encounter each other at a sufficiently high frequency to induce the phonon-assisted process efficiently.

After 3 h of illumination by the assisting light, the cured substances were extracted from the mixed solution by centrifugation at 10,000 rpm for 5 min. The extracted cured substances, containing a large number of nanophotonic droplets, were dispersed in a toluene solution and uniformly spin-coated on a Si substrate. Figure 3a, b, respectively, show SEM images and microscope emission

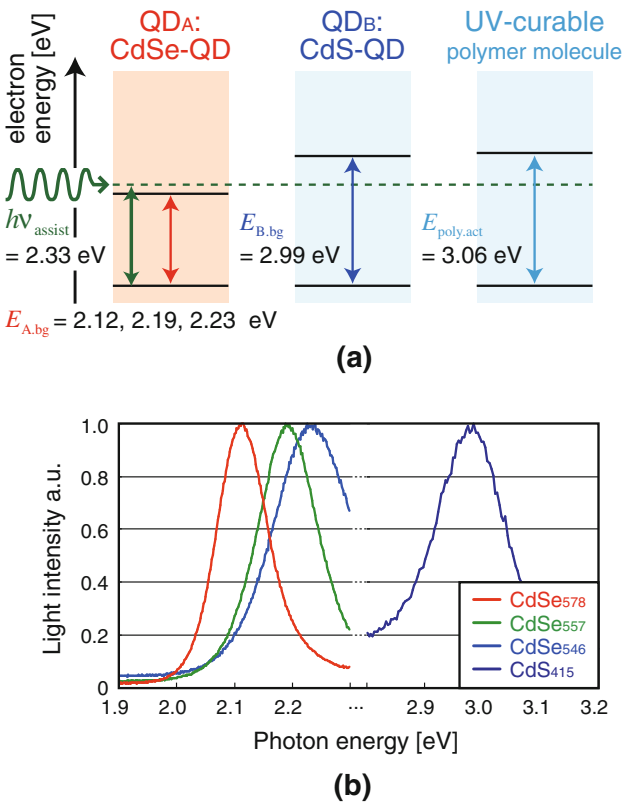

Fig. 2 **a** Energy diagram of the experimental conditions for forming nanophotonic droplets containing paired CdSe QDs and CdS QDs. To verify the size-dependency, three sorts of CdSe QDs were individually used. **b** Emission spectra of QDs under UV light irradiation

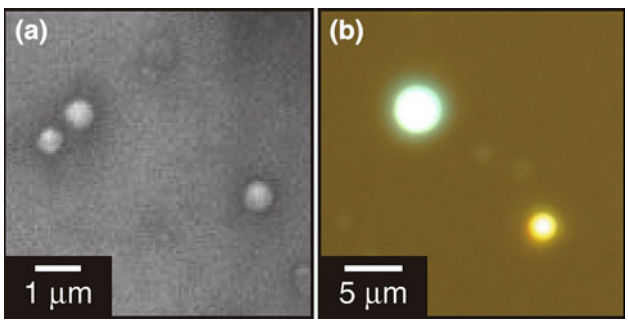

Fig. 3 **a** SEM images and **b** microscope emission images of formed nanophotonic droplets

images under UV light illumination. As shown, homogeneous-sized spherical nanophotonic droplets were successfully obtained, exhibiting bright emission light spots.

4 Size- and temperature-dependencies in the formation process

The nanophotonic droplet formation process is studied by measuring the temporal evolution of their emission spectra

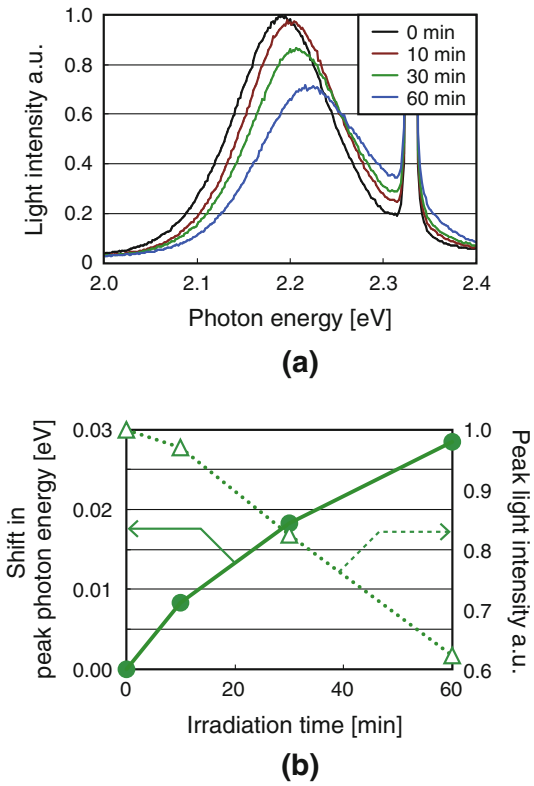

Fig. 4 **a** Experimentally obtained temporal evolution of the emission spectra from CdSe QDs in a mixed solution during illumination by assisting light. **b** Plotted results of the shifted value of the peak photon energy and its light intensity

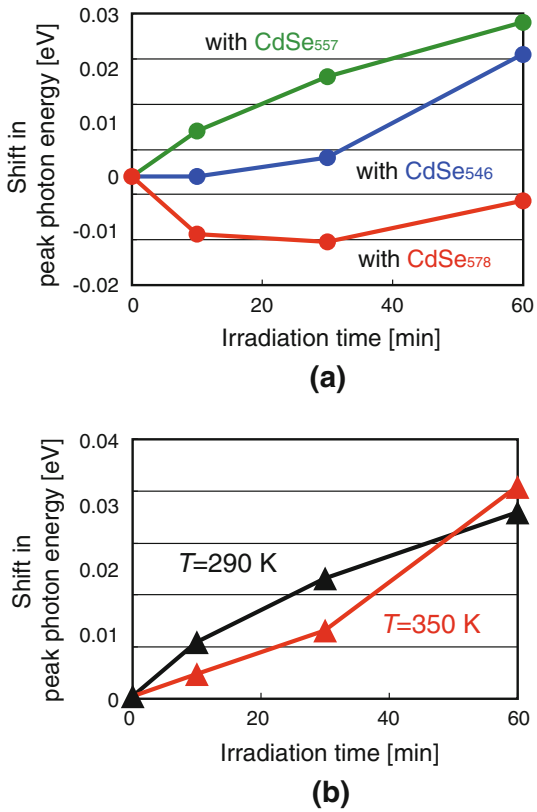

Fig. 5 Temporal evolution of shift in peak photon energy emitted from the mixed solution of CdSe QDs, CdS QDs, and UV-curable polymer during illumination by assisting light **a** using CdSe QDs with various size distributions and **b** with mixed solutions at different temperatures to induce various levels of velocity-fluctuation

while radiating the assisting light. As we previously reported in [19], because each QD preferably make a pair with another QD of similar size due to the size-resonance effect [20], emission from paired CdSe QDs decreases as a result of the energy transfer to its partner of the pairing, i.e., to CdS QD with resonant size. As a result, the peak photon energy of the total emission spectrum from CdSe and CdS necessarily shifts. The magnitude of the shift depends on the sizes of these QDs. Moreover, because only paired QDs are allowed to transfer the irradiated optical energy to the surrounding polymer for its activation, the light intensity of the emission from paired QDs necessarily decreases in the formation process of nanophotonic droplets.

Figure 4a shows the experimentally obtained temporal evolution of the emission spectra from CdSe QDs in a mixed solution of $CdSe_{557}$ QDs, CdS_{415} QDs, and UV-curable polymer during irradiation with assisting light. Their peak photon energies and their emission intensities are plotted as a function of time in Fig. 4b, which monotonously change, as are expected. Here, we focus on the shift of the peak photon energy and describe below.

Figure 5a shows the magnitude of the shift in photon energy during the pairing between CdS_{415} QDs, and $CdSe_{546}$, $CdSe_{557}$, and $CdSe_{578}$ QDs. In this figure, because average size of the $CdSe_{557}$ QDs is tuned to size-resonant to the CdS_{415} QDs, they showed the steepest gradient of the blue shift in the photon energy. On the other hand, the average sizes of $CdSe_{546}$ and $CdSe_{578}$ are slightly off-resonant to CdS_{415} QDs, resulting in red shift, which is exhibited at an early phase in the coupling process, from 0 to 30 min. The magnitude of such the red shift depends on the degree of off-resonance.

Next, to verify the dependence of the velocity-fluctuation on the temperature during the pairing process, further experiments were performed to measure the temporal evolution of the emission spectra using a hot-water bath. Its temperature, T, was fixed to 350 and 290 K, that is, the temperature in the former was 1.2 times that in the latter. Size-resonant $CdSe_{557}$ QDs and CdS_{415} QDs were used for this experiment. Figure 5b shows the observed time variation of the peak photon energy of the emission during irradiation with assisting light. Similarly to the cases of blue circles in Fig. 5a, a lower gradient was observed at an early phase of the variation in the case of $T = 350$ K. Moreover, after this early phase, a steeper gradient was observed, and a larger shift than in the case of $T = 290$ K

is obtained. Such differences are due to increased frequency of encounters driven by higher temperature.

5 Stochastic modeling of the coupling process

In order to numerically model the QD pairing process, we defined a pairing rate and constructed a stochastic model. The pairing rate depends on two factors, the frequency of encounter and the pairing, as schematically shown in Fig. 1b. Thus, our model consists of two stochastic procedures. For the sake of simplicity, one-dimensional coordinate space is considered in the modeling.

As shown by the experiments described above, the pairing rate depends on the size-resonance. It is numerically modeled by considering the size distribution of QD_Bs. Figure 6a shows assumed size distributions of three sorts of QD_Bs, QD_{small}, QD_{medium}, and QD_{large}, which correspond to the actual emission spectra observed in the above experimental demonstrations, as shown in Fig. 2b. Here, we define the allowance size for pairing, $\Delta\phi_{pref}$, which was experimentally estimated to be $3.90 < \Delta\phi_{pref} < 3.98$. At the first step of the numerical trial in our model, the size of QD_B is randomly selected. Then, the following sequence is executed only when the selected size is within the distribution of $\Delta\phi_{pref}$. Otherwise, the trial is terminated and another trial is launched.

The frequency of encounter experimentally depends on the temperature. Here, two one-dimensional coordinates are assumed for its estimation. Each coordinate representing the position of QD randomly fluctuates within an appropriate range until the coordinates of the two QDs crosses, or until a sufficient number of numerical steps is processed. Here, the range of the coordinate fluctuation corresponds to the temperature. Figure 6b shows the calculated temporal evolutions of the coordinate for higher and lower temperature, where the amplitude of the former was on average 1.2 times larger than the latter. This ratio was approximately set based on the difference in velocity-fluctuation due to the temperature in the cases of $T = 350$ and 290 K, which correspond to the experimental conditions in the demonstration described above. In the following, corresponding cases to $T = 350$ and 290 K in the experimental demonstrations are described as high-T and low-T cases, respectively. As shown, the high-T case shows that the QDs encounter within shorter period than the low-T case. After the two QDs successfully encounter, another trial is started selecting other sized QDs. After a sufficient number of iterations, pairing rate of the QDs is calculated as the ratio of the total number of successful encounters to the number of trials.

Based on the above modeling, the dependency of the size-resonance and the temperature on the pairing rate was

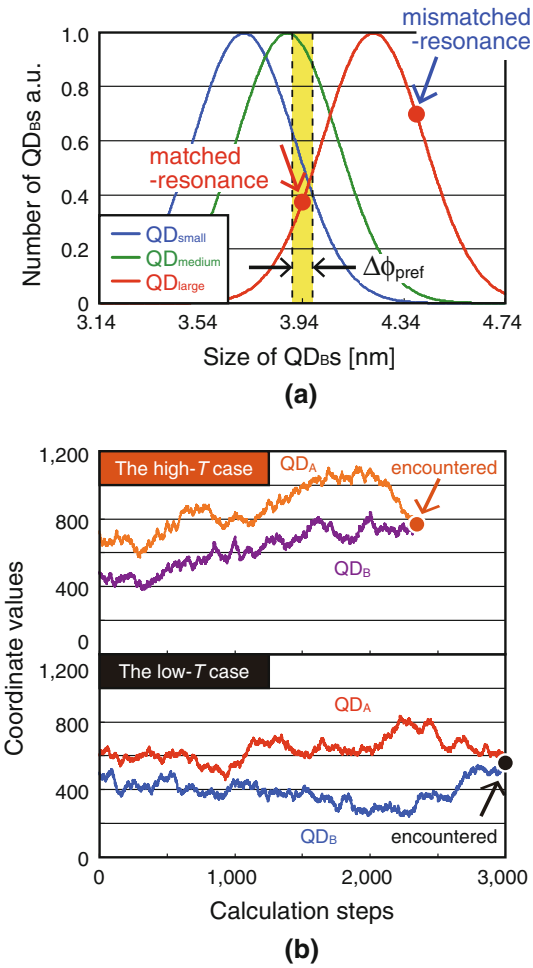

Fig. 6 **a** Numerically assumed size distributions of QD_Bs in the stochastic model. **b** Comparison of random fluctuations of one-dimensional coordinates between the high-T and low-T cases in the stochastic model

numerically verified. The results are shown in Fig. 7a, b, respectively. As shown, all curves showed monotonous increases of the pairing rate. In particular, in Fig. 7a, the increase with the steepest gradient was found with QD_{medium}, rather than QD_{small} and QD_{large}, agreeing with the previous experimental results in Fig. 5a. Moreover, in Fig. 7b, the pairing rate for the high-T case was higher than for the low-T case agreeing with the experimental results in Fig. 5b.

In our stochastic model, only the frequency of successful pairing between QDs is considered, and subsequent shifts in the peak photon energy of their emission spectra are ignored for the sake of simplicity. This may be one explanation for some of the differences between the experimental and numerical results, especially the red shift in the early phase of the coupling process. Nevertheless, with such approximations in our models, the time-evolving behaviors were in sufficient agreement. The results

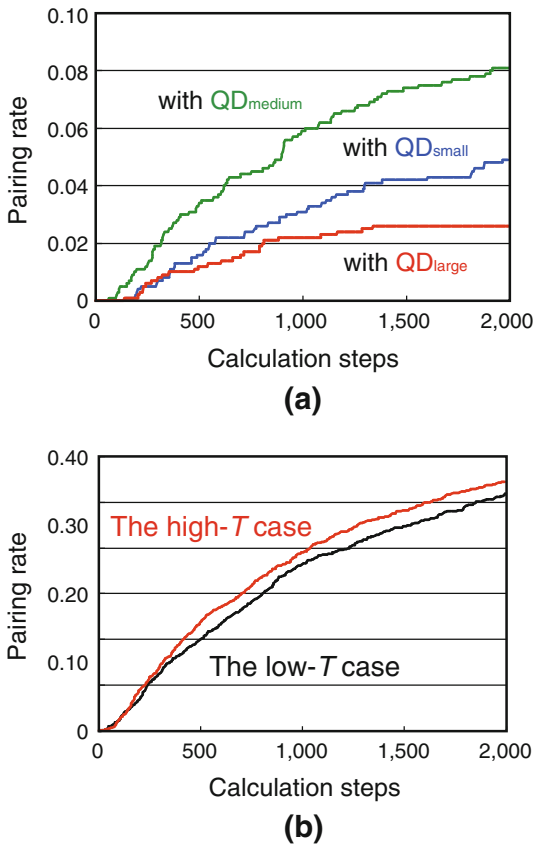

Fig. 7 Numerical verification of dependency of pairing rate on **a** the size difference and **b** the temperature based on the stochastic model

strongly indicate that the autonomy of the process and the homogeneity of the products depend on the size-resonance and the temperature, as we expected.

6 Summary

We have described some experiments demonstrating the formation of nanophotonic droplets consisting of CdSe QDs, CdS QDs, and UV-curable polymer. Temporal evolutions of the emission spectra were experimentally obtained to verify the effects of size-dependency and temperature on the pairing process. To numerically verify the dependency of each factor, a numerical model based on two stochastic procedures was constructed, and temporal evolutions of the QD pairing rate were calculated. Comparison of the experimental and numerical time variations showed sufficient agreement. These results strongly indicate that the characteristics of the phonon-assisted photocuring method for formation of nanophotonic droplets, namely, the autonomy of the process and the homogeneity of the products, depend on the size-resonance of DPP interactions and the temperature. In future research, based on the findings described here, it should be possible to assemble nanophotonic droplets that exhibit particular optical properties.

Acknowledgments This work was supported in part by the Research and Development Program for Innovative Energy Efficiency Technology funded by the New Energy and Industrial Technology Development Organization (NEDO), Japan.

References

1. M. Ohtsu, T. Kawazoe, T. Yatsui, M. Naruse, IEEE J. Sel. Top. Quantum Electron **14**, 1404 (2008)
2. T. Kawazoe, K. Kobayashi, S. Sangu, M. Ohtsu, Appl. Phys. Lett. **82**(18), 2957 (2003)
3. S. Yukutake, T. Kawazoe, T. Yatsui, W. Nomura, K. Kitamura, M. Ohtsu, Appl. Phys. B-Lasers Opt. **99**, 415 (2010)
4. H. Fujiwara, T. Kawazoe, M. Ohtsu, Appl. Phys. B-Lasers Opt. **98**, 283 (2010)
5. T. Kawazoe, M.A. Mueed, M. Ohtsu, Appl. Phys. B-Lasers Opt. **104**, 747 (2011)
6. K. Kitamura, T. Kawazoe, M. Ohtsu, Appl. Phys. B-Lasers Opt. **107**, 293 (2012)
7. T. Kawazoe, K. Kobayashi, M. Ohtsu, Appl. Phys. Lett. **86**(10), 103102 (2005)
8. W. Nomura, T. Yatsui, T. Kawazoe, M. Ohtsu, J. Nanophotonics **1**, 011591 (2007)
9. M. Naruse, K. Leibnitz, F. Peper, N. Tate, W. Nomura, T. Kawazoe, M. Murata, M. Ohtsu, Nano Commun. Netw. **2**(4), 189 (2011)
10. T. Kawazoe, M. Ohtsu, S. Aso, Y. Sawado, Y. Hosoda, K. Yoshizawa, K. Akahane, N. Yamamoto, M. Naruse, Appl. Phys. B **103**(3), 537 (2011)
11. B.Q. Wei, R. Vajtai, Y. Jung, J. Ward, R. Zhang, G. Ramanath, P.M. Ajayan, Nature **416**, 495 (2002)
12. B.A. Parviz, D. Ryan, G.M. Whitesides, IEEE Trans. Adv. Packaging **26**, 233 (2003)
13. Y.I. Mazur, Z.M. Wang, G.G. Tarasov, M. Xiao, G.J. Salamo, J.W. Tomm, V. Talalaev, H. Kissel, Appl. Phys. Lett. **86**, 063102 (2005)
14. M.P. Stoykovich, M. Müller, S. Ouk Kim, H.H. Solak, E.W. Edwards, J.J. de Pablo, P.F. Nealey, Science **308**, 1442 (2005)
15. T. Yatsui, K. Hirata, W. Nomura, Y. Tabata, M. Ohtsu, Appl. Phys. B **93**(5), 55 (2008)
16. Y. Liu, T. Morishima, T. Yatsui, T. Kawazoe, M. Ohtsu, Nanotechnology **22**(21), 215605 (2011)
17. T. Kawazoe, M.A. Mueed, M. Ohtsu, Appl. Phys. B **104**(4), 747 (2011)
18. N. Tate, Y. Liu, T. Kawazoe, M. Naruse, T. Yatsui, M. Ohtsu, Appl. Phys. B-Lasers Opt. **110**, 39 (2013)
19. N. Tate, Y. Liu, T. Kawazoe, M. Naruse, T. Yatsui, M. Ohtsu, Appl. Phys. B-Lasers Opt. **110**, 293 (2013)
20. S. Sangu, K. Kobayashi, M. Ohtsu, J. Microsc. **202**, 279 (2001)

[II] PRESENTATIONS

IN INTERNATIONAL CONFERENCES

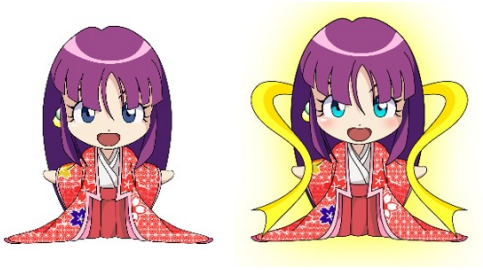

Dressed Photon Technology

Motoichi Ohtsu

Department of Electrical Eng. and Information Systems, Graduate School of Eng., the Univ. of Tokyo,

also with Nanophotonics Research Center, the Univ. of Tokyo

ohtsu@ee.t.u-tokyo.ac.jp

Dressed photon (DP) technology utilizes the electromagnetic fields localized in nanometric space. These fields have been named optical near-fields due to their non-propagating feature[1]. The principles and concepts of DP technology are quite different from those of conventional wave-optical technology encompassing photonic crystals, plasmonics, metamaterials, silicon photonics, and quantum-dot photonic devices. This is because these devices use propagating light even though the materials or particles used may be nanometer-sized. The theoretical picture of DP has been proposed to describe the electromagnetic interactions between nanometric particles located in close proximity to each other. The optical near-field is a virtual cloud of photons that always exists around an illuminated nanometric particle. A real photon (, i.e., conventional propagating scattered light) can be emitted from an electron in an illuminated nanometric particle. Independently of the real photon, another photon is emitted from the electron, and this photon can be re-absorbed within a short duration. This photon, i.e., a virtual photon, is nothing more than the optical near-field, and its energy is localized at the surface of the nanometric particle. Since the virtual photon remains in the proximity of the electron, it can couple with the electron in a unique manner. This coupled state is a quasi-particle from the standpoint of photon energy transfer. It is the DP that carries the material excitation energy. The DP has been theoretically described by assuming a multipolar quantum electrodynamic Hamiltonian in a Coulomb gauge in a finite nano-system. The creation and annihilation operators of the DP are expressed as the sum of the operators of the real photon and an electron–hole pair. A real nanometric material is composed not only of electrons but also of a crystal lattice. In this case, after a DP is generated on an illuminated nanometric particle, its energy can be exchanged with the crystal lattice. By this exchange, the crystal lattice can excite the vibration mode coherently, creating a multi-mode coherent phonon state. As a result, the DP and the coherent phonon can form a coupled state (dressed-photon – phonon: DPP). This coupled state is a quasi-particle and is generated only when the particle size is small enough to excite the crystal lattice vibration coherently. Novel LEDs[2] and a laser[3] will be demonstrated by using indirect transition-type semiconductors (Si and SiC), which are fabricated and operated by DPP. Future problems to be solved will be also presented.

Keywords: dressed photons, phonons, LED, laser

Nanophotonic droplet: a novel optical device consisting of autonomously-coupled quantum dots

Naoya Tate, Motoichi Ohtsu

Department of Electrical Engineering and Information Systems, The University of Tokyo, Tokyo, Japan
Email:tate@nanophotonics.t.u-tokyo.ac.jp, web site: http://naoya-tate.net

Various fabrication technologies are being actively developed for realizing novel devices and systems that operate on the nanometric scale. Among these technologies, self-assembly is one promising method of achieving mass-production of nanometric devices. Recently, we have been studying an original technique for autonomously forming nanophotonic droplets (NDs) [1–3], which are micro-scale spherical polymer structures containing coupled quantum dots (QDs). The sort-selectivity and alignment accuracy of coupled QDs and the related homogeneity of NDs' optical functions are due to a characteristic fabrication process based on dressed-photon–phonon (DPP) interactions between each component [4]. As schematically shown in Fig. 1(a), the fabrication method only requires irradiating a mixture of QDs and several types of curable polymers with light having a much lower photon energy than the curing energy of the polymer to induce multistep electron excitation due to DPP interactions, which locally cures the polymer via excited phonon levels only when heterogeneous QDs encounter each other.

To experimentally demonstrate our idea, we mass-produced NDs by irradiating a mixed solution of CdSe-QDs, CdS-QDs, and a thermocurable polymer with visible light. As shown in the microscope emission images in Fig. 1(b), similar-sized spherical regions of cured polymer were successfully obtained. Moreover, we also demonstrated the homogeneity of their optical properties, which indicates homogeneous combinations and alignment of coupled QDs in each ND.

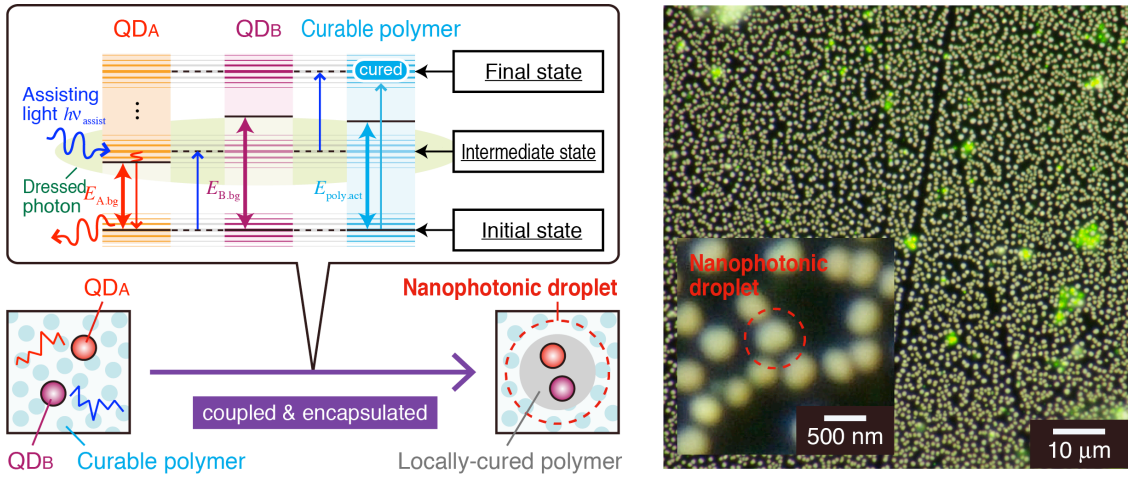

Fig. 1. (a) Schematic diagram of basic mechanism of ND formation. (b) Microscope emission image of fabricated NDs and (inset) a magnified view of them.

Our method can be easily used in a number of applications where the development of novel nanometric optical devices will be required. Concurrently with this, we have been studying the implementation of an optical functional system that works based on the fundamental characteristics of ND formation, as a representative implementation of a nano-photonic information system.

Part of this work was supported by the "Development of next-generation high-performance technology for photovoltaic power generation system" program of NEDO, Japan.

1. N. Tate, et al. *Appl. Phys. B*, **110**, Issue 1, 39 (2013).
2. N. Tate, et al. *Appl. Phys. B*, **110**, Issue 3, 293 (2013).
3. N. Tate, et al. *Appl. Phys. B*, **112**, Issue 4, 587 (2013).
4. M. Ohtsu, et al. *IEEE J. Sel. Top. Quant. Ele.*, **14**, 1404 (2008).

Presentation Method (Invited):

10:45-11:10AM

B26: Nanophotonics for computing and security applications

Makoto Naruse[1], N. Tate[2], M. Aono[3], S.-J. Kim[4], M. Ohtsu[2]

[1]*Photonic Network Research Institute, National Institute of Information and Communications Technology, Tokyo, Japan*

[2]*Department of Electrical Engineering and Information Systems / Nanophotonics Research Center, Graduate School of Engineering, The University of Tokyo, Tokyo, Japan*

[3]*Earth-Life Science Institute, Tokyo Institute of Technology, Tokyo, Japan*

[4]*WPI Center for Materials Nanoarchitectonics, National Institute for Materials Science, Ibaraki, Japan*

Nanophotonics has been extensively studied with the aim of unveiling and exploiting light–matter interactions that occur at a scale below the diffraction limit of light, and recent progress made in experimental technologies—both in nanomaterial fabrication and characterization—is driving further advancements in the field. From the viewpoint of information, on the other hand, novel architectures, design and analysis principles, and even novel computing paradigms should be considered so that we can fully benefit from the potential of nanophotonics. [1,2,3]

In this presentation, we first we present some fundamental and emergent information properties that stem from optical excitation transfer mediated by optical near-field interactions and the hierarchical properties inherent in optical near-fields. We theoretically and experimentally investigate aspects such as unidirectional signal transfer, energy efficiency and networking effects. [1] In particular, toward achieving a computing paradigm that surpasses the classical von Neumann architecture, we describe stochastic solution searching and decision making, which exploits the spatiotemporal dynamics of optical excitation transfer. [4-6]

Second, we show information security applications based on optical near-field processes together with their theoretical and experimental foundations. [2] Optics has been playing crucial roles in security applications ranging from authentication and watermarks to anti-counterfeiting. However, since the fundamental physical principle used in conventional technologies involves optical far-fields, or propagating light, diffraction of light causes severe difficulties, for example in device scaling and system integration. Moreover, conventional security technologies in use today have been facing increasingly stringent demands to safeguard against threats such as counterfeiting of holograms, requiring innovative physical principles and technologies to overcome their limitations. Nanophotonics can break through the diffraction limit of conventional propagating light. Moreover, unique physical attributes in nanophotonics, such as the hierarchical nature of optical near-field interactions, pave the way for novel security functionalities. We present the physical principles and some experimental demonstrations of systems based on nanophotonics with respect to security applications such as tamper resistance against non-invasive and invasive attacks, hierarchical information retrieval, hierarchical holograms, and authentication. [3]

Acknowledgement: This work was supported in part by the SCOPE of the Ministry of Internal Affairs and Communications and Grant-in-Aid for scientific research from the Japan Society for the Promotion of Science.

1. M. Naruse, N. Tate, M. Aono, M. Ohtsu, *Reports on Progress in Physics* **76**, 056401 (2013).
2. C. Pistol, C. Dwyer, A.R. Lebeck, *IEEE Micro* **28**, 7 (2008).
3. M. Naruse, N. Tate, M. Ohtsu, *J. Optics* **14**, 094002 (2012).
4. M. Naruse, M. Aono, S.-J. Kim, T. Kawazoe, W. Nomura, H. Hori, M. Hara, M. Ohtsu, *Phys. Rev. B* **86**, 125407 (2012)
5. M. Aono, M. Naruse, S.-J. Kim, M. Wakabayashi, H. Hori, M. Ohtsu, M. Hara, *Langmuir* **29**, 7557 (2013).
6. S.-J. Kim, M. Naruse, M. Aono, M. Ohtsu, M. Hara, *Scientific Reports* **4**, 2370 (2013).

Near-field nanophotonics for computing and security

Makoto Naruse[1], Naoya Tate[2], Masashi Aono[3], and Motoichi Ohtsu[2]
1. Photonic Network Research Institute, National Institute of Information and Communications Technology, Tokyo, Japan
2. Department of Electrical Engineering and Information Systems / Nanophotonics Research Center, Graduate School of Engineering, The University of Tokyo, Tokyo, Japan
3. Earth-Life Science Institute, Tokyo Institute of Technology, Tokyo, Japan

Nanophotonics has been extensively studied with the aim of unveiling and exploiting light–matter interactions that occur at a scale below the diffraction limit of light. From the viewpoint of information, novel architectures, design and analysis principles, and even novel computing paradigms should be considered so that we can fully benefit from the potential of nanophotonics for various applications. In this presentation, we first present some fundamental and emergent attributes associated with optical excitation transfer mediated by optical near-field interactions. Toward achieving a computing paradigm that surpasses the classical von Neumann architecture, we describe stochastic solution searching, which exploits the spatiotemporal dynamics of optical excitation transfer. Second, we show information security applications based on optical near-field processes together with their theoretical and experimental foundations. A common feature across all of these demonstrations is the extraction of "*intelligent*" functions and behaviors from optical near-field processes in the nanoscale based on an information-based standpoint.
Acknowledgement: Part of this work was supported in part by SCOPE of the Ministry of Internal Affairs and Communications and Grant-in-Aid for scientific research from the Japan Society for the Promotion of Science.

PROCEEDINGS OF THE INTERNATIONAL CONFERENCE
NANOMATERIALS: APPLICATIONS AND PROPERTIES
Vol. **2** No 1, 01PCSI09(3pp) (2013)

Dressed Photon-phonon Technology for Ultra Flat Surface

T. Yatsui*, M. Ohtsu

[1]*School of Engineering, the University of Tokyo, 2-11-16 Yayoi, Bunkyo, 113-8656 Tokyo, Japan*

(Received 20 May 2013; published online 31 August 2013)

A reduction of the surface roughness, *Ra*, is required in various applications including electronic devices and / or optical devices. Although chemical-mechanical polishing (CMP) has been used to flatten the surfaces, it is generally limited to reducing *Ra* to about 2 Å because the polishing pad roughness is as large as 10 μm, and the polishing-particle diameters in the slurry are as large as 100 nm. We therefore developed a new polishing method, dressed-photon and phonon etching (DPP etching), that uses dressed photon based on an autonomous phonon-assisted process. DPP etching does not use any polishing pad, with which we obtained ultra-flat silica surface with angstrom-scale average roughness as small as *Ra* of 0.1 nm. Additionally, we succeeded in reduction of the Ra for the three-dimensional structures.

Keywords: Dressed-photon method, Phonon etching method, Surface roughness.

PACS numbers: 81.16. – c, 81.16.Dn

1. INTRODUCTION

Ultra-flat substrate surfaces with sub-nanometer scale roughness are required for various applications, including optical components for the extreme ultraviolet (UV) region and high-power lasers, and future optoelectronics devices on a sub-100 nm scale. To obtain a flat surface, conventional methods have used chemical-mechanical polishing (CMP) [1]. We have studied the application of the optical near-field to nanostructure fabrication using its properties of resolution beyond the diffraction limit and a novel nonadiabatic photochemical reaction. For chemical vapor deposition, we demonstrated photodissociation with a light source, with a photon energy lower than the absorption band edge energy of the molecules. The optical near-field is a virtual photon that can couple with an excited electron. In the coupled state, it is known as a dressed photon. Additionally, it can be coupled with multiple-mode of phonons, and thus, the quasi-particles of coupled state as dressed-photon-phonon (DPP). Thus, the energy of the DPP, is larger than the energy of a free photon due to coupling with and excited electron [2]. This DPP theory has been used to explain numerous experiments on topics such as photochemical vapour deposition [3], photolithography [4], and visible-light water splitting [5], as well as studies on photovoltaic devices [6] and energy up-conversion devices [7].

2. DPP ETCHING

Chlorine gas was used as the etching gas source. A continuous wave (CW) laser ($\lambda = 532$ nm) was used as the light source to dissociate the Cl_2. Since its photon energy is lower than the absorption band edge energy of Cl_2 ($\lambda = 400$ nm [5]), this avoids conventional adiabatic photo-etching. However, since the substrate surface has nanometer-scale protrusions, depending on its roughness, a strong optical near-field can be generated at the edge of such a protrusion (Fig. 1a). Since the optical near-field has a steep spatial gradient, a higher molecular vibrational state can be excited in the Cl_2, although the photon energy is lower than the absorption band energy of Cl_2, which cannot be excited by a uniform optical far-field. As a result, Cl_2 is selectively photodissociated and the activated Cl atoms etch away the protrusions on the substrate. Finally, the etching process automatically comes to a halt when the surface becames sufficiently flat so that the optical near-field disappears (Fig. 1b).

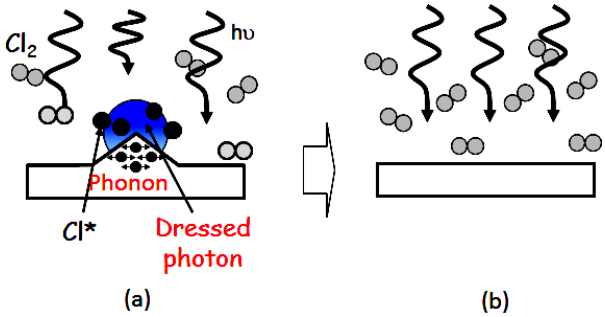

Fig. 1 – Schematic of DPP etching

We used silica substrates. The Cl_2 pressure was 100 Pa. Figures 2(a) and 2(b) show typical atomic force microscopy (AFM) images of a 10 μm × 10 μm of the scanning area of the silica substrate before and after DPP etching, respectively. By comparing these images, the drastic decrease in surface roughness was realized. Additonally, the cross-sectional profiles revealed this technique can reduced the pits, as well as bumps [8].

DPP etching does not require the polishing pad, it can be applicable to the three dimensional structures (Figs. 3(a) and 3(b)). We performed DPP etching on the grating structures of the soda lime glass. The comparison between Figs. 3(a) and 3(b) of before and after DPP etching confirmed that the DPP etching can etch the side wall of the three dimensional structures [9].

* yatsui@ee.t.u-tokyo.ac.jp

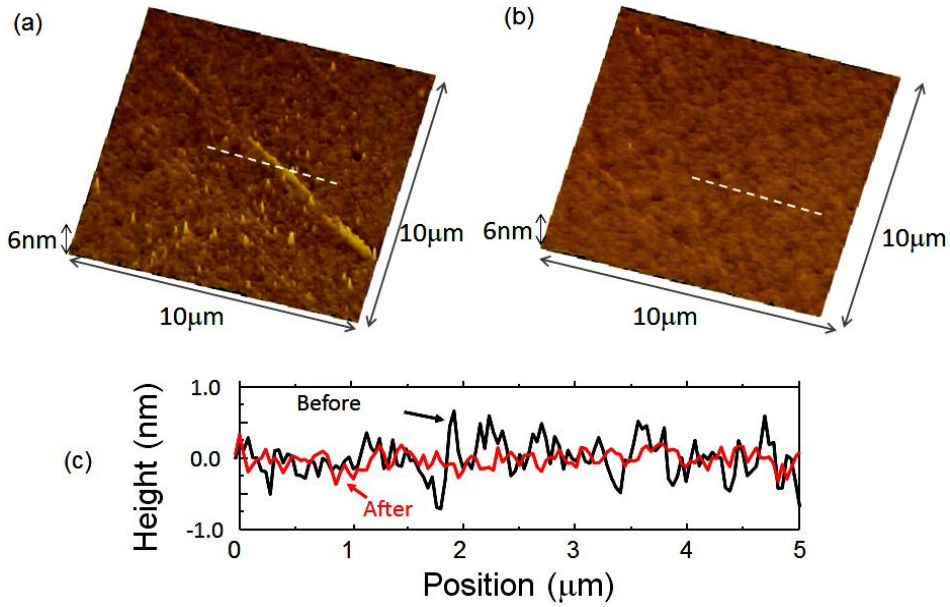

Fig. 2 – AFM images: (a) before and (b) after DPP etching. (c) Cross-sectional profiles along the dashed white lines in (a), and (b)

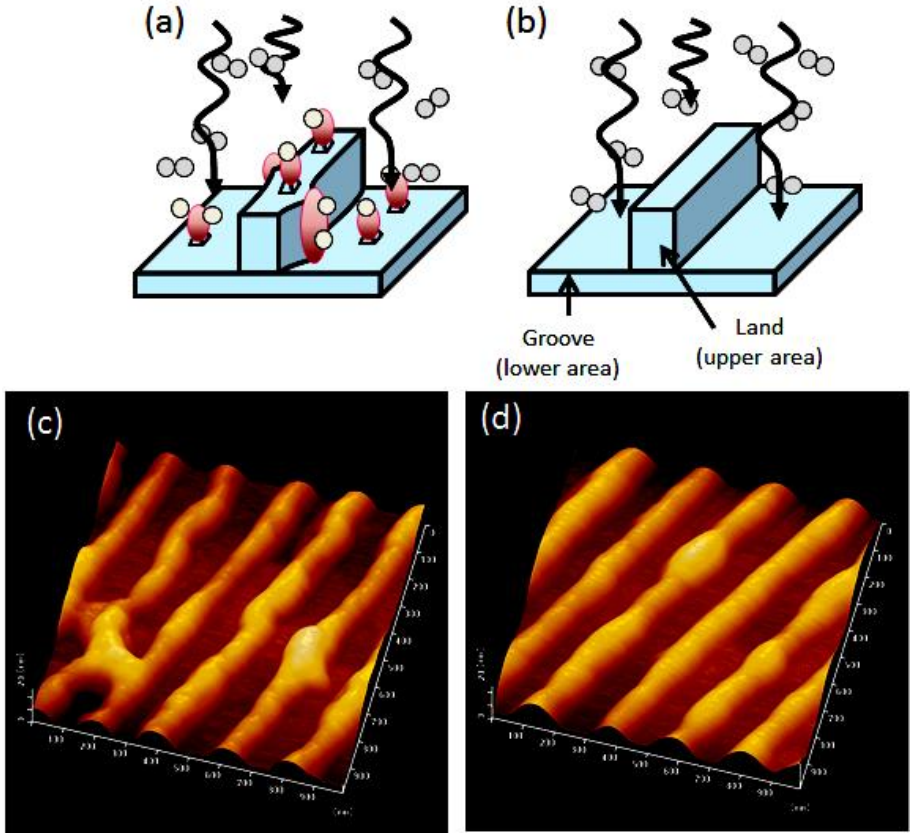

Fig. 3 – (a and b) Schematic of DPP etching on three dimensional structure. AFM images: (c) before and (d) after DPP etching

3. CONCLUSION

We reviewed recent developement of DPP etching. DPP etching is based on photo-chemical reaction, it can be applicable to other materials, including semiconductor, metal, plastic, and so on.

AKNOWLEDGEMENTS

A part of this work was supported by the "Development of Next-generation High-performance Technology for Photovoltaic Power Generation System" Program, NEDO, Japan.

REFERENCES

1. L.M. Cook, *J. Non-Crystalline Solids* **120**, 152 (1990).
2. A. Sato, Y. Tanaka, F. Minami, K. Kobayashi, *J. Lumin.* **129**, 1718 (2009).
3. T. Kawazoe, K. Kobayashi, S. Takubo, M. Ohtsu *J. Chem. Phys.* **122**, 024715 (2005).
4. H. Yonemitsu, T. Kawazoe, K. Kobayashi, M. Ohtsu. *J Lumin.* **122-123**, 230 (2007).
5. T.H.H. Le, K. Mawatari, Y. Pihosh, T. Kawazoe, T. Yatsui, M. Ohtsu, T. Kitamori, *Appl. Phys. Lett.* **99**, 213105 (2011).
6. S. Yukutake, T. Kawazoe, T. Yatsui, W. Nomura, K. Kitamura, M. Ohtsu. *Appl. Phys. B: Lasers O.* **99**, 415 (2010).
7. T. Kawazoe, H. Fujiwara, K. Kobayashi, M. Ohtsu, *Appl. Phys. B: Lasers O.* **15**, 1380 (2009).
8. T. Yatsui, K. Hirata, W. Nomura, Y. Tabata, M. Ohtsu, *Appl. Phys. B: Lasers O.* **93**, 55 (2008)
9. T. Yatsui, K. Hirata, Y. Tabata, Y. Miyake, Y. Akita, M. Yoshimoto, W. Nomura, T. Kawazoe, M. Naruse, M. Ohtsu, *Appl. Phys. B: Lasers O.* **103**, 527 (2011).

17p-D5-1

Basics of optical processing system based on nanophotonic droplets

Naoya Tate[1], Makoto Naruse[2], Motoichi Ohtsu[1]

[1] The University of Tokyo, [2] National Institute of Information and Communications Technology
E-mail: tate@nanophotonics.t.u-tokyo.ac.jp

We have previously demonstrated a novel technique for autonomously forming a nanophotonic droplet (ND) [1–3], which is a micro-scale spherical polymer structure that contains coupled heterogeneous nanometric components, such as quantum dots (QDs) and organic dye molecules. The sort-selectivity and alignment accuracy of the nanometric components in each ND, and the related homogeneity of their optical functions, are due to a characteristic coupling and encapsulation process based on a phonon-assisted photo-curing method involving dressed-photon–phonon interactions [4]. The method only requires irradiating a mixture of components with light to induce optical near-field interactions between each component, and subsequent processes based on these interactions.

As schematically shown in Fig. 1, the basic concept of an ND enables hierarchical interconnection between the scale of nanometric optical behavior and macro-scale applications. Our recent work on the development of a system for mass-producing NDs has shown that it is possible to achieve arbitrary sizes and optical properties. Concurrently with this, we have been studying the implementation of an optical functional system that works on fundamental characteristics of NDs, as an example of a nanophotonic information system [5].

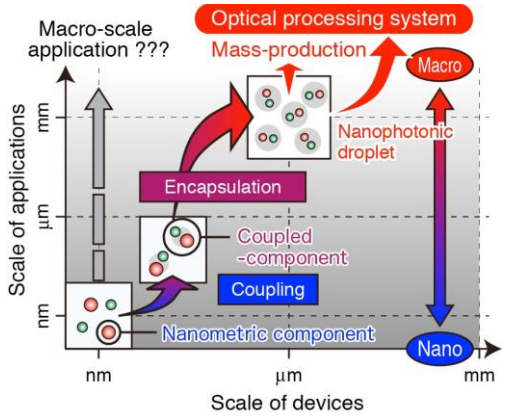

Figure 1: Basic concept of ND based on hierarchical interconnection between nano and macro scales.

Recent research in the field of *beyond von Neumann computing* [6] suggests that effective utilization of *fluctuations* in a physical setup forms an essential part of such a computing system. On the other hand, autonomy observed in the formation of NDs and the homogeneity of their optical properties are affected by fluctuations of the components in the mixture, which depend on thermal and size-resonant effects [7] of optical near-field interactions that occur when the components encounter each other. Due to such effects, the components freely float in the mixture and couple with heterogeneous components of similar size, and higher intensity interactions can be expected between them. Such behavior corresponds to a kind of solution solving in which a particular solution that satisfies appropriate conditions is sought. Figure 2 shows some results of demonstrations, indicating successive searching of a particular size of CdSe-QDs by utilizing coupling with CdS-QDs, and the subsequent increase in emission intensity. The accuracy and efficiency of such processes can be quantified with results of experimental measurements, such as optical spectrometry and small angle scattering.

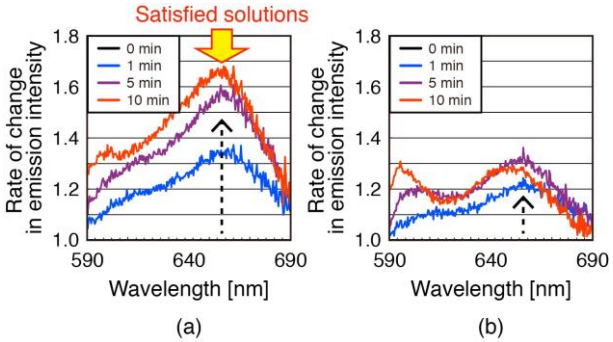

Figure 2: Rate of change of emission intensity from CdSe-QDs, (a) when coupled with CdS-QDs and (b) without CdS-QDs. The increased intensity at particular wavelengths indicates that CdSe-QDs of a particular size are successfully coupled with CdS-QDs of corresponding size.

Furthermore, while the formation process of NDs is fundamentally irreversible, more advanced processing operations can be realized by incorporating a reversible photoreaction mechanism, such as photoisomerization, into the formation process, to provide an additional control system enabling more advanced processing. These studies on NDs are expected to suggest other approaches to practical implementations of beyond von Neumann computing.

Acknowledgements

A part of this work was supported by the “Development of next-generation high-performance technology for photovoltaic power generation system” program, NEDO, Japan.

References

[1] N. Tate, et al. Appl. Phys. B, **110**, Issue 1, (2013) 39.
[2] N. Tate, et al. Appl. Phys. B, **110**, Issue 3, (2013) 293. [3] N. Tate, et al. Appl. Phys. B, DOI 10.1007/s00340-013-5442-1 [4] M. Ohtsu, et al. IEEE J. Sel. Top. Quant. Ele., **14**, (2008) 1404.
[5] http://nano.i-photonics.jp
[6] E. Verhulst, *Networks on Chip* (Springer, 2004) 217. [7] S. Sangu et al., J. Microsc. **202** (2001) 279.

Multiscale Surface Roughness Measure for Dressed-Photon–Phonon Etching

Makoto Naruse[1], Takashi Yatsui[2], Wataru Nomura[2],
Tadashi Kawazoe[2], Masaki Aida[3], and Motoichi Ohtsu[2]

1 Photonic Network Research Institute, National Institute of Information and Communications Technology, 4-2-1 Nukui-kita, Koganei, Tokyo 184-8795, Japan
2 Department of Electrical Engineering and Information Systems / Nanophotonics Research Center, School of Engineering, The University of Tokyo, 2-11-16 Yayoi, Bunkyo-ku, Tokyo 113-8656, Japan
3 Tokyo Metropolitan University, 6-6 Asahigaoka, Hino, Tokyo 191-0065, Japan
Email: naruse@nict.go.jp

Abstract– Dressed-photon–phonon (DPP) etching is a disruptive technology in planarizing material surfaces because it completely eliminates mechanical contact processes. However, adequate metrics for evaluating the surface roughness and the underlying physical mechanisms are still not well understood. Here we propose a two-dimensional multiscale surface roughness measure that represents the effectiveness of DPP etching while conserving the original two-dimensional surface topology. Also, we created a simple physical model of DPP etching that agrees well with the experimental observations, which clearly shows the involvement of the intrinsic multiscale properties of dressed photons, or optical near-fields, in the surface processing.

1. Introduction

Nanophotonics, which exploits light–matter local interactions on the nanometer scale, has been intensively investigated from a variety of aspects, ranging from fundamental science, such as atom/molecule and optical near-field interactions [1], and spectroscopy [2], to a number of practical applications, including information security [3], computing [4], the environment and energy [5], and healthcare [6], to name a few. What we particularly address in this paper is nanofabrication involving optical near-field processes [7,8].

The idea is to induce a nanofabrication process, either in the form of material desorption or deposition, selectively in a region where optical near-fields are present. Nowadays, the optical near-field is understood as a virtual photon coupled with an excited electron, called a dressed photon (DP). DPs can interact with phonons in the crystal lattice structure of nanomaterials in a coherent manner [7]. The combined coupled state of a DP and a coherent phonon, which is referred to as dressed-photon–phonon (DPP), has a higher energy than those of the DP and the incident photon [7]. Therefore, a DPP can induce photochemical reactions even under irradiation with a low photon energy at which photochemical reactions are conventionally inactive [8,9]. Such a process has been called a phonon-assisted process and has been applied to numerous demonstrations, including photochemical vapor deposition [10], photolithography [11], among others [12,13].

In particular, the DPP-based surface etching, or flattening, proposed by Yatsui *et al.*, which planarizes the surfaces of devices without any mechanical contact processes, is an interesting and industrially important technique [8,9,14,15]. It selectively induces photochemical reactions in regions on a surface where DPPs are excited, namely, in the vicinity of regions possessing fine-scale rough structures, leading to reduced surface roughness. Planarization of surfaces is important for various devices such optical elements [8], solid-state materials, such as silicon wafers, diamonds [9], and so on.

There are, however, several unsolved, important issues associated with DPP etching. The first concerns a suitable metric for evaluating the surface roughness. Conventionally, the roughness average, R_a, defined as the average of the absolute values of the deviation from the average height, has been widely used. However, by definition, R_a depends on the size of the region-of-interest (ROI). Furthermore, with such a measure, the effects provided by DPPs are concealed, and so it has been difficult to obtain physical insights into the underlying mechanisms which would serve to reveal the ultimate limitations of the method and to improve/optimize fabrication processes.

In fact, with a view to resolving these issues, we have previously proposed a parametric statistical spectrum analysis method for evaluating surfaces flattened by DPP etching [15]. Furthermore, in Ref. [9], we developed another measure, namely, the standard deviation of the height differences of two adjacent areas averaged over every l pixels, inspired by the Allan variance [16] that is widely applied in evaluating the stability of time-domain signals. Specifically, letting $\overline{z_k^{(l)}}$ be the average height over every l pixels, the measure was defined as $R(l)=\sqrt{\left\langle\left(\overline{z_{k+1}^{(l)}}-\overline{z_k^{(l)}}\right)^2/2\right\rangle}$. These methods allowed us to see the reduction in surface roughness correlated with spatially finer/coarser structures [9,15].

Nevertheless, important concerns still remain. One is that both of the above-mentioned methods must convert the original two-dimensional (2D) surface profile data to

one-dimensional (1D) data, on which the analysis is made. Namely, the topology inherent in the experimental data is destroyed, which is a large impediment to gaining an accurate physical understanding of the mechanisms involved. By overcoming these weaknesses, we will be able to understand the fundamental mechanisms of DPP etching.

In this paper, we propose a metric for evaluating surface roughness while preserving the original topology, what we call the *two-dimensional, multiscale surface roughness measure*, or MRM for short. Furthermore, taking into consideration the intrinsic multiscale properties of dressed photons, we propose a physical model representing the principal attributes of DPP etching. The resultant data agrees well with experiments.

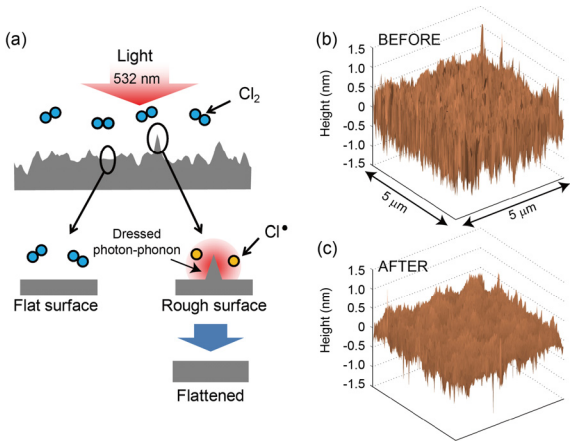

Fig. 1 (a) Schematic illustration of the dressed-photon–phonon etching. (b,c) Surface height profiles of a (001) GaN substrate (b) before and (c) after 30-minute irradiation with continuous-wave (CW) light at a wavelength of 532 nm in a Cl_2 atmosphere at 200 Pa. The roughness average, Ra, decreased from 0.23 nm to 0.14 nm.

2. Multiscale Roughness Measure

We first review the principles of DPP etching proposed by Yatsui *et al* [8]. The surface of a device to be etched is irradiated with a light beam. If the surface is rough, DPPs will be generated in the vicinity of the corresponding rough structures, and photochemical reactions can be induced selectively in the regions where the DPPs are generated [8,9]. More specifically, in the case of the experiments described below, chlorine gas (Cl_2) is filled in the space around the device to be processed, and chlorine radicals ($Cl^{\bullet}$) are selectively produced from the Cl_2 gas in the regions where DPPs are generated. The $Cl^{\bullet}$ then reacts with and etches the material, decreasing the local surface roughness, or bumps. Once the rough structures are eliminated, the DPPs will disappear, thus automatically terminating the photochemical reaction process. This physical principle is schematically shown in Fig. 1(a). In the experiment, the device under study was a (001) GaN substrate, which was subjected to 30 minutes of irradiation with continuous-wave (CW) light having a wavelength of 532 nm in a chlorine gas (Cl_2) atmosphere at 200 Pa. Figures 1(b) and (c) respectively show surface profile images taken by an atomic force microscope (AFM) before and after the etching process. The surface heights were measured at 256 × 256 equally spaced sampling points in a 5 μm × 5 μm area. The value of R_a decreased from 0.23 nm to 0.14 nm.

Now, assume that the height of a surface profile is given by $h(i,j)$, where the indexes (i,j) specify the position among $N \times N$ sampling points. Both i and j are positive integers ranging from 1 to N. The idea of the proposed measure, MRM, is (1) to evaluate the average height over $l \times l$ pixels (denoted by $h_P^{(l)}$); (2) to see how $h_P^{(l)}$ differs from the average height of its four neighbors, namely, the north ($h_N^{(l)}$), south ($h_S^{(l)}$), east ($h_E^{(l)}$), and west ($h_W^{(l)}$) areas; and then (3) to calculate the variance of such differences in the entire region of the sample. A schematic illustration of $h_P^{(l)}$ is shown in Fig. 2(a). As a function of the scale parameter, or the size of the local area (l), the MRM is defined by

$$\sigma_{2D}^2(l) = \left\langle \left(h_P^{(l)} - \left(\frac{h_N^{(l)} + h_S^{(l)} + h_E^{(l)} + h_W^{(l)}}{4} \right) \right)^2 \right\rangle \quad (1)$$

where $\langle\ \rangle$ means taking the average over all areas of a given sample. For simplicity, we assume that N and l are both powers of 2. When the size of a single local area is given by $l=2^k$, there are in total $(N/l)^2$ areas at the corresponding scale, and the average height in an area specified by (s,t), corresponding to $h_P^{(l)}$ in eq. (1), is given by

$$h^{(l)}(s,t) = \sum_{m=1,\cdots,l} \sum_{n=1,\cdots,l} h(l\times(s-1)+m, l\times(t-1)+n) \Big/ l^2 . \quad (2)$$

Here, $h_N^{(l)}$, $h_S^{(l)}$, $h_E^{(l)}$, and $h_W^{(l)}$ respectively correspond to $h^{(l)}(s,t+1)$, $h^{(l)}(s,t-1)$, $h^{(l)}(s+1,t)$, and $h^{(l)}(s-1,t)$. The indexes s and t are natural numbers ranging from 1 to $N/2^k$.

In an experimental demonstration using GaN as the sample, N was 256, and we used scale parameters l of 1, 2, 4, 8, 32, and 64 pixels, corresponding to physical lengths of about 19.5, 39.0, 78.1, 156.2, 312.5, 625, and 1250 nm, respectively. Figures 2(b) and (c) schematically represent the scale- and position-dependent metric $E_P^{(l)} = h_P^{(l)} - (h_N^{(l)} + h_S^{(l)} + h_E^{(l)} + h_W^{(l)})/4$, which we call the *multiscale etching score* (MES), before and after the optical processing, respectively. As demonstrated in Fig. 3(a), we can clearly see that the dashed curve, which is the MRM of the surface after DPP etching, is reduced compared with the solid curve, which is the MRM of the surface before the etching.

As mentioned above, the surface etching is autonomously induced at locations where the DPPs are generated by the roughness of the sample under study. We may envisage a physical picture in which etching is preferentially induced in regions where a tiny bumps exist.

Namely, the etching may be dominated by the MES of the tiniest scale, $E_P^{(1)}$, concerning the surface roughness at the tiniest scale. Based on such a picture, we can construct a physical model of the DPP etching such that the position that gives the maximum $E_P^{(1)}$ decrease the height of that position by an amount Δ_h. Note that the MES *at the tiniest scale* is considered.

We applied the above surface etching strategy to the original, unpolished surface profile of the GaN device. Through such modeling, the resultant surface roughness indeed decreased as compared with the original one, but the resulting MRM, $\sigma_{2D}^2(l)$, was as shown in Fig. 3(b-1), which did *not* agree with the experimental reality shown in Fig. 3(a).

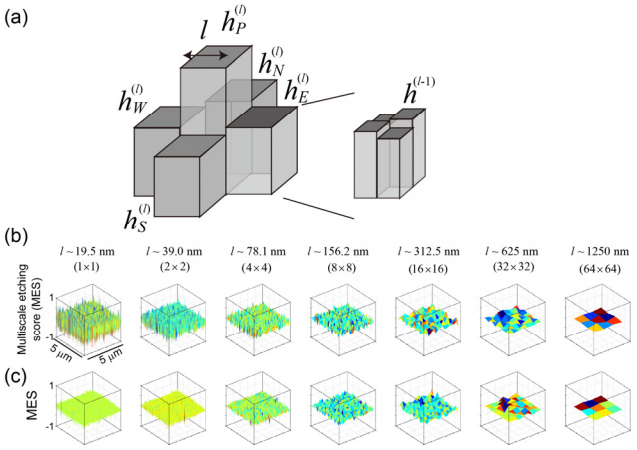

Fig.2 (a) Schematic diagram of the proposed two-dimensional multiscale surface roughness measure (MRM). (b,c) The two-dimensional distribution of the multiscale etching score (MES) (b) before and (c) after the DPP etching.

3. Multiscale Property of Optical Near-Field

We should consider that this is clear evidence that the DPP etching does *not* depend only on the finer structures. In fact, dressed photons, or optical near-fields, appear in a hierarchical manner depending on the spatial fine/coarse structures [17,18]. Suppose that there are two spheres whose radii are respectively given by a_P and a_S (Fig. 4(a)). The near-field optical potential is given by [18]

$$V(r) = \sum_{i=S}^{P} \frac{\exp(-\pi r / a_i)}{r}. \tag{3}$$

The scattered signal obtained from the interaction between these two spheres is given by

$$I(r_{SP}) \equiv \left| \iint \nabla_{r_P} V(|\boldsymbol{r}_P - \boldsymbol{r}_S|) d^3 r_S d^3 r_P \right|^2 \tag{4}$$
$$\propto \left[a_P^3 \left\{ \frac{a_S}{a_P} \cosh\left(\frac{\pi a_S}{a_P}\right) - \frac{1}{\pi} \sinh\left(\frac{\pi a_S}{a_P}\right) \right\} \left(\frac{1}{r_{SP}} + \frac{a_P}{\pi r_{SP}^2} \right) \exp\left(-\frac{\pi r_{SP}}{a_P} \right) \right]^2$$

where the center positions of the two spheres are respectively given by $\boldsymbol{r}_S$ and $\boldsymbol{r}_P$, and the distance between $\boldsymbol{r}_S$ and $\boldsymbol{r}_P$ is given by r_{SP} [18]. We can consider that a_S represents the surface roughness, whereas a_P indicates the size of the environment, containing chlorine radicals, that

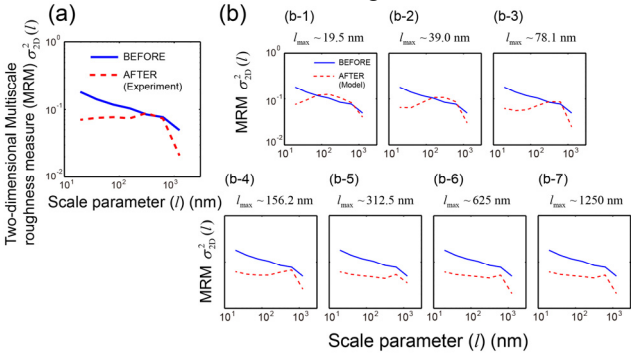

Fig. 3 The MRM, $\sigma_{2D}^{(l)}$, based on experimental results for GaN surfaces. (b) Evaluation of MRM, $\sigma_{2D}^{(l)}$, with respect to the calculated surface profiles derived through the proposed DPP etching model for different values of the maximum physical scale, $l_{\max}$.

could interact with the surface roughness. The effect of the interactions involving these two spheres is defined by the quantity given by eq. (4) divided by the square of the total volume of the two spheres, so that the evaluation is made in the dimension of per unit area. The solid, dotted, and dashed curves in Fig. 4(a) indicate the normalized quantity given by eq. (4) divided by $(a_P^3 + a_S^3)^2$, which represents the strength of the interaction between the two spheres, as a function of a_P when a_S is given by 10, 20, and 40 nm, respectively. Notice that the peak of the signal is obtained when the sizes of the two spheres are comparable. It turns out that, by regarding a_S as the spatial fine/coarse surface roughness of the structure, the interaction may be stronger at a coarser scale, rather than at a finer scale, when the roughness of the sample dominates on a large scale. Therefore, we should modify the DPP etching model above by taking into account the hierarchical attributes of dressed photons, so that the surface flatness is evaluated on multiple scales, and a reduction in surface roughness may be induced in a region that gives the maximum MES.

Specifically:

(a) Calculate the MES at each of the regions of a given device *and* at multiple scales: l=1,2,...,$l_{\max}$. The maximum scale considered is given by $l_{\max}$.

(b) Find the area that gives the maximum $E_P^{(l)}$ among all of the calculated positions and scales. Decrease the height of the corresponding area by an amount Δ_h.

(c) Repeat the process until all values calculated at step (a) are smaller than a certain threshold value.

In this model, we modify the maximum scale to be considered, $l_{\max}$, in step (a) and investigate the physical scales that affect the surface etching. The threshold at step (c) was assumed to be sufficiently small, and was set at 0.1. Figure 3(b) shows the MRM, $\sigma_{2D}^2(l)$, for different

values of l_{max}, namely, 1, 2, 4, 8, 16, 32, and 64. We can see that the resultant $\sigma^2_{2D}(l)$ is consistent with the experimental demonstrations shown in Fig. 3(b-3) when l_{max} is 4, corresponding to a physical length of 78.1 nm. Also, Fig. 4(b) shows the simulated time evolution of R_a depending on different l_{max} values. The resultant R_a in the experiment was 0.14 nm, whereas the converged R_a obtained through the modeling was 0.13 nm when l_{max} was 78.1 nm. This is another indication of the consistency between the proposed model and the experiment. These results suggest that the hierarchical properties of dressed photons inevitably affect the surface etching. With this model, we can predict the converged surface characteristics and the achievable flatness of given initial surfaces.

Finally, we remark on the converged surface characteristics. Minimizing the multiscale etching score (MES) to zero, in the best case, indicates that the height at a particular area is equal to the average of its surrounding areas. This is the property of the so-called harmonic functions, which are solutions of Laplace's equations [19]. What is particularly different from the conventional harmonic functions is that the solutions should minimize the MES at multiple scales (not just at a single scale). Nevertheless, such considerations inspired by harmonic functions support the fact that completely flat surfaces may *not* be the only converged pattern of DPP etching.

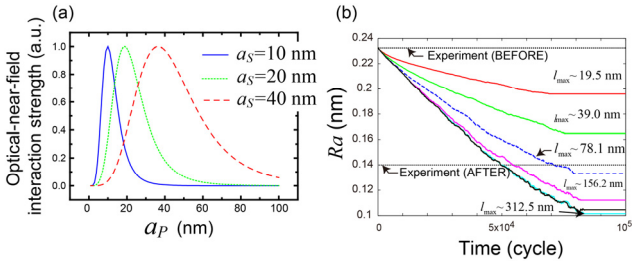

Fig. 4 (a) The hierarchical, or multiscale, nature of near-field interactions based on two-sphere model where the radii are respectively given by a_S and a_P. (b) Simulated time evolution of the roughness average (R_a) with respect to the maximum physical scale in the DPP etching model.

4. Conclusion

In conclusion, we proposed a two-dimensional multiscale surface roughness measure (MRM) for evaluating the surface roughness of a surface planarized by DPP etching. Taking into account the intrinsic hierarchical properties of dressed photons, we built a simplified physical model of the DPP etching, which agreed well with the experimental demonstration. It clearly demonstrates that the DPP etching involves multi-scale structures of the rough surface being processed. This study has unveiled one fundamental mechanism of nanofabrication, and we consider that the method described here will help to predict the achievable performance of nanofabrication and to optimize fabrication processes [20]. The application of the proposed measure to other fields, such as image processing [21], will also be an interesting future issue.

Acknowledgements

A part of this work was supported by Japan Society for the Promotion of Science, Japan Science and Technology Agency, New Energy and Industrial Technology Development Organization, TEPCO Memorial Foundation, and SCOPE of the Ministry of Internal Affairs and Communications.

References

[1] S. Tojo and M. Hasuo, Phys. Rev. A **71,** 012508 (2005).
[2] M. Aeschlimann, M. Bauer, D. Bayer, T. Brixner, F. Javier, G. de Abajo, W. Pfeiffer, M. Rohmer, C. Spindler, and F. Steeb, Nature **446**, 301 (2007).
[3] M. Naruse, N. Tate, and M. Ohtsu, J. Optics **14**, 094002 (2012)
[4] M. Naruse, M. Aono, S.-J. Kim, T. Kawazoe, W. Nomura, H. Hori, M. Hara, and M. Ohtsu, Phys. Rev. B **86**, 125407 (2012).
[5] T. Franzl, T. A. Klar, S. Schietinger, A. L. Rogach, and J. Feldmann, Nano Lett. **4**, 1599 (2004).
[6] C. Pistol, C. Dwyer, and A. R. Lebeck, IEEE Micro **28**, 7 (2008).
[7] A. Sato, Y. Tanaka, F. Minami, and K. Kobayashi, J. Lumin. **129**, 1718 (2009).
[8] T. Yatsui, K. Hirata, W. Nomura, Y. Tabata, and M. Ohtsu, Appl. Phys. B. **93**, 55 (2008).
[9] T. Yatsui, W. Nomura, M. Naruse, and M. Ohtsu, J. Phys. D **45**, 475302 (2012).
[10] T. Kawazoe, K. Kobayashi, S. Takubo, and M. Ohtsu, J. Chem. Phys. **122**, 024715 (2005).
[11] H. Yonemitsu, T. Kawazoe, K. Kobayashi, and M. Ohtsu, J. Lumin. **122-123**, 230 (2007).
[12] M. Naruse, T. Yatsui, H. Hori, K. Kitamura, and M. Ohtsu, Opt. Express **15**, 11790 (2007).
[13] H. Fujiwara, T. Kawazoe, and M. Ohtsu, Appl. Phys. B **98**, 283 (2010).
[14] T. Yatsui, K. Hirata, Y. Tabata, Y. Miyake, Y. Akita, M. Yoshimoto, W. Nomura, T. Kawazoe, M. Naruse, and M. Ohtsu, Appl. Phys. B **103**, 527 (2011).
[15] M. Naruse, T. Yatsui, W. Nomura, K. Hirata, Y. Tabata, and M. Ohtsu, J. Appl. Phys. **105**, 063516 (2009).
[16] D. W. Allan, Proc. IEEE **54**, 221 (1966).
[17] M. Naruse, T. Inoue, and H. Hori, Jpn. J. Appl. Phys. **46**, 6095 (2007).
[18] K. Kobayashi, S. Sangu, and M. Ohtsu, Quantum theoretical approach to optical near-fields and some related applications, in *Progress in Nano-Electro-Optics I* (M. Ohtsu ed. Springer-Verlag, Berlin 2003) pp. 119-157.
[19] L. C. Evans, *Partial Differential Equations* (American Mathematical Society, Providence, 2010)
[20] M. Naruse, T. Yatsui, W. Nomura, T. Kawazoe, M. Aida, and M. Ohtsu, Appl. Phys. Lett. **102**, 071603 (2013).
[21] A. Zawada-Tomkiewicz, Metrol. Meas. Syst. **XVII**, 493 (2010).

[III] REVIEW PAPERS

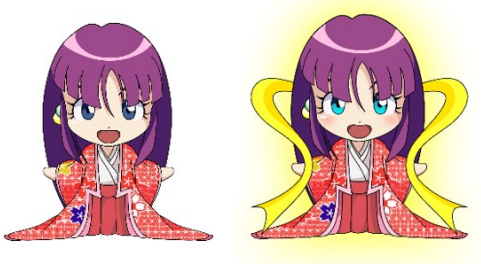

Beilstein Journal of Nanotechnology

Challenges in realizing ultraflat materials surfaces

Takashi Yatsui*[1,2], Wataru Nomura[1], Fabrice Stehlin[3], Olivier Soppera[3], Makoto Naruse[4] and Motoichi Ohtsu[1]

Review

Open Access

Address:
[1]School of Engineering, University of Tokyo, Bunkyo-ku, Tokyo 113-8656, Japan, [2]Advanced Low Carbon Technology Research and Development Program, Japan Science and Technology Agency, 7, Gobancho, Chiyoda-ku, Tokyo 102-0076, Japan, [3]Institut de Sciences des Materiaux de Mulhouse (IS2M), CNRS UMR 7361, 15, rue Jean Starcky, BP 2488, Mulhouse Cedex 68057, France and [4]National Institute of Information and Communications Technology, 4-2-1 Nukui-kita, Koganei, Tokyo 184-8795, Japan

Email:
Takashi Yatsui* - yatsui@ee.t.u-tokyo.ac.jp

* Corresponding author

Keywords:
dressed photon–phonon; phonon-assisted process; polishing; self-organized process

Beilstein J. Nanotechnol. **2013,** *4,* 875–885.
doi:10.3762/bjnano.4.99

Received: 15 September 2013
Accepted: 27 November 2013
Published: 11 December 2013

Associate Editor: P. Leiderer

Abstract

Ultraflat surface substrates are required to achieve an optimal performance of future optical, electronic, or optoelectronic devices for various applications, because such surfaces reduce the scattering loss of photons, electrons, or both at the surfaces and interfaces. In this paper, we review recent progress toward the realization of ultraflat materials surfaces. First, we review the development of surface-flattening techniques. Second, we briefly review the dressed photon–phonon (DPP), a nanometric quasiparticle that describes the coupled state of a photon, an electron, and a multimode-coherent phonon. Then, we review several recent developments based on DPP-photochemical etching and desorption processes, which have resulted in angstrom-scale flat surfaces. To confirm that the superior flatness of these surfaces that originated from the DPP process, we also review a simplified mathematical model that describes the scale-dependent effects of optical near-fields. Finally, we present the future outlook for these technologies.

Review

Introduction

In order to improve device performance and to conserve energy, a reduction of the surface roughness (R_a) is the most important challenge for the future of the electronic and opto-electronic industry. As for the optics in the extreme ultraviolet (EUV) region, in which the wavelength is extremely short, i.e., down to values of 13.4 nm, R_a must be brought down to around 1 Å in order to reduce the light-scattering loss [1]. The use of ultraflat mirrors is expected to help in realizing the high-power lasers that are required for future applications such as EUV system [2]. In addition, the necessity of shortening the pulse widths of

lasers is a major topic in the field of laser-machining processes, in which a flattened mirror can increase the laser durability [3]. The electron scattering losses must also be reduced for various industrial and scientific applications. To realize high-power light-emitting diodes (LEDs), the surface roughness of the substrate can be a serious problem, because substrates with large R_a values induce defects or dislocations in the deposited active layer [4]. Diamond is a promising material for future power devices because of its many excellent characteristics including high values for hardness and thermal conductivity, and excellent semiconductor properties such as a high dielectric breakdown field and a high carrier mobility [5]. However, at the same time, the hardness of diamond makes it difficult to realize a flattened surface, and therefore the performance of diamond devices has not been as good as expected. Furthermore, diamond is also a promising material for future quantum computing, because diamond with nitrogen vacancies can be a stable single-photon emitter at room temperature [6]. However, the high surface roughness of the diamond due to its hardness limits its performance.

Conventionally, mechanical polishing has been used to flatten surfaces. However, this method is generally limited to reducing R_a to around several angstroms, because the minimum value is governed by the roughness of the polishing pad, which is on the order of 10 μm, or the diameter of the polishing particles in the slurry, which can be as small as 100 nm. The slurries that are used for chemical–mechanical polishing (CMP) [7] consist of a large amount of the rare-earth material CeO_2, which chemically polishes the substrate. Owing to issues of cost and material availability, there has recently been an effort to reduce the usage of such rare-earth materials [8]. To reduce the usage of the CeO_2, many groups have attempted to develop alternative polishing pads [9] and slurries [10]. Watanabe et al. developed a surface treatment for SiC and diamond that uses a photocatalytic effect [11]. To induce this photocatalytic effect, they use a light source of shorter wavelengths to excite the carriers in TiO_2, so that the generated electrons and holes induce a photocatalytic effect and etch the substrate [12]. Those techniques resulted in ultraflat surfaces with R_a values as small as 2 Å. Although CeO_2 is not required in this technique, it does require a polishing pad to heat the substrate through friction between the polishing pad and substrate. Thus, the light must be introduced through the substrate, which should therefore be thin. Furthermore, mechanical polishing causes surface damage (scratches or pits) when the polishing particles and/or impurities in the slurry abrade the substrate.

A recent increase in electron mobility was achieved by introducing Ge in an Si device [13]. The higher electron mobility was realized through the modification of the band structure by in-plane tensile strain due to the wider interatomic distance for Ge compared to Si [14]. Furthermore, the wider interatomic distance induced a stretching force and resulted in a flattening of the interface between Si and Ge. However, the surface still remained rough. These problems can be overcome by eliminating contact polishing entirely. One promising approach for reducing the surface roughness is ion-beam smoothing [15]. Ion-beam irradiation at angles that are near grazing incidence preferentially removes large protrusions from the surface. This way a smoothing of wide areas can be achieved, while the surface damage is reduced. In addition, the use of a clustered ion beam to reduce the surface damage can lead to ultraflat surfaces of several hundred mm in diameter with a small R_a of 1 Å [16]. Although ion-beam smoothing does not require a polishing pad, it can still cause damage due to ion bombardment, and this technique also requires high-vacuum conditions, which is another obstacle to its widespread application.

In the context of these challenges, researchers have developed nanophotonic methods as alternative polishing techniques. Before reviewing recent studies of nanophotonic smoothing, we first provide an overview of the development of nanophotonics in the next section.

Optical near field: dressed photon–phonon

Near-field optics has made it possible to reduce the size of photonic devices to the sub-wavelength scale or smaller [17]. In particular, nanoscale photonic devices such as AND-gates, NOT-gates, and focusing devices have been developed that utilize the optical near field generated in nanoscale semiconductor quantum structures and the dipole-forbidden near-field energy transfer. Moreover, near-field optics has been used to fabricate nanoscale structures beyond the diffraction limit of light. For example, photolithography has been used to fabricate structures of several tens of nanometres in size by introducing near fields with the use of a visible light source [18]. Such advances can lead to the realization of systems that do not require EUV light sources, which are currently of limited practical use in industry because the equipment involved is large and expensive [19]. Thus, with further development, near-field lithography will be able to satisfy the requirements of future semiconductor electronic devices, such as highly integrated DRAMs.

The physics of these nanoscale optics has been developed under the assumption of a conventional multipolar quantum electrodynamic Hamiltonian in a Coulomb gauge and of single-particle states in a finite nanosystem [20]. In such a system, fluctuations in the electromagnetic field (e.g., zero-point fluctuations of the vacuum) cause nanomaterials to emit or absorb virtual photons, i.e., the optical near fields are continuously present

around illuminated materials. These so-called virtual absorption and emission processes violate the energy conservation law but are consistent with the Heisenberg uncertainty principle, and to take these processes into account, nanomaterial can be considered to be covered with a cloud of virtual photons. Within this framework, the virtual photon can be described as a coupled state of an electron and a real photon (i.e., a free photon (FP); Figure 1a). This virtual photon, also referred to as a *dressed photon* (DP) [21], is distinguished from the FP because it carries a material excitation energy. Therefore, the energy of the DP, $h\nu_{DP}$, is larger than that of the FP, $h\nu_{DP}$.

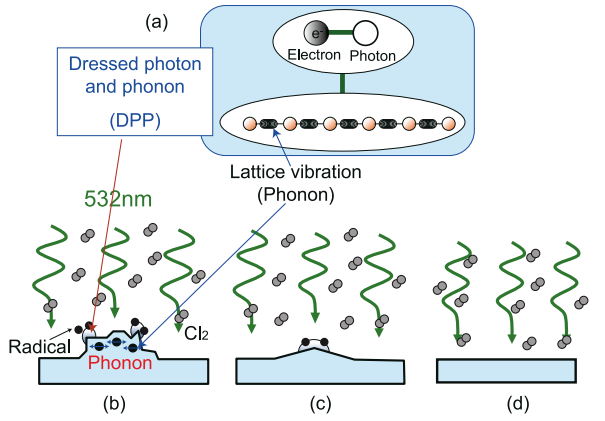

Figure 1: (a) Schematic diagram of a dressed photon–phonon (DPP). (b–d) Schematic diagrams of DPP etching. The etching gas is selectively photodissociated at the protrusions. The activated etching gas atoms etch away the protrusions. DPP etching stops automatically when the substrate becomes sufficiently flat.

To take advantage of nanoscale optics, a thorough understanding of the nanoscale material is required. Such nanoscale materials are composed of a crystal lattice, and after a DP is generated at the surface of an illuminated nanoscale particle, its energy can be exchanged with this crystal lattice. Through this exchange, vibrational modes can be coherently excited in the crystal lattice, creating multiple modes of coherent phonon states [22]. Consequently, the DP and a coherent phonon form a coupled state (Figure 1a). This state (the dressed photon and a phonon: DPP) constitutes a quasi-particle that is generated only when the particle size is sufficiently small so that the crystal lattice vibration is excited coherently. In contrast, vibrational modes cannot be excited coherently in bulk materials, and energy is instead dissipated as heat throughout the material. Therefore, the energy of the DPP, $h\nu_{DPP}$, is higher than $h\nu_{DP}$ ($h\nu_{FP} < h\nu_{DP} < h\nu_{DPP}$).

This DPP theory has been used to explain numerous experiments on topics such as photochemical vapour deposition [23], photolithography [24], and visible-light water splitting [25], as well as studies on photovoltaic devices [26] and energy up-conversion devices [27]. The efficiency of energy up-conversion by using DPP is reported to be more than three-fold higher than that of up-conversion by using conventional two-photon absorption for the generation of second harmonics, because the phonon state cannot be coupled with propagating light in the far-field [27]. Furthermore, DPPs have been reported to be localized selectively at disordered nanostructures such as impurity sites or protrusion edges [28].

As described above, the principles and concepts of DPP technology differ significantly from those of conventional wave-optical technologies such as photonic crystals [29], plasmonics [30], metamaterials [31], or quantum-dot photonic devices [32], in which the size and function are governed by the light diffraction limit. Therefore, we next use the framework of the DPP theory to review a nanophotonic fabrication process that realizes angstrom-scale flattening of substrate surfaces.

Dressed photon–phonon etching

DPPs can be consistently generated by irradiating a rough material surface with nanoscale structures. The generated DPPs induce the photodissociation of molecules at protrusions on the substrate (Figure 1b) even when the incident photon energy is smaller than the photodissociation energy, E_d. The dissociated molecules in turn induce the etching of the protrusion and the flattening the substrate (Figure 1c). This etching process stops automatically when the surface becomes flat and more homogeneous, because then the DPPs disappear. Therefore, surface smoothing by utilising DPPs is a self-organized process [26].

The DPP etching technique was developed to smooth various materials, including SiO_2 (fused silica and soda lime glass), plastic films, and crystal substrates. DPP etching on a diamond substrate [33] was performed by using O_2 gas, which has an E_d of 5.12 eV (wavelength, λ, of 242 nm) [34]. A continuous-wave (CW) He–Cd laser (λ = 325 nm, 3.81 eV, excitation power 0.8 W/cm^2) was used to dissociate the O_2 gas in the DPP etching, which produced the oxygen radicals O* to etch the protrusions of the diamond substrate and ultimately yielded an ultra-flat surface. Since the photon energy of the laser is lower than E_d of O_2, the conventional O_2 adiabatic photochemical reaction was avoided. Furthermore, the laser power density of approx. 1 W·cm^{-2} was 10^{15} times smaller than that associated with multi-photon processes using ultra-short pulse (femtosecond) lasers [35]. Therefore, the DPP etching process cannot be attributed to conventional multi-photon excitation processes [36]. A comparison of atomic force microscopy (AFM) images before (Figure 2a) and after 60 min of DPP etching (Figure 2b) confirmed that this treatment resulted in an ultra-flat surface with a small R_a value of 0.154 nm. The

minimum value of R_a is to be determined by the interatomic distance. As reported in [33], the surface roughness after 30 min was 0.181 nm, which is almost as small as that after 60 min (0.154 nm). These values are comparable to the interatomic distance of 0.206 nm for (111) diamond [37], which indicates that the surface roughness reduction might be completed already after 30 min of etching. This was also supported by the fact that the R_a value remained the same after 24 hours of etching.

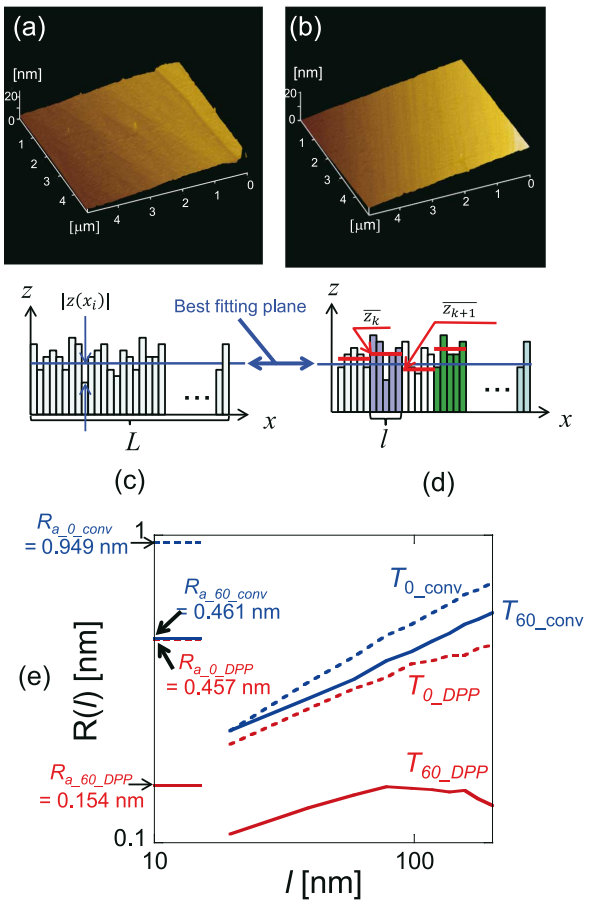

Figure 2: Typical atomic force microscopy (AFM) images of a type-Ib diamond (111) substrate with a 5 μm × 5 μm scanning area. The images were 256 × 256 pixels, which corresponds to a spatial resolution of 20 nm. AFM images were obtained for etching times of (a) 0 min (before etching) and (b) 60 min (after etching). The corresponding surface roughness values R_a were 0.457 nm and 0.154 nm, respectively. Schematic diagrams of the (c) surface roughness R_a and (d) standard deviation $R(l)$. (e) Calculated values of $R(l)$. Dashed and solid red lines show values before (T_{0_DPP} (0 min)) and after (T_{60_DPP} (60 min)) DPP etching (3.81 eV), respectively. Dashed and solid blue lines show values before (T_{0_conv} (0 min)) and after (T_{60_conv} (60 min)) conventional adiabatic etching (5.82 eV), respectively. Reproduced with permission from [33]. Copyright 2012 IOP Publishing.

To verify that the smoothing effect originated from the DPP process, the surface roughness was compared by using AFM images taken after conventional photoetching, in which a photon energy higher than E_d was used and after DPP etching (i.e., nonadiabatic photoetching). We note that in the AFM images shown, the tilt in the scan was compensated by using the third-order least-squares method. The light source for the conventional photoetching was a 5.82 eV light (λ = 213 nm; 20 Hz; pulse width 5 ns), the energy of which was higher than E_d of O_2 (5.12 eV). This light source induced adiabatic photodissociation of the O_2 molecules. For this comparison, instead of using the usual value of R_a, which is the average value of the absolute surface height deviations from the best-fitting plane (dashed blue line in Figure 2c), we developed a simplified mathematical model to describe the scale-dependent DPP effect. The value of R_a is determined as

$$R_a = \frac{1}{L}\int_0^L |z(x)|dx \cong \frac{1}{n}\sum_{i=1}^{n}|z(x_i)|,$$

where $|z(x_i)|$ are the absolute deviations from the best-fitting plane, L is the evaluation length, dx is the spatial resolution of $z(x)$, and n (= sL/dx) is the number of pixels in the measurement. R_a thus provides information about the average surface roughness for the entire scanning region. The standard deviation of the height difference function is given by

$$R(l) = \sqrt{\left\langle \left(\overline{z_{k+1}^{(l)}} - \overline{z_k^{(l)}} \right)^2 / 2 \right\rangle},$$

where l is the bin size, z is the height from the best-fitting plane, and $\overline{z_k^{(l)}}$ is the average z value of the bin (Figure 2d) [38]. This $R(l)$ can be used to determine the contributions of the surface roughness values at different length scales to the overall surface roughness.

The red curves labelled T_{0_DPP} and T_{60_DPP} in Figure 2e show the calculated $R(l)$ after 0 and 60 min of DPP etching, respectively. These results show that $R(l)$ decreased for all scales of l. Furthermore, the $R(l)$ values were comparable in magnitude to the R_a values shown on the left side in Figure 2e and they decreased as R_a decreased. The blue curves labelled T_{0_conv} and T_{60_conv} in Figure 2e represent the $R(l)$ values calculated after 0 and 60 min of conventional photochemical etching, respectively. Etching for 60 min with 5.82 eV light (conventional adiabatic photochemical etching) resulted in a marked reduction in surface roughness from 0.949 nm ($R_{a\_0\_conv}$) to 0.461 nm ($R_{a\_60\_conv}$), as shown on the left side of Figure 2e. However, comparing the $R(l)$ curves for 5.82 eV etching (T_{0_conv} (0 min) and T_{60_conv} (60 min)) revealed that $R(l)$ was unchanged at l = 20 nm. Since the apex of the protrusion has a larger surface area and thus a higher etching rate, a reduction in the surface roughness is expected. However, the 5.82 eV light induced an adiabatic photochemical reaction in the gas-phase molecules,

and there was no selective etching in this case. Therefore, etching with the 5.82 eV light did not the change the small-scale surface roughness profile. Moreover, it is noteworthy that this information could be revealed only by considering the $R(l)$ values. The results shown in Figure 2e also indicate that conventional photochemical etching changes the large-scale surface roughness profile. Therefore, if the initial structure has a large surface roughness, at the beginning states, conventional photochemical etching can reduce the large-scale surface roughness faster than DPP etching only.

DPP etching was also performed on GaN(001) substrates while using Cl_2 gas at a pressure of 200 Pa. A 532 nm light (2.33 eV, CW laser, power density of 0.28 W·cm^{-2}) was used for this photochemical etching, because E_d of Cl_2 is 3.10 eV (which corresponds to a wavelength of 400 nm) [39]. The low power density also prevented any multiphoton excitation associated with irradiation from ultrashort-pulse lasers. The AFM images taken before (Figure 3a) and after 30 min (Figure 3b) of etching show that R_a decreased from 0.23 to 0.14 nm. GaN is a compound semiconductor, so the R_a value of 0.140 nm obtained for GaN might be limited by the value of the interatomic distance between Ga and N of 0.195 nm for hexagonal GaN [40]. Furthermore, $R(l)$ again shows the individual contributions of the surface roughness at different length scales to the overall surface roughness, as shown in Figure 3e. In this figure, the solid blue circles and solid green diamonds in represent the $R(l)$ values before the etching began (corresponding to the AFM image in Figure 3a) and after 30 min into the etching process (corresponding to the AFM image in Figure 3b), respectively. The horizontal axis corresponds to the scale l in units of length. It can be seen that $R(l)$ decreased at both finer and broader scales. In addition, the open blue circle and open red square in Figure 3e correspond to the R_a values for Figure 3a and Figure 3b, respectively. The $R(l)$ values were comparable to the R_a values and decreased as R_a decreased. It is noteworthy that $R(l)$ decreased to less than 0.10 nm, which indicates that an ultrasmooth surface was obtained. This result is supported by the fact that R_a also decreased to 0.10 nm (open black triangle in Figure 3e for the smaller (1.0 μm × 1.0 μm) scanned area in Figure 3c).

To simulate the time evolution of the surface roughness and evaluate the scale-dependent attributes of DPP etching, we developed a *scale-dependent etching score* defined as

$$E_k^{(l=n\Delta)} = \left(\overline{Y_{k+1}^{(n\Delta)}} - \overline{Y_k^{(n\Delta)}}\right) + \left(\overline{Y_k^{(n\Delta)}} - \overline{Y_{k-1}^{(n\Delta)}}\right),$$

where Δ is the spatial resolution of the AFM image and the scale l is defined as $n\Delta$, Y is the height, and $\overline{Y_k^{(n\Delta)}}$ is the average Y value of the pixels, and n is the number of pixels (Figure 3d). In this approach, a highly convex region exhibits a larger score than regions that are more flat, which is useful because etching is more likely to occur at these sites. By using this scoring system, a virtual etching process was repeated and the etched surface profile was compared with the initial surface profile in the same experiment (Figure 3a). Meanwhile, a multiscale etching score was evolved for scales of $n = 2^m$ pixels (m = 0 to 4), as shown in Figure 3f. Over 10,000 repetition cycles, the surface height profile produced the $R(l)$ values shown by the solid red squares in Figure 3e, which are consistent with the experimental results. Furthermore, the time evolution of R_a was investigated by calculating the scale-dependent etching scores (Figure 3f). The calculated R_a values decrease with the etching time when all etching scores $E_k^{(l=n\Delta)}$ ($n = 2^m$, m = 0 to 4) are considered (red curve in Figure 3g). In comparison, when the progress of the etching depended only on the etching score at the finest scale ($n = 2^0$), the calculated R_a values (considering the finest etching score $E_k^{(l=\Delta)}$) increase (blue curve in Figure 3g), whereas the finest-scale etching score decreased over time. This is another clear manifestation of the scale-dependent nature of optical near-fields and of the crucial role they play in DPP etching.

DPP etching is potentially applicable to various three-dimensional surfaces including concave and convex lenses, diffraction gratings, and the inner wall surfaces of cylinders, because it is a non-contact method, i.e., it does not require polishing pads. These potential applications have been confirmed by using the procedure to smooth a substrate with a nanostripe corrugation pattern (Figure 4a and Figure 4b). In particular, the side walls of diffraction grating corrugations in soda lime glass were polished by using DPP etching [41]. Consequently, the R_a values decreased for both the substrate and the grooved surface, and an additional reduction in the line edge roughness was observed. Another application of this technique involved the fabrication of a nanostripe pattern on TiO_2. Direct ArF-laser photopatterning was followed by the application of a sol–gel negative tone photoresist to produce TiO_2 nanostructures by using deep-UV (DUV) direct-write imaging [42,43]. Figure 4c and Figure 4f show representative AFM images taken at different positions (positions A and B, respectively) of a TiO_2 sol–gel photoresist nanostripe corrugation pattern on a Si wafer.

DPP etching was performed under CW laser illumination (λ = 532 nm; power density (spatially uniform) 0.28 W·cm^{-2}) and Cl_2 gas exposure. Figure 4d and Figure 4f show typical AFM images after 10 min and 30 min of DPP etching, where reductions in both the width and the height of corrugations were observed as compared to those in the images taken before etching (Figure 4c and Figure 4f). Figure 4i shows the depend-

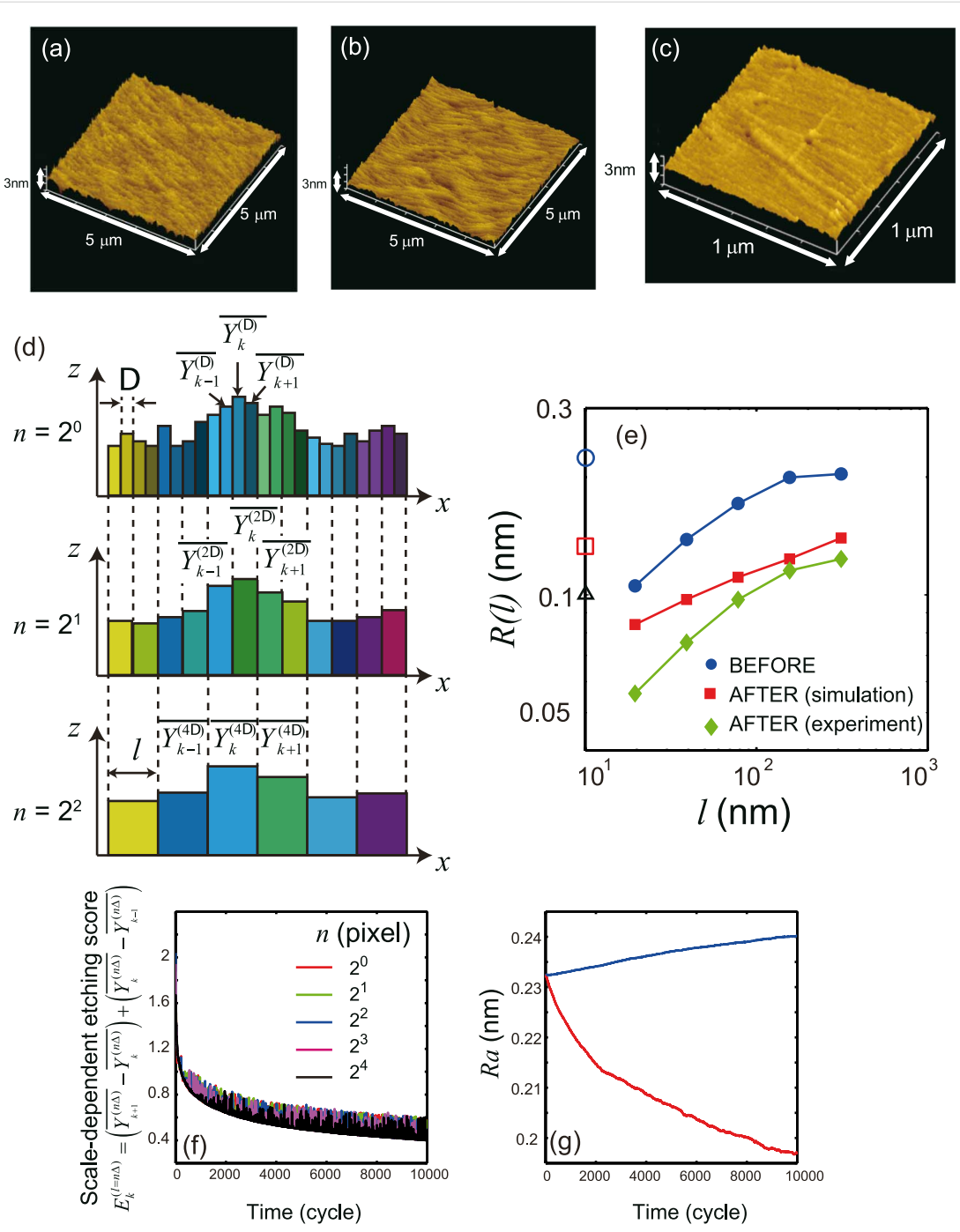

Figure 3: AFM images of the GaN surface (a) before and (b) after DPP etching. (c) Enlarged view (1.0 μm × 1.0 μm area) of the etched GaN surface. (d) Evaluation of surface roughness considering scale dependence. (e) Calculated $R(l)$. Solid blue circles denote results before DPP etching; solid green diamonds, after DPP etching; and solid red squares, after 10,000 cycles of virtual etching. (f) Time evolution of the scale-dependent etching score $E_k^{(l=n\Delta)}$ (see main text). (g) Calculated time evolution of R_a during virtual etching using the scale-dependent etching score. Red denotes the results for the multidimensional scale considering all etching scores, $E_k^{(l=n\Delta)}$($n = 2^m$, m = 0 to 4), and blue, the unidimensional scale considering only finest-scale etching score $E_k^{(l=\Delta)}$.

ence of the corrugation width and height on the etching time, from which the etching rate for the width and height were determined to be 2.6 nm/min and 1.8 nm/min, respectively. The higher etching rate for the width should originate from the developing process. As indicated by the white arrows in Figure 4c, undeveloped material remained at the sides of the land structures. These remaining structures induced DPPs and resulted in a higher etching rate. Table 1 shows the R_a value that

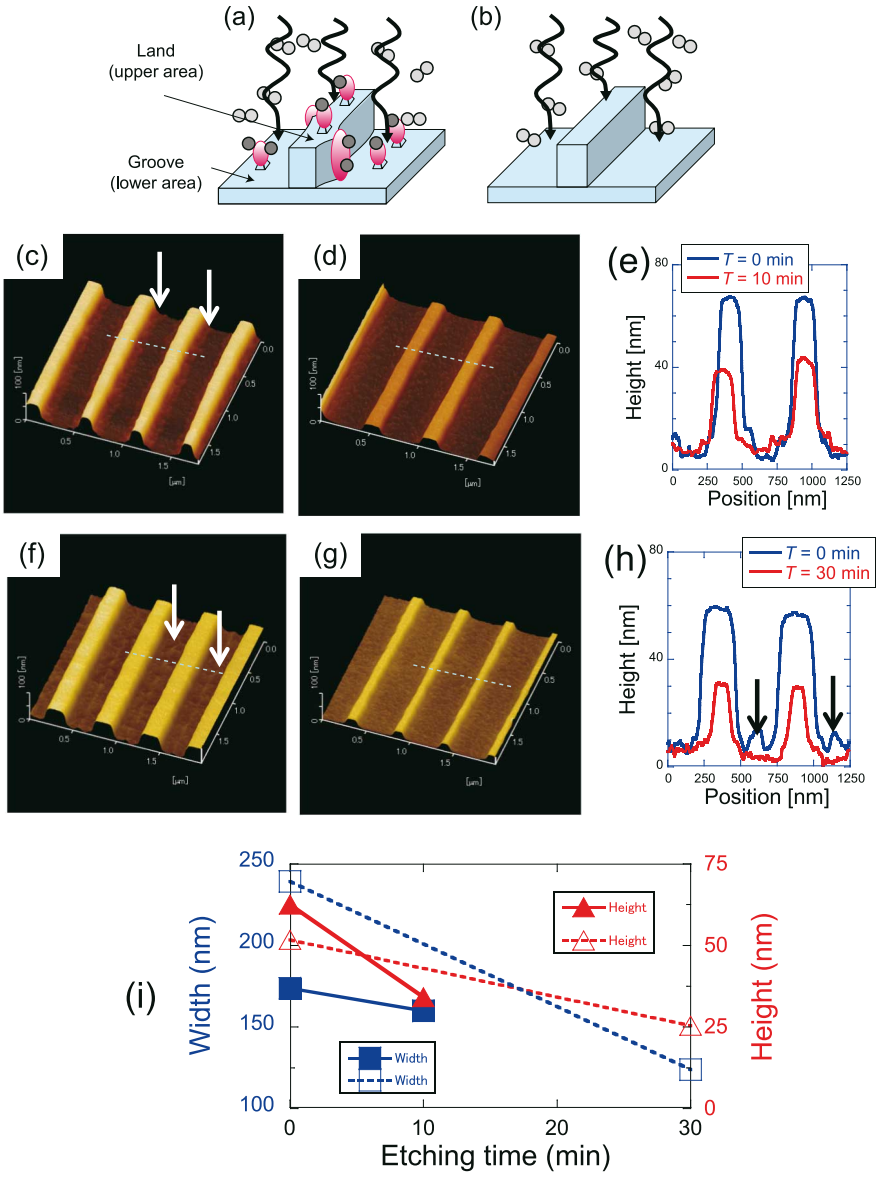

Figure 4: (a, b) Schematic diagrams of the DPP etching of substrates with nanostripe patterns. AFM images of TiO_2 (c, f) before and (d, g) after DPP etching (after etching times of (d) 10 min and (g) 30 min). (e) Cross-sectional profiles along the white dashed lines in (c) and (d). (h) Cross-sectional profiles along the white dashed lines in (f) and (g). (i) Dependence of corrugation width and height on the etching time. Blue solid squares and red solid triangles are data for (c) and (d), blue open squares and red open triangles are for (f) and (g).

Table 1: Dependence of the surface roughness on the etching time. A_L is measured along the land structures at position A (Figure 4c and Figure 4d), and A_G is measured along the grooves at position A (Figure 4c and Figure 4d). B_L is measured along the land structures at position B (Figure 4f and Figure 4g), and B_G is measured along the grooves at position B (Figure 4f and Figure 4g).

etching time (min)	A_L (nm)	A_G (nm)	B_L (nm)	B_G (nm)
0	0.39	0.50	0.41	1.25
10	0.29	0.41	—	—
30	—	—	0.33	0.84

was taken along the nanostripes, from which the decrease in surface roughness along both land structures and grooves is confirmed. In addition, the undeveloped structures at the bottom of the grooves (arrows in Figure 4f and Figure 4h) disappeared. TiO_2 was transparent to the incident light, so the coherent oscillation of electrons over its periodic structure was negligible. Therefore, plasmonic effects, which can sometimes originate from periodic enhancement of the local field [35], did not contribute to the smoothing of the corrugation pattern. Based on the results in Figure 4, the maximum roughness for which DPP etching will be applicable is in the range of 100 nm if the structure has a small roughness within the roughness envelope (see Figure 1b and Figure 1c), because the land structures of 100 nm in height were etched by using this process.

Dressed photon–phonon desorption

A DPP desorption process has also been developed for smoothing the surfaces of transparent ceramics such as alumina (Al_2O_3), which is a hard polycrystalline ceramic [44]. Alumina can be used as a low-loss gain medium for ceramic lasers [45] that are used in laser-driven spark plugs for ignition systems in automobile engines [46]. We expect that the surface roughness (e.g., scratches) of such media could be reduced by sputtering with Al_2O_3 nanoparticles, followed by DPP desorption [47]. In this study, radio frequency (RF) sputtering was used to deposit Al_2O_3 nanoparticles on an alumina substrate. In the case of conventional RF sputtering, the migration length of the Al_2O_3 nanoparticles on the substrate surface depends on the Schwöbel barrier [48] in the free energy profile. The migration length is short near the scratches because the Schwöbel barrier is high at their rims. Thus, the rate of deposition of the Al_2O_3 nanoparticles is higher at ridge sites than in flat areas. Hence, since the Al_2O_3 nanoparticles preferentially aggregate at the ridges, repairing the scratches by conventional deposition techniques is impossible. To overcome this difficulty, Al_2O_3 nanoparticles were deposited under illumination with visible light from a CW laser (λ = 473 nm; power density 2.7 W·cm^{-2}) with a wavelength longer than that of the absorption band edge of Al_2O_3 (λ_{ab} = 260 nm) [49]. This condition prevented a heating of the substrate surface. Hence, the DPPs generated on the ridges of the scratches activated the Al_2O_3 particles and increased their migration length, thereby allowing them to desorb from the ridge [50]. In contrast, the Al_2O_3 particles on the slopes and flat regions of the substrate were deposited at the same rate in the absence of DPPs. We note that DPPs were not generated near the bottom of the scratches because the substrate material around this area did not have dimensions at the nanometer-scale, and thus coherent phonons could not be excited. Deposition at the ridges was suppressed by this phonon-assisted process, whereas the bottoms of scratches were filled with Al_2O_3 particles. In this way, the scratches were finally repaired. Again, this demonstrates self-organized smoothing of the surface by using DPPs. Figure 5a and Figure 5b show AFM images before and after the RF sputtering of Al_2O_3 (30 min sputtering time) under visible light illumination. The average width of the scratches was found to decrease from 128 to 92 nm when this method was adopted, according to a statistical analysis, which employed a Hough transform. Furthermore, the average depth decreased from 3 to 1 nm.

In order to confirm the selective desorption of nanoparticles at the ridge edges, the DPP method was applied to a sapphire substrate with a uniform step-and-terrace structure [51]. Figure 5c and Figure 5d show AFM images after RF sputtering (sputtering time of 30 s), without and with visible light illumination, respectively. To determine the sites of nanoparticle deposition, we obtained the flattened gray-scale images in Figure 5e and Figure 5f, which correspond to Figure 5c and Figure 5d, respectively. Figure 5g and Figure 5h show the cross-sectional profiles along the dashed lines in Figure 5c and Figure 5e, respectively. These images confirm the selective deposition at the terrace edges during conventional RF sputtering. Furthermore, as a further confirmation that DPP desorption prevented the growth of Al_2O_3 nanoparticles on the terrace edges, no clear Al_2O_3 nanoparticle growth sites were formed during RF sputtering under visible light illumination. After 10 min of RF sputtering under illumination, an ultra-flat sapphire surface with an R_a value of 0.08 nm was obtained. In contrast, R_a increased as the sputtering time increased without illumination i.e., when using conventional sputtering (Figure 5i).

Conclusion

We have reviewed recent progress on the realization of ultraflat materials surfaces. In summary, DPs can be generated in transparent materials when the wavelength used for illumination is longer than the length of the absorption edge of the materials, and the DPP-based technique can be applied to other materials including semiconductors, dielectric materials, insulators, and plastics. DPP etching is a noncontact method and therefore does not cause damage owing to mechanical polishing, and hence, this technique should help to improve the electrical, optical, and/or electro-optical performance of devices in a variety of applications. We also described how the surface roughness changes when the proposed technique is used. Further surface characterization is required to verify that DPP etching is effective for optics and electronics. Because it does not require a contact pad, this technique can also be easily applied for the flattening of larger areas [52] by enlarging the beam spot, or by introducing an LED array. The use of Cl_2 in the DPP-etching process may induce substrate erosion. Hence, DPP etching requires a vacuum chamber. However, oxygen gas could smooth a diamond substrate at atmospheric pressure. These

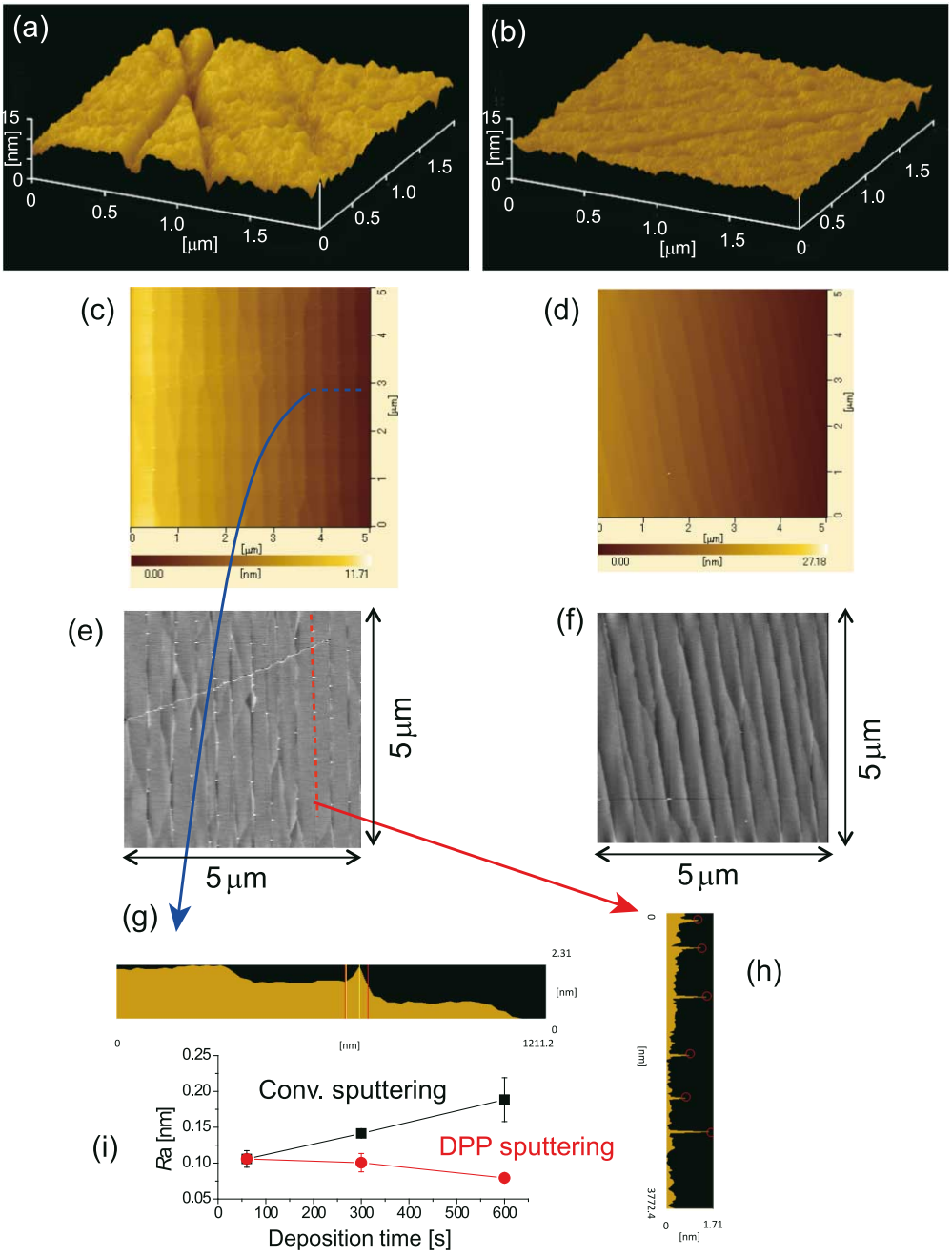

Figure 5: AFM images of the alumina substrate surface after RF sputtering (a) without and (b) with visible light illumination (Reproduced with permission from [46]. Copyright 2010 Springer Science+Business Media). Flattened AFM images of the sapphire substrate surface after RF sputtering (c) without and (d) with visible light illumination. (e, f) Flattened AFM images of (c) and (d), respectively, shown in gray-scale. (g, h) Cross-sectional profiles along the dashed lines in (c) and (e), respectively. (i) Dependence of R_a on the sputtering time. Solid black squares denote results for conventional RF sputtering, and solid red circles, for RF sputtering under visible light irradiation.

findings should accelerate the progress of DPP etching of various substrates.

Acknowledgements

This research was supported in part by the New Energy and Industrial Technology Development Organization (NEDO) under the Research and Development Program of Innovative Energy Efficiency Technology, under the program of Strategic Development on Rationalization Technology using Energy, and under the program of Development of Next-generation High-performance Technology for Photovoltaic Power Generation System; by a Grant-in-Aid for Young Scientists (A), Scientific

Research (B), and Exploratory Research from MEXT; by a research grant (Basic Research) from The TEPCO Memorial Foundation, and by a research grant from The Asahi Glass Foundation.

References

1. Wu, B.; Kumar, A. *J. Vac. Sci. Technol., B* **2007,** *25,* 1743–1761. doi:10.1116/1.2794048
2. Dunne, M. *Nat. Phys.* **2006,** *2,* 2–5. doi:10.1038/nphys208
3. Tien, A.-C.; Backus, S.; Kapteyn, H.; Murnane, M.; Mourou, G. *Phys. Rev. Lett.* **1999,** *82,* 3883–3886. doi:10.1103/PhysRevLett.82.3883
4. Nakamura, S. *Science* **1998,** *281,* 956–961. doi:10.1126/science.281.5379.956
5. Chow, T. P. *Microelectron. Eng.* **2006,** *83,* 112–122. doi:10.1016/j.mee.2005.10.057
6. Gruber, A.; Dräbenstedt, A.; Tietz, C.; Fleury, L.; Wrachtrup, J.; von Borczyskowski, C. *Science* **1997,** *276,* 2012–2014. doi:10.1126/science.276.5321.2012
7. Cook, L. M. *J. Non-Cryst. Solids* **1990,** *120,* 152–171.
8. Kato, Y.; Fujinaga, K.; Nakamura, K.; Takaya, Y.; Kitamura, K.; Ohta, J.; Toda, R.; Nakashima, T.; Iwamori, H. *Nat. Geosci.* **2011,** *4,* 535–539. doi:10.1038/ngeo1185
9. Ichinoho, N.; Murata, J.; Tani, Y.; Yanagihara, T.; Yamada, M. *Key Eng. Mater.* **2012,** *516,* 321–325. doi:10.4028/www.scientific.net/KEM.516.321
10. Jiang, M.; Wood, N. O.; Komanduri, R. *Wear* **1998,** *220,* 59–71. doi:10.1016/S0043-1648(98)00245-2
11. Ishikawa, Y.; Matsumoto, Y.; Nishida, Y.; Taniguchi, S.; Watanabe, J. *J. Am. Chem. Soc.* **2003,** *125,* 6558–6562. doi:10.1021/ja020359i
12. Tatsuma, T.; Tachibana, S.-i.; Fujishima, A. *J. Phys. Chem. B* **2001,** *105,* 6987–6992. doi:10.1021/jp011108j
13. Tezuka, T.; Sugiyama, N.; Mizuno, T.; Suzuki, M.; Takagi, S.-i. *Jpn. J. Appl. Phys.* **2001,** *40,* 2866–2874. doi:10.1143/JJAP.40.2866
14. Nayak, D. K.; Woo, J. C. S.; Park, J. S.; Wang, K. L.; MacWilliams, K. P. *Appl. Phys. Lett.* **1993,** *62,* 2853–2855. doi:10.1063/1.109205
15. Johnson, L. F.; Ingersoll, K. A. *Appl. Opt.* **1983,** *22,* 1165–1167. doi:10.1364/AO.22.001165
16. Yamada, I.; Matsuo, J.; Toyoda, N.; Kirkpatrick, A. *Mater. Sci. Eng., R* **2001,** *34,* 231–295. doi:10.1016/S0927-796X(01)00034-1
17. Ohtsu, M.; Kawazoe, T.; Yatsui, T.; Naruse, M. *IEEE J. Sel. Top. Quantum Electron.* **2008,** *14,* 1404–1417. doi:10.1109/JSTQE.2008.918110
18. Rogers, J. A.; Paul, K. E.; Jackman, R. J.; Whitesides, G. M. *Appl. Phys. Lett.* **1997,** *70,* 2658–2660. doi:10.1063/1.118988
19. Ito, T.; Okazaki, S. *Nature* **2000,** *406,* 1027–1031. doi:10.1038/35023233
20. Cohen-Tannoudji, C.; Dupont-Roc, J.; Grynberg, G. Quantum electrodynamics in the Coulomb gauge. *Photons and Atoms: Introduction to Quantum Electrodynamics;* Wiley-VCH Verlag GmbH: Weinheim, Germany, 2007; pp 169–252.
21. Ohtsu, M. *Nanophotonics* **2012,** *1,* 83–97. doi:10.1515/nanoph-2011-0001
22. Tanaka, Y.; Kobayashi, K. *J. Microsc. (Oxford, U. K.)* **2008,** *229,* 228–232. doi:10.1111/j.1365-2818.2008.01891.x
23. Kawazoe, T.; Kobayashi, K.; Takubo, S.; Ohtsu, M. *J. Chem. Phys.* **2005,** *122,* 024715. doi:10.1063/1.1828034
24. Yonemitsu, H.; Kawazoe, T.; Kobayashi, K.; Ohtsu, M. *J. Lumin.* **2007,** *122–123,* 230–233. doi:10.1016/j.jlumin.2006.01.115
25. Le, T. H. H.; Mawatari, K.; Pihosh, Y.; Kawazoe, T.; Yatsui, T.; Ohtsu, M.; Tosa, M.; Kitamori, T. *Appl. Phys. Lett.* **2011,** *99,* 213105. doi:10.1063/1.3663632
26. Yukutake, S.; Kawazoe, T.; Yatsui, T.; Nomura, W.; Kitamura, K.; Ohtsu, M. *Appl. Phys. B* **2010,** *99,* 415–422. doi:10.1007/s00340-010-3999-5
27. Kawazoe, T.; Fujiwara, H.; Kobayashi, K.; Ohtsu, M. *IEEE J. Sel. Top. Quantum Electron.* **2009,** *15,* 1380–1386. doi:10.1109/JSTQE.2009.2014781
28. Sato, A.; Tanaka, Y.; Minami, F.; Kobayashi, K. *J. Lumin.* **2009,** *129,* 1718–1721. doi:10.1016/j.jlumin.2009.02.032
29. Yablonovitch, E. *Phys. Rev. Lett.* **1987,** *58,* 2059–2062. doi:10.1103/PhysRevLett.58.2059
30. Ozbay, E. *Science* **2006,** *311,* 189–193. doi:10.1126/science.1114849
31. Shelby, R. A.; Smith, D. R.; Schultz, S. *Science* **2001,** *292,* 77–79. doi:10.1126/science.1058847
32. Eberl, K. *Phys. World* **1997,** 47–52.
33. Yatsui, T.; Nomura, W.; Naruse, M.; Ohtsu, M. *J. Phys. D: Appl. Phys.* **2012,** *45,* 475302. doi:10.1088/0022-3727/45/47/475302
34. Keilin, D.; Hartree, E. F. *Nature* **1950,** *165,* 543–544. doi:10.1038/165543a0
35. Miyaji, G.; Miyazaki, K. *Opt. Express* **2008,** *16,* 16265–16271. doi:10.1364/OE.16.016265
36. Kawata, S.; Sun, H.-B.; Tanaka, T.; Takada, K. *Nature* **2001,** *412,* 697–698. doi:10.1038/35089130
37. Tokuda, N.; Umezawa, H.; Kato, H.; Ogura, M.; Gonda, S.; Yamabe, K.; Okushi, H.; Yamasaki, S. *Appl. Phys. Express* **2009,** *2,* 055001. doi:10.1143/APEX.2.055001
38. Allan, D. W. *Proc. IEEE* **1966,** *54,* 221–230. doi:10.1109/PROC.1966.4634
39. Kullmer, R.; Bäuerle, D. *Appl. Phys. A* **1987,** *43,* 227–232. doi:10.1007/BF00615982
40. Leszczynski, M.; Teisseyre, H.; Suski, T.; Grzegory, I.; Bockowski, M.; Jun, J.; Porowski, S.; Pakula, K.; Baranowski, J. M.; Foxon, C. T.; Cheng, T. S. *Appl. Phys. Lett.* **1996,** *69,* 73–75. doi:10.1063/1.118123
41. Yatsui, T.; Hirata, K.; Tabata, Y.; Miyake, Y.; Akita, Y.; Yoshimoto, M.; Nomura, W.; Kawazoe, T.; Naruse, M.; Ohtsu, M. *Appl. Phys. B* **2011,** *103,* 527–530. doi:10.1007/s00340-011-4569-1
42. Ridaoui, H.; Wieder, F.; Ponche, A.; Soppera, O. *Nanotechnology* **2010,** *21,* 065303. doi:10.1088/0957-4484/21/6/065303
43. Stehlin, F.; Wieder, F.; Spangenberg, A.; Le Meins, J.-M.; Soppera, O. J. *J. Mater. Chem. C* **2014,** *2,* 277–285. doi:10.1039/c3tc31326c
44. Krell, A.; Blank, P.; Ma, H.; Hutzler, T.; Nebelung, M. *J. Am. Ceram. Soc.* **2003,** *86,* 546–553. doi:10.1111/j.1151-2916.2003.tb03339.x
45. Krell, A.; Blank, P.; Ma, H.; Hutzler, T.; van Bruggen, M. P. B.; Apetz, R. *J. Am. Ceram. Soc.* **2003,** *86,* 12–18. doi:10.1111/j.1151-2916.2003.tb03270.x
46. Pavel, N.; Tsunekane, M.; Taira, T. *Opt. Express* **2011,** *19,* 9378–9384. doi:10.1364/OE.19.009378
47. Nomura, W.; Yatsui, T.; Yanase, Y.; Suzuki, K.; Fujita, M.; Kamata, A.; Naruse, M.; Ohtsu, M. *Appl. Phys. B* **2010,** *99,* 75–78. doi:10.1007/s00340-009-3797-0
48. Menke, E. J.; Li, Q.; Penner, R. M. *Nano Lett.* **2004,** *4,* 2009–2014. doi:10.1021/nl048627t
49. Benabid, F.; Notcutt, M.; Loriette, V.; Ju, L.; Blair, D. G. *J. Phys. D* **2000,** *33,* 589. doi:10.1088/0022-3727/33/6/301

50. MacDonald, K. F.; Fedotov, V. A.; Pochon, S.; Ross, K. J.; Stevens, G. C.; Zheludev, N. I.; Brocklesby, W. S.; Emel'yanov, V. I. *Appl. Phys. Lett.* **2002,** *80,* 1643–1645. doi:10.1063/1.1456260
51. Yoshimoto, M.; Maeda, T.; Ohnishi, T.; Koinuma, H.; Ishiyama, O.; Shinohara, M.; Kubo, M.; Miura, R.; Miyamoto, A. *Appl. Phys. Lett.* **1995,** *67,* 2615–2617. doi:10.1063/1.114313
52. Teki, R.; Kadakshm, A. J.; Goodwin, F.; Yatsui, T.; Ohtsu, M. *Proc. SPIE* **2013,** *8679,* 86790F. doi:10.1117/12.2011260

License and Terms

新製品・新技術紹介

ドレストフォトンナノポリッシングを用いた超平滑加工技術の開発

八井　崇，大津元一

東京大学大学院工学系研究科（〒113-8656　東京都文京区弥生 2-11-16）

Development of Ultra-flat Surface Using Dressed Photon Nano-polishing

YATSUI Takashi and OHTSU Motoichi

（Received December 10, 2012）

Key words：dressed photon, ultra-flat surface, three-dimensional, self-organized process

1. はじめに

近年，近接場光を利用することで，デバイス寸法や加工寸法が光の回折限界を超えて微小化可能となった．さらに，従来の光技術では実現不可能だった新機能，新現象が可能となっている．この新しい光技術を考える上で，近接場光は局在している光子単体とし捉えるのではなく，物質励起と光子が結合した（物質励起の衣をまとった）仮想光子（Dressed photon．以下 DP と略記）と考えることが適切である[1]．

この DP は，さらに，格子振動（フォノン）とも結合しうることで，本来電気双極子禁制であるエネルギー準位にも電子，励起子が励起可能となるという重要な性質をもつ．このようにして電気双極子許容となった実在準位を介した多段階遷移が可能となるため，バルク材料のバンドギャップ以下の光子エネルギーをもった光が入射された場合でも，伝導帯への電子励起が可能となる．この現象は，入射光の光子エネルギーが上方変換されたことを意味する．このフォノン援用エネルギー上方変換は，実在準位を介した遷移となるため，たとえ入射光パワーが低い場合であっても高効率にエネルギー上方変換が実現し，第 2 次高調波発生のための 2 光子吸収過程によるエネルギー上方変換の発生効率と比較して，三桁以上高くなることが確認されている[2]．

本稿では，この DP によってもたらされる新しい加工技術として，表面平坦化加工技術の進展について紹介する．

2. ドレストフォトンナノポリッシング

従来の表面平坦化手法は，機械化学研磨（Chemical Mechanical Polishing：CMP）が用いられている[3]．この手法は，研磨パットと被研磨物を機械的に接触して研磨するため，表面粗さの低減に限界があり，また研磨傷の生成を避けることができない．

上記の諸問題を解決する手法がドレストフォトンナノポリッシング（Dressed Photon Nano-Polishing：DPNP）である[4-7]．合成石英を用いて DPNP の詳細を述べる．合成石英のエッチングガスとしては塩素ラジカル（Cl*：塩素分子が分解されたもの）がある．合成石英とは反応しない塩素分子（光吸収端波長 400 nm）雰囲気中に基板を導入し，光（波長 532 nm）を照射する（**Fig. 1**（a））．

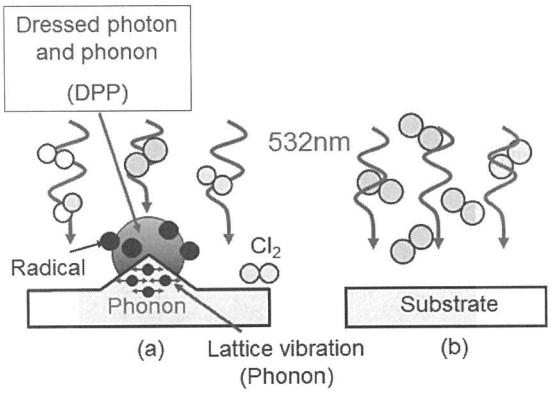

Fig. 1　DPNP

この光の波長は光吸収端波長より長いので，塩素分子に吸収されず Cl* は発生しない．一方，この光により，基板表面の局所的な凸部に DP が発生すると，フォノン援用過程によるエネルギー上方変換された光（短波長の光）によって塩素分子は分解し Cl* が発生する（**Fig. 1**（a））．その結果，この Cl* が合成石英と反応し，凸構造のみがエッチングされ基板が平坦化される．そして，最終的に基板に凸部がなくなると DP は発生しなくなるため，反応が自動的に停止し余計なエッチングを防ぐことが可能となる（**Fig. 1**（b））．

3. DPNP による超平坦化

3.1 ガラス基板の平坦化

上記原理を利用した合成石英平面基板の平坦化について紹介する．合成石英基板は，高出力レーザや短波長用光源の光学素子としての利用が期待されており，高性能化のためには，Ra 値を 1Å 以下に低減することが望まれている．

表面粗さ Ra 値の評価方法には，原子間力顕微鏡（AFM）

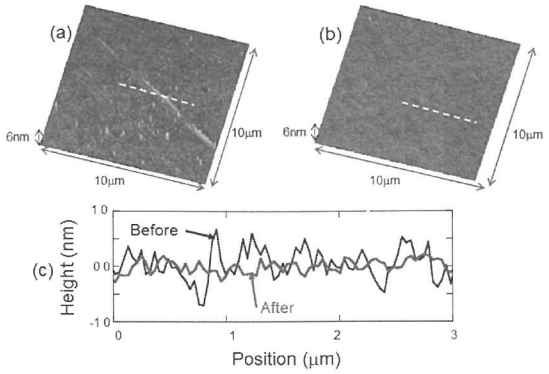

Fig. 2　AFM image of (a) before and (b) after DPNP. (c) Cross-sectional profiles along the white dashed lines in (a) an (b)

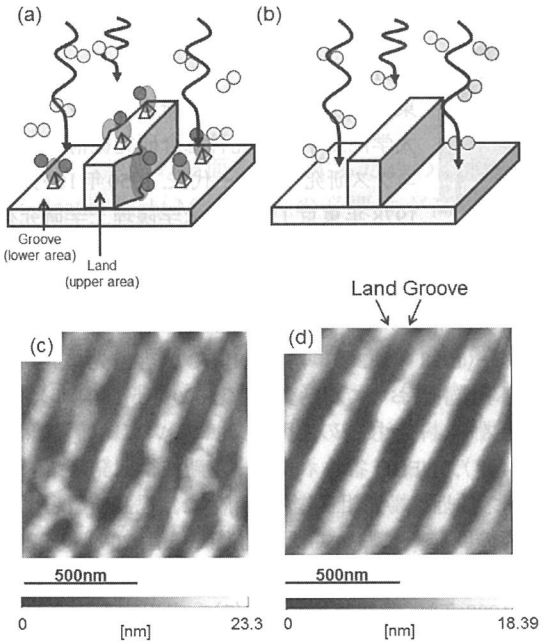

Fig. 3　DPNP on three-dimensional structures. AFM image of (c) before and (d) after DPNP.

を用いた. 基板エッチングのためのガスには塩素を選択し, 塩素導入後のチャンバーの圧力を 100 Pa とした. 照射光源についてはレーザ(波長 532 nm)を使用した.

Fig. 2 は DPNP エッチング前(**Fig. 2**(a))と後(**Fig. 2**(b))の AFM 像の比較を示している. この比較像より表面の凹凸が低減することが明らかである. さらに, この AFM 図の変化をより詳細に比較するために, それぞれの像における断面図を **Fig. 2**(c)に示す. この図からピーク-バレー値が近接場光エッチングによって 1.2 nm から 0.5 nm に減少していることがわかる. エッチング後の Ra 値として最小 1.1Å であった[4].

3.2　3 次元構造の平坦化

DP は基板表面に光が照射されていれば発生するため, 平面基板以外の 3 次元形状を有する素子に対しても平坦化が可能であると期待される(**Fig. 3**(a)および **Fig. 3**(b)). 3 次元構造を有する基板には, ナノインプリントにより作製

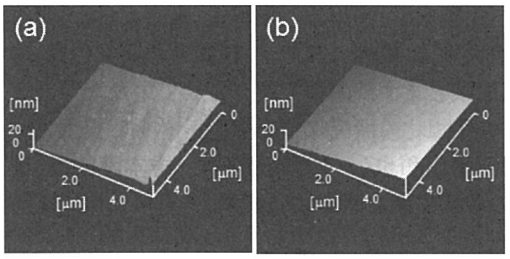

Fig. 4　AFM image of (c) before and (d) after DPNP on diamond substrates.

されたソーダライムガラスのナノウォール基板を用いた[8]. **Fig. 3**(d)は, 30 分間 DPNP を施した後の AFM 像を示す. この結果から, ランド部の Ra 値は 0.68 nm から 0.36 nm に低減し, 同様にグルーブ部の Ra 値は 0.76 nm から 0.26 nm に低減しており, 3 次元構造の平坦化が実証された[7].

3.3　ダイヤモンド基板の平坦化

本稿で紹介する表面平坦化技術はガラスのみならず, その他の結晶やプラスチックなどにも適用可能であると期待される. そこで, 近年パワーデバイスとして注目される, ダイヤモンド結晶基板に対する DPNP を行った. ダイヤモンドのエッチングガスとしては, 大気中の酸素を利用し, ダイヤモンド表面の凹凸において酸素を分解する光として波長 325 nm の光を利用した. **Fig. 4**(a)に DPNP 前の AFM 像を示す(Ra 値 0.456 nm). 本基板に対して, 60 分 DPNP を施したところ Ra 値 0.154 nm を達成した.

4.　結　　論

本稿では DP を利用することで可能となる全く新しい加工方法について紹介した. DP がナノ構造のみに局在するという特長を利用することで, 従来の CMP 法では到達不可能な表面性が得られることで, 電子デバイス, 光デバイスにおける, エネルギー利用効率の大幅な向上が期待される. さらに, 本手法は光化学反応を利用したものであるため, 本稿で紹介した材料以外にも応用可能である. また, 従来の加工法では不可能であった, 中空構造の内壁の平滑化が可能になるなど様々な応用が期待される. 上記に述べたように, DP を利用することで, 従来の伝搬光を用いた光技術では原理的に実現不可能な現象が実現可能になる, つまり光技術のパラダイムシフトが達成されると期待される.

謝　　辞

本研究の一部は, 東電記念財団研究助成(基礎研究), NEDO 省エネルギー革新技術開発事業・先導研究フェーズ「近接場光エッチングを用いた光学素子用基板表面のサブナノ平坦化技術の開発」, NEDO 省エネルギー革新技術開発事業・挑戦研究フェーズ「近接場光相互作用を用いた自己完結型超平坦物質形成技術の開発」, 戦略的創造研究推進事業 先端的低炭素化技術開発(ALCA)の援助の基に行われた.

本研究を遂行するにあたり, 多大なる協力を頂いた小林

潔教授(山梨大学)，川添　忠博士(東京大学)，野村　航博士(東京大学)，成瀬　誠博士(情報通信研究機構)の各氏に深く感謝致します．本稿で紹介させていただいたオングストローム平坦化の研究についてデータをご提供下さった多幡能徳，平田和也(シグマ光機㈱)，吉本護教授(東京工業大学)の各氏に深く感謝致します．

参考文献

1) Ohtsu, M., Kobayashi, K., Kawazoe, T., Yatsui T. and Naruse, M.: Principles of Nanophotonics, Principles of Nanophotonics, Taylor & Francis, (2008).
2) Kawazoe, T., Fujiwara, H., Kobayashi K. and Ohtsu, M.: Visible light emission from dye molecular grains via infrared excitation based on the nonadiabatic transition induced by the optical near field, IEEE J. Select. Top. Quant. Electron., **15**(5), (2009), 1380-1386.
3) Cook, L.M., Non-Crystal, J.: Chemical processes in glass polishing, Sol **120**(1-3), (1990), 152-171.
4) Yatsui, T., Hirata, K., Nomura, W., Tabata, Y. and Ohtsu, M.: Realization of an ultra-flat silica surface with angstrom-scale average roughness using nonadiabatic optical near-field etching, Appl. Phys., B **93**(1), (2008), 55-57.
5) Yatsui, T., Hirata, K., Tabata, Y., Nomura, W., Kawazoe, T., Naruse, M. and Ohtsu, M.: In situ real-time monitoring of changes in the surface roughness during nonadiabatic optical near-field etching, Nanotech., **21**(35), (2010).
6) Takashi, Y., Wataru, N., Makoto, N. and Motoichi, O.: Realization of an atomically flat surface of diamond using dressed-photon phonon etching, Journal of Physics D: Appl. Phys., **45**(47), (2012), 475302.
7) Yatsui, T., Hirata, K., Tabata, Y., Miyake, Y., Akita, Y., Yoshimoto, M., Nomura, W., Kawazoe, T., Naruse, M. and Ohtsu, M.: Self-organized near-field etching of the sidewalls of glass corrugations, Appl. Phys., B **103**(3), (2011), 527-530.
8) Akita, Y., Kato, Y., Hosaka, M., Ono, Y., Suzuki, S., Nakajima, A. and Yoshimoto, M.: Nanostripe patterning of glass surface by nanoimprint using self-organized oxide mold, Mat. Sci. Eng., B **161**(1-3), (2009), 151-154.

著者紹介

八井　崇
YATSUI Takashi
東京大学大学院工学系研究科准教授．1972年1月生まれ．2000年東京工業大学総合理工学研究科博士課程修了．博士(工学)．00年より科学技術振興事業団ERATO大津局在フォトンプロジェクト研究員，03年より科学技術振興機構SORSTナノフォトニクスチーム研究員，08年より現職．近接場光を用いたデバイス・加工の開発に従事．ゴッドフリード・ワグネル賞(2011年)，第6回大阪大学近藤賞 技術貢献賞(2012年)，Erlangen Innovation Award (2012年)等を受賞．
E-mail: yatsui@ee.t.u-tokyo.ac.jp

大津元一
OHTSU Motoichi
東京大学大学院工学系研究科教授．東京大学大学院工学系研究科総合研究機構ナノフォトニクス研究センター代表．1950年10月生まれ．1978年東京工業大学大学院理工学研究科　電子物理工学専攻博士後期課程修了．工学博士．1982年東京工業大学助教授，1991年同教授，2004年より現職．この間，JST ERATO「大津局在フォトンプロジェクト」においてプロジェクトリーダー(1998年～2003年)，「NEDO大容量光ストレージ技術の開発事業」において総括責任者(2000年～2004年)，「NEDO大容量光ストレージ技術の開発事業」において総括責任者(2000年～2004年)，NEDO省エネルギー革新技術開発事業・挑戦研究フェーズ「近接場光相互作用を用いた自己完結型超平坦物質形成技術の開発」において研究開発責任者(2009年～2011年)などを歴任．ナノフォトニクスの研究開発に従事．日本IBM科学賞(1988年)，紫綬褒章(2004年)，応用物理学会フェロー(2007年)，Julius Springer Prize(2009年)等を受賞．
E-mail: ohtsu@ee.t.u-tokyo.ac.jp

[Ⅳ] PUBLISHED BOOKS

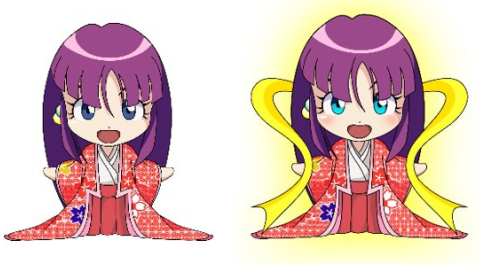

光科学技術革命

ドレスト光子はやわかり！

異次元の光技術入門

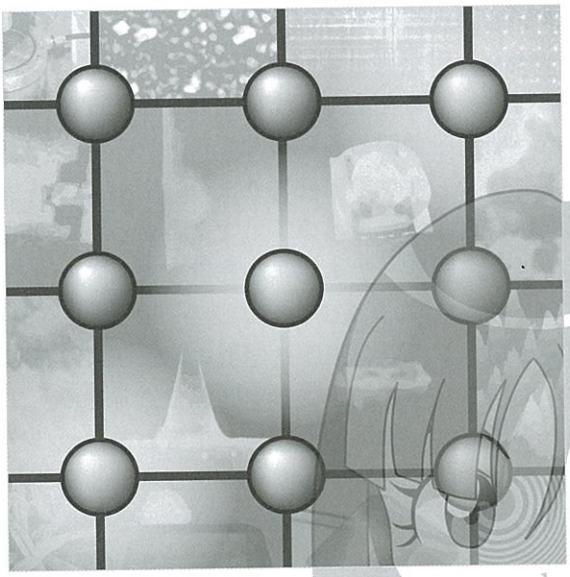

大津　元一 著
ナノフォトニクス工学推進機構　杉森　輝彦 編

丸善プラネット
139

目　次

第７章　さらに発展する技術とひろがる応用

こぼれ話

Chapter 9
A Nanophotonic Computing Paradigm: Problem-Solving and Decision-Making Systems Using Spatiotemporal Photoexcitation Transfer Dynamics

Masashi Aono, Song-Ju Kim, Makoto Naruse, Masamitsu Wakabayashi, Hirokazu Hori, Motoichi Ohtsu and Masahiko Hara

Abstract In contrast to conventional digital computers that operate as instructed by programmers, biological organisms solve problems and make decisions through intrinsic spatiotemporal dynamics in which their dynamic components process

M. Aono (✉)
Earth-Life Science Institute, Tokyo Institute of Technology, 201202 Ookayama, Meguro-ku, Tokyo 152-8550, Japan
e-mail: masashi.aono@elsi.jp

S.- J. Kim (✉)
Atomic Electronics Group, WPI Center for Materials Nanoarchitectonics (MANA), National Institute for Materials Science (NIMS), 1-1 Namiki, Tsukuba, Ibaraki 305-0044, Japan
e-mail: KIM.Songju@nims.go.jp

M. Naruse
Photonic Network Research Institute, National Institute of Information and Communications Technology, 4-2-1 Nukui-kita, Tokyo 184-8795, Koganei, Japan

M. Naruse · M. Ohtsu
Nanophotonics Research Center, Graduate School of Engineering, The University of Tokyo, 2-11-16 Yayoi, Bunkyo-ku 113-8656, Tokyo, Japan

M. Wakabayashi
Department of Biomolecular Engineering, Tokyo Institute of Technology, 4259 Nagatsuta, Midori-ku 226-8501, Yokohama, Japan

H. Hori
Interdisciplinary Graduate School of Medicine and Engineering, University of Yamanashi, Takeda 4-3-11, Kofu 400-8511, Yamanashi, Japan

M. Ohtsu
Department of Electrical Engineering and Information Systems Graduate School of Engineering, The University of Tokyo, 2-11-16 Yayoi, Bunkyo-ku 113-8656, Tokyo, Japan

M. Hara
Department of Electronic Chemistry, Interdisciplinary Graduate School of Science and Engineering, Tokyo Institute of Technology, 4259 Nagatsuta, Midori-ku, Yokohama 226-8503, Japan
e-mail: masahara@echem.titech.ac.jp

M. Naruse (ed.), *Nanophotonic Information Physics*,
Nano-Optics and Nanophotonics, DOI: 10.1007/978-3-642-40224-1_9,

Chapter 7
Engineering of a Nanometric Optical System Based on Optical Near-Field Interactions for Macro-Scale Applications

Naoya Tate, Makoto Naruse and Motoichi Ohtsu

Abstract The operating principle of our nanometric optical system is based on its hierarchical structure. This hierarchy is due to the characteristic behavior of optical near-fields induced by nanometric interactions between light and materials. In order to exploit such nanometric phenomena in macro-scale applications, it is essential to design and engineer each component of the system so that the optical near-field behavior can be extracted as macro-scale optical responses. Here we introduce the basic concept of our nanometric optical system, and we describe some demonstrations of macro-scale applications whose operation is based on this concept.

7.1 Introduction

Conventional optical phenomena are described by various physical quantities of light, such as intensity, wavelength, phase, and polarization. In the research field of optical computing [1] and its related technologies, several characteristics of conventional *propagating* light are used for implementing multidimensional information elements to realize novel kinds of information processing. The propagation speed, spatial parallelism, and multi-dimensionality of related phenomena made significant contributions to a number of developments in the 1980s, particularly the progress made in high-speed optical communications and high-density optical storage. On the other hand, conventional propagating light exhibits wave-like behavior

N. Tate (✉) · M. Ohtsu
The University of Tokyo, Tokyo, Japan
e-mail: tate@nanophotonics.t.u-tokyo.ac.jp

M. Ohtsu
e-mail: ohtsu@ee.t.u-tokyo.ac.jp

M. Naruse
National Institute of Information and Communications Technology, Tokyo, Japan
e-mail: naruse@nict.go.jp

M. Naruse (ed.), *Nanophotonic Information Physics*,
Nano-Optics and Nanophotonics, DOI: 10.1007/978-3-642-40224-1_7,

Chapter 1
Nanointelligence: Information Physics Fundamentals for Nanophotonics

Makoto Naruse, Naoya Tate, Masashi Aono and Motoichi Ohtsu

Abstract Nanophotonics has been extensively studied with the aim of unveiling and exploiting light-matter interactions that occur at a scale below the diffraction limit of light. From the viewpoint of information, novel architectures, novel design and analysis principles, and even novel computing paradigms should be considered so that we can fully benefit from the potential of nanophotonics for various applications. In this chapter, we first present some fundamental and emergent attributes associated with optical excitation transfer mediated by optical near-field interactions. Toward achieving a computing paradigm that surpasses the classical von Neumann architecture, we describe stochastic solution searching, which exploits the spatiotemporal dynamics of optical excitation transfer. Second, we show information security applications based on near-field applications, together with their theoretical and experimental foundations. Finally, we present a stochastic analysis of light-assisted self-organized material formation in order to gain a deeper understanding of the underlying physics. We consider that a common feature across all of these demonstrations is the extraction of "intelligent" functions and behaviors from an information-based standpoint—an idea represented by the title of this chapter, "*nanointelligence*".

M. Naruse (✉)
Photonic Network Research Institute, National Institute of Information and Communications Technology, 4-2-1 Nukui-kita, Koganei, Tokyo 184-8795, Japan
e-mail: naruse@nict.go.jp

N. Tate · M. Ohtsu
Department of Electrical Engineering and Information Systems and Nanophotonics Research Center, Graduate School of Engineering, The University of Tokyo, 2-11-16 Yayoi, Bunkyo-ku, Tokyo 113-8656, Japan

M. Aono
Earth-Life Science Institute, Tokyo Institute of Technology, 201202 Ookayama, Meguro-ku, Tokyo 152-8550, Japan
e-mail: masashi.aono@elsi.jp

M. Naruse (ed.), *Nanophotonic Information Physics*,
Nano-Optics and Nanophotonics, DOI: 10.1007/978-3-642-40224-1_1,

Motoichi Ohtsu

Dressed Photons

Concepts of Light–Matter Fusion Technology

Springer

Contents

Motoichi Ohtsu
Editor

Handbook of Nano-Optics and Nanophotonics

Volume 1

With 732 Figures and 24 Tables

Springer Reference

Motoichi Ohtsu
Editor

Handbook of Nano-Optics and Nanophotonics

Volume 2

With 732 Figures and 24 Tables

Springer Reference

Contents

Volume 1

Volume 2

Makoto Naruse
Editor

Nanophotonic Information Physics

Nanointelligence and Nanophotonic Computing

Springer

Contributors

Masashi Aono Earth-Life Science Institute, Tokyo Institute of Technology, 201201 Ookayama, Meguro-ku, Tokyo 152-8850, Japan, e-mail: masashi.aono@elsi.jp

Chris Dwyer Department of Electrical and Computer Engineering, Department of Computer Science, Duke University, Durham, NC, USA, e-mail: dwyer@ece.duke.edu

Masahiko Hara Department of Electronic Chemistry, Interdisciplinary Graduate School of Science and Engineering, Tokyo Institute of Technology, 4259 Nagatsuta, Midori-ku, Yokohama 226-8503, Japan, e-mail: masahara@echem.titech.ac.jp

Hirokazu Hori Interdisciplinary Graduate School of Medicine and Engineering, University of Yamanashi, 4-3-11 Takeda, Kofu, Yamanashi 400-8511, Japan, e-mail: hirohori@yamanashi.ac.jp

Keiichiro Kagawa Research Institute of Electronics, Shizuoka University, Hamamatsu, Japan, e-mail: kagawa@idl.rie.shizuoka.ac.jp

Seiya Kasai Graduate School of Information Science and Technology and Research Center for Integrated Quantum Electronics, Hokkaido University, N14, W9, Sapporo 060-0814, Japan, e-mail: kasai@rciqe.hokudai.ac.jp

Shoji Kawahito Research Institute of Electronics, Shizuoka University, Hamamatsu, Japan, e-mail: kawahito@idl.rie.shizuoka.ac.jp

Song-Ju Kim Atomic Electronics Group, WPI Center for Materials Nanoarchitectonics (MANA), National Institute for Materials Science (NIMS), 1-1 Namiki, Tsukuba, Ibaraki 305-0044, Japan, e-mail: KIM.Songju@nims.go.jp

Tarmer Mohamed Department of Electrical and Computer Engineering, University of Calgary, Calgary, Alberta, T2N 1N4, Canada, e-mail: tamer.mohamed@ucalgary.ca

Mohammad Mottaghi Department of Computer Science, Duke University, Durham, NC, USA, e-mail: mamad@cs.duke.edu